Theoretical X-ray Spectroscopy of Iron Complexes

Zur Erlangung des akademischen Grades eines

Doktors der Naturwissenschaften

(Dr. rer. nat.)

der Fakultät für Chemie und Biowissenschaften des
Karlsruher Instituts für Technologie (KIT) - Universitätsbereich
genehmigte

Dissertation

von

MChem

Andrew J. Atkins

aus Leicester,
England

Dekan:	Prof. Dr. M. Bastmeyer
Referent:	Dr. Ch. R. Jacob
Korreferent:	Prof. Dr. W. Klopper
	Prof. Dr. M. Kappes

Tag der mündlichen Prüfung: 25. Oktober 2013

Contents

1. Introduction

Transition metals are those elements which reside within the *d*-block of the Periodic Table.[1] The inclusion of the *d*-orbitals into the valence electronic structure of transition metals leads to an exhibition of many new and interesting properties usually not present in main group chemistry. One of the most important features of transition metal complexes is their ability to form highly coordinated complexes. Simply speaking, the reason transition metals form such complexes is that the partially filled *d*-shell is not the most stable electronic configuration. However, it is the partially filled *d*-orbitals which introduce many of the interesting properties of transition metals. This leads to many transition metal complexes having a magnetic moment, which can be exploited in work on single molecule magnets [2–4]. Also, many transition metal complexes can take part in redox reactions because many of their oxidation states are stable. This property is seen in many biochemical reactions, such as electron transport by photosystem I and II in photosynthesis [5]. Most importantly, transition metal complexes act as catalysts for many chemical reactions [6–8].

A catalyst is an entity which reduces the energy barrier of the reaction and hence, speeds up the reaction. In the field of catalysis we must distinguish two individual categories: homogenous and heterogenous. Heterogenous catalysis is defined as a catalytic system where the reactants and products are in a different phase to the catalyst, i.e., solid-phase catalyst and gaseous-phase reactant. It is the most common form found in industrial applications (e.g., Haber-Bosch process, sulphuric acid production, Fischer-Tropsch process), in part due to the simplicity of separating the reactants and products from the catalyst [8]. On the other hand, homogenous catalysis is defined as a catalytic system where the reactants and products are in the same phase as the catalyst, i.e., both in liquid-phase and miscible. It has also become more prevalent in industry (e.g., Wilkinson's catalyst, Wacker process), in part because of a higher specificity of the catalyst to the reaction [8]. However, homogenous catalysts also introduce an additional problem with the need for a separation step of the catalyst and the products [8]. Many homogenous catalysts contain a transition metal, e.g., $RhCl(PPh_3)_3$ used for the hydrogenation of alkenes, $RuCl_2(P(C_6H_{11})_3)(CHPh)$ used for the reorganisation of alkene substituents etc. A lot of interest has been given to the development of homogenous catalysts as their increased specificity provides a means to tune the catalyst and optimise performance, which is achieved for transition metal complexes by exchanging and/or modifying the ligands. To this end, characterisation of the complexes through spectroscopy is essential and as catalytic activity can be linked to the underlying electronic structure, specifically electronic spectroscopy. X-ray spectroscopic methods have been proven to be a powerful tool in the study of catalysts [9–16].

X-ray spectroscopy provides an element specific tool which probes the local nature of the chemical environment around the absorbing atom [17]. The element specificity of X-ray spectroscopy arises because X-ray spectroscopy probes transitions from or to core electronic states. These are usually not involved in bonding and therefore, can be considered to be more atomic in nature. In this respect the energies of the core states will then be primarily determined by the charge of the nucleus. X-ray spectroscopy covers a variety of techniques which utilise the X-ray region of the

[1] The IUPAC definition of a transition element is an element containing an incomplete d-shell [1] and therefore, excluding the d^{10} elements.

electromagnetic spectrum. Here, we will only mention the two main X-ray spectroscopic methods which probe the electronic structure: X-ray absorption and X-ray emission spectroscopy. X-ray absorption spectroscopy measures the intensity of the absorption of an X-ray photon by the absorber. It excites an electron originating in a core orbital into an unoccupied or continuum electronic state. X-ray emission measures the intensity of the emission of an X-ray photon by the process of an electron from a higher occupied state filling a core hole. Therefore, it provides a probe for the occupied electronic states of a complex. The combination of both absorption and emission spectroscopic methods enables, in part, a picture of the electronic states (both occupied and unoccupied) within the complex to be constructed.

In catalytic complexes this information on the electronic structure can then be related to the catalytic activity and any modification of the catalyst and the subsequent change in catalytic activity can be related to the changes in the electronic structure probed through X-ray spectroscopy. This might enable a process of ligand optimisation through understanding how the ligands affect the catalytic activity. However, a purely experimental approach to X-ray spectroscopy has limitations. In X-ray absorption spectroscopy, only the extended X-ray absorption fine structure (EXAFS) region of the spectra can be used to directly extract structural information [17, 18]. The X-ray absorption near edge structure (XANES) region at lower energies can only be analysed and information gathered through the use of model complexes (which are well characterised) for comparison [19, 20]. Hence, information on the electronic structure cannot be directly inferred from the spectra. However, the field of quantum-chemistry provides another tool with which to extract more information from the experimental spectra.

Quantum-chemistry provides a tool which enables us to calculate the electronic structure of a molecule. Many of the methods that are available make it possible to simulate the electronic spectra of molecules and thus, interpret the experimental spectra by assignment to electronic transitions in the calculated spectra.

Within this thesis we only consider iron complexes. Many industrial processes, such as the Monsanto process, Grubbs catalysis or carbon–carbon bond formation, use expensive and rare transition metals as their catalysts (Rh, Ir, Ru, Pd etc.). However, in nature we often observe catalytic processes using the more abundant transition metals, such as iron, in the reduction of atmospheric nitrogen to ammonia [21] or in the oxidation of H_2 by hydrogenases [22]. Along with this observation of iron catalysts in nature, the abundance of iron as a raw material also makes it attractive for the development of new catalysts because it is cheap. This is especially important in industry where large-scale processes are considered and the costs need to be minimised. However, development of catalysts needs tools to allow an informed design for a specific purpose and improved efficiency. To this end, we focus on X-ray spectroscopy at the K-edge, absorption or emission from or to the $1s$ orbital, respectively. Experimentally, the K-edge has the advantage that it requires "hard" X-rays, which enable *in situ* measurements [16, 23]. *In situ* measurements have the benefit of not requiring any sample preparation and the data can be collected under the catalytic reaction conditions. Such X-ray spectroscopic measurements on iron catalysts are present in the literature. For example, in reference [24] X-ray absorption spectra helped elucidate the oxidation state and that the palladium not the iron atom was the active site of the catalyst. In another paper they followed and elucidated information about the Michael addition reaction by iron catalysts using X-ray absorption techniques [12]. These studies illustrate how important a tool X-ray spectroscopy is in catalyst research.

This work is organised as follows. Chapter 2 discusses the available electronic spectroscopic methods and introduces X-ray spectroscopy. Chapter 3 elaborates on the calculation of the oscillator strengths in an origin-independent formalism, which are essential for the calculation of

K-edge X-ray spectra. Chapter 4 reviews the available methods in quantum-chemistry for solving the electronic Schrödinger equation, with a focus on the available methods for the calculation of X-ray spectra. Chapter 5 considers other aspects of the calculations, such as the basis set; exchange–correlation functional choice for (time-dependent) density functional theory; inclusion of relativistic effects and the comparability of results between programs.

After having introduced the discussion of computational aspects, we turn to the calculation of X-ray spectra of iron complexes. We have considered well-known complexes, ferrocene and carbonyl complexes. First, chapter 6 considers a test set of ferrocene derivatives. Within the chapter we calculated the X-ray absorption and X-ray emission spectra and thus, interpret the experimental observations. Chapter 7 concludes our applications by calculating the X-ray absorption spectra for a set of five iron carbonyl complexes. Finally we end this work with the inclusion of a summary in both English and German (chapters 8 and 9, respectively) with a short conclusion at the end.

2. Excited States in Chemistry

In chemistry, we are primarily concerned with molecules, their properties, and their reactivity. Quantum mechanics postulates that a molecule can be described through its wave function, $\Psi(\boldsymbol{R}, \boldsymbol{r})$. It depends on the nuclear coordinates of the system $\boldsymbol{R} = (\boldsymbol{R}_1, \boldsymbol{R}_2, \boldsymbol{R}_3, \ldots, \boldsymbol{R}_N)$, and the electron coordinates $\boldsymbol{r} = (\boldsymbol{r}_1, \boldsymbol{r}_2, \boldsymbol{r}_3, \ldots, \boldsymbol{r}_n)$. The wave function contains all information about the molecular system and a physical observable of the system corresponds to an operator acting on the wave function. The total energy of a system can be determined using the molecular Hamiltonian operator $\hat{H}_{\text{mol}}$. Therefore, using the time-independent Schrödinger equation, the energy levels of the system can be determined,

$$\hat{H}_{\text{mol}} \Psi_m^{\text{tot}}(\boldsymbol{R}, \boldsymbol{r}) = E_m^{\text{tot}} \Psi_m^{\text{tot}}(\boldsymbol{R}, \boldsymbol{r}), \tag{2.1}$$

where E_m^{tot} is the total energy for the system with the wave function Ψ_m^{tot}. The molecular Hamiltonian operator contains five terms,

$$\begin{aligned}\hat{H}_{\text{mol}} &= \hat{T}_N + \hat{T}_e + \hat{V}_{NN} + \hat{V}_{Ne} + \hat{V}_{ee} \\ &= -\sum_I^N \frac{\hbar^2}{2M_I} \nabla_I^2 - \sum_i^n \frac{\hbar^2}{2m_e} \nabla_i^2 + \frac{1}{2} \sum_{IJ}^N \frac{Z_I Z_J e^2}{4\pi\epsilon_0 |\boldsymbol{R}_{IJ}|} - \sum_I^N \sum_i^n \frac{Z_I e^2}{4\pi\epsilon_0 |\boldsymbol{R}_I - \boldsymbol{r}_i|} + \frac{1}{2} \sum_{ij}^n \frac{e^2}{4\pi\epsilon_0 |\boldsymbol{r}_{ij}|},\end{aligned} \tag{2.2}$$

where $\hat{T}_N$ and $\hat{T}_e$ are the kinetic energies of the nuclei and the electrons, respectively, and $\hat{V}_{NN}$, $\hat{V}_{Ne}$ and $\hat{V}_{ee}$ are the potential energies for the nuclear–nuclear repulsion, nuclear–electron attraction and electron–electron repulsion, respectively. M_I is the mass of nucleus I, m_e is the mass of an electron, Z_I is the charge of nucleus I and e is the charge of the electron. Finally, $|\boldsymbol{R}_{IJ}| = |\boldsymbol{R}_I - \boldsymbol{R}_J|$ is the distance between nucleus I and nucleus J and $|\boldsymbol{r}_{ij}| = |\boldsymbol{r}_i - \boldsymbol{r}_j|$ is the distance between electron i and electron j.

To simplify this full molecular Schrödinger equation, the Born-Oppenheimer (BO) approximation is usually applied. This states that because the nuclei are much more massive than the electrons, they can be considered stationary with regard to the electrons. As a consequence, one can employ a separation of variables where the total wave function is then expressed as a product of a nuclear, $\chi_N(\boldsymbol{R})$ and an electronic wave function, $\Psi_n^{(\boldsymbol{R})}(\boldsymbol{r})$,

$$\Psi_m^{\text{tot}}(\boldsymbol{R}, \boldsymbol{r}) = \chi_N(\boldsymbol{R}) \Psi_n^{(\boldsymbol{R})}(\boldsymbol{r}) \tag{2.3}$$

Here the electronic wave function is obtained by solving the Schrödinger equation for fixed positions of the nuclei,

$$\hat{H}_e \Psi_n^{(\boldsymbol{R})}(\boldsymbol{r}) = E_{e,n}^{(\boldsymbol{R})} \Psi_n^{(\boldsymbol{R})}(\boldsymbol{r}), \tag{2.4}$$

where $E_{e,n}^{(\boldsymbol{R})}$ is the electronic energy of the electronic wave function $\Psi_n^{(\boldsymbol{R})}(\boldsymbol{r})$ and $\hat{H}_e$ is the electronic Hamiltonian,

$$\hat{H}_e = \hat{T}_e + \hat{V}_{NN} + \hat{V}_{Ne} + \hat{V}_{ee}. \tag{2.5}$$

The electronic wave function still has a parametric dependence on the nuclear coordinates because of the operator $\hat{V}_{Ne}$ in the electronic Hamiltonian. Solving the electronic Schrödinger equation to determine the electronic wave function and the energy of the ground and possibly excited states is the central task of quantum chemistry. The approximations that have been developed to this end will be discussed in chapter 4.

The nuclear wave function $\chi_N(\boldsymbol{R})$ describes the motion of the nuclei and only depends on the nuclear coordinates. However, to calculate the total energy of the system, both the nuclear and electronic wave functions have to be considered and so we need to solve the full molecular Schrödinger equation (2.1) of which we can substitute in equations (2.3) and (2.5) and get

$$\left(\hat{T}_N + \hat{H}_e\right)\chi_N(\boldsymbol{R})\Psi_n^{(\boldsymbol{R})}(\boldsymbol{r}) = E_m^{\text{tot}}\chi_N(\boldsymbol{R})\Psi_n^{(\boldsymbol{R})}(\boldsymbol{r}), \tag{2.6}$$

which can be simplified to an equation only dependent on the nuclear wave function,

$$\left(\hat{T}_N + \hat{E}_{e,n}^{(\boldsymbol{R})}\right)\chi_N(\boldsymbol{R}) = E_m^{\text{tot}}\chi_N(\boldsymbol{R}). \tag{2.7}$$

In chemistry we are in many cases interested in the electronic ground-state properties of the molecules, and so usually solve the electronic Schrödinger equation (equation (2.4)) for the electronic ground-state only. However, when considering spectroscopic properties, knowledge of the excited states is also required. Such a situation is the calculation of electronic spectroscopy. For the calculation of electronic spectra, one considers the transitions between the different electronic states. In the following sections we will discuss different types of electronic spectroscopy.

If we consider absorption spectroscopy, the main transitions occur from the ground state to an excited state. This evolution of the ground state to the excited state induced by the interaction with electromagnetic radiation can be described using the time-dependent Schrödinger equation,

$$\hat{H}(t)\Psi(\boldsymbol{r},t) = i\hbar\frac{d\Psi(\boldsymbol{r},t)}{dt}. \tag{2.8}$$

This equation must be solved for a molecule interacting with an external electromagnetic field. However, solving this equation directly is very expensive as the time evolution of the high-dimensional wave function must be calculated. Therefore, time-dependent perturbation theory is applied instead [25]. We can rewrite the time-dependent Hamiltonian as,

$$\hat{H}(t) = \hat{H}_e + \hat{H}_{ext}(t) = \hat{H}^0 + \hat{H}^1(t), \tag{2.9}$$

where $\hat{H}_{ext}(t)$ is the operator pertaining to the time-dependent perturbation. Assuming that we know how to find the solution for the time-independent contribution, we need only account for the time-dependent perturbation, which is assumed to be small in comparison to the time-independent contribution.

One example of a time-dependent perturbation is an electromagnetic field that oscillates in time and space. Through the use of time-dependent perturbation theory, one can derive Fermi's golden rule [25, 26], which describes the probability of seeing a transition between the ground and the nth excited state,

$$\Gamma_{0n}(\omega) \propto |T_{0n}|^2\delta(\omega - \omega_{0n}), \tag{2.10}$$

where ω is the angular frequency of the incident radiation and ω_{0n} is the angular frequency required for a transition from the ground state to the n^{th} state, with $\hbar\omega_{0n} = (E_n - E_0) = E_{0n}$. Two parts

of Fermi's golden rule determine whether the transition occurs: the term $\delta(\omega - \omega_{0n})$, which will only be non-zero when the frequency of the electromagnetic radiation matches the frequency gap between the ground and an excited state, and the transition moment T_{0n} between the ground and n^{th} excited state, which has the form [26, 27],

$$T_{0n} = \frac{e}{m_e} \sum_i \langle \Psi_0 | \exp(i\boldsymbol{k} \cdot \boldsymbol{r}_i)(\hat{\boldsymbol{p}}_i \cdot \boldsymbol{\mathcal{E}}) + i\frac{g}{2} \exp(i\boldsymbol{k} \cdot \boldsymbol{r}_i)(\boldsymbol{k} \times \boldsymbol{\mathcal{E}}) \cdot \hat{\boldsymbol{s}}_i | \Psi_n \rangle, \tag{2.11}$$

where $\boldsymbol{\mathcal{E}}$ is the polarisation vector of the electromagnetic field and $\boldsymbol{k}$ is its wave vector, $\hat{\boldsymbol{p}}_i$ is the momentum operator, g is the electron g-factor and $\hat{\boldsymbol{s}}_i$ is the spin operator of electron i. Finally, Ψ_0 is the ground-state (electronic) wave function and Ψ_n is the (electronic) wave function of the n^{th} excited state. The transition moment contains the time-independent part of the external perturbation. It determines the probability of observing a transition between states by including how the electromagnetic radiation connects the states. The normal convention is to introduce the dimensionless oscillator strengths in place of the transition probability,

$$f_{0n} = \frac{2m_e}{e^2 E_{0n}} |T_{0n}|^2. \tag{2.12}$$

The dimensionless oscillator strength is proportional to the absorption cross section that can be observed in experiment.

The lowest energy transitions between electronic states, determined using the electronic Schrödinger equation, correspond to transitions observed experimentally when using visible and ultra-violet electromagnetic radiation and belongs to the technique UV-Vis spectroscopy. The higher energy transitions correspond to transitions observed experimentally when using X-ray radiation.

2.1. Ultra-Violet–Visible Spectroscopy (UV-Vis)

UV-Vis spectroscopy primarily utilises light in the wavelength region of 250 nm to 800 nm, even though the UV-region extends down to 10 nm. Light in this wavelength region interacts with the valence electrons in a molecule and excites them to the lowest unoccupied excited states.

Experimentally, UV-Vis is a very common tool used in characterising molecules, as the production of the correct wavelengths is relatively simple and can be housed in a simple apparatus. Commonly it is used as a fingerprint method [28–30] because each molecule will have specific transition wavelengths. But this is not the only use of UV-Vis spectroscopy, which has a wide range of applications, for example, following the progress of a reaction [31–34] and determining the number of species involved in a reaction [35].

In terms of a molecular system, the wavelengths used in the UV-Vis region of the electromagnetic spectrum are large; usually larger than the "size" of the considered molecule. This means that the electronic state only "sees" a constant electric field and none of the spatial oscillations in the electromagnetic radiation. This enables an approximation to the oscillator strengths (2.12) to be made. A Taylor expansion of $\exp(i\mathbf{k} \cdot \mathbf{r_i})$, describing the spatial oscillations, is performed and we approximate it as $\exp(i\mathbf{k} \cdot \mathbf{r_i}) \approx 1$. Using this approximation, we can express the oscillator strength using the electric-dipole operator (velocity representation), $\hat{\boldsymbol{\mu}}^p$, as

$$f_{0n} = \frac{2m_e}{e^2 E_{0n}} (\boldsymbol{\mathcal{E}} \langle \Psi_0 | \hat{\boldsymbol{\mu}}^p | \Psi_n \rangle)^2, \tag{2.13}$$

where,

$$\hat{\boldsymbol{\mu}}^p = \frac{e}{m_e} \sum_i \hat{\boldsymbol{p}}_i. \tag{2.14}$$

When considering the possibility of a transition, a transition will only be observed if the dipole matrix element is non-zero, i.e., $\langle \Psi_0 | \hat{\mu} | \Psi_n \rangle \neq 0$.

To determine whether this transition matrix element is non-zero, selection rules are most commonly used. The atomic selection rules are initially derived by evaluating the matrix element $\langle \phi_{n_1,l_1,m_{l1}} | \hat{\mu} | \phi_{n_2,l_2,m_{l2}} \rangle$ for the hydrogen-like atomic orbitals. Upon evaluation of the integral, only atomic orbitals with $\Delta l = \pm 1$, $\Delta n \geq 0$ and $\Delta m_l = 0, \pm 1$ provide a non-zero value for a dipole transition. However, the atomic selection rules can only be strictly applied to atoms where spherical symmetry is present. For molecules the atomic selection rules can provide an idea of the probability of a transition, but due to distortion of the atomic orbitals these selection rules are no longer strictly adhered to. On the other hand, if a molecule possesses strict point group symmetry, the probability of a transition occurring with dipole intensity for the molecule can be evaluated. An example would be to assess the probability of a *d*–*d* transition occurring in a transition metal complex with an octahedral O_h or a tetrahedral T_d point group. Each molecular orbital belongs to an irreducible representation (irrep) of the point group and for O_h symmetry the molecular orbitals containing a *d*-orbital contribution belong to the T_{2g} and E_g irreps, whilst for T_d they belong to the T_2 and E irreps. The product of two irreducible representations transforms as other irreducible representations of the point group. One of these irreps must pertain to the symmetry of the dipole operator (T_{1u} and T_2 for O_h and T_d, respectively) for a dipole transition to be allowed,

$$\text{For } O_h \quad E_g \times T_{2g} = T_{1g} + T_{2g}, \tag{2.15}$$

$$\text{For } T_d \quad T_2 \times E = T_1 + T_2. \tag{2.16}$$

Therefore, we can see that a dipole transition between the *d*-orbitals will not occur in a molecule with O_h symmetry, but will occur in T_d symmetry. A note here is that this only follows if the point group symmetry is strictly adhered to. In reality molecules might be distorted and so transitions may occur with dipole intensity that are formally forbidden by selection rules. Moreover, the presence of spin-orbit coupling can relax the selection rules.

An important variant of UV-Vis absorption spectroscopy is circular dichroism (CD) [36, 37]. It considers the interaction of left and right-handed circularly polarised light with a molecule and the difference in the absorption of the left and right-handed circularly polarised light provides information normal UV-Vis spectroscopy does not. However, this difference in intensity cannot be described using the dipole approximation anymore. Therefore, we must include more terms from the multipole expansion, specifically the magnetic-dipole and electric-quadrupole. The intensity within the CD spectra then comes from the interference between either the magnetic-dipole and the electric-dipole or the electric-quadrupole and the electric-dipole terms.

CD in the UV-Vis wavelength region has many applications. First one must distinguish that two types of CD are available: natural and magnetic. For natural CD (NCD) the molecule has to possess chirality, otherwise both the left and right-handed circularly polarised light will interact equally. For a chiral molecule the left and right-handed circularly polarised light will interact differently with the R or S-enantiomer. Therefore, NCD provides a method for differentiation of enantiomers within a solution. With the increase in interest in biological systems [38, 39] and the mimicking of these [40, 41], the capability to differentiate between enantiomers is very important. This is also important when considering reactions that produce chiral products and allows for the determination of the selectivity of the reaction mechanism [42–44] and hence, the enantiomeric excess of the final product. A final note on NCD is that it has also been used to study the chirality of interactions. An example is shown in reference [45] where an achiral chromophore has a chiral interaction with a metal complex.

Magnetic CD (MCD) measures the absorption of left and right-handed circularly polarised light of a non-chiral molecule in a magnetic field. For a difference in the absorption to occur, a molecule must contain unpaired electrons, which orient within the magnetic field. One of the uses of MCD is the capability to follow a change of spin state within a complex [36].

The UV-Vis spectra usually have very broad peaks which can provide difficulties with the interpretation. This problem arises, in part, due to the valence electronic structure having many discrete states which are very close in energy and which many have allowed transitions in the spectra as well as coupling of vibrations to the electronic transitions and the environment effects (such as solvent interactions). A secondary consideration is that the valence states are also delocalised over several atoms as they are the bonding/anti-bonding states. Therefore, the information which can be extracted is non-specific to an atom within the molecule. If we use higher energy wavelengths within the electromagnetic spectrum, such as X-rays, we start exciting core electrons, which are element specific.

2.2. X-ray Spectroscopy

X-ray spectroscopy is concerned with transitions involving core electronic states. It has become a widely used tool, even though experimentally it is more difficult to measure, due to the requirement of synchrotrons to produce X-rays of sufficient intensity and tuneable wavelengths [46]. A wide variety of techniques have been developed utilising X-ray sources to enable a large variety of information to be attained about a molecule, such as absorption and emission.

With the increase in energy of the electromagnetic radiation, the approximation to Fermi's golden rule, equation (2.10), is no longer sufficient. In experiment, peaks are present which cannot be attributed to dipole intensity alone. The reason the dipole approximation was considered valid in UV-Vis spectroscopy is that the wavelength is usually large compared to the "size" of the molecule. Therefore, the molecule only sees a constant electromagnetic field during its interaction. X-rays have a much shorter wavelength, which can become comparable to the dimensions of the molecule. Therefore, it "sees" the oscillations in the electromagnetic field and higher-order interactions must be included within Fermi's golden rule to describe all peaks present in the experimental spectra.

As mentioned, two of the methods used in X-ray spectroscopy are absorption and emission, which involve the excitation from the ground state or a relaxation from an excited state, respectively.

2.2.1. X-ray Absorption Spectroscopy (XAS)

XAS measures the absorption of X-rays by a molecule taking it from the ground state to an excited state via the excitation of a core electron. One of the major benefits of XAS is that the energy of a core electron is unique to an element [17], providing site specific information. Usually the core electronic states are not involved in any bonding. Therefore, XAS provides very local information.

X-ray absorption spectra are defined by the edge which is probed. An edge is defined as the energy required to excite a core electron into the continuum. This energy required to eject the core electron is specific to an element and for each element there are different core orbitals available and hence, different edges. The nomenclature for the different edges available within XAS experiments stems from the principle quantum number of the initial state. The highest energy edge for an element is the K-edge, which considers excitations from the $1s$ core orbital. The next edge category available is the L-edge, which can be separated into three individual L-edges. The L_1 edge considers

excitations from the $2s$ core orbital. The L_2 and L_3 edges consist of transitions from the $2p_{1/2}$ and $2p_{3/2}$ orbitals, respectively. The splitting of the $2p$ L-edge is due to the presence of spin–orbit coupling when $l \geq 1$. The size of the splitting and the ratio of the intensities at each edge does provide information on the spin–orbit coupling present [47]. As the principle quantum number increases, the label for the edge moves to the next letter, i.e., M for n=3; N for n=4 and so on. Figure 2.1 shows the edges available up to n=3.

Due to the different energies of the edges, they utilise different wavelength ranges in the X-ray spectrum. One usually distinguishes two categories for X-rays: hard and soft. Experimentally the distinction between the soft and hard X-rays is made by a difference in the equipment which must be used. A hard X-ray is defined as a wavelength which requires the use of crystals within the apparatus, whereas soft X-rays can be manipulated using gratings. However, hard and soft X-rays also provide specific advantages. Soft X-rays, due to having lower energy, have a low penetration depth and hence, require special sample preparation, such as large concentrations of the absorbing atom and thin samples. Soft X-ray spectroscopy is particularly important for characterising surfaces. Hard X-rays have a high penetration depth and allow for *in situ* measurements [16, 23]. Nevertheless, the edges probed by soft X-rays have their own advantages over those probed by hard X-rays. The K-edge of transition metals utilise hard X-rays, which have the advantages already mentioned, but the main transitions are the $1s \rightarrow np$ transitions. These final p-states usually reside close to the ionisation edge or within the continuum. However, the K-edge also contains low intensity transitions before the edge which are $1s \rightarrow nd$ transitions. Due to the weak intensity and usually very broad peaks, the information available on the d-states is limited. On the other hand the $L_{2/3}$ edges are composed of strong $2p \rightarrow nd$ transitions and are very sensitive to changes in the valence orbital composition. This enables detailed information to be determined about the complex, such as the amount of back-bonding present in a complex [48] or presence of multiple valence states [49]. However, for the first row transition metals the L-edge uses soft X-rays and therefore, the problems previously mentioned are encountered. For the second and third row transition metals the L-edge can be used *in situ* [50] as the energies required are very large and therefore hard X-rays must be used. In the heavier elements (second row) we also start observing the M-edges [51]. However, the $M_{4/5}$ edges are not used until the f-block elements [52, 53] where the $3d \rightarrow nf$ transitions are observed. A final consideration of the different edges is the lifetime of the final state, which is the primary source of the broadening observed in the spectra. In the K-edge very large broadening is observed due to the very short lifetime of the $1s$ core-hole [54], which can hide features. The lower energy edges have a longer lifetime of the core-hole states and therefore, a smaller broadening in the spectra. The reduced broadening seen in the $L_{2/3}$ edges compared to the K-edge is part of the reason of their high sensitivity to changes in the valence electronic structure.

Up to this point we have only considered the edges available within one element, specifically a transition metal. In a transition metal complex one can further distinguish between the edges on the transition metal and the edges of the ligands. The ligand and metal edges both provide complimentary information in determining characteristics of a transition metal complex. However, ligand edges are often very complicated to interpret due to the presence of several atoms of the same element which will all absorb at the same or similar energies. Nevertheless, information can be extracted from the ligand edges on the characteristics of the covalent bonding between the ligand and metal [55–58]. Within a transition metal complex, usually only one transition metal atom is present and therefore, the metal edges are more unique. However, there are cases where multiple metal atoms are present, which makes the interpretation more complicated, especially if metal-metal bonds are involved, see chapter 7 for an example.

Figure 2.1.: Diagrammatic representation of the absorption edges found in an element for up to n=3

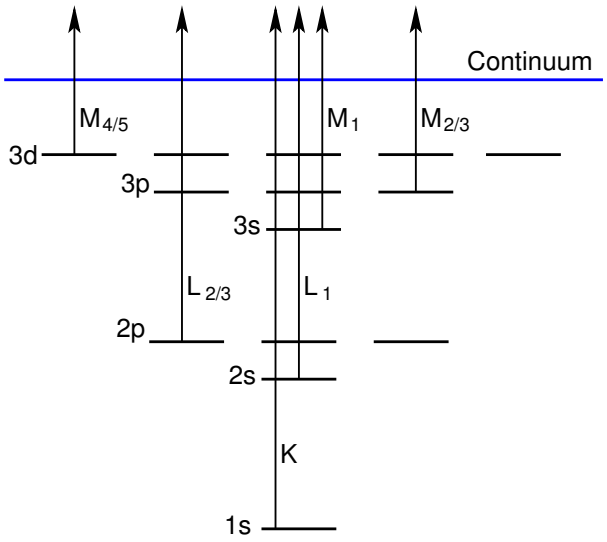

The X-ray absorption spectra can then be split into two regions which both provide specific information with regards to the absorber. This is shown in figure 2.2 for the K-edge. X-ray absorption near edge structure (XANES) is the lower energy region and includes the edge and any features up to approximately 50 eV above the edge [9]. XANES also has a sub-region which is identified as the pre-edge region, which consists of any features in the spectrum that occur before the edge. For example, in the K-edge of a transition metal complex these pre-edge peaks are the $1s \rightarrow 3d$ dipole-forbidden transitions. Extended X-ray absorption fine structure (EXAFS) is the region of the spectra greater than 50 eV above the edge.

Figure 2.2.: The separate regions of the K-edge spectra. The XANES region includes all features up to approximately 50 eV above the edge and any features occurring before the edge, also separated into a sub-region called the pre-edge. The EXAFS region contains all features greater than 50 eV above the edge.

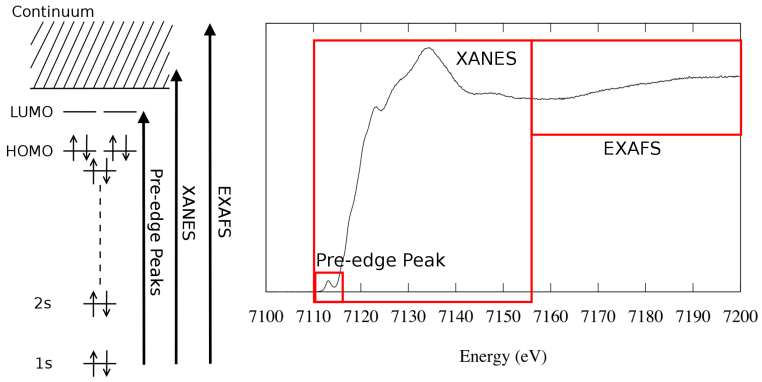

EXAFS is used to obtain structural information around the absorbing atom. It probes excitations to continuum states, which can be discussed in terms of the scattering of the electron by the nearest neighbour atoms. Using a Fourier transform of an EXAFS spectrum, the nearest neighbour distances and coordination number (within 20%) of the absorbing atom can be extracted [17,18,59].

The XANES region contains excitations to well defined unoccupied states before the edge (pre-edge) and the post-edge consists of multiple scattering events. Quantum-chemistry provides a way to interpret the pre-edge directly in terms of the electronic structure. However, experimentally the pre-edge features are primarily interpreted through the use of model complexes as a fingerprint technique [19,20]. Such studies have shown that the pre-edge peaks are determined by a number of factors in the environment of the absorbing atom. For instance, they can be used to determine the oxidation state of the absorber along with its symmetry and coordination environment [19,60–63].

In the discussion of the K-edge spectra, we mentioned the presence of $1s \rightarrow nd$ transitions. These transitions are dipole-forbidden by atomic selection rules, however they can be explained when going to higher-order transition moments through the transition having quadrupole intensity. The atomic selection rules for a quadrupole transition can once again be determined by evaluation of the transition matrix element, $\langle \phi_{n_2,l_2,m_{l2}} | \hat{Q} | \phi_{n_2,l_2,m_{l2}} \rangle$, for hydrogen-like atomic orbitals. Upon evaluation of the integral, only atomic orbitals with a $\Delta l = 0, \pm 2$ and $\Delta m_l = 0, \pm 1, \pm 2$ provide a non-zero value for a quadrupole transition. However, when dealing with molecules the atomic selection rules can not be rigorously applied and symmetry provides a better indication, if the molecule has a point group symmetry. Therefore, if we take the case of a molecule which belongs to the octahedral point group O_h, the s-orbital belongs to the A_{1g} irrep and the d-orbitals to the T_{2g} and E_g irreps. The quadrupole operator also belongs to the d-orbital irreducible representations. Now the product of the irreducible representation of the s-orbital and the d-orbitals are calculated,

$$\text{For } O_h \quad A_{1g} \times T_{2g} = T_{2g}, \tag{2.17}$$

$$A_{1g} \times E_g = E_g. \tag{2.18}$$

Therefore, a quadrupole transition can occur between an s- and a d-orbital according to symmetry. With regards to the quadrupole intensity present within the X-ray spectra, there has been a lot of interest in separating the dipole and quadrupole transitions experimentally, without the use of computational methods. Using linearly polarised light with an oriented sample was found to provide a means to perform this separation. The dipole transitions are isotropic and will be present at all angles, however, the quadrupole transitions are angle dependent. Therefore, by changing the angle of the incident radiation with respect to the oriented sample, the percentage of the transition attributed to quadrupole intensity can be deduced through the decrease in the intensity of the peak at the different angles [61,64].

2.2.2. X-ray Emission Spectroscopy (XES)

XES occurs after the absorption process and involves one of the higher energy electrons "dropping" into the core hole left by absorption. Therefore, it is a two-step process. For XES one may also define edges which are dependent on the location of the core hole and on the electronic state that the electron filling the core hole originates from. Here we will focus on the naming convention when the core hole resides in the $1s$ orbital (K-edge). Figure 2.3 shows the transitions and their labels (Siegbahn notation) that can be observed in such an experiment.

For a first row transition metal we can define three main edges available in X-ray emission. The lowest energy edge is the Kα in which the electron originates from the $2p$ orbitals. As mentioned for X-ray absorption, spin–orbit coupling is important for the $2p$ states and we can define a Kα_1 and Kα_2 edge for the $2p_{3/2}$ and $2p_{1/2}$, respectively. The next edge is the K$\beta_{1,3}$, where the electron originates from the $3p$ orbitals. The final edge is the K$\beta_{2,5}$ edge, also termed as valence-to-core (V2C) emission, where the electron originates from the valence orbitals in transition metal complexes. Each edge has found uses within the literature. The Kα edges have been used to

Figure 2.3.: Diagrammatic representation of the emission edges found in an element for up to n=3

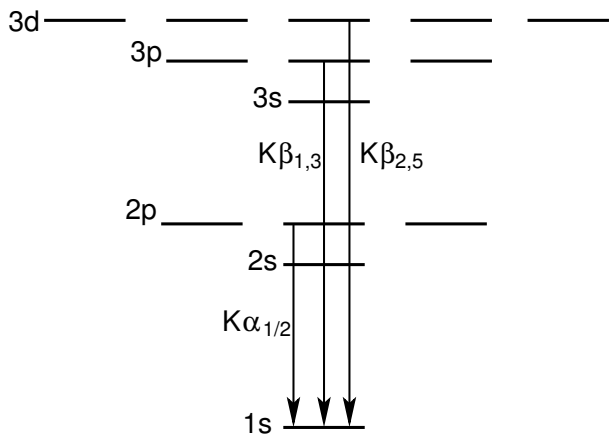

Figure 2.4.: The process of XES. Absorption of a photon into the continuum, followed by the transition of an electron in the occupied states to the unoccupied core-state, emitting an X-ray photon to dissipate its energy. Here a K$\beta_{2,5}$ transition is shown.

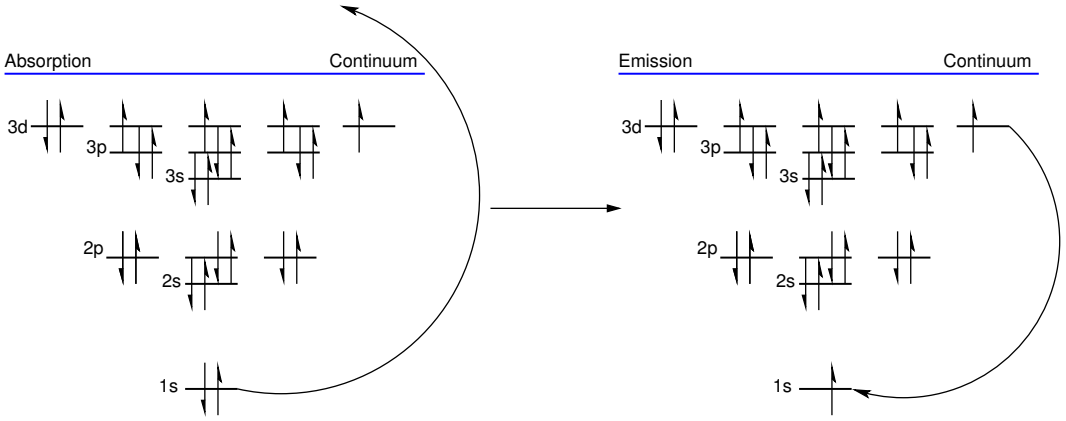

distinguish between molecules with the same absorber atom, e.g. nitrogen, where the $2p$ orbitals are involved in bonding [65]. The K$\beta_{1,3}$ is used to normalise emission spectra and has also been shown to be an indicator of the spin state of a molecule (high or low spin) [66]. Finally, the K$\beta_{2,5}$ edge has been shown to provide information on the nature of the bound ligand [67] as well as determining the interactions between an absorbing atom and its surrounding atoms [68, 69]. An important note when considering X-ray emission is that each transition that occurs within the spectra has a different peak broadening as the final state, and therefore the lifetime, of each transition is unique.

X-ray emission has an inherent problem. The molecular system is trying to dissipate the increase in its energy from the initial excitation, and two alternative pathways are present: non-radiative and radiative. The non-radiative pathway, also termed as Auger emission, is the major pathway for energy dissipation. The process involves the transfer of energy to another electron, which is now ejected into the continuum and the non-ejected electron decays into the core-hole. Radiative emission (fluorescence) is the minor pathway where the decaying electron emits a photon. In X-ray emission we measure the intensity of the emitted photon, which can then provide information on

the electronic state the electron originated from. However, with radiative decay being the minor pathway, the photon flux in X-ray emission is small compared to a unit of absorption and very sensitive detectors are required.

2.2.3. Resonant Inelastic X-ray Scattering (RIXS)

RIXS is a spectroscopic method which employs the principles of X-ray absorption and X-ray emission spectroscopy to measure the inelastic scattering of photons by a molecular system. The first step in RIXS is the absorption of an X-ray photon by the ground state to form the core ionised state (final state of XAS pre-edge peaks but intermediate state here) with the core electron now residing in the valence shell. Due to instability of the core ionised state, an electron "falls" down from a higher energy state to fill the core hole. This process is depicted in figure 2.5 for the example of the K-edge. The intermediate state formed is $1s^1 3d^{n+1}$, and the final state measured shown here is $2p^5 3d^{n+1}$, the same as when measuring the L-edge of a transition metal.

Figure 2.5.: The process of RIXS. Going from the initial state through absorption to the intermediate state, which then decays into the final state through emission.

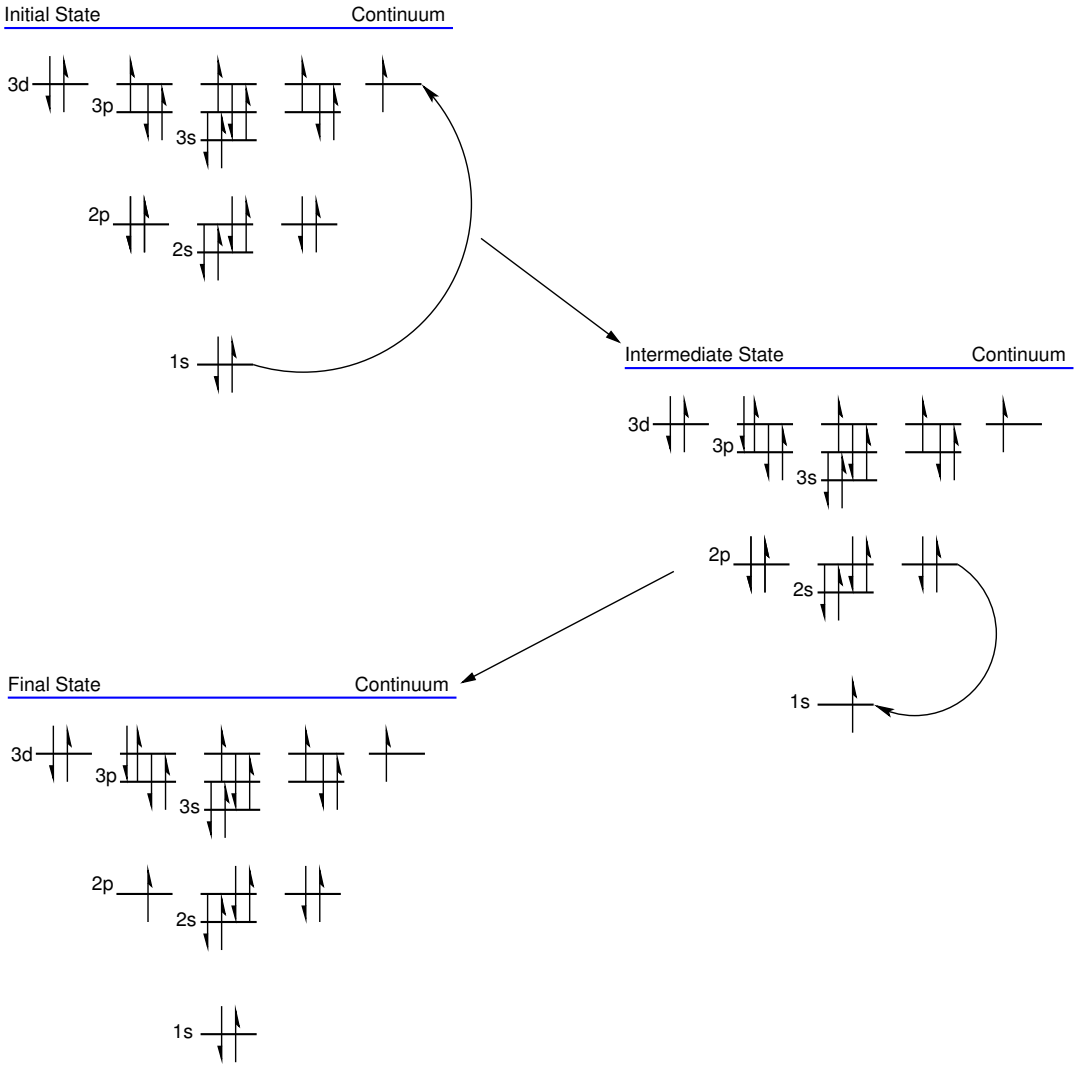

The full RIXS plane consists of three axes, the incident photon energy Ω_{abs}, the emitted photon energy Ω_{em} and the energy transfer $\Omega_{abs} - \Omega_{em}$. The energy transfer axis then pertains to the increased energy of the final state relative to the ground state. The most common plots used are the energy transfer versus the incident energy [70, 71]. Plotting over one axis and integrating the intensities of the peaks along that axis provides insights into different properties of the electronic states of a molecular system or may provide the original spectra done from a conventional XAS or XES measurement (for more information on the different axis and plots that can be formed, see reference [70]).

RIXS has been used for many purposes, the primary being the increase in lifetime resolution of XAS [12, 72], see below. Also polarisation-dependent RIXS has been employed to separate excitations within crystal structures [73–75]. For more information on RIXS see references [70, 71, 76, 77].

High Energy Resolution Fluorescence Detection XANES (HERFD-XANES)

HERFD-XANES is a variant of RIXS, where the resolution of conventional XAS measurements is significantly improved, showing more detail in the spectra [78, 79]. To carry out a HERFD-XANES measurement one tunes the emission detector to a specific energy, such as the K$\beta_{1,3}$ line, of the complex and then scans over the incident energy. The absorption spectrum is then plotted as function of the emission intensity, which varies with the changes in the absorption of the incident energy. This reduces the lifetime broadening of the peaks because the final state has a longer lifetime than the intermediate state (i.e., the final state of XAS). In conventional K-edge absorption measurements the broadening is usually so large because the final state has an extremely short lifetime [11, 80]. For more information on HERFD-XANES, see chapter 6.

2.2.4. Chiral Variants of X-ray Spectroscopy

The element specificity of X-ray spectroscopy has lead to the development of several variants which enable the study of other local properties of molecules. As for UV-Vis spectroscopy, circular dichroism (CD) can also be observed in XAS. The use of circularly polarised light at the X-ray wavelengths can provide more detailed information on the local environment of the absorber. One distinguishes two types of circular dichroism experiments available in X-ray spectroscopy: natural (NCD) and magnetic (MCD).

For both types of CD, a measure of the difference in absorption between left and right-handed circularly polarised light is the Kuhn dissymmetry factor,

$$g = 2\frac{(I_L - I_R)}{I_L + I_R}, \tag{2.19}$$

where I_L is the intensity of absorption for left-handed circularly polarised light and I_R is the intensity of the absorption for right-handed circularly polarised light and the intensity I is related to the oscillator strength f_{0n} by an unknown constant factor. The magnitude of the Kuhn dissymmetry factor is an indicator of the size of the effect. So far, the largest effect has been seen for X-ray magnetic circular dichroism (XMCD), up to 10^{-1} for XMCD and is a couple of orders of magnitude smaller for XNCD [81].

The intensity in XNCD measurements arise from the electric-dipole–electric-quadrupole interference term, and it has also been determined that this is the only term which will contribute to an XNCD spectra due to time reversal rules for the electronic properties [82]. The electric–dipole–magnetic-dipole interference term will not contribute to XNCD due to the magnetic-dipole

selection rules ($\Delta l = 0$ and $\Delta n = 0$). For XMCD the intensity of the transitions is due to the electric-dipole term.

XMCD measures the interaction of circularly polarised light with a complex in a magnetic field and was the first of the two variants to be detected and used in 1987 by Shutz et al. [83]. An advantage XMCD has is that the magnetic field induces the chiral effect and the reversal of the magnetic field reverses the sign of the absorption. This entails that only either left or right-handed circularly polarised light is needed, not both [81]. As the production of circularly polarised light in the X-ray wavelengths of sufficient intensity was problematic, this reduced the size of the problem as only one form was needed.

The size of the absorption difference in XMCD has several determining factors, of which one of the largest is relativistic effects, primarily spin-orbit coupling. Moreover, a larger problem arises in relating the XMCD spectra to the magnetic properties of the molecule, such as the magnetic moment, which is related to the number of unpaired electrons or the local magnetic moment of the initial state. Therefore, a set of rules was derived that allow the absorption difference to be related to these properties of the molecular system and are stated as magneto-optical sum rules [84–88]. The veracity of these sum rules was verified at the L-edge for transition metals [89].

Here, we must also mention that not all the absorption edges provide the same information in XMCD spectra as they probe different final states. An interesting example is that of the K-edge ($1s \rightarrow np$), which for transition metals, the final states usually reside in the continuum or are very diffuse. This infers that the data which can be extracted is different from that of any lower energy edge. However, for transition metal complexes the $L_{2/3}$-edges are mainly used, due to the dipole transitions being to the *nd* states, which determine most of the magnetic properties of the complex [90]. Moreover, the preference for the $L_{2/3}$-edge is not only due to the final state probed, but also the magnitude of the observed absorption differences. Spin-orbit coupling plays a role in the magnitude of these effects and as it is negligible in both the $1s$ state and the final p-states at the K-edge [91], whilst these are very far from the nucleus, they are significant at the $L_{2/3}$-edge in the initial $2p$-states as well as non-negligible in the final d-states [47].

X-ray natural circular dichroism (XNCD) measures the interaction of circularly polarised light with a complex in its natural state that possesses chirality and was believed to be first observed several years later than XMCD by Siddons et al. in 1990 for cobalt and its compounds [92]. However, this observation was later disputed as not a true observation of XNCD due to the use of elliptically polarised light [93]. Nevertheless, the presence of a natural circular dichroism effect in the X-ray wavelengths was believed possible [94] and the main restriction was the experimental apparatus until 1996 [81]. Not long after 1996, the first unambiguous measurement of XNCD was made by Goulon et al. for the $LiIO_3$ crystal [95]. One of the problems faced in XNCD measurements is that the intensities tend to be small. This is due to the electric-dipole–electric-quadrupole interference term, which also vanishes in most systems. To observe XNCD a crystal must have a structure which has chirality and, therefore, the interference term does not disappear, such as the $LiIO_3$ crystal which is gyrotropic. Most observations made of a significant XNCD effect were not performed at the K-edge, only the L-edge [93]. However, Stewart et al. measured a large XNCD effect at the K-edge of a chiral cobalt complex, which was chosen due to a large pre-edge feature in the normal absorption spectra [96]. Although these measurements were made, the amount of literature in which XNCD has been used is minimal. Nonetheless, interest is still present with a paper published on the presence of an XNCD effect observed in a copper crystal ($CsCuCl_3$) in 2008 [97]. For more information, we refer to two review articles on the optical activity of X-rays, one by Goulon et al. [98] and one by Rogalev et al. [99].

The next chapter will cover in more detail the calculation of the intensities for electronic spectroscopy, of which many of the ideas and some of the details have been introduced within this chapter.

3. Origin-Independent Intensities

In the previous chapter the importance of electronic spectroscopy for the determination of many properties of molecules was highlighted. Specifically for X-ray spectroscopy, the use of purely experimental techniques is limited. The spectroscopic methods are often relegated to a fingerprint technique, in which comparison with model complexes is essential [19, 20, 60, 63, 100]. With the advent of theoretical methods for the prediction of X-ray spectra it becomes possible to interpret the experimental spectra without the use of model complexes [65, 67, 68, 101–104]. However, to attain even more information from X-ray spectra it is essential that further development of the theoretical methods is carried out [105].

Many theoretical methods have been developed to calculate excitation energies for electronic spectroscopy which will be discussed in more detail in chapter 4. Calculating only the excitation energies is, however, not enough for interpreting the spectra, as not all calculated transitions will actually contribute to the spectra. To predict the full spectra the calculation of intensities for each transition is also necessary.

To derive the equations needed for calculating the intensities we revisit the theory of interaction of electromagnetic radiation with a molecule. The electromagnetic radiation consists of time-dependent external electric and magnetic fields and can be expressed through the scalar potential $\phi(\boldsymbol{r})$ and the vector potential $A(\boldsymbol{r}, t)$ as,

$$\phi(\boldsymbol{r}, t) = 0 \tag{3.1}$$

$$\boldsymbol{A}(\boldsymbol{r}, t) = -A_0 \, \boldsymbol{\mathcal{E}} \cos(\boldsymbol{k} \cdot \boldsymbol{r} - \omega t), \tag{3.2}$$

where A_0 is the amplitude of the wave, ω is the angular frequency, $\boldsymbol{k}$ is the wave vector which points in the direction of propagation, $k = |\boldsymbol{k}|$, and $\boldsymbol{\mathcal{E}}$ is the polarisation vector that is perpendicular to the direction of propagation. From these scalar and vector potentials one obtains the oscillating electric and magnetic fields,

$$\boldsymbol{E}(\boldsymbol{r}, t) = -\boldsymbol{\nabla}\phi(\boldsymbol{r}, t) - \frac{1}{c}\frac{\partial \boldsymbol{A}(\boldsymbol{r}, \boldsymbol{t})}{\partial t} = A_0 k \, \boldsymbol{\mathcal{E}} \sin(\boldsymbol{k} \cdot \boldsymbol{r} - \omega t) \tag{3.3}$$

$$\boldsymbol{B}(\boldsymbol{r}, t) = \boldsymbol{\nabla} \times \boldsymbol{A}(\boldsymbol{r}, t) = A_0(\boldsymbol{k} \times \boldsymbol{\mathcal{E}}) \sin(\boldsymbol{k} \cdot \boldsymbol{r} - \omega t). \tag{3.4}$$

These are then considered as a time-dependent perturbation and included with time-dependent perturbation theory (for details, see reference [25]). Fermi's golden rule can be derived as a result, which describes the probability of a transition occurring when the energy, $\hbar\omega$, of the external field is equal to an energy gap, $\hbar\omega_{0n} = (E_n - E_0)$, between the ground state and an excited state of the molecule,

$$\Gamma_{0n}(\omega) = \frac{\pi A_0^2}{2\hbar c^2} \, |T_{0n}|^2 \; \delta(\omega - \omega_{0n}). \tag{3.5}$$

Where $\Gamma_{0n}(\omega)$ is the transition probability at a given wavelength, c is the speed of light. Here the

transition moment, T_{0n}, is introduced,

$$T_{0n} = \frac{e}{m_e} \sum_i \left\langle 0 \middle| \exp(\mathrm{i}\boldsymbol{k} \cdot \boldsymbol{r}_i) \, (\hat{\boldsymbol{p}}_i \cdot \boldsymbol{\mathcal{E}}) + \mathrm{i} \, \frac{g}{2} \exp(\mathrm{i}\boldsymbol{k} \cdot \boldsymbol{r}_i) \, (\boldsymbol{k} \times \boldsymbol{\mathcal{E}}) \cdot \hat{\boldsymbol{s}}_i \middle| n \right\rangle, \tag{3.6}$$

where e and m_e are the charge and mass of an electron, respectively, $\hat{\boldsymbol{p}}_i$ is the momentum operator, g is the electron g-factor, $\hat{\boldsymbol{s}}_i$ is the spin operator, Ψ_0 is the ground-state wave function and Ψ_n is the nth excited state wave function.

Instead of the transition moment, one commonly introduces the dimensionless oscillator strength,

$$f_{0n} = \frac{2m_e}{e^2 E_{0n}} |T_{0n}|^2. \tag{3.7}$$

Calculating the matrix elements in equation (3.7) is in principle possible, but is cumbersome and in general not feasible. The required integrals are difficult to compute analytically (for a possible approach, see reference [106]), and because of the dependence on the wave vector $\boldsymbol{k}$, the operator in T_{0n} is different for each excitation. Usually, a Taylor expansion of $\exp(i\boldsymbol{k} \cdot \boldsymbol{r}_i)$ is performed, and the most common approximation is to include only the first term, $\exp(i\boldsymbol{k} \cdot \boldsymbol{r}_i) \approx 1$. This is sufficient for typical molecules and wavelengths in the ultraviolet or visible range where the wavelength is large compared to the molecular size. This approximation is termed as the dipole approximation and has been discussed in the previous chapter. This approximation corresponds to assuming that the oscillating electric field is constant over the whole molecule.

However, for the short wavelengths used in hard X-ray spectroscopy this approximation is not adequate and higher-order terms need to be included, i.e.,

$$\exp(\mathrm{i}\boldsymbol{k} \cdot \boldsymbol{r}_i) = 1 + \mathrm{i}(\boldsymbol{k} \cdot \boldsymbol{r}_i) - \frac{1}{2}(\boldsymbol{k} \cdot \boldsymbol{r}_i)^2 + \cdots . \tag{3.8}$$

The failure of the dipole approximation becomes apparent for the K-edge of transition metal complexes. In this case the edge itself consists of $1s \rightarrow 4p$ transitions, which are dipole allowed. The pre-edge features consist of excitations from the $1s$ core orbital to valence-states. For transition metal complexes the lowest unoccupied valence-states contain metal $3d$ orbitals. Such transitions are dipole-forbidden, but nevertheless have an experimentally observable intensity in the spectrum. Thus it becomes necessary to go beyond the dipole approximation.

For the calculation of hard X-ray spectra, the Taylor expansion has previously been extended to the first order-terms [107], which were found to be origin-dependent in the presence of a dipole contribution to the intensity. To counteract this dependence on the origin, a scheme was proposed to minimise the higher-order contributions to the intensity with respect to the dipole contribution. This method moves the origin for each excitation to the point at which the higher-order contributions are minimised. Usually, this is equivalent to placing the origin at the atom where the excitation occurs. However, if there are very small dipole contributions compared to the quadrupole, then the origin is placed at unfeasibly large distances from the molecule and the resulting intensity is significantly affected [108]. Moreover, this scheme will also fail in situations where the excitations are delocalised over different atomic centres, such as for metal K-edge spectra in polynuclear transition metal clusters or for ligand edge spectra.

When considering a physical observable there should be no dependence on the origin of the system. Thus, a theoretical framework needs to be devised for the calculation of origin-independent oscillator strengths. Within this chapter we will outline a theory for calculating oscillator strengths that are origin-independent.

3.1. Multipole Expansion

As a starting point for the theory of origin-independent oscillator strengths, the Taylor expansion of equation (3.8) is inserted into the transition moment, given in equation (3.6). In this we can separate the terms depending on their order in the wave vector $\boldsymbol{k}$,

$$T_{0n} = T_{0n}^{(0)} + T_{0n}^{(1)} + T_{0n}^{(2)} + \cdots \tag{3.9}$$

From here the next step is to consider the form of the transition moment for each order of $\boldsymbol{k}$.

3.1.1. Zeroth Order: Electric Dipole

For zeroth order in the wave vector we have

$$T_{0n}^{(0)} = \frac{e}{m_e} \sum_i \langle 0 | \hat{\boldsymbol{p}}_i \cdot \boldsymbol{\mathcal{E}} | n \rangle = \boldsymbol{\mathcal{E}} \cdot \langle 0 | \hat{\boldsymbol{\mu}}^p | n \rangle, \tag{3.10}$$

where $\hat{\boldsymbol{\mu}}^p$ is the electric-dipole operator in the velocity representation.

$$\hat{\boldsymbol{\mu}}^p = \frac{e}{m_e} \sum_i \hat{\boldsymbol{p}}_i \tag{3.11}$$

The velocity representation for the operator can be converted to the more common length representation by using the commutator,

$$[r_{i,\alpha}, \hat{H}_0] = \frac{\mathrm{i}\hbar}{m} \hat{p}_{i,\alpha} \,, \tag{3.12}$$

which provides the relationship for the electric-dipole transition moment (for more details, see Appendix A of reference [27]),

$$\langle 0 | \hat{p}_{i,\alpha} | n \rangle = -\mathrm{i} E_{0n} \frac{m}{\hbar} \langle 0 | r_{i,\alpha} | n \rangle. \tag{3.13}$$

For exact eigenfunctions of the Schrödinger equation the length and velocity representations are equivalent and switching between them has no effect on the final result. This is however, not the case for approximate solutions obtained in a finite basis set. We will return to this point in section 3.4.

Using equation (3.13), one obtains,

$$\langle 0 | \hat{\boldsymbol{\mu}}^p | n \rangle = -\frac{\mathrm{i}}{\hbar} E_{0n} \langle 0 | \hat{\boldsymbol{\mu}} | n \rangle, \tag{3.14}$$

where we introduced the electric-dipole moment operator in the length representation

$$\hat{\boldsymbol{\mu}} = e \sum_i \hat{\boldsymbol{r}}_i. \tag{3.15}$$

Thus, for the zeroth-order contribution, we arrive at

$$T_{0n}^{(0)} = T_{0n}^{(\mu)} = -\mathrm{i} \frac{E_{0n}}{\hbar} \Big(\boldsymbol{\mathcal{E}} \cdot \langle 0 | \hat{\boldsymbol{\mu}} | n \rangle \Big). \tag{3.16}$$

3.1.2. First Order: Electric Quadrupole and Magnetic Dipole

In the first order in $\boldsymbol{k}$, we find

$$T_{0n}^{(1)} = \frac{\mathrm{i}\,e}{m_e} \sum_i \big\langle 0\big|(\boldsymbol{k}\cdot\boldsymbol{r}_i)(\hat{\boldsymbol{p}}_i\cdot\boldsymbol{\mathcal{E}})\big|n\big\rangle + \frac{\mathrm{i}\,eg}{2m_e} \sum_i \big\langle 0\big|(\boldsymbol{k}\times\boldsymbol{\mathcal{E}})\cdot\hat{\boldsymbol{s}}_i\big|n\big\rangle. \tag{3.17}$$

The matrix elements in the first term can be split into one term that is symmetric and one that is antisymmetric with respect to interchanging the wave vector $\boldsymbol{k}$ and the polarisation vector $\boldsymbol{\mathcal{E}}$ via

$$\begin{aligned}\big\langle 0\big|(\boldsymbol{k}\cdot\boldsymbol{r}_i)(\hat{\boldsymbol{p}}_i\cdot\boldsymbol{\mathcal{E}})\big|n\big\rangle =& \frac{1}{2}\big\langle 0\big|(\boldsymbol{k}\cdot\boldsymbol{r}_i)(\hat{\boldsymbol{p}}_i\cdot\boldsymbol{\mathcal{E}}) + (\boldsymbol{k}\cdot\hat{\boldsymbol{p}}_i)(\boldsymbol{r}_i\cdot\boldsymbol{\mathcal{E}})\big|n\big\rangle \\ &+ \frac{1}{2}\big\langle 0\big|(\boldsymbol{k}\cdot\boldsymbol{r}_i)(\hat{\boldsymbol{p}}_i\cdot\boldsymbol{\mathcal{E}}) - (\boldsymbol{k}\cdot\hat{\boldsymbol{p}}_i)(\boldsymbol{r}_i\cdot\boldsymbol{\mathcal{E}})\big|n\big\rangle.\end{aligned} \tag{3.18}$$

From the symmetric first term and using Einstein's convention of implicit summation over repeated Greek indices, which we use to label the Cartesian components x, y, and z, we obtain

$$T_{0n}^{(Q)} = \frac{\mathrm{i}\,e}{2m_e} \sum_i k_\alpha \mathcal{E}_\beta \big\langle 0\big|r_{i,\alpha}\hat{p}_{i,\beta} + \hat{p}_{i,\alpha} r_{i,\beta}\big|n\big\rangle = \frac{\mathrm{i}}{2}\, k_\alpha \mathcal{E}_\beta \left\langle 0\middle|\hat{Q}^p_{\alpha\beta}\middle|n\right\rangle \tag{3.19}$$

Once more, by using the commutator,

$$[r_{i,\alpha} r_{i,\beta}, \hat{H}_0] = \frac{\mathrm{i}\hbar}{m}(\hat{p}_{i,\alpha} r_{i,\beta} + r_{i,\alpha}\hat{p}_{i,\beta})\,, \tag{3.20}$$

the matrix elements in the velocity representation can be related to those in the conventional length representation, and one arrives at

$$T_{0n}^{(Q)} = \frac{E_{0n}}{2\hbar}\, k_\alpha \mathcal{E}_\beta \left\langle 0\middle|\hat{Q}_{\alpha\beta}\middle|n\right\rangle, \tag{3.21}$$

where

$$\hat{Q}_{\alpha\beta} = e\sum_i r_{i,\alpha} r_{i,\beta} \tag{3.22}$$

is the operator of the electric-quadrupole moment in the length representation. In contrast to many other authors [107, 109], a traceless version of the quadrupole tensor is not introduced here. The traceless definition arises from the expansion of $1/|\boldsymbol{r}|$ that is often introduced in the context of intermolecular interactions, whereas in the case of an expansion of the exponential $\exp(i\boldsymbol{k}\cdot\boldsymbol{r})$ considered here the definition of equation (3.22) is more natural. Nevertheless, because the wave vector $\boldsymbol{k}$ and the polarization vector $\boldsymbol{\mathcal{E}}$ are orthogonal, the diagonal elements of the electric-quadrupole transition moments do not enter here and it would, therefore, be possible to alter their trace without consequences.

For the antisymmetric second term, we can use that $(\boldsymbol{k}\cdot\boldsymbol{r}_i)$ and $(\hat{\boldsymbol{p}}_i\cdot\boldsymbol{\mathcal{E}})$ commute because $\boldsymbol{k}$ and $\boldsymbol{\mathcal{E}}$ are orthogonal and then apply the vector identity

$$(\boldsymbol{a}\cdot\boldsymbol{c})(\boldsymbol{b}\cdot\boldsymbol{d}) - (\boldsymbol{b}\cdot\boldsymbol{c})(\boldsymbol{a}\cdot\boldsymbol{d}) = (\boldsymbol{a}\times\boldsymbol{b})(\boldsymbol{c}\times\boldsymbol{d}) \tag{3.23}$$

to obtain,

$$\begin{aligned}T_{0n}^{(m')} &= \frac{\mathrm{i}\,e}{2m_e}\sum_i \big\langle 0\big|(\boldsymbol{k}\cdot\boldsymbol{r}_i)(\hat{\boldsymbol{p}}_i\cdot\boldsymbol{\mathcal{E}}) - (\boldsymbol{k}\cdot\hat{\boldsymbol{p}}_i)(\boldsymbol{r}_i\cdot\boldsymbol{\mathcal{E}})\big|n\big\rangle \\ &= \mathrm{i}\frac{e}{2m_e}\sum_i \big\langle 0\big|(\boldsymbol{k}\times\boldsymbol{\mathcal{E}})(\boldsymbol{r}_i\times\hat{\boldsymbol{p}}_i)\big|n\big\rangle = \mathrm{i}c\,(\boldsymbol{k}\times\boldsymbol{\mathcal{E}})\big\langle 0\big|\hat{\boldsymbol{m}}'\big|n\big\rangle,\end{aligned} \tag{3.24}$$

with the (spin-independent) orbital magnetic-dipole moment operator

$$\hat{\boldsymbol{m}}' = \frac{e}{2m_e c}\sum_i (\boldsymbol{r}_i \times \hat{\boldsymbol{p}}_i). \tag{3.25}$$

Thus, this antisymmetric term $T_{0n}^{(m')}$ adopts the same form as the last, spin-dependent term in equation (3.17),

$$T_{0n}^{(m^s)} = \mathrm{i}\frac{e}{2m_e}\sum_i (\boldsymbol{k}\times\boldsymbol{\mathcal{E}})\big\langle 0\big|g\,\hat{\boldsymbol{s}}_i\big|n\big\rangle = \mathrm{i}c\,(\boldsymbol{k}\times\boldsymbol{\mathcal{E}})\big\langle 0\big|\hat{\boldsymbol{m}}^s\big|n\big\rangle, \tag{3.26}$$

with the spin magnetic-dipole operator is

$$\hat{\boldsymbol{m}}^s = \frac{e}{2m_e c}\sum_i g\,\hat{\boldsymbol{s}}_i. \tag{3.27}$$

Combining the two contributions, we arrive at the magnetic-dipole transition moment,

$$T_{0n}^{(m)} = \mathrm{i}\frac{e}{2m_e}\sum_i (\boldsymbol{k}\times\boldsymbol{\mathcal{E}})\big\langle 0\big|(\boldsymbol{r}_i\times\hat{\boldsymbol{p}}_i) + g\,\hat{\boldsymbol{s}}_i\big|n\big\rangle = \mathrm{i}c\,(\boldsymbol{k}\times\boldsymbol{\mathcal{E}})\big\langle 0\big|\hat{\boldsymbol{m}}\big|n\big\rangle, \tag{3.28}$$

and the total magnetic-dipole moment operator,

$$\hat{\boldsymbol{m}} = \frac{e}{2m_e c}\sum_i \Big[(\boldsymbol{r}_i\times\hat{\boldsymbol{p}}_i) + g\,\hat{\boldsymbol{s}}_i\Big]. \tag{3.29}$$

Altogether, the first-order transition moments consist of an electric-quadrupole and a magnetic-dipole contribution, i.e.,

$$T_{0n}^{(1)} = T_{0n}^{(Q)} + T_{0n}^{(m')} + T_{0n}^{(m^s)} = T_{0n}^{(Q)} + T_{0n}^{(m)}. \tag{3.30}$$

3.1.3. Second Order: Electric Octupole and Magnetic Quadrupole

In second order in $\boldsymbol{k}$, we find,

$$T_{0n}^{(2)} = -\frac{e}{2m_e}\sum_i \big\langle 0\big|(\boldsymbol{k}\cdot\boldsymbol{r}_i)(\boldsymbol{k}\cdot\boldsymbol{r}_i)(\hat{\boldsymbol{p}}_i\cdot\boldsymbol{\mathcal{E}})\big|n\big\rangle - \frac{eg}{2m_e}\sum_i \big\langle 0\big|(\boldsymbol{k}\cdot\boldsymbol{r}_i)(\boldsymbol{k}\times\boldsymbol{\mathcal{E}})\cdot\hat{\boldsymbol{s}}_i\big|n\big\rangle. \tag{3.31}$$

In a similar fashion as for the first-order term above, the matrix elements in the first term are split into a part that is symmetric and one that is antisymmetric with respect to interchanging the polarisation vector $\boldsymbol{\mathcal{E}}$ with one of the wave vectors $\boldsymbol{k}$,

$$\begin{aligned}
&\big\langle 0\big|(\boldsymbol{k}\cdot\boldsymbol{r}_i)(\boldsymbol{k}\cdot\boldsymbol{r}_i)(\hat{\boldsymbol{p}}_i\cdot\boldsymbol{\mathcal{E}})\big|n\big\rangle \\
&\quad= \frac{1}{3}\big\langle 0\big|(\boldsymbol{k}\cdot\boldsymbol{r}_i)(\boldsymbol{k}\cdot\boldsymbol{r}_i)(\hat{\boldsymbol{p}}_i\cdot\boldsymbol{\mathcal{E}}) \\
&\qquad\qquad + (\boldsymbol{k}\cdot\boldsymbol{r}_i)(\boldsymbol{k}\cdot\hat{\boldsymbol{p}}_i)(\boldsymbol{r}_i\cdot\boldsymbol{\mathcal{E}}) + (\boldsymbol{k}\cdot\hat{\boldsymbol{p}}_i)(\boldsymbol{k}\cdot\boldsymbol{r}_i)(\boldsymbol{r}_i\cdot\boldsymbol{\mathcal{E}})\big|n\big\rangle \\
&\quad+ \frac{1}{3}\big\langle 0\big|2(\boldsymbol{k}\cdot\boldsymbol{r}_i)(\boldsymbol{k}\cdot\boldsymbol{r}_i)(\hat{\boldsymbol{p}}_i\cdot\boldsymbol{\mathcal{E}}) \\
&\qquad\qquad - (\boldsymbol{k}\cdot\boldsymbol{r}_i)(\boldsymbol{k}\cdot\hat{\boldsymbol{p}}_i)(\boldsymbol{r}_i\cdot\boldsymbol{\mathcal{E}}) - (\boldsymbol{k}\cdot\hat{\boldsymbol{p}}_i)(\boldsymbol{k}\cdot\boldsymbol{r}_i)(\boldsymbol{r}_i\cdot\boldsymbol{\mathcal{E}})\big|n\big\rangle.
\end{aligned} \tag{3.32}$$

For the symmetric first term, we obtain

$$\begin{aligned}
T_{0n}^{(O)} &= -\frac{e}{6m_e}\sum_i k_\alpha k_\beta \mathcal{E}_\gamma \big\langle 0\big|r_{i,\alpha}r_{i,\beta}\hat{p}_{i,\gamma} + r_{i,\alpha}\hat{p}_{i,\beta}r_{i,\gamma} + \hat{p}_{i,\alpha}r_{i,\beta}r_{i,\gamma}\big|n\big\rangle \\
&= -\frac{1}{6}\sum_i k_\alpha k_\beta \mathcal{E}_\gamma \big\langle 0\big|\hat{O}^p_{\alpha\beta\gamma}\big|n\big\rangle,
\end{aligned} \tag{3.33}$$

with the operator of the electric-octupole moment in velocity representation

$$\hat{O}^{p}_{\alpha\beta\gamma} = \frac{e}{m_e}\sum_i \big(r_{i,\alpha}r_{i,\beta}\hat{p}_{i,\gamma} + r_{i,\alpha}\hat{p}_{i,\beta}r_{i,\gamma} + \hat{p}_{i,\alpha}r_{i,\beta}r_{i,\gamma}\big). \tag{3.34}$$

Using the commutator,

$$[r_{i,\alpha}r_{i,\beta}r_{i,\gamma}, \hat{H}_0] = \frac{\mathrm{i}\hbar}{m}(\hat{p}_{i,\alpha}r_{i,\beta}r_{i,\gamma} + r_{i,\alpha}\hat{p}_{i,\beta}r_{i,\gamma} + r_{i,\alpha}r_{i,\beta}\hat{p}_{i,\gamma}), \tag{3.35}$$

these matrix elements in the velocity representation can be converted to those in the conventional length representation,

$$T^{(O)}_{0n} = \mathrm{i}\frac{E_{0n}}{6\hbar}k_\alpha k_\beta \mathcal{E}_\gamma \big\langle 0\big|\hat{O}_{\alpha\beta\gamma}\big|n\big\rangle, \tag{3.36}$$

with the octupole operator in the length representation given by

$$\hat{O}_{\alpha\beta\gamma} = e\sum_i r_{i,\alpha}r_{i,\beta}r_{i,\gamma}. \tag{3.37}$$

Again this definition differs from that given elsewhere [109], as the traceless form is not introduced. In fact, for the expansion of the exponential $\exp(i\boldsymbol{k}\cdot\boldsymbol{r})$ it turns out that introducing such a traceless definition here is not possible because only the terms depending on the trace of the octupole moments, $\hat{O}_{\alpha\alpha\beta}$, will contribute to the isotropically-averaged oscillator strengths later on. In contrast, when describing intermolecular interactions starting from an expansion of $1/|\boldsymbol{r}|$, these terms are zero and do not appear.

After some algebra, the antisymmetric part of equation (3.31) can be expressed as

$$\begin{aligned} T^{(\mathcal{M}')}_{0n} &= -\frac{e}{6m_e}\sum_i (\boldsymbol{k}\times\boldsymbol{\mathcal{E}})\cdot\big\langle 0\big|(\boldsymbol{k}\cdot\boldsymbol{r}_i)\cdot(\boldsymbol{r}_i\times\hat{\boldsymbol{p}}_i) + (\boldsymbol{r}_i\times\hat{\boldsymbol{p}}_i)(\boldsymbol{k}\cdot\boldsymbol{r}_i)\big|n\big\rangle \\ &= -\frac{e}{6m_e}\sum_i (\boldsymbol{k}\times\boldsymbol{\mathcal{E}})_\alpha\, k_\beta\, \big\langle 0\big|r_{i,\beta}\,(\boldsymbol{r}_i\times\hat{\boldsymbol{p}}_i)_\alpha + (\boldsymbol{r}_i\times\hat{\boldsymbol{p}}_i)_\alpha\, r_{i,\beta}\big|n\big\rangle \\ &= -\frac{c}{2}\,(\boldsymbol{k}\times\boldsymbol{\mathcal{E}})_\alpha\, k_\beta\, \big\langle 0\big|\hat{\mathcal{M}}'_{\alpha\beta}\big|n\big\rangle, \end{aligned} \tag{3.38}$$

with the (spin-independent) orbital magnetic-quadrupole operator [109, 110],

$$\hat{\mathcal{M}}'_{\alpha\beta} = \frac{e}{2m_e c}\sum_i \frac{2}{3}\Big(r_{i,\beta}(\boldsymbol{r}_i\times\hat{\boldsymbol{p}}_i)_\alpha + (\boldsymbol{r}_i\times\hat{\boldsymbol{p}}_i)_\alpha r_{i,\beta}\Big). \tag{3.39}$$

Note that this operator is not symmetric with respect to interchanging α and β.

The remaining spin-dependent part of equation (3.31) is given by

$$\begin{aligned} T^{(\mathcal{M}^s)}_{0n} &= -\frac{eg}{2m_e}\sum_i (\boldsymbol{k}\times\boldsymbol{\mathcal{E}})\cdot\big\langle 0\big|(\boldsymbol{k}\cdot\boldsymbol{r}_i)\cdot\hat{\boldsymbol{s}}_i\big|n\big\rangle \\ &= -\frac{c}{2}\sum_i (\boldsymbol{k}\times\boldsymbol{\mathcal{E}})_\alpha\, k_\beta\, \big\langle 0\big|\hat{\mathcal{M}}^s_{\alpha\beta}\big|n\big\rangle \end{aligned} \tag{3.40}$$

with the spin contribution to the magnetic-quadrupole operator

$$\hat{\mathcal{M}}^s_{\alpha\beta} = \frac{e}{2m_e c}\sum_i g\Big(r_{i,\beta}\,\hat{\boldsymbol{s}}_{i,\alpha}\Big). \tag{3.41}$$

Finally, the full magnetic-quadrupole contribution is obtained by adding the orbital and spin contributions to obtain

$$T_{0n}^{(\mathcal{M})} = T_{0n}^{(\mathcal{M}')} + T_{0n}^{(\mathcal{M}^s)} = -\frac{c}{2}\,(\boldsymbol{k}\times\boldsymbol{\mathcal{E}})_\alpha\, k_\beta\,\langle 0|\hat{\mathcal{M}}'_{\alpha\beta} + \hat{\mathcal{M}}^s_{\alpha\beta}|n\rangle. \tag{3.42}$$

Altogether, the second-order transition moments consist of an electric-octupole and a magnetic-quadrupole contribution, i.e.,

$$T_{0n}^{(2)} = T_{0n}^{(O)} + T_{0n}^{(\mathcal{M}')} + T_{0n}^{(\mathcal{M}^s)} = T_{0n}^{(O)} + T_{0n}^{(\mathcal{M})}. \tag{3.43}$$

3.2. Origin-Dependence of Transition Moments

In summary, we can approximate the transition moment of equation (3.6), with the terms up to second order of the multipole expansion, which results in five contributions.

$$T_{0n} = T_{0n}^{(\mu)} + T_{0n}^{(Q)} + T_{0n}^{(m)} + T_{0n}^{(O)} + T_{0n}^{(\mathcal{M})} \tag{3.44}$$

In table 3.1 the equations derived in section (3.1) are collected for each order in **k**.

Table 3.1.: Overview of the different contributions appearing in the multipole expansion of the transition moments of equation (3.6) up to second order.

order	electric	magnetic
0	$T_{0n}^{(\mu)} = -\mathrm{i}\frac{E_{0n}}{\hbar}\sum_\alpha \mathcal{E}_\alpha\langle 0\|\hat{\mu}_\alpha\|n\rangle$	–
1	$T_{0n}^{(Q)} = \frac{E_{0n}}{2\hbar}\sum_{\alpha\beta} k_\alpha\mathcal{E}_\beta\,\langle 0\|\hat{Q}_{\alpha\beta}\|n\rangle$	$T_{0n}^{(m)} = \mathrm{i}c\sum_\alpha(\boldsymbol{k}\times\boldsymbol{\mathcal{E}})_\alpha\,\langle 0\|\hat{m}_\alpha\|n\rangle$
2	$T_{0n}^{(O)} = \mathrm{i}\frac{E_{0n}}{6\hbar}\sum_{\alpha\beta\gamma} k_\alpha k_\beta\mathcal{E}_\gamma\,\langle 0\|\hat{O}_{\alpha\beta\gamma}\|n\rangle$	$T_{0n}^{(\mathcal{M})} = -\frac{c}{2}\sum_{\alpha\beta}(\boldsymbol{k}\times\boldsymbol{\mathcal{E}})_\alpha\, k_\beta\,\langle 0\|\hat{\mathcal{M}}_{\alpha\beta}\|n\rangle$

If we restrict our considerations to a spin–orbit coupling free framework in the absence of static external magnetic fields, the wave function can always be chosen as a real function. In this case, the electric transition integrals, $\langle 0|\hat{\mu}_\alpha|n\rangle$, $\langle 0|\hat{Q}_{\alpha\beta}|n\rangle$, and $\langle 0|\hat{O}_{\alpha\beta\gamma}|n\rangle$, as defined here are always real. Moreover, for the magnetic transition moments, the spin contributions can be neglected because for states with a multiplicity larger than zero (i.e., for $S > 0$) the different M_S-components of the multiplet will be degenerate [111, 112] and the components with $+M_S$ and $-M_S$ provide spin contributions to the magnetic transition moments that cancel each other. Therefore, these spin contributions, $\langle 0|\hat{m}^s_\alpha|n\rangle$ and $\langle 0|\hat{\mathcal{M}}^s_{\alpha\beta}|n\rangle$, will not be considered further in the following. The remaining orbital contribution to the magnetic transition integrals, $\langle 0|\hat{m}_\alpha|n\rangle$ and $\langle 0|\hat{\mathcal{M}}_{\alpha\beta}|n\rangle$, are then purely imaginary. As a consequence, we notice that the zeroth-order and second-order transition moments are purely imaginary, whereas the first-order transition moments are purely real. This holds both for the electric and for the magnetic contributions.

As stated earlier, the higher-order transition moments are origin-dependent. In the following, we investigate how these individual contributions to the transition moment change with respect to the position of the origin of the coordinate system.

3.2.1. Electric Transition Moments

First, we consider the electric-dipole transition moment for a system where we have shifted the origin from $\boldsymbol{O}$ to $\boldsymbol{O}+\boldsymbol{a}$, which corresponds to a shift in the coordinates, $\boldsymbol{r}$, to $\boldsymbol{r}-\boldsymbol{a}$. Then the integral in equation (3.16) becomes,

$$\begin{aligned}\big\langle 0\big|\hat{\mu}_\alpha(\boldsymbol{O}+\boldsymbol{a})\big|n\big\rangle &= e\sum_i \big\langle 0\big|r_{i,\alpha}-a_\alpha\big|n\big\rangle \\ &= \big\langle 0\big|\hat{\mu}_\alpha(\boldsymbol{O})\big|n\big\rangle - eN\,a_\alpha\langle 0|n\rangle = \big\langle 0\big|\hat{\mu}_\alpha(\boldsymbol{O})\big|n\big\rangle, \end{aligned} \tag{3.45}$$

As $\boldsymbol{a}$ is a constant, it can be moved outside the integral in the second term. Then this term is just an overlap integral between the ground state and the excited state, which is always zero. Consequently, the electric-dipole transition moment is origin-independent.

Next, we include this shift of the origin into the electric-quadrupole transition moment, and obtain

$$\begin{aligned}\big\langle 0\big|\hat{Q}_{\alpha\beta}(\boldsymbol{O}+\boldsymbol{a})\big|n\big\rangle &= e\sum_i \big\langle 0\big|(r_{i,\alpha}-a_\alpha)(r_{i,\beta}-a_\beta)\big|n\big\rangle \\ &= e\sum_i \big\langle 0\big|r_{i,\alpha}r_{i,\beta}-r_{i,\alpha}a_\beta-r_{i,\beta}a_\alpha+a_\alpha a_\beta\big|n\big\rangle \\ &= \big\langle 0\big|\hat{Q}_{\alpha\beta}(\boldsymbol{O})\big|n\big\rangle - a_\beta\big\langle 0\big|\hat{\mu}_\alpha\big|n\big\rangle - a_\alpha\big\langle 0\big|\hat{\mu}_\beta\big|n\big\rangle, \end{aligned} \tag{3.46}$$

Again, the fourth term is a constant multiplied by an overlap integral that is zero. However, the second and third term contain an electric-dipole matrix element, which may not be zero. Therefore, the magnitude of the change of the electric-quadrupole matrix element is dependent on the size of the electric-dipole contributions multiplied by the shift in the origin of the coordinate system.

Finally, we have to consider the effect of a shift in the origin on the electric-octupole transition moment,

$$\begin{aligned}\big\langle 0\big|\hat{O}_{\alpha\beta\gamma}(\boldsymbol{O}+\boldsymbol{a})\big|n\big\rangle &= e\sum_i \big\langle 0\big|(r_{i,\alpha}-a_\alpha)(r_{i,\beta}-a_\beta)(r_{i,\gamma}-a_\gamma)\big|n\big\rangle \\ &= \big\langle 0\big|\hat{O}_{\alpha\beta\gamma}(\boldsymbol{O})\big|n\big\rangle \\ &\quad - a_\gamma\big\langle 0\big|\hat{Q}_{\alpha\beta}(\boldsymbol{O})\big|n\big\rangle - a_\beta\big\langle 0\big|\hat{Q}_{\alpha\gamma}(\boldsymbol{O})\big|n\big\rangle - a_\alpha\big\langle 0\big|\hat{Q}_{\beta\gamma}(\boldsymbol{O})\big|n\big\rangle \\ &\quad + a_\alpha a_\beta\big\langle 0\big|\hat{\mu}_\gamma\big|n\big\rangle + a_\alpha a_\gamma\big\langle 0\big|\hat{\mu}_\beta\big|n\big\rangle + a_\beta a_\gamma\big\langle 0\big|\hat{\mu}_\alpha\big|n\big\rangle. \end{aligned} \tag{3.47}$$

Again, one term arises that is only dependent on the overlap between the initial and final state. All the other terms will include either $r_{i,\alpha}$ or $r_{i,\alpha}r_{i,\beta}$. These correspond to a shift in one or two of the axis of the coordinate system multiplied by either an electric-quadrupole or electric-dipole matrix element, respectively. Therefore, the magnitude of the change in the electric-octupole matrix element with respect to a change in the origin of the coordinate system, is dependent on the electric-quadrupole and electric-dipole transition moments.

Thus, the electric-quadrupole and electric-octupole transition moments are only origin-independent if all lower-order electric transition moments vanish. The above expressions hold both for the length and velocity representations. A note here is that these equations are employing the non-traceless definition of the higher order moments as given in section 3.1. If a traceless definition is used, these equations will differ for all terms with two or more equivalent indices.

3.2.2. Magnetic Transition Moments

For the magnetic-dipole transition moment, a shift of the origin of the coordinate system results in,

$$\begin{aligned}
\langle 0|m'_\alpha(\boldsymbol{O}+\boldsymbol{a})|n\rangle &= \frac{e}{2m_e c}\sum_i \langle 0|((\boldsymbol{r}_i-\boldsymbol{a})\times\hat{\boldsymbol{p}}_i)_\alpha|n\rangle \\
&= \frac{e}{2m_e c}\sum_i \langle 0|(\boldsymbol{r}_i\times\hat{\boldsymbol{p}}_i)_\alpha|n\rangle - \frac{e}{2m_e c}\sum_i \langle 0|(\boldsymbol{a}\times\hat{\boldsymbol{p}}_i)_\alpha|n\rangle \\
&= \langle 0|m'_\alpha(\boldsymbol{O})|n\rangle - \varepsilon_{\alpha\beta\gamma}a_\beta\frac{e}{2m_e c}\sum_i \langle 0|\hat{p}_{i,\gamma}|n\rangle \\
&= \langle 0|m'_\alpha(\boldsymbol{O})|n\rangle - \varepsilon_{\alpha\beta\gamma}a_\beta\frac{1}{2c}\langle 0|\hat{\mu}^p_\gamma|n\rangle \\
&= \langle 0|m'_\alpha(\boldsymbol{O})|n\rangle + \frac{\mathrm{i}}{2}\,\varepsilon_{\alpha\beta\gamma}a_\beta\frac{E_{0n}}{\hbar c}\langle 0|\hat{\mu}_\gamma|n\rangle,
\end{aligned} \tag{3.48}$$

where $\varepsilon_{\alpha\beta\gamma}$ is the Levi-Civita tensor. Thus, a term depending on the electric-dipole moment in the velocity representation arises. This can be converted into the length representation using equation (3.13). The origin-dependence of the magnetic-dipole transition moments vanishes if the electric-dipole transition moment is zero.

Finally, for the magnetic-quadrupole transition moment the origin-dependence is given by [110,113]

$$\begin{aligned}
\langle 0|\mathcal{M}'_{\alpha\beta}(\boldsymbol{O}+\boldsymbol{a})|n\rangle &= \frac{e}{2m_e c}\sum_i \frac{2}{3}\langle 0|(r_{i,\beta}-a_\beta)((\boldsymbol{r}_i-\boldsymbol{a})\times\hat{\boldsymbol{p}}_i)_\alpha + ((\boldsymbol{r}_i-\boldsymbol{a})\times\hat{\boldsymbol{p}}_i)_\alpha(r_{i,\beta}-a_\beta)|n\rangle \\
&= \frac{e}{2m_e c}\sum_i \frac{2}{3}\langle 0|r_{i,\beta}(\boldsymbol{r}_i\times\hat{\boldsymbol{p}}_i)_\alpha + (\boldsymbol{r}_i\times\hat{\boldsymbol{p}}_i)_\alpha r_{i,\beta}|n\rangle \\
&\quad - \frac{e}{2m_e c}\sum_i \frac{2}{3}\langle 0|r_{i,\beta}(\boldsymbol{a}\times\hat{\boldsymbol{p}}_i)_\alpha + (\boldsymbol{a}\times\hat{\boldsymbol{p}}_i)_\alpha r_{i,\beta}|n\rangle \\
&\quad - \frac{e}{2m_e c}\sum_i \frac{2}{3}\langle 0|a_\beta(\boldsymbol{r}_i\times\hat{\boldsymbol{p}}_i)_\alpha + (\boldsymbol{r}_i\times\hat{\boldsymbol{p}}_i)_\alpha a_\beta|n\rangle \\
&\quad + \frac{e}{2m_e c}\sum_i \frac{2}{3}\langle 0|a_\beta(\boldsymbol{a}\times\hat{\boldsymbol{p}}_i)_\alpha + (\boldsymbol{a}\times\hat{\boldsymbol{p}}_i)_\alpha a_\beta|n\rangle \\
&= \langle 0|\mathcal{M}'_{\alpha\beta}(\boldsymbol{O})|n\rangle - \frac{e}{2m_e c}\sum_i \frac{2}{3}\langle 0|\varepsilon_{\alpha\gamma\delta}a_\gamma(r_{i,\beta}\hat{p}_{i,\delta}+\hat{p}_{i,\delta}r_{i,\beta})|n\rangle \\
&\quad - \frac{4e}{6m_e c}\sum_i a_\beta\langle 0|(\boldsymbol{r}_i\times\hat{\boldsymbol{p}}_i)_\alpha|n\rangle + \frac{4e}{6m_e c}\sum_i \varepsilon_{\alpha\gamma\delta}\,a_\beta a_\gamma\langle 0|\hat{p}_{i,\delta}|n\rangle \\
&= \langle 0|\mathcal{M}'_{\alpha\beta}(\boldsymbol{O})|n\rangle - \frac{e}{2m_e c}\sum_i \frac{2}{3}\langle 0|\varepsilon_{\alpha\gamma\delta}a_\gamma(r_{i,\beta}\hat{p}_{i,\delta}+\hat{p}_{i,\delta}r_{i,\beta})|n\rangle \\
&\quad - \frac{4}{3}a_\beta\langle 0|m'_\alpha(\boldsymbol{O})|n\rangle + \frac{2}{3c}\varepsilon_{\alpha\gamma\delta}\,a_\beta a_\gamma\langle 0|\hat{\mu}^p_\delta|n\rangle
\end{aligned} \tag{3.49}$$

While the third and fourth term, depending on the electric-dipole and magnetic-dipole transition moments, respectively, are already in their final form, the second term still has to be rewritten to arrive at known transition moments. To this end one uses (for details, see supporting information of reference [27])

$$\begin{aligned}
\langle 0|\varepsilon_{\alpha\gamma\delta}a_\gamma(r_{i,\beta}\hat{p}_{i,\delta}+\hat{p}_{i,\delta}r_{i,\beta})|n\rangle =& \langle 0|\varepsilon_{\alpha\gamma\delta}a_\gamma(r_{i,\beta}\hat{p}_{i,\delta}+\hat{p}_{i,\beta}r_{i,\delta})|n\rangle \\
&+ a_\beta\langle 0|(\boldsymbol{r}_i\times\hat{\boldsymbol{p}}_i)_\alpha|n\rangle - \delta_{\alpha\beta}\,a_\gamma\langle 0|(\boldsymbol{r}_i\times\hat{\boldsymbol{p}}_i)_\gamma|n\rangle.
\end{aligned} \tag{3.50}$$

The second term then contains a contribution from the electric-quadrupole transition moments and two terms containing the magnetic-dipole transition moments. With equation (3.50) substituted into equation (3.49), we arrive at the final equation for the origin-dependence of the magnetic-quadrupole matrix elements,

$$\begin{aligned}\langle 0|\mathcal{M}'_{\alpha\beta}(\boldsymbol{O}+\boldsymbol{a})|n\rangle &= \langle 0|\mathcal{M}'_{\alpha\beta}(\boldsymbol{O})|n\rangle - \frac{e}{2m_e c}\sum_i \frac{2}{3}\langle 0|\varepsilon_{\alpha\gamma\delta}a_\gamma(r_{i,\beta}\hat{p}_{i,\delta}+\hat{p}_{i,\beta}r_{i,\delta})|n\rangle \\ &\quad - \frac{e}{2m_e c}\sum_i \frac{2}{3}\,a_\beta\langle 0|(\boldsymbol{r}_i\times\hat{\boldsymbol{p}}_i)_\alpha|n\rangle + \frac{e}{2m_e c}\sum_i \frac{2}{3}\,\delta_{\alpha\beta}\,a_\gamma\langle 0|(\boldsymbol{r}\times\hat{\boldsymbol{p}})_\gamma|n\rangle \\ &\quad - \frac{4}{3}a_\beta\langle 0|m'_\alpha(\boldsymbol{O})|n\rangle + \frac{2}{3c}\varepsilon_{\alpha\gamma\delta}\,a_\beta a_\gamma\langle 0|\hat{\mu}^p_\delta|n\rangle \\ &= \langle 0|\mathcal{M}'_{\alpha\beta}(\boldsymbol{O})|n\rangle - \frac{1}{3c}\,\varepsilon_{\alpha\gamma\delta}a_\gamma\langle 0|\hat{Q}^p_{\beta\delta}(\boldsymbol{O})|n\rangle + \frac{2}{3c}\varepsilon_{\alpha\gamma\delta}\,a_\beta a_\gamma\langle 0|\hat{\mu}^p_\delta|n\rangle \\ &\quad + \frac{2}{3}\delta_{\alpha\beta}\left(\boldsymbol{a}\cdot\langle 0|\boldsymbol{m}'(\boldsymbol{O})|n\rangle\right) - 2a_\beta\langle 0|m'_\alpha(\boldsymbol{O})|n\rangle. \end{aligned} \tag{3.51}$$

Again, the electric-dipole and electric-quadrupole transition moments in the velocity representation can be converted to the length representation to finally arrive at

$$\begin{aligned}\langle 0|\mathcal{M}'_{\alpha\beta}(\boldsymbol{O}+\boldsymbol{a})|n\rangle &= \langle 0|\mathcal{M}'_{\alpha\beta}(\boldsymbol{O})|n\rangle \\ &\quad + \frac{\mathrm{i}}{3}\frac{E_{0n}}{\hbar c}\,\varepsilon_{\alpha\gamma\delta}a_\gamma\langle 0|\hat{Q}_{\beta\delta}(\boldsymbol{O})|n\rangle - \frac{2\mathrm{i}}{3}\frac{E_{0n}}{\hbar c}\,\varepsilon_{\alpha\gamma\delta}\,a_\beta a_\gamma\langle 0|\hat{\mu}_\delta|n\rangle \\ &\quad + \frac{2}{3}\delta_{\alpha\beta}\left(\boldsymbol{a}\cdot\langle 0|\boldsymbol{m}'(\boldsymbol{O})|n\rangle\right) - 2a_\beta\langle 0|m'_\alpha(\boldsymbol{O})|n\rangle. \end{aligned} \tag{3.52}$$

Here, we notice that upon shifting the origin, the magnetic-quadrupole transition moment generates all lower-order contributions, i.e., terms depending on the electric-dipole and electric-quadrupole transition moments as well as on the magnetic-dipole transition moments.

3.3. From Transition Moments to Oscillator Strengths

The multipole expansion of the full transition moments T_{0n} can now be inserted into equation (3.7) to obtain an expression for calculating the oscillator strengths,

$$\begin{aligned} f_{0n} &= \frac{2m_e}{e^2E_{0n}}\left|T^{(0)}_{0n}+T^{(1)}_{0n}+T^{(2)}_{0n}+\cdots\right|^2 \\ &= \frac{2m_e}{e^2E_{0n}}\left|T^{(\mu)}_{0n}+T^{(Q)}_{0n}+T^{(m)}_{0n}+T^{(O)}_{0n}+T^{(\mathcal{M})}_{0n}+\cdots\right|^2. \end{aligned} \tag{3.53}$$

Here different truncations can be employed, such as the dipole approximation, where only the zeroth order term is retained. In this case we arrive at the well-known equation in which the oscillator strength is proportional to the squared absolute value of the electric-dipole transition moments. This approximation is commonly employed in UV-Vis spectroscopy.

Here, we are interested in cases where the dipole approximation is insufficient to describe the spectra, such as for K-edge XAS of transition metal complexes. In these situations, higher order terms have to be included, and the currently used approach is to truncate after the first order in the expansion,

$$f_{0n} \approx \frac{2m_e}{e^2E_{0n}}\left|T^{(0)}_{0n}+T^{(1)}_{0n}\right|^2. \tag{3.54}$$

However, these terms are dependent on the choice of the origin of the coordinate system and the resulting oscillator strength is origin-dependent [107].

To obtain an origin-independent formulation, we return to equation (3.53) and realise that the squared absolute value results in a sum of products of multipole transition moments. These products are of different orders in the wave vector $\boldsymbol{k}$, as is illustrated in figure 3.1. Hence, it seems

Figure 3.1.: Schematic illustration of the different terms arising from the squared absolute value in equation (3.53). The entries in the table indicate the order of the different terms in the wave vector $\boldsymbol{k}$. We retain all terms up to second order, as indicated by the red line.

		$T_{0n}^{(0)}$	$T_{0n}^{(1)}$		$T_{0n}^{(2)}$	
		$T_{0n}^{(\mu)}$	$T_{0n}^{(Q)}$	$T_{0n}^{(m)}$	$T_{0n}^{(O)}$	$T_{0n}^{(\mathcal{M})}$
$T_{0n}^{(0),*}$	$T_{0n}^{(\mu),*}$	0	1	1	2	2
$T_{0n}^{(1),*}$	$T_{0n}^{(Q),*}$	1	2	2	3	3
	$T_{0n}^{(m),*}$	1	2	2	3	3
$T_{0n}^{(2),*}$	$T_{0n}^{(O),*}$	2	3	3	4	4
	$T_{0n}^{(\mathcal{M}),*}$	2	3	3	4	4

logical to retain all terms up to a given order in $\boldsymbol{k}$ in the expression for the oscillator strengths instead of truncating the multipole expansion of the transition moments. By collecting terms that are of the same order, the oscillator strengths can be expressed as

$$f_{0n} = f_{0n}^{(0)} + f_{0n}^{(1)} + f_{0n}^{(2)} + \cdots \tag{3.55}$$

where

$$f_{0n}^{(0)} = \frac{2m_e}{e^2 E_{0n}} \left| T_{0n}^{(0)} \right|^2 \tag{3.56}$$

$$f_{0n}^{(1)} = \frac{2m_e}{e^2 E_{0n}} 2\mathrm{Re}\big(T_{0n}^{(0),*}\, T_{0n}^{(1)}\big) = 0 \tag{3.57}$$

$$f_{0n}^{(2)} = \frac{2m_e}{e^2 E_{0n}} \Big[\left| T_{0n}^{(1)} \right|^2 + 2\mathrm{Re}\big(T_{0n}^{(0),*}\, T_{0n}^{(2)}\big) \Big], \tag{3.58}$$

where the star denotes complex conjugation. Because $T_{0n}^{(0)}$ is purely imaginary and $T_{0n}^{(1)}$ is real, their product is also purely imaginary and the first-order contribution $f_{0n}^{(1)}$ vanishes. In the following, we will retain all terms up to second order and it turns out that the resulting approximation for the oscillator strengths is independent of the choice of the origin.

3.3.1. Origin-Independence of Oscillator Strengths

Starting from the definitions of $T_{0n}^{(0)}$, $T_{0n}^{(1)}$, and $T_{0n}^{(2)}$ in equations (3.16), (3.17), and (3.31), respectively, one can easily see that their origin dependence is given by

$$T_{0n}^{(0)}(\boldsymbol{O}+\boldsymbol{a}) = T_{0n}^{(0)}(\boldsymbol{O}), \tag{3.59}$$

$$T_{0n}^{(1)}(\boldsymbol{O}+\boldsymbol{a}) = T_{0n}^{(1)}(\boldsymbol{O}) + \mathrm{i}(\boldsymbol{k}\cdot\boldsymbol{a})\, T_{0n}^{(0)}(\boldsymbol{O}), \tag{3.60}$$

$$T_{0n}^{(2)}(\boldsymbol{O}+\boldsymbol{a}) = T_{0n}^{(2)}(\boldsymbol{O}) + \mathrm{i}(\boldsymbol{k}\cdot\boldsymbol{a})\, T_{0n}^{(1)}(\boldsymbol{O}) - \frac{1}{2}(\boldsymbol{k}\cdot\boldsymbol{a})^2\, T_{0n}^{(0)}(\boldsymbol{O}). \tag{3.61}$$

Therefore, the zeroth-order contribution to the oscillator strengths $f_{0n}^{(0)}$, i.e., the expression obtained in the dipole approximation, is obviously origin-independent. For the second-order contribution, we have

$$\begin{aligned} f_{0n}^{(2)}(\boldsymbol{O}+\boldsymbol{a}) &= \frac{2m_e}{e^2 E_{0n}}\left[\left|T_{0n}^{(1)}(\boldsymbol{O}+\boldsymbol{a})\right|^2 + 2\mathrm{Re}\Big(T_{0n}^{(0),*}(\boldsymbol{O})\, T_{0n}^{(2)}(\boldsymbol{O}+\boldsymbol{a})\Big)\right] \\ &= \frac{2m_e}{e^2 E_{0n}}\left[\left|T_{0n}^{(1)}(\boldsymbol{O})\right|^2 + 2\mathrm{Re}\Big(\mathrm{i}(\boldsymbol{k}\cdot\boldsymbol{a})T_{0n}^{(0)}(\boldsymbol{O})T_{0n}^{(1),*}(\boldsymbol{O})\Big) + (\boldsymbol{k}\cdot\boldsymbol{a})^2\left|T_{0n}^{(0)}(\boldsymbol{O})\right|^2\right. \\ &\qquad \left. + \mathrm{Re}\Big(T_{0n}^{(0),*}(\boldsymbol{O})\left[2T_{0n}^{(2)}(\boldsymbol{O}) + 2\mathrm{i}(\boldsymbol{k}\cdot\boldsymbol{a})\, T_{0n}^{(1)}(\boldsymbol{O}) - (\boldsymbol{k}\cdot\boldsymbol{a})^2\, T_{0n}^{(0)}(\boldsymbol{O})\right]\Big)\right] \\ &= f_{0n}^{(2)}(\boldsymbol{O}), \end{aligned} \tag{3.62}$$

and find that this contribution is independent of the choice of the origin. In fact, this can be shown for each order in the wave vector, that the oscillator strength will be origin-independent if all terms of the same order are included. For the proof, see Appendix C in reference [27].

3.3.2. Second-Order Oscillator Strengths

After having established an origin-independent definition of the different approximations to the oscillator strengths, we will now turn to deriving explicit expressions. Considering only the zeroth-order contribution corresponds to the dipole approximation, in which the *dipole oscillator strengths* are given by

$$f_{0n} \approx f_{0n}^{(0)} = f_{0n}^{(\mu^2)} = \frac{2m_e}{e^2\hbar^2}\, E_{0n}\left|\boldsymbol{\mathcal{E}}\cdot\langle 0|\hat{\boldsymbol{\mu}}|n\rangle\right|^2 = \frac{2m_e}{e^2\hbar^2}\, E_{0n}\left(\mathcal{E}_\alpha\langle 0|\hat{\mu}_\alpha|n\rangle\right)^2. \tag{3.63}$$

Since the first-order contributions vanish, the next step to go beyond the dipole approximation is to include all second-order contributions. Thus, the oscillator strengths can be approximated as the sum of the dipole (zeroth-order) oscillator strengths and the *quadrupole (second-order) oscillator strengths*,

$$f_{0n} \approx f_{0n}^{(0)} + f_{0n}^{(2)} = \left|T_{0n}^{(0)}\right|^2 + \left|T_{0n}^{(1)}\right|^2 + 2\mathrm{Re}\big(T_{0n}^{(0),*}T_{0n}^{(2)}\big). \tag{3.64}$$

We will refer to this approximation as the *quadrupole approximation*. For the quadrupole oscillator strengths, we can insert the individual multipole transition moments, and obtain five different terms,

$$\begin{aligned} f_{0n}^{(2)} &= \frac{2m_e}{e^2 E_{0n}}\left[\left|T_{0n}^{(Q)}\right|^2 + \left|T_{0n}^{(m)}\right|^2 + 2\mathrm{Re}\big(T_{0n}^{(Q),*}T_{0n}^{(m)}\big) + 2\mathrm{Re}\big(T_{0n}^{(\mu),*}T_{0n}^{(O)}\big) + 2\mathrm{Re}\big(T_{0n}^{(\mu),*}T_{0n}^{(\mathcal{M})}\big)\right] \\ &= f_{0n}^{(Q^2)} + f_{0n}^{(m^2)} + f_{0n}^{(Qm)} + f_{0n}^{(\mu O)} + f_{0n}^{(\mu\mathcal{M})}. \end{aligned} \tag{3.65}$$

First, there are three contributions arising from products of first-order transition moments, an electric-quadrupole–electric-quadrupole contribution,

$$f_{0n}^{(Q^2)} = \frac{m_e}{2e^2\hbar^2} E_{0n} \left(k_\alpha \mathcal{E}_\beta \left\langle 0 \middle| \hat{Q}_{\alpha\beta} \middle| n \right\rangle \right)^2, \tag{3.66}$$

a magnetic-dipole–magnetic-dipole contribution,

$$f_{0n}^{(m^2)} = \frac{2m_e c^2}{e^2 E_{0n}} \left| (\boldsymbol{k} \times \boldsymbol{\mathcal{E}})_\alpha \left\langle 0 \middle| \hat{m}_\alpha \middle| n \right\rangle \right|^2 = \frac{2m_e c^2}{e^2 E_{0n}} \left((\boldsymbol{k} \times \boldsymbol{\mathcal{E}})_\alpha \operatorname{Im} \left\langle 0 \middle| \hat{m}_\alpha \middle| n \right\rangle \right)^2, \tag{3.67}$$

and a cross-term, the electric-quadrupole–magnetic-dipole contribution,

$$f_{0n}^{(Qm)} = -\frac{2m_e c}{e^2\hbar} \left(k_\alpha \mathcal{E}_\beta \left\langle 0 \middle| \hat{Q}_{\alpha\beta} \middle| n \right\rangle \right) \left((\boldsymbol{k} \times \boldsymbol{\mathcal{E}})_\alpha \operatorname{Im} \left\langle 0 \middle| \hat{m}_\alpha \middle| n \right\rangle \right). \tag{3.68}$$

These three contributions have been considered previously in the calculation of the quadrupole oscillator strengths in reference [107]. In addition, two additional contributions have to be included in order to collect all terms that are of second order and to arrive at an origin-independent approximation. These are the electric-dipole–electric-octupole contribution,

$$f_{0n}^{(\mu O)} = -\frac{2m_e}{3\hbar^2 e^2} E_{0n} \left(\mathcal{E}_\alpha \left\langle 0 \middle| \hat{\mu}_\alpha \middle| n \right\rangle \right) \left(k_\alpha k_\beta \mathcal{E}_\gamma \left\langle 0 \middle| \hat{O}_{\alpha\beta\gamma} \middle| n \right\rangle \right), \tag{3.69}$$

and the electric-dipole–magnetic-quadrupole contribution,

$$f_{0n}^{(\mu \mathcal{M})} = \frac{2m_e c}{e^2\hbar} \left(\mathcal{E}_\alpha \left\langle 0 \middle| \hat{\mu}_\alpha \middle| n \right\rangle \right) \left((\boldsymbol{k} \times \boldsymbol{\mathcal{E}})_\alpha \, k_\beta \, \operatorname{Im} \left\langle 0 \middle| \hat{\mathcal{M}}_{\alpha\beta} \middle| n \right\rangle \right). \tag{3.70}$$

Now we choose the wave vector as $\boldsymbol{k} = k\boldsymbol{e}_x$ along the x-axis and the polarisation vector as $\boldsymbol{\mathcal{E}} = \boldsymbol{e}_y$ along the y-axis. Consequently, $(\boldsymbol{e}_x \times \boldsymbol{\mathcal{E}})$ becomes the unit vector $\boldsymbol{e}_z$ along the z-axis. This is no loss of generality, as the molecule can still have an arbitrary orientation in the coordinate system. Using

$$k = \frac{E_{0n}}{\hbar c}, \tag{3.71}$$

the different contributions to the oscillator strengths become

$$f_{0n}^{(\mu^2)} = \frac{2m_e}{e^2\hbar^2} E_{0n} \left\langle 0 \middle| \hat{\mu}_y \middle| n \right\rangle^2 \tag{3.72}$$

$$f_{0n}^{(Q^2)} = \frac{m_e}{2e^2\hbar^4 c^2} E_{0n}^3 \left\langle 0 \middle| \hat{Q}_{xy} \middle| n \right\rangle^2 \tag{3.73}$$

$$f_{0n}^{(m^2)} = \frac{2m_e}{e^2\hbar^2} E_{0n} \left[\operatorname{Im} \left\langle 0 \middle| \hat{m}_z \middle| n \right\rangle \right]^2 \tag{3.74}$$

$$f_{0n}^{(Qm)} = -\frac{2m_e}{e^2\hbar^3 c} E_{0n}^2 \left\langle 0 \middle| \hat{Q}_{xy} \middle| n \right\rangle \operatorname{Im} \left\langle 0 \middle| \hat{m}_z \middle| n \right\rangle \tag{3.75}$$

$$f_{0n}^{(\mu O)} = -\frac{2m_e}{3e^2\hbar^4 c^2} E_{0n}^3 \left\langle 0 \middle| \hat{\mu}_y \middle| n \right\rangle \left\langle 0 \middle| \hat{O}_{xxy} \middle| n \right\rangle \tag{3.76}$$

$$f_{0n}^{(\mu \mathcal{M})} = \frac{2m_e}{e^2\hbar^3 c} E_{0n}^2 \left\langle 0 \middle| \hat{\mu}_y \middle| n \right\rangle \operatorname{Im} \left\langle 0 \middle| \hat{\mathcal{M}}_{zx} \middle| n \right\rangle. \tag{3.77}$$

These oscillator strengths refer to an experimental setup in which the incident radiation has a well-defined polarisation and in which the molecules have a fixed orientation with respect to the radiation.

Using the expressions derived in section 3.2 the origin-dependence of the individual terms can be determined. Then it can be seen that in the total oscillator strength up to second-order the terms dependent on the shift of the origin cancel and the total oscillator strength is origin-independent for the oriented sample. For the proof, we refer to reference [27].

3.3.3. Isotropic Averaging of Oscillator Strengths

In many cases, the molecules are not oriented with respect to the incident radiation in experiments. Instead, the measurement is performed in either solution or for a powdered solid, where the molecules can either freely rotate or are randomly orientated, respectively. To arrive at final expressions for the oscillator strengths in these situations, we need to perform an average over all possible orientations of the molecule.

The expressions for performing this averaging are derived, for instance, in reference [109] (see in particular chapter 4.2). For the isotropic averages of tensors with two, three, and four Cartesian indices, one finds

$$\langle T_{xx}\rangle_{\mathrm{iso}} = \sum_{\alpha\beta} \langle i_\alpha i_\beta\rangle_{\mathrm{iso}}\, T_{\alpha\beta} \tag{3.78}$$

$$\langle T_{xyz}\rangle_{\mathrm{iso}} = \sum_{\alpha\beta\gamma} \langle i_\alpha j_\beta k_\gamma\rangle_{\mathrm{iso}}\, T_{\alpha\beta\gamma} \tag{3.79}$$

$$\langle T_{xxyy}\rangle_{\mathrm{iso}} = \sum_{\alpha\beta\gamma\delta} \langle i_\alpha i_\beta j_\gamma j_\delta\rangle_{\mathrm{iso}}\, T_{\alpha\beta\gamma\delta}, \tag{3.80}$$

where the isotropic averages of the Cartesian unit vector $\boldsymbol{i} = \boldsymbol{e}_x$, $\boldsymbol{j} = \boldsymbol{e}_y$, and $\boldsymbol{k} = \boldsymbol{e}_z$ are given by

$$\langle i_\alpha i_\beta\rangle_{\mathrm{iso}} = \frac{1}{3}\delta_{\alpha\beta}\,, \tag{3.81}$$

$$\langle i_\alpha j_\beta k_\gamma\rangle_{\mathrm{iso}} = \frac{1}{6}\epsilon_{\alpha\beta\gamma}\,, \tag{3.82}$$

$$\langle i_\alpha i_\beta j_\gamma j_\delta\rangle_{\mathrm{iso}} = \frac{1}{30}\left(4\delta_{\alpha\beta}\delta_{\gamma\delta} - \delta_{\alpha\gamma}\delta_{\beta\delta} - \delta_{\alpha\delta}\delta_{\beta\gamma}\right). \tag{3.83}$$

For all other tensor components, such as, e.g., $\langle T_{xy}\rangle_{\mathrm{iso}}$ or $\langle T_{xxy}\rangle_{\mathrm{iso}}$, the isotropic averages are zero.

Using these expressions, we obtain for the isotropically averaged electric-dipole–electric-dipole contribution to the oscillator strengths,

$$\langle f_{0n}^{(\mu^2)}\rangle_{\mathrm{iso}} = \frac{2m_e}{3e^2\hbar^2}\, E_{0n} \sum_\alpha \left\langle 0\middle|\hat{\mu}_\alpha\middle|n\right\rangle^2 = \frac{2m_e}{3e^2\hbar^2}\, E_{0n} \left\langle 0\middle|\hat{\boldsymbol{\mu}}\middle|n\right\rangle^2. \tag{3.84}$$

Similarly, for the electric-quadrupole–electric-quadrupole contribution, we find

$$\begin{aligned}\langle f_{0n}^{(Q^2)}\rangle_{\mathrm{iso}} &= \frac{m_e}{60e^2\hbar^4c^2}E_{0n}^3 \sum_{\alpha\beta\gamma\delta}\left(4\delta_{\alpha\gamma}\delta_{\beta\delta} - \delta_{\alpha\beta}\delta_{\gamma\delta} - \delta_{\alpha\delta}\delta_{\beta\gamma}\right)\left\langle 0\middle|\hat{Q}_{\alpha\beta}\middle|n\right\rangle\left\langle 0\middle|\hat{Q}_{\gamma\delta}\middle|n\right\rangle \\ &= \frac{m_e}{20e^2\hbar^4c^2}E_{0n}^3\left[\sum_{\alpha\beta}\left\langle 0\middle|\hat{Q}_{\alpha\beta}\middle|n\right\rangle^2 - \frac{1}{3}\Big(\sum_\alpha \left\langle 0\middle|\hat{Q}_{\alpha\alpha}\middle|n\right\rangle\Big)^2\right].\end{aligned} \tag{3.85}$$

We note that this is identical to the expression in reference [107], were a traceless definition of the quadrupole moment is used. For the magnetic-dipole–magnetic-dipole contribution, the isotropic average is,

$$\langle f_{0n}^{(m^2)}\rangle_{\mathrm{iso}} = \frac{2m_e}{3e^2\hbar^2}E_{0n}\sum_\alpha \mathrm{Im}\left\langle 0\middle|\hat{m}_\alpha\middle|n\right\rangle^2 = \frac{2m_e}{3e^2\hbar^2}E_{0n}\left(\mathrm{Im}\left\langle 0\middle|\hat{\boldsymbol{m}}\middle|n\right\rangle\right)^2. \tag{3.86}$$

The isotropic average of the electric-quadrupole–magnetic-dipole contribution to the oscillator strengths,

$$\langle f_{0n}^{(Qm)}\rangle_{\mathrm{iso}} = -\frac{m_e}{3e^2\hbar^3c}E_{0n}^2\sum_{\alpha\beta\gamma}\varepsilon_{\alpha\beta\gamma}\left\langle 0\middle|\hat{Q}_{\alpha\beta}\middle|n\right\rangle\left\langle 0\middle|\hat{m}_\gamma\middle|n\right\rangle = 0 \tag{3.87}$$

turns out to be zero because $\langle 0|\hat{Q}_{\alpha\beta}|n\rangle = \langle 0|\hat{Q}_{\beta\alpha}|n\rangle$. Finally, for the electric-dipole–electric-octupole contribution to the oscillator strengths, we obtain

$$\begin{aligned}\langle f_{0n}^{(\mu O)}\rangle_{\text{iso}} &= -\frac{m_e}{45e^2\hbar^4c^2}E_{0n}^3 \sum_{\alpha\beta\gamma\delta}\left(4\delta_{\alpha\beta}\delta_{\gamma\delta} - \delta_{\alpha\gamma}\delta_{\beta\delta} - \delta_{\alpha\delta}\delta_{\beta\gamma}\right)\langle 0|\hat{\mu}_\delta|n\rangle\langle 0|\hat{O}_{\alpha\beta\gamma}|n\rangle \\ &= -\frac{2m_e}{45e^2\hbar^4c^2}E_{0n}^3 \sum_{\alpha\beta}\langle 0|\hat{\mu}_\beta|n\rangle\langle 0|\hat{O}_{\alpha\alpha\beta}|n\rangle, \end{aligned} \tag{3.88}$$

where we used the symmetry of the octupole moments with respect to the exchange of indices, and for the electric-dipole–magnetic-quadrupole contribution,

$$\langle f_{0n}^{(\mu\mathcal{M})}\rangle_{\text{iso}} = \frac{m_e}{3e^2\hbar^3c}E_{0n}^2 \sum_{\alpha\beta\gamma}\varepsilon_{\alpha\beta\gamma}\langle 0|\hat{\mu}_\beta|n\rangle \,\mathrm{Im}\langle 0|\hat{\mathcal{M}}_{\gamma\alpha}|n\rangle. \tag{3.89}$$

Note again that the magnetic-quadrupole transition moments are in general not symmetric or antisymmetric with respect to the interchange of the two Cartesian indices, i.e., $\langle 0|\mathcal{M}_{\alpha\beta}|n\rangle \neq \pm\langle 0|\mathcal{M}_{\beta\alpha}|n\rangle$.

In total, there are five contributions to the isotropically averaged oscillator strengths up to second order. Note that the individual contributions to the oscillator strength are still origin-dependent. Only by taking the sum of all five contributions does the oscillator strength become origin-independent.

3.3.4. Origin-Independence of Isotropic Oscillator Strengths

Now we have arrived at the final expressions for the oscillator strength. Even though this already follows from the results of section 3.3.1, we want to verify that the total oscillator strength to second order is origin-independent for an isotropic sample. We will consider the origin-dependence of each term individually. The starting point is to insert the origin-dependence of the matrix elements derived in section 3.2. The electric-dipole–electric-dipole term is origin-independent and the first equation to consider is the electric-quadrupole–electric-quadrupole contribution to the oscillator strengths. The resulting equation is

$$\begin{aligned}\langle f_{0n}^{(Q^2)}(\boldsymbol{O}+\boldsymbol{a})\rangle_{\text{iso}} &= \frac{m_e}{20e^2\hbar^4c^2}E_{0n}^3\Bigg[\sum_{\alpha\beta}\Big(\langle 0|\hat{Q}_{\alpha\beta}(\boldsymbol{O})|n\rangle - a_\beta\langle 0|\hat{\mu}_\alpha|n\rangle - a_\alpha\langle 0|\hat{\mu}_\beta|n\rangle\Big)^2 \\ &\qquad - \frac{1}{3}\Big(\sum_\alpha\langle 0|\hat{Q}_{\alpha\alpha}(\boldsymbol{O})|n\rangle - 2a_\alpha\langle 0|\hat{\mu}_\alpha|n\rangle\Big)^2\Bigg] \\ &= \langle f_{0n}^{(Q^2)}(\boldsymbol{O})\rangle_{\text{iso}} \\ &\quad - \frac{m_e}{15e^2\hbar^4c^2}E_{0n}^3\Bigg[3\sum_{\alpha\beta}a_\beta\langle 0|\hat{\mu}_\alpha|n\rangle\langle 0|\hat{Q}_{\alpha\beta}(\boldsymbol{O})|n\rangle \\ &\qquad\qquad - \Big(\boldsymbol{a}\cdot\langle 0|\hat{\boldsymbol{\mu}}|n\rangle\Big)\Big(\sum_\alpha\langle 0|\hat{Q}_{\alpha\alpha}(\boldsymbol{O})|n\rangle\Big)\Bigg] \\ &\quad + \frac{m_e}{20e^2\hbar^4c^2}E_{0n}^3\left[2\boldsymbol{a}^2\langle 0|\hat{\boldsymbol{\mu}}|n\rangle^2 + \frac{2}{3}\sum_{\alpha\beta}\Big(\boldsymbol{a}\cdot\langle 0|\hat{\boldsymbol{\mu}}|n\rangle\Big)\right] \end{aligned} \tag{3.90}$$

For the magnetic-dipole–magnetic-dipole contribution, we get

$$\begin{aligned}
f_{0n}^{(m^2)}(\boldsymbol{O}+\boldsymbol{a}) = \frac{2m_e}{3e^2\hbar^2}E_{0n}\sum_{\alpha}\left(\mathrm{Im}\langle 0|\hat{m}_\alpha(\boldsymbol{O})|n\rangle + \frac{1}{2}\varepsilon_{\alpha\beta\gamma}a_\beta\frac{E_{0n}}{\hbar c}\langle 0|\hat{\mu}_\gamma|n\rangle\right)^2 \\
=& f_{0n}^{(m^2)}(\boldsymbol{O}) \\
&+ \frac{2m_e}{3e^2\hbar^3c}E_{0n}^2\,\varepsilon_{\alpha\beta\gamma}a_\beta\langle 0|\hat{\mu}_\gamma|n\rangle\mathrm{Im}\langle 0|\hat{m}_\alpha(\boldsymbol{O})|n\rangle \\
&+ \frac{m_e}{6e^2\hbar^4c^2}E_{0n}^3\,(\varepsilon_{\alpha\beta\gamma}\varepsilon_{\alpha\delta\epsilon})a_\beta a_\delta\langle 0|\hat{\mu}_\gamma|n\rangle\langle 0|\hat{\mu}_\epsilon|n\rangle \\
=& f_{0n}^{(m^2)}(\boldsymbol{O}) \\
&+ \frac{2m_e}{3e^2\hbar^3c}E_{0n}^2\left[\boldsymbol{a}\cdot\left(\langle 0|\hat{\boldsymbol{\mu}}|n\rangle\times\mathrm{Im}\langle 0|\hat{\boldsymbol{m}}(\boldsymbol{O})|n\rangle\right)\right] \\
&+ \frac{m_e}{6e^2\hbar^4c^2}E_{0n}^3\left[\boldsymbol{a}^2\langle 0|\hat{\boldsymbol{\mu}}|n\rangle^2 - \left(\boldsymbol{a}\cdot\langle 0|\hat{\boldsymbol{\mu}}|n\rangle\right)\right]
\end{aligned} \tag{3.91}$$

Here, we used the identity $\varepsilon_{\alpha\beta\gamma}\varepsilon_{\alpha\delta\epsilon} = \delta_{\beta\delta}\delta_{\gamma\epsilon} - \delta_{\beta\epsilon}\delta_{\gamma\delta}$. For the electric-dipole–electric-octupole contribution, we obtain

$$\begin{aligned}
f_{0n}^{(\mu O)}(\boldsymbol{O}+\boldsymbol{a}) = & -\frac{2m_e}{45e^2\hbar^4c^2}E_{0n}^3\sum_{\alpha\beta}\langle 0|\hat{\mu}_\beta|n\rangle\Big[\langle 0|\hat{O}_{\alpha\alpha\beta}(\boldsymbol{O})|n\rangle \\
&- 2a_\alpha\langle 0|\hat{Q}_{\alpha\beta}|n\rangle - a_\beta\langle 0|\hat{Q}_{\alpha\alpha}|n\rangle + 2a_\alpha a_\beta\langle 0|\hat{\mu}_\alpha|n\rangle + a_\alpha^2\langle 0|\mu_\beta|n\rangle\Big] \\
= & f_{0n}^{(\mu O)}(\boldsymbol{O}) \\
&+ \frac{2m_e}{45e^2\hbar^4c^2}E_{0n}^3\left[2\sum_{\alpha\beta}a_\alpha\langle 0|\hat{\mu}_\beta|n\rangle\langle 0|\hat{Q}_{\alpha\beta}|n\rangle + \sum_{\alpha\beta}a_\beta\langle 0|\hat{\mu}_\beta|n\rangle\langle 0|\hat{Q}_{\alpha\alpha}|n\rangle\right] \\
&- \frac{2m_e}{45e^2\hbar^4c^2}E_{0n}^3\left[2\sum_{\alpha\beta}a_\alpha a_\beta\langle 0|\hat{\mu}_\alpha|n\rangle\langle 0|\hat{\mu}_\beta|n\rangle + \sum_{\alpha\beta}a_\alpha^2\langle 0|\hat{\mu}_\beta|n\rangle^2,\right]
\end{aligned} \tag{3.92}$$

and for the electric-dipole–magnetic-quadrupole contribution, we have

$$
\begin{aligned}
f_{0n}^{(\mu\mathcal{M})}(\boldsymbol{O}+\boldsymbol{a}) =& f_{0n}^{(\mu\mathcal{M})}(\boldsymbol{O}) + \frac{m}{3e^2\hbar^3c}E_{0n}^2 \sum_{\alpha\beta\gamma}\varepsilon_{\alpha\beta\gamma}\langle 0|\hat{\mu}_\beta|n\rangle \Bigg[\\
& \frac{1}{3}\frac{E_{0n}}{\hbar c}\varepsilon_{\gamma\epsilon\nu}a_\epsilon\langle 0|\hat{Q}_{\alpha\nu}|n\rangle - \frac{2}{3}\frac{E_{0n}}{\hbar c}\varepsilon_{\gamma\epsilon\nu}a_\alpha a_\epsilon\langle 0|\hat{\mu}_\nu|n\rangle \\
& + \frac{2}{3}\delta_{\gamma\alpha}\Big(\boldsymbol{a}\cdot\langle 0|\hat{\boldsymbol{m}}|n\rangle\Big) - 2a_\alpha\langle 0|\hat{m}_\gamma|n\rangle\Bigg] \\
=& f_{0n}^{(\mu\mathcal{M})}(\boldsymbol{O}) \\
& + \frac{m_e}{9e^2\hbar^4c^2}E_{0n}^3\,(\delta_{\alpha\epsilon}\delta_{\beta\nu}-\delta_{\alpha\nu}\delta_{\beta\epsilon})a_\epsilon\langle 0|\hat{\mu}_\beta|n\rangle\langle 0|\hat{Q}_{\alpha\nu}|n\rangle \\
& - \frac{2m_e}{9e^2\hbar^4c^2}E_{0n}^3\,(\delta_{\alpha\epsilon}\delta_{\beta\nu}-\delta_{\alpha\nu}\delta_{\beta\epsilon})a_\alpha a_\epsilon\langle 0|\hat{\mu}_\beta|n\rangle\langle 0|\hat{\mu}_\nu|n\rangle \\
& - \frac{2m_e}{3e^2\hbar^3c}E_{0n}^2\Big[\boldsymbol{a}\cdot\Big(\langle 0|\hat{\boldsymbol{\mu}}|n\rangle\times\langle 0|\hat{\boldsymbol{m}}|n\rangle\Big)\Big] \\
=& f_{0n}^{(\mu\mathcal{M})}(\boldsymbol{O}) \\
& + \frac{m_e}{9e^2\hbar^4c^2}E_{0n}^3\Big[\sum_{\alpha\beta}a_\alpha\langle 0|\hat{\mu}_\beta|n\rangle\langle 0|\hat{Q}_{\alpha\beta}|n\rangle - \Big(\boldsymbol{a}\cdot\langle 0|\hat{\boldsymbol{\mu}}|n\rangle\Big)\Big(\sum_\alpha\langle 0|\hat{Q}_{\alpha\alpha}|n\rangle\Big)\Big] \\
& - \frac{2m_e}{9e^2\hbar^4c^2}E_{0n}^3\Big[\boldsymbol{a}^2\langle 0|\hat{\boldsymbol{\mu}}|n\rangle^2 - \Big(\boldsymbol{a}\cdot\langle 0|\hat{\boldsymbol{\mu}}|n\rangle\Big)\Big] \\
& - \frac{2m_e}{3e^2\hbar^3c}E_{0n}^2\Big[\boldsymbol{a}\cdot\Big(\langle 0|\hat{\boldsymbol{\mu}}|n\rangle\times\langle 0|\hat{\boldsymbol{m}}|n\rangle\Big)\Big]
\end{aligned}
\tag{3.93}
$$

Upon inspection of the terms describing the origin-dependence for each contribution to the total oscillator strength, it can be seen that terms in different contributions cancel and that then the total oscillator strength is only dependent on the terms with no dependence on $\boldsymbol{a}$.

3.4. Implementation into the ADF Program Package

To test the outlined approach on real molecular systems, the implementation into a computational program package is required. The theory presented here for the origin-independent calculation of quadrupole oscillator strengths is applicable in combination with any quantum-chemical method that is capable of providing excited states, either via a time-independent formulation or with response theory. Here, we select TD-DFT which has become an important tool in computational X-ray spectroscopy in the past years [114–117]. The theory will be discussed in more detail in chapter 4. We implemented the calculation of second-order oscillator strengths into the TD-DFT module [118–120] of the ADF program package [121, 122].

Within the ADF program package atomic units are used, which means that m_e, e, $\hbar$ are all equal to 1. The electric oscillator strengths, $f^{(\mu^2)}$, $f^{(Q^2)}$ and $f^{(\mu O)}$ (equations (3.84), (3.85) and (3.88)), contain integrals which are calculated directly within the ADF program package and so no further considerations need to be made. However, for the magnetic transition moments, ADF does not calculate directly the integrals present in equations (3.86) and (3.89). For the magnetic-dipole transition moment, ADF calculates the integrals $\langle 0|\boldsymbol{r}\times\boldsymbol{\nabla}|n\rangle$. From these, we can obtain the magnetic dipole transition moments (in atomic units) as.

$$
\langle 0|\hat{\boldsymbol{m}}|n\rangle = \frac{1}{2c}\langle 0|\boldsymbol{r}\times\hat{\boldsymbol{p}}|n\rangle = \frac{1(-i)}{2c}\langle 0|\boldsymbol{r}\times\boldsymbol{\nabla}|n\rangle, \tag{3.94}
$$

where we used that in atomic units,

$$\hat{\boldsymbol{p}} = -i\boldsymbol{\nabla}. \tag{3.95}$$

The imaginary part is then,

$$\mathrm{Im}\langle 0|\hat{\boldsymbol{m}}|n\rangle = \frac{-1}{2c}\langle 0|\boldsymbol{r}\times\boldsymbol{\nabla}|n\rangle. \tag{3.96}$$

Here, a pre-factor of $\frac{-1}{2c}$ is required to convert the integral calculated by ADF to the one in equation (3.86).

The same is required for the magnetic-quadrupole transition moments, where the calculated integrals in ADF are $\langle 0|r_\beta(\boldsymbol{r}\times\boldsymbol{\nabla})_\alpha + (\boldsymbol{r}\times\boldsymbol{\nabla})_\alpha r_\beta|n\rangle$. From this, the magnetic quadrupole transition can be calculated as,

$$\begin{aligned}\langle 0|\hat{\mathcal{M}}_{\gamma\alpha}|n\rangle &= \frac{1}{3c}\langle 0|r_\beta(\boldsymbol{r}\times\hat{\boldsymbol{p}})_\alpha + (\boldsymbol{r}\times\hat{\boldsymbol{p}})_\alpha r_\beta|n\rangle \\ &= \frac{1(-i)}{3c}\langle 0|r_\beta(\boldsymbol{r}\times\boldsymbol{\nabla})_\alpha + (\boldsymbol{r}\times\boldsymbol{\nabla})_\alpha r_\beta|n\rangle,\end{aligned} \tag{3.97}$$

and its imaginary part is,

$$\mathrm{Im}\langle 0|\hat{\mathcal{M}}_{\gamma\alpha}|n\rangle = \frac{-1}{3c}\langle 0|r_\beta(\boldsymbol{r}\times\boldsymbol{\nabla})_\alpha + (\boldsymbol{r}\times\boldsymbol{\nabla})_\alpha r_\beta|n\rangle. \tag{3.98}$$

Again, a pre-factor is needed, $\frac{-1}{3c}$. Finally, the calculated integrals and their pre-factors can be substituted into the oscillator strength. The magnetic-dipole oscillator strength becomes (in atomic units),

$$\langle f_{0n}^{(m^2)}\rangle_{\mathrm{iso}} = \frac{2}{12c^2}E_{0n}\left(\langle 0|\boldsymbol{r}\times\boldsymbol{\nabla}|n\rangle\right)^2, \tag{3.99}$$

and the electric-dipole–magnetic-quadrupole cross-term oscillator strength becomes (in atomic units),

$$\langle f_{0n}^{(\mu\mathcal{M})}\rangle_{\mathrm{iso}} = \frac{-1}{9c^2}E_{0n}^2\sum_{\alpha\beta\gamma}\varepsilon_{\alpha\beta\gamma}\langle 0|\hat{\mu}_\beta|n\rangle\,\langle 0|r_\beta(\boldsymbol{r}\times\boldsymbol{\nabla})_\alpha + (\boldsymbol{r}\times\boldsymbol{\nabla})_\alpha r_\beta|n\rangle. \tag{3.100}$$

All the theory presented thus far considers the case of having exact eigenfunctions available, but additional difficulty arises in approximate calculations using finite basis sets. In this case, the length and velocity representations of the electric transition moments will differ. The two representations converge to the exact result at different rates and will only be identical with an infinite basis set.

For the (origin-independent) zeroth order contribution, the electric-dipole, the choice of representation is not as important, especially when a large basis set is used. But the choice of representation is important for the second-order contributions as the origin-dependent terms need to cancel. For the magnetic transition moments, the electric-dipole and electric-quadrupole transition moments in the velocity representation arise when shifting the origin. Therefore, for the electric multipole transition moments to cancel with those of the magnetic contributions, these terms must also be in the velocity representation. Otherwise any differences between the length and velocity representations will manifest as a small origin-dependence in the total oscillator strength.

Therefore, in the implementation, the electric-dipole oscillator strength is calculated in the length representation, but all higher-order contributions are calculated with the velocity representation.

A note here is that when calculating the higher-order moments a large basis set is usually required to achieve suitable convergence in the magnitude of the oscillator strengths (see chapter 5). Therefore, there are usually only small differences in the values of the matrix elements in the length and velocity representation.

3.5. Validation of Theory

3.5.1. Computational Details

For the calculation of X-ray absorption spectra in the following, we have employed the scheme of Stener *et al.* [123] to allow only excitations from the relevant core orbital (see also Refs. [124–129] for related schemes). For the Cl K-edge in $TiCl_4$, only excitations from the $1s$ orbital of one of the chlorine atoms were considered, while a frozen core was used for the other three chlorine atoms in order to obtain a localized core hole [124]. For the Fe K-edge in vinylferrocene, only excitations from the iron $1s$ orbital were included. All molecular structures were optimized using the BP86 exchange–correlation functional [130, 131] and ADF's TZP basis set. The TD-DFT calculations were performed using the BP86 functional and the TZ2P basis set and employed a fine numerical integration grid (integration accuracy 8). All calculations were performed with the scalar-relativistic zeroth-order regular approximation (ZORA) [132–135].

3.5.2. Results

To illustrate the origin-independent calculation of quadrupole intensities in X-ray absorption spectroscopy (XAS) using the theory derived above and to verify our implementation, we consider two test cases. As the first example, we use titaniumtetrachloride $TiCl_4$ (see figure 3.2a for the molecular structure) and calculate the Cl K-edge XAS spectrum. This example was considered earlier in Refs. [107, 123, 136]. For such ligand K-edge spectra, the pre-edge peak transitions are dipole-allowed, and the second-order contribution to the oscillator strength should be small compared to the dipole contribution.

Figure 3.2.: Molecular structures of the model systems considered for the calculation of X-ray absorption spectra. (a) Titaniumtetrachloride ($TiCl_4$) and (b) Vinylferrocene. The orientation of the molecules within the coordinate system is also indicated.

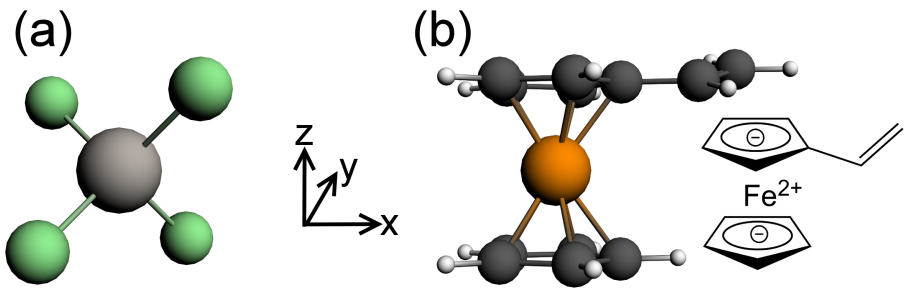

For the lowest-energy Cl K-edge excitation, the different contributions to the isotropically averaged oscillator strengths are calculated using equations (3.84)–(3.89), and are listed in Table 3.2

for different choices of the origin. In addition, we included the oscillator strengths calculated using the approximation of reference [107], i.e., considering only the electric-dipole–electric-dipole, electric-quadrupole–electric-quadrupole, and the magnetic-dipole–magnetic-dipole contributions [cf. equation (3.54)] as well as the full second-order oscillator strengths $f_{0n}^{(0)} + f_{0n}^{(2)}$ [cf. equation (3.64)].

The most natural choice for the origin is the chlorine atom from which the $1s$-electron is excited. In this case, the electric-dipole–electric-dipole contribution $f_{0n}^{(\mu^2)}$ to the oscillator strength is several orders of magnitude larger than all the second-order contributions, and the approximation of reference [107] gives results that are identical to the full second-order oscillator strengths. In this example, the scheme suggested in reference [107] to choose the origin such that the sum of the electric-quadrupole–electric-quadrupole $f_{0n}^{(Q^2)}$ and the magnetic-dipole–magnetic-dipole contributions $f_{0n}^{(m^2)}$ is minimised leads to an almost identical choice of the origin. Thus, this scheme is appropriate here.

The situation changes if the origin is not placed at the chlorine atom. To demonstrate this, we moved the origin to the titanium atom. Now, the electric-quadrupole–electric-quadrupole $f_{0n}^{(Q^2)}$ and the magnetic-dipole–magnetic-dipole contributions $f_{0n}^{(m^2)}$ increase significantly and become several times larger than the dipole oscillator strength $f_{0n}^{(\mu^2)}$. As a consequence, within the approximation of reference [107] the oscillator strength increases by more than a factor of two when shifting the origin from the chlorine to the titanium atom. However, also the magnitudes of electric-dipole–electric-octupole and the electric-dipole–magnetic-quadrupole contributions, $f_{0n}^{(\mu O)}$ and $f_{0n}^{(\mu\mathcal{M})}$, increase and since these have a negative sign, they exactly cancel the increase of $f_{0n}^{(Q^2)}$ and $f_{0n}^{(m^2)}$. Thus, the full second-order oscillator strength remains unchanged.

In addition, we also shifted the origin away from the molecule by larger amounts. In particular, we used shifts of 10 Å, 50 Å, and 100 Å along the negative x-direction. Here, a similar observation can be made. The electric-quadrupole–electric-quadrupole, $f_{0n}^{(Q^2)}$, and the magnetic-dipole–magnetic-dipole, $f_{0n}^{(m^2)}$, contributions increase substantially, and for a shift of 100 Å, the oscillator strength within the approximation of reference [107] is four orders of magnitude larger than for the origin at the chlorine atom. On the other hand, when including the electric-dipole–electric-octupole and the electric-dipole–magnetic-quadrupole contributions, the full second-order oscillator strengths are unchanged, even though the individual contributions differ.

As a second example, we consider vinylferrocene, which is a ferrocene molecule bearing a vinyl substituent at one of the cyclopentadienyl rings (see figure 3.2b for the molecular structure). Here, we consider the Fe K-edge XAS spectrum and specifically the lowest-energy (pre-edge peak) excitation, which is a $1s \rightarrow 3d$ transition. In unsubstituted ferrocene, this pre-edge peak excitation is dipole-forbidden, for symmetry reasons, and its oscillator strength is solely due to the second-order contributions. In this case, the electric-quadrupole–electric-quadrupole and the magnetic-dipole-magnetic-dipole contributions become origin independent (see section 3.2), whereas the remaining second-order contributions $f_{0n}^{(\mu O)}$ and $f_{0n}^{(\mu\mathcal{M})}$ vanish. However, in vinylferrocene this symmetry is lost and the lowest-energy transition gains a small dipole oscillator strength (for a detailed discussion, see chapter 6).

The oscillator strengths and their contributions calculated for the lowest-energy Fe K-edge excitation using different choices of the origin are shown in Table 3.3. First, the most natural choice for the origin is the iron atom. In this case, the electric-dipole–electric-dipole and the electric-quadrupole–electric-quadrupole contributions to the oscillator strength are comparable in size.

Table 3.2.: X-ray absorption oscillator strength for $TiCl_4$, calculated for the lowest-energy transition at the Cl K-edge (excitation energy 2755.6 eV). The total isotropically averaged oscillator strength and its different contributions are given for different positions of the origin of the coordinate system.

origin		$\boldsymbol{O}$	$\boldsymbol{O}+\boldsymbol{a}$	$\boldsymbol{O}+\boldsymbol{a}$	$\boldsymbol{O}+\boldsymbol{a}$
	Cl atom	Ti atom	$a_x = -10$ Å	$a_x = -50$ Å	$a_x = -100$ Å
$\langle f_{0n}^{(\mu^2)} \rangle_{\text{iso}}$	$4.57 \cdot 10^{-4}$	$4.57 \cdot 10^{-4}$	$4.58 \cdot 10^{-4}$	$4.57 \cdot 10^{-4}$	$4.58 \cdot 10^{-4}$
$\langle f_{0n}^{(Q^2)} \rangle_{\text{iso}}$	$6.04 \cdot 10^{-10}$	$7.24 \cdot 10^{-4}$	$1.09 \cdot 10^{-2}$	$3.65 \cdot 10^{-1}$	1.35
$\langle f_{0n}^{(m^2)} \rangle_{\text{iso}}$	$6.61 \cdot 10^{-13}$	$1.21 \cdot 10^{-3}$	$1.80 \cdot 10^{-2}$	$3.58 \cdot 10^{-1}$	2.23
$\langle f_{0n}^{(\mu O)} \rangle_{\text{iso}}$	$-8.94 \cdot 10^{-7}$	$-3.23 \cdot 10^{-4}$	$-4.89 \cdot 10^{-3}$	$-2.46 \cdot 10^{-1}$	$-6.03 \cdot 10^{-1}$
$\langle f_{0n}^{(\mu \mathcal{M})} \rangle_{\text{iso}}$	$-9.88 \cdot 10^{-7}$	$-1.61 \cdot 10^{-3}$	$-2.40 \cdot 10^{-2}$	$-4.77 \cdot 10^{-1}$	-2.97
$\langle f_{0n}^{(\mu^2)} + f_{0n}^{(Q^2)} + f_{0n}^{(m^2)} \rangle_{\text{iso}}$	$4.57 \cdot 10^{-4}$	$2.39 \cdot 10^{-3}$	$2.94 \cdot 10^{-2}$	$7.24 \cdot 10^{-1}$	3.58
Full $\langle f_{0n}^{(0)} + f_{0n}^{(2)} \rangle_{\text{iso}}$	$4.55 \cdot 10^{-4}$	$4.55 \cdot 10^{-4}$	$4.55 \cdot 10^{-4}$	$4.55 \cdot 10^{-4}$	$4.55 \cdot 10^{-4}$

The remaining contributions are orders of magnitude smaller. Therefore, the oscillator strength calculated with the approximation of reference [107] is identical to the full second-order oscillator strength.

To investigate the dependence on the origin, we shifted the origin far away from the molecule using a shift of 100 Å in the negative x-direction, a shift of 100 Å in the negative z-direction, and a shift of 50 Å in both the negative x-direction and the negative z-direction. In all three cases, the electric-quadrupole–electric-quadrupole and the magnetic-dipole–magnetic-dipole contributions, $f_{0n}^{(Q^2)}$ and $f_{0n}^{(m^2)}$, increase by several orders of magnitude compared to the calculation in which the origin is placed at the iron atom. As a result, the oscillator strengths calculated with the approximation of reference [107] also increase by up to five orders of magnitude. However, at the same time the two remaining second-order contributions, i.e., the electric-dipole–electric-octupole contribution $f_{0n}^{(\mu O)}$ and the electric-dipole–magnetic-quadrupole contribution $f_{0n}^{(\mu \mathcal{M})}$, assume large negative values and exactly cancel the increase of $f_{0n}^{(Q^2)}$ and $f_{0n}^{(m^2)}$ such that the total second-order oscillator strength remains origin independent.

Finally, we used the scheme suggested in reference [107] for fixing the origin of the coordinate system, i.e., we chose the origin such that the sum of $f_{0n}^{(Q^2)}$ and $f_{0n}^{(m^2)}$ is minimised. In the situation considered here, where the electric-dipole–electric-dipole and the electric-quadrupole–electric-quadrupole contributions to the oscillator strengths are of similar size, this scheme moves the origin away from the iron atom. The resulting shift is given in the caption of the last column of Table 3.3. As a consequence, the oscillator strength within the approximation of reference [107] decreases by ca. 30 %. Again, this decrease is compensated for if the remaining second-order contributions are included. Thus, the scheme of reference [107] can lead to a spurious decrease of the oscillator strength in some cases. Previously, we found that this problem is even more severe in cases where the electric-dipole–electric-dipole contribution to the oscillator strength is significantly smaller than the quadrupole oscillator strength [108]. However, if all second-order terms are included consistently the quadrupole oscillator strengths become origin-independent and no special placement of the origin is necessary.

Table 3.3.: X-ray absorption oscillator strength for Vinylferrocene, calculated for the lowest-energy transition at the Fe K-edge (excitation energy 7051.3 eV). The total isotropically averaged oscillator strength and its different contributions are given for different positions of the origin of the coordinate system.

origin	$\boldsymbol{O}$ Fe atom	$\boldsymbol{O}+\boldsymbol{a}$ $a_x = -100$Å	$\boldsymbol{O}+\boldsymbol{a}$ $a_z - 100$ Å	$\boldsymbol{O}+\boldsymbol{a}$ $a_x = -50$ Å $a_z = -50$ Å	$\boldsymbol{O}+\boldsymbol{a}$ $a_x = +0.128$ Å $a_y = +0.195$ Å $a_z = +0.007$ Å
$\langle f_{0n}^{(\mu^2)} \rangle_{\text{iso}}$	$2.55 \cdot 10^{-6}$	$2.55 \cdot 10^{-6}$	$2.55 \cdot 10^{-6}$	$2.55 \cdot 10^{-6}$	$2.55 \cdot 10^{-6}$
$\langle f_{0n}^{(Q^2)} \rangle_{\text{iso}}$	$3.09 \cdot 10^{-6}$	$8.63 \cdot 10^{-2}$	$7.30 \cdot 10^{-2}$	$4.47 \cdot 10^{-2}$	$1.28 \cdot 10^{-6}$
$\langle f_{0n}^{(m^2)} \rangle_{\text{iso}}$	$1.14 \cdot 10^{-12}$	$2.29 \cdot 10^{-2}$	$9.04 \cdot 10^{-2}$	$5.87 \cdot 10^{-3}$	$1.56 \cdot 10^{-7}$
$\langle f_{0n}^{(\mu O)} \rangle_{\text{iso}}$	$-1.71 \cdot 10^{-8}$	$-7.83 \cdot 10^{-2}$	$-4.24 \cdot 10^{-2}$	$-4.23 \cdot 10^{-2}$	$6.33 \cdot 10^{-7}$
$\langle f_{0n}^{(\mu \mathcal{M})} \rangle_{\text{iso}}$	$-1.52 \cdot 10^{-8}$	$-3.09 \cdot 10^{-2}$	$-1.21 \cdot 10^{-1}$	$-8.19 \cdot 10^{-3}$	$9.83 \cdot 10^{-7}$
$\langle f_{0n}^{(\mu^2)} + f_{0n}^{(Q^2)} + f_{0n}^{(m^2)} \rangle_{\text{iso}}$	$5.64 \cdot 10^{-6}$	$1.09 \cdot 10^{-1}$	$1.63 \cdot 10^{-1}$	$5.05 \cdot 10^{-2}$	$3.99 \cdot 10^{-6}$
Full $\langle f_{0n}^{(0)} + f_{0n}^{(2)} \rangle_{\text{iso}}$	$5.61 \cdot 10^{-6}$	$5.61 \cdot 10^{-6}$	$5.61 \cdot 10^{-6}$	$5.61 \cdot 10^{-6}$	$5.61 \cdot 10^{-6}$

3.6. Conclusions

Herein, we have derived origin-independent expressions for calculating XAS intensities beyond the dipole approximation. In particular, we have shown that for a consistent formulation, it is necessary to retain all contributions to the oscillator strengths that are of the same order in the wave vector. This differs from the previous approach [107], in which the multipole expansion was truncated for the transition moments. Here, two additional contributions to the second-order (quadrupole) oscillator strengths arise, which are cross-terms depending on products of electric-dipole and electric-octupole transition moments and of electric-dipole and magnetic-quadrupole transition moments, respectively. Thus, the origin-dependence of the sum of electric-quadrupole–electric-quadrupole and magnetic-dipole–magnetic-dipole contributions pointed out earlier [107] is not a fundamental limitation of the use of the multipole expansion.

We have applied this approach for the calculation of origin-independent oscillator strengths to two test cases, $TiCl_4$ and vinylferrocene. It can clearly be seen that the oscillator strengths no longer depend on the placement of the origin if we include the electric-dipole–electric-octupole and electric-dipole–magnetic-quadrupole cross-terms. Nevertheless, the results shown here do not invalidate any results obtained with the scheme shown in reference [107]. Our results confirm that if the origin of the coordinate system is placed at the atom where the core excitation occurs, the two additional second order terms become negligible and both methods provide comparable results.

However, with the theory presented here the placement of the origin need no longer be considered. Moreover, calculations will not suffer the problems of the origin placement scheme proposed in reference [107] that when a small dipole contribution is present, the origin of the coordinate system might be placed far away from the origin of the excitation. Moreover, it enables the calculation of spectra for complexes where the excitation orbital is delocalised over several atoms, without the need to transform to localised core orbitals.

Our approach, though shown here using TD-DFT, is not restricted to TD-DFT and can be used in conjunction with any method where the calculation of intensities is required, as long as the method can provide the required transition moments. Moreover, it is not restricted to XAS spectroscopy, but is also applicable for calculating XES intensities, for instance using the approach of reference [137] (see chapter 4). Finally, we note that it becomes necessary to go beyond the dipole approximation not only for short wavelengths, such as those employed in hard X-ray spectroscopy, but also for extended molecular systems. Therefore, for describing the optical response in an extended nanostructure in the visible spectrum, it becomes necessary to go beyond the dipole approximation as well. Thus, the origin-independent formalism derived here will also be essential for predicting optical properties of nanostructured materials, such as metamaterials [138].

4. Theoretical Approaches to X-ray Spectroscopy

Quantum-chemistry has developed many approximations for solving the electronic Schrödinger equation, which was introduced in chapter 2. Within this chapter we will first introduce the basic concepts of the two main strategies of quantum-chemistry. Next, we will consider the methods available for the calculation of X-ray spectra and discuss their benefits and limitations.

4.1. Methods for the Calculation of the Ground Electronic State

4.1.1. Wave Function-Based Quantum-Chemistry

The problem we are trying to solve is to find the ground-state electronic energy and wave function of a molecular system. This requires solving the time-independent electronic Schrödinger equation,

$$\hat{H}_e \Psi_n^{(\boldsymbol{R})}(\boldsymbol{r}_1, \boldsymbol{r}_2, \ldots, \boldsymbol{r}_n) = E_{e,n}^{(\boldsymbol{R})} \Psi_n^{(\boldsymbol{R})}(\boldsymbol{r}_1, \boldsymbol{r}_2, \ldots, \boldsymbol{r}_n), \tag{4.1}$$

where the electronic Hamiltonian $\hat{H}_e$ has been introduced in equation (2.5). Solving the Schrödinger equation analytically is only possible for some one-electron systems. Therefore, approximate methods have to be devised. This section follows the theory as outlined in reference [139]. A suitable starting point for approximating the ground state is the variational principle. The variational principle states,

$$E_0 \leq \langle \tilde{\Psi} | \hat{H} | \tilde{\Psi} \rangle \tag{4.2}$$

where E_0 is the ground state energy of the system and $\tilde{\Psi}$ is a normalised trial wave function. This means that any choice of the trial wave function will always provide an energy greater than or equal to the ground-state energy. Therefore, to find the ground state energy we can minimise the expectation value of the energy,

$$E_0 \leq \min(\langle \tilde{\Psi} | \hat{H} | \tilde{\Psi} \rangle) \tag{4.3}$$

The ground-state wave function Ψ_0 is the one for which the minimum is obtained. To apply the variational principle, we have to choose a suitable form of the trial wave function.

Hartree-Fock (HF)

Hartree originally proposed to separate the many-electron wave function into a product of one-electron functions and to use this as the trial wave function. This is called the Hartree product Π,

$$\tilde{\Psi}(\boldsymbol{r}_1, \boldsymbol{r}_2, \ldots, \boldsymbol{r}_n) \approx \Pi(\boldsymbol{r}_1, \boldsymbol{r}_2, \ldots, \boldsymbol{r}_n) = \phi_1(\boldsymbol{r}_1) \cdot \phi_2(\boldsymbol{r}_2) \cdot \cdots \cdot \phi_n(\boldsymbol{r}_n). \tag{4.4}$$

The one-electron functions $\phi_i(\boldsymbol{r})$ have to be orthonormal, that is the overlap integral between one-electron functions must equal 1 when $i = j$ and 0 when $i \neq j$,

$$\langle i|j\rangle = \int \phi_i^*(\boldsymbol{r})\phi_j(\boldsymbol{r})d^3r = \delta_{ij} = \begin{cases} i = j & 1 \\ i \neq j & 0 \end{cases}. \tag{4.5}$$

The one-electron functions are what is often referred to as "orbitals". The problem with the Hartree product approximation to the wave function is that it treats the electrons as distinguishable particles, because a different orbital is assigned to each electron. However, all electrons are identical and, therefore, indistinguishable and according to the Pauli principle the wave function should change its sign on swapping any two electrons. As a consequence, the Hartree product does not obey the Pauli principle and the wave function is different if two electrons are interchanged.

Hence, Fock proposed a modification to the idea of the Hartree product where an antisymmetrisation operator is introduced,

$$\tilde{\Psi}(\boldsymbol{r}_1, \boldsymbol{r}_2, \ldots, \boldsymbol{r}_n) = \hat{\mathcal{A}}\Pi(\boldsymbol{r}_1, \boldsymbol{r}_2, \ldots, \boldsymbol{r}_n) = \hat{\mathcal{A}}(\phi_1(\boldsymbol{r}_1) \cdot \phi_2(\boldsymbol{r}_2) \ldots \phi_n(\boldsymbol{r}_n)). \tag{4.6}$$

The antisymmetriser $\hat{\mathcal{A}}$ can be written as a sum of permutation operators, $\hat{\mathcal{A}} = \sum_\mu (-1)^\mu \hat{P}_\mu$, where $\hat{P}_\mu$ are all possible permutations of electrons and $(-1)^\mu$ is the parity of permutation $\hat{P}_\mu$. The antisymmetrisation ensures that the Pauli principle is fulfilled. We can rewrite the antisymmetrised Hartree product as a Slater determinant,

$$\begin{aligned} \tilde{\Psi}(\boldsymbol{r}_1, \boldsymbol{r}_2, \ldots, \boldsymbol{r}_n) &= \mathcal{A} \cdot \Pi(\boldsymbol{r}_1, \boldsymbol{r}_2, \ldots, \boldsymbol{r}_n) \\ &= \mathcal{A}(\phi(\boldsymbol{r}_1) \cdot \phi(\boldsymbol{r}_2) \ldots \phi(\boldsymbol{r}_n)) \\ &= \Phi_{HF}(\boldsymbol{r}_1, \boldsymbol{r}_2, \ldots, \boldsymbol{r}_n) = \frac{1}{\sqrt{N_{\text{elec}}!}} \begin{vmatrix} \phi_1(\boldsymbol{r}_1) & \phi_1(\boldsymbol{r}_2) & \cdots & \phi_1(\boldsymbol{r}_n) \\ \phi_2(\boldsymbol{r}_1) & \phi_2(\boldsymbol{r}_2) & \cdots & \phi_2(\boldsymbol{r}_n) \\ \vdots & \vdots & \cdots & \vdots \\ \phi_n(\boldsymbol{r}_1) & \phi_n(\boldsymbol{r}_2) & \cdots & \phi_n(\boldsymbol{r}_n) \end{vmatrix} \end{aligned} \tag{4.7}$$

where N_{elec} is the number of electrons. This form of the trial wave function now fulfils the Pauli principle and is used in the HF method. HF is the most basic approximation to solve the electronic Schrödinger equation used in quantum chemistry and also forms the basis of most wave function methods.

To find the ground-state wave function, using the HF trial wave function, we first rewrite the electronic Hamiltonian (see equation (2.5)) and separate it into one- and two-electron terms,

$$\hat{H}_e = \sum_i^{N_{\text{elec}}} \hat{h}_i + \frac{1}{2} \sum_{ij}^{N_{\text{elec}}} \hat{g}_{ij} + V_{NN} \tag{4.8}$$

where V_{NN} is the nuclear-nuclear repulsion and is constant for a fixed molecular geometry, $\hat{h}_i$ contains the kinetic energy of the electrons $\hat{T}_e$ and the nuclear–electron attraction potential energy $\hat{V}_{Ne}$. In atomic units, it is given by,

$$\hat{h}_i = -\frac{\nabla_i^2}{2} - \sum_I^N \frac{Z_I}{|\boldsymbol{R}_I - \boldsymbol{r}_i|}. \tag{4.9}$$

Finally, $\hat{g}_{ij}$ describes the two-electron interactions contained in the electron–electron repulsion potential energy $\hat{V}_{ee}$ and is (in atomic units) given by,

$$\hat{g}_{ij} = \frac{1}{|\boldsymbol{r}_i - \boldsymbol{r}_j|}. \tag{4.10}$$

To evaluate the expectation value of $\hat{H}_e$ for the HF trial wave function the next step is to look at the integrals of the HF trial wave function with the one- and two-electron operators of the electronic Hamiltonian. First, for the one-electron operator $\hat{h}_i$ one finds,

$$\begin{aligned}\langle\Pi|\hat{h}_i|\Pi\rangle &= \langle\phi_i(\boldsymbol{r}_i)\phi_j(\boldsymbol{r}_j)\dots\phi_n(\boldsymbol{r}_n)|\hat{h}_i|\phi_i(\boldsymbol{r}_i)\phi_j(\boldsymbol{r}_j)\dots\phi_n(\boldsymbol{r}_n)\rangle \\ &= \langle\phi_i(\boldsymbol{r}_i)|\hat{h}_i|\phi_i(\boldsymbol{r}_i)\rangle\langle\phi_j(\boldsymbol{r}_j)|\phi_j(\boldsymbol{r}_j)\rangle\dots\langle\phi_n(\boldsymbol{r}_n)|\phi_n(\boldsymbol{r}_n)\rangle \\ &= \langle\phi_i(\boldsymbol{r}_i)|\hat{h}_i|\phi_i(\boldsymbol{r}_i)\rangle = h_i.\end{aligned} \tag{4.11}$$

$\hat{h}_i$ will only interact with orbital i and all the other integrals are overlap integrals which due to orthonormalisation are equal to 1 for the non-permuted Hartree product. If a permutation operator is applied to one of the Hartree products the integral is 0 because the one-electron functions are orthogonal. Next is the two-electron operator $\hat{g}_{ij}$ with the non-permuted Hartree product,

$$\begin{aligned}\langle\Pi|\hat{g}_{ij}|\Pi\rangle &= \langle\phi_i(\boldsymbol{r}_i)\phi_j(\boldsymbol{r}_j)\phi_k(\boldsymbol{r}_k)\dots\phi_n(\boldsymbol{r}_n)|\hat{g}_{ij}|\phi_i(\boldsymbol{r}_i)\phi_j(\boldsymbol{r}_j)\phi_k(\boldsymbol{r}_k)\dots\phi_n(\boldsymbol{r}_n)\rangle \\ &= \langle\phi_i(\boldsymbol{r}_i)\phi_j(\boldsymbol{r}_j)|\hat{g}_{ij}|\phi_i(\boldsymbol{r}_i)\phi_j(\boldsymbol{r}_j)\rangle\langle\phi_k(\boldsymbol{r}_k)|\phi_k(\boldsymbol{r}_k)\rangle\dots\langle\phi_n(\boldsymbol{r}_n)|\phi_n(\boldsymbol{r}_n)\rangle \\ &= \langle\phi_i(\boldsymbol{r}_i)\phi_j(\boldsymbol{r}_j)|\hat{g}_{ij}|\phi_i(\boldsymbol{r}_i)\phi_j(\boldsymbol{r}_j)\rangle = J_{ij},\end{aligned} \tag{4.12}$$

where $\hat{g}_{ij}$ will only interact with orbitals i and j and the integrals remaining are just overlap integrals which equal 1. These integrals are the Coulomb integrals J_{ij}. However, for $\hat{g}_{ij}$, the permuted Hartree product integrals give a non-zero value,

$$\begin{aligned}-\langle\Pi|\hat{g}_{ij}|\hat{P}_{ij}\Pi\rangle &= -\langle\phi_i(\boldsymbol{r}_i)\phi_j(\boldsymbol{r}_j)\phi_k(\boldsymbol{r}_k)\dots\phi_n(\boldsymbol{r}_n)|\hat{g}_{ij}|\phi_i(\boldsymbol{r}_j)\phi_j(\boldsymbol{r}_i)\phi_k(\boldsymbol{r}_k)\dots\phi_n(\boldsymbol{r}_n)\rangle \\ &= -\langle\phi_i(\boldsymbol{r}_i)\phi_j(\boldsymbol{r}_j)|\hat{g}_{ij}|\phi_i(\boldsymbol{r}_j)\phi_j(\boldsymbol{r}_i)\rangle\langle\phi_k(\boldsymbol{r}_k)|\phi_k(\boldsymbol{r}_k)\rangle\dots\langle\phi_n(\boldsymbol{r}_n)|\phi_n(\boldsymbol{r}_n)\rangle \\ &= -\langle\phi_i(\boldsymbol{r}_i)\phi_j(\boldsymbol{r}_j)|\hat{g}_{ij}|\phi_i(\boldsymbol{r}_j)\phi_j(\boldsymbol{r}_i)\rangle = -K_{ij}.\end{aligned} \tag{4.13}$$

The remaining overlap integrals are the same as the non-permuted situation and so the integrals do not disappear when considering the two-electron operator. The integrals considering the case when the electrons are permuted are the exchange integrals K_{ij}. The higher-order permutations of the Hartree product give zero values for the integrals. This set of rules for the evaluation of the expectation values of Slater determinants are called the Slater-Condon rules.

Using the Slater-Condon rules, the energy expectation value of the trial Slater determinant can be written as,

$$\langle\tilde{\Psi}_{HF}(\boldsymbol{r}_1,\boldsymbol{r}_2,\dots,\boldsymbol{r}_n)|\hat{H}_e|\tilde{\Psi}_{HF}(\boldsymbol{r}_1,\boldsymbol{r}_2,\dots,\boldsymbol{r}_n)\rangle = \sum_i^{N_{\text{elec}}} h_i + \frac{1}{2}\sum_{ij}^{N_{\text{elec}}}(J_{ij}-K_{ij}) + V_{NN} = E_{HF}^{(\text{trial})} \tag{4.14}$$

With a trial wave function and a way to calculate the energy of the wave function, we now need to find the ground-state wave function by minimising the energy. The only variables present within the wave function are the one-electron functions. Consequently, to minimise the wave function we must find the optimum form of the one-electron functions, keeping in mind the orthonormality constraints. Therefore we perform a constrained optimisation using a Lagrange equation,

$$L = E - \sum_{ij}^{N_{\text{elec}}} \lambda_{ij}(\langle\phi_i|\phi_j\rangle - \delta_{ij}), \tag{4.15}$$

where λ_{ij} is a matrix of Lagrange multipliers. We must now find the point at which the first derivative of L is zero. Therefore, we solve the equation,

$$\delta L = \delta E - \sum_{ij}^{N_{\text{elec}}} \lambda_{ij}(\langle\delta\phi_i|\phi_j\rangle - \langle\phi_i|\delta\phi_j\rangle) = 0. \tag{4.16}$$

From equation (4.14) it is clear to see the energy of the wave function is dependent on the one-electron functions. Therefore, we need to determine when a change in the orbitals leads to a zero change in the energy. In equation (4.14), i is an index present in all terms and therefore, the equation can be rewritten as

$$E = \sum_{i}^{N_{\text{elec}}} \left[h_i + \frac{1}{2} \int \phi_i^*(\boldsymbol{r})(\hat{J} - \hat{K})\phi_i(\boldsymbol{r}) d\boldsymbol{r} \right] + V_{NN} \tag{4.17}$$

where we define $\hat{J}$ and $\hat{K}$ acting on $\phi_i(\boldsymbol{r}_i)$ as,

$$\hat{J}\phi_i(\boldsymbol{r}) = \sum_{j}^{N_{\text{elec}}} \int \phi_j^*(\boldsymbol{r}')\hat{g}_{ij}\phi_j(\boldsymbol{r}')d\boldsymbol{r}'\phi_i(\boldsymbol{r}), \tag{4.18}$$

$$\hat{K}\phi_i(\boldsymbol{r}) = \sum_{j}^{N_{\text{elec}}} \int \phi_j^*(\boldsymbol{r}')\hat{g}_{ij}\phi_i(\boldsymbol{r}')d\boldsymbol{r}'\phi_j(\boldsymbol{r}). \tag{4.19}$$

The indices can be switched in this equation. With these equations we obtain δE,

$$\begin{aligned} \delta E = &\sum_{i}^{N_{\text{elec}}} \left(\int \phi_i^*(\boldsymbol{r})\hat{h}_i\delta\phi_i(\boldsymbol{r})d\boldsymbol{r} + \int \delta\phi_i^*(\boldsymbol{r})\hat{h}_i\phi_i(\boldsymbol{r})d\boldsymbol{r} \right) + \\ &+ \frac{1}{2}\sum_{i}^{N_{\text{elec}}} \left(\int \phi_i^*(\boldsymbol{r})(\hat{J} - \hat{K})\delta\phi_i(\boldsymbol{r})d\boldsymbol{r} + \int \delta\phi_i^*(\boldsymbol{r})(\hat{J} - \hat{K})\phi_i(\boldsymbol{r})d\boldsymbol{r} \right) + \\ &+ \frac{1}{2}\sum_{j}^{N_{\text{elec}}} \left(\int \phi_j^*(\boldsymbol{r}')(\hat{J} - \hat{K})\delta\phi_j(\boldsymbol{r}')d\boldsymbol{r}' + \int \delta\phi_j^*(\boldsymbol{r}')(\hat{J} - \hat{K})\phi_j(\boldsymbol{r}')d\boldsymbol{r}' \right). \end{aligned} \tag{4.20}$$

As i and j run over all electrons and thus, all one-electron functions, the two-electron terms are all counted double and therefore, the factor $\frac{1}{2}$ is cancelled. Hence, equation (4.20) can be written as,

$$\begin{aligned} \delta E = &\sum_{i}^{N_{\text{elec}}} \left(\int \phi_i^*(\boldsymbol{r})\hat{h}\delta\phi_i(\boldsymbol{r})d\boldsymbol{r} + \int \delta\phi_i^*(\boldsymbol{r})\hat{h}\phi_i(\boldsymbol{r}) \right) + \\ &\sum_{i}^{N_{\text{elec}}} \left(\int \phi_i^*(\boldsymbol{r})(\hat{J} - \hat{K})\delta\phi_i(\boldsymbol{r})d\boldsymbol{r} + \int \delta\phi_i(\boldsymbol{r})(\hat{J} - \hat{K})\phi_i(\boldsymbol{r})d\boldsymbol{r} \right). \end{aligned} \tag{4.21}$$

The operators in equation (4.21) can be combined and written as one operator, the Fock operator,

$$\hat{F} = \hat{h} + \hat{J} - \hat{K}, \tag{4.22}$$

and now δE can be written in terms of the $\hat{F}$,

$$\delta E = \sum_{i}^{N_{\text{elec}}} \left(\int \phi_i^*(\boldsymbol{r})\hat{F}\delta\phi_i(\boldsymbol{r})d\boldsymbol{r} + \int \delta\phi_i(\boldsymbol{r})\hat{F}\phi_i(\boldsymbol{r})d\boldsymbol{r} \right). \tag{4.23}$$

We can substitute this expression for δE into equation (4.16),

$$\begin{aligned} \delta L = &\sum_{i}^{N_{\text{elec}}} \left(\int \phi_i^*(\boldsymbol{r})\hat{F}\delta\phi_i(\boldsymbol{r})d\boldsymbol{r} + \int \delta\phi_i^*(\boldsymbol{r})\hat{F}\phi_i(\boldsymbol{r})d\boldsymbol{r} \right) - \\ &\sum_{ij}^{N_{\text{elec}}} \lambda_{ij} \left(\int \delta\phi_i(\boldsymbol{r})\phi_j(\boldsymbol{r})d\boldsymbol{r} - \lambda_{ij} \int \phi_i(\boldsymbol{r})\delta\phi_j(\boldsymbol{r})d\boldsymbol{r} \right) = 0. \end{aligned} \tag{4.24}$$

This equation has to be fulfilled for every possible $\delta\phi_i$. Therefore, we arrive at the equation,

$$\hat{F}\phi_i(\boldsymbol{r}) = \sum_j^n \lambda_{ij}\phi_j(\boldsymbol{r}). \tag{4.25}$$

If the Lagrange multiplier matrix λ_{ij} is diagonalised we form the canonical orbitals ϕ_i'. The use of the canonical orbitals then gives a one-electron eigenvalue equation,

$$\hat{F}\phi_i'(\boldsymbol{r}) = \epsilon_i\phi_i'(\boldsymbol{r}), \tag{4.26}$$

where ϵ_i is the one-electron (orbital) energy of function i. An important note here is that the Hartree-Fock energy E_{HF} is not equal to the sum of the orbital energies as there is no inclusion of the nuclear–nuclear repulsion and the two electron-terms are counted twice.

Here we have described a situation where each electron is described by a different one-electron function, as is the case for unrestricted Hartee-Fock (UHF), except a spin function must also be included within UHF. For restricted HF (RHF), the two-electron integrals are counted differently, as all orbitals are doubly occupied and so only $\frac{N_{\mathrm{elec}}}{2}$ one-electron functions are optimised. Therefore, in RHF the energy is,

$$E = 2\sum_i^{N_{\mathrm{elec}}/2} h_i + \sum_{ij}^{N_{\mathrm{elec}}/2} (2J_{ij} - K_{ij}) + V_{NN}, \tag{4.27}$$

as each orbital is occupied by two-electrons, the sum runs over $\frac{N_{\mathrm{elec}}}{2}$ functions.

However, so far we have not considered the form of the one-electron functions. In practice, a basis set is used and the one-electron functions are expanded as a linear combination of the different functions within the basis set,

$$\phi_i(\boldsymbol{r}) = \sum_j c_j^{(i)}\chi_j(\boldsymbol{r}) \tag{4.28}$$

where $\chi_j(\boldsymbol{r})$ is a basis function (for more information see chapter 5). Moreover, the introduction of the basis set into the Fock equation leads to the Roothaan-Hall equations,

$$\boldsymbol{FC} = \boldsymbol{SC\epsilon}, \tag{4.29}$$

where $\boldsymbol{C}$ is the matrix of basis set coefficients, ϵ is a vector containing the orbital energies, $\boldsymbol{S}$ is the overlap matrix between the basis functions and $\boldsymbol{F}$ is the Fock matrix with the elements,

$$\langle\chi_\alpha|\hat{F}|\chi_\beta\rangle. \tag{4.30}$$

With the introduction of the basis set, these matrix elements of the fock operator become,

$$\begin{aligned}\langle\chi_\alpha|\hat{F}|\chi_\beta\rangle &= \langle\chi_\alpha|\hat{h}|\chi_\beta\rangle + \sum_j^{Occ.MO}\sum_{\gamma\delta}^{M_{\mathrm{Basis}}} c_{\gamma j}c_{\delta j}\langle\chi_\alpha\chi_\gamma|\hat{g}_{ij}|\chi_\beta\chi_\delta\rangle - \langle\chi_\alpha\chi_\gamma|\hat{g}_{ij}|\chi_\delta\chi_\beta\rangle, \\ &= \langle\chi_\alpha|\hat{h}|\chi_\beta\rangle + \sum_{\gamma\delta}^{M_{\mathrm{Basis}}} D_{\gamma\delta}\langle\chi_\alpha\chi_\gamma||\chi_\beta\chi_\delta\rangle,\end{aligned} \tag{4.31}$$

where $c_{\gamma j}$ is the basis function coefficient for orbital j and $D_{\gamma\delta}$ is the one-electron density matrix,

$$D_{\gamma\delta} = \sum_j c_{\gamma j}c_{\delta j}. \tag{4.32}$$

For more information on the inclusion of an atomic basis set into the HF equations see reference [139].

Extensions of the HF Method

HF is a mean-field approach, which means the electrons see the potential field created by the other electrons but only in an "averaged" way. Hence, HF neglects all electron correlation. To reclaim the correlation energy lost by the approximations made in HF theory, wave function theories offer a method for systematic improvement. To this end, the correlation is recovered by including excited Slater determinants,

$$\Psi_{CI}(\boldsymbol{r}_1, \ldots, \boldsymbol{r}_n) = C_{HF}\Phi_{HF} + \sum_{ia}^{n} C_i^a \Phi_i^a + \sum_{ijab}^{n} C_{ij}^{ab}\Phi_{ij}^{ab} \ldots \tag{4.33}$$

where the C's are the coefficients of the respective Slater determinants, Φ_{HF} is the HF determinant, Φ_i^a is an excited Slater determinant where the electron from the occupied orbital i is in the virtual orbital a and Φ_{ij}^{ab} is a doubly excited slater determinant, where two electrons from the occupied orbitals i and j are in the virtual orbitals a and b.

The first method using this approach is called configuration interaction (CI) theory and within this method the HF orbitals are used as a basis for all determinants and only the coefficients of the Slater determinants are optimised. The next step which may be taken is to also optimise the one-electron orbitals of the Slater determinants. This is called complete active space self-consistent field (CASSCF) method. However, CASSCF is too expensive if all orbitals are optimised within the calculation and therefore, usually an active space is chosen which includes the required orbitals to describe the system more accurately.

However, CI and CASSCF have an inherent problem in that they are not size-extensive. To this end, coupled cluster (CC) theory was developed. This has a similar expansion as to CI but a different (exponential) parametrisation is used to express the coefficients of the excited determinants. The extra terms this parametrisation introduces are why coupled cluster theory is size-extensive [139, 140].

4.1.2. Density Functional Theory (DFT)

Though HF is the basis of many methods available in quantum chemistry, a different school of methods have also developed and is classified as DFT. The discussion of DFT in this section mainly follows that presented in reference [141]. The basic idea of DFT is that the molecular system can be described by the electron density only instead of using the wave function. However, the wave function and the electron density are intrinsically linked. Obviously, the electron density is derived from the wave function,

$$\rho(\boldsymbol{r}_1) = N_{\text{elec}} \int |\Psi(\boldsymbol{r}_1, \boldsymbol{r}_2, \ldots, \boldsymbol{r}_n)|^2 \, d\boldsymbol{r}_2 \ldots d\boldsymbol{r}_n, \tag{4.34}$$

where N_{elec} is the number of electrons and $\rho(\boldsymbol{r}_1)$ is the electron density describing the probability density of finding any electron in a volume element $d\boldsymbol{r}_1$. The number of electrons in the system can also be calculated from the density,

$$\int \rho(\boldsymbol{r}) d\boldsymbol{r} = N_{\text{elec}} \tag{4.35}$$

To set up an equivalent theory in terms of the electron density, it is necessary that also the wave function is uniquely determined by the electron density. This was proven by Hohenberg and

Kohn in the 1960's [142]. The first Hohenberg-Kohn theorem states that the electron density ρ determines the Hamiltonian and therefore, the ground-state wave function. Hence, the ground-state energy can be expressed as a functional of the electron density as,

$$E[\rho] = V_{ne}[\rho] + T[\rho] + V_{ee}[\rho] = \int \rho(\boldsymbol{r}) V_{\text{nuc}}(\boldsymbol{r}) d\boldsymbol{r} + F[\rho], \tag{4.36}$$

where $V_{ne}[\rho]$ and $V_{ee}[\rho]$ are the nuclear–electron attraction and electron–electron repulsion potential energy functionals, respectively, $T[\rho]$ is the kinetic energy functional, $V_{nuc}(\boldsymbol{r}) = -\frac{Z_I}{|\boldsymbol{R}_I - \boldsymbol{r}_i|}$ is the nuclear potential and where $F[\rho] = T[\rho] + V_{ee}[\rho]$ and is a universal functional of ρ.

So far we have only shown that we can use the electron density in place of the wave function. The second Hohenberg-Kohn theorem provides a variational principle based on the electron density [141], equivalent to the variational principle described at the beginning of section 4.1.1. This constrained minimisation can be expressed through a Lagrange equation,

$$\frac{\delta}{\delta\rho(\boldsymbol{r})} \left(E[\rho] - \mu \Big[\int \rho(\boldsymbol{r}) d\boldsymbol{r} - N \Big] \right) = 0, \tag{4.37}$$

where the constraint is that the density should still integrate to the number of electrons and μ is the Lagrange multiplier. This leads to the condition,

$$\mu = V_{nuc}(\boldsymbol{r}) + \frac{\delta F[\rho]}{\delta\rho(\boldsymbol{r})}, \tag{4.38}$$

which is known as the Euler-Lagrange equation. This analysis involves a minimisation over all V-representable densities, i.e., electron densities that are the ground-state of a local potential. However, this poses a problem as the conditions for a density to be V-representable is unknown and a physically reasonable density may not be V-representable. Levy suggested a way to circumvent this problem [143]. The exact energy is the minimum of the expectation value of the N-electron Hamiltonian over all (antisymmetrised) N-electron wave functions. As each wave function yields a specific density we can split this minimisation into two parts. First over the wave functions, then over the densities, that is

$$E_0 = \min_\rho \left(\min_{\Psi\to\rho} \langle \Psi | \hat{T} + \hat{V}_{ee} | \Psi \rangle + \int V_{nuc}(\boldsymbol{r}) \rho(\boldsymbol{r}) d(\boldsymbol{r}) \right). \tag{4.39}$$

This now means we can consider all N-representable densities, which is that the density represents an antisymmetric N-electron wave function, and the conditions for this are known. The density should everywhere be positive, integrate to the number of electrons and satisfy $\int |\nabla \rho^{1/2}|^2 d(\boldsymbol{r}) < \infty$ for finite systems [141].

With this, the ground-state density and energy can be determined exactly if we have the exact functional $F[\rho]$. However, we have the problem that the functionals $T_e[\rho]$ and $V_{ee}[\rho]$ are not known in an analytically usable form. Therefore, in practice we must develop approximations to these functionals. Kohn and Sham introduced orbitals, allowing for a more accurate calculation of the kinetic energy albeit a small residual correction is still needed [144]. To this end, Kohn and Sham expressed $F[\rho]$ in equation (4.36) as,

$$F[\rho] = T_s[\rho] + J[\rho] + E_{xc}[\rho], \tag{4.40}$$

where $J[\rho]$ is the classical Coulomb repulsion of the density with itself,

$$J[\rho] = \frac{1}{2} \iint \frac{\rho(\boldsymbol{r})\rho(\boldsymbol{r}')}{|\boldsymbol{r} - \boldsymbol{r}'|} d\boldsymbol{r} d\boldsymbol{r}', \tag{4.41}$$

and $T_s[\rho]$ is the kinetic energy of a system of non-interacting electrons with density ρ. Given that the exact $F[\rho] = T[\rho] + V_{ee}[\rho]$ we can identify that the exchange–correlation energy $E_{xc}[\rho]$ is defined as,

$$E_{xc}[\rho] = T[\rho] - T_s[\rho] + V_{ee}[\rho] - J[\rho] \tag{4.42}$$

Now we need to minimise the Kohn-Sham energy expression,

$$E[\rho] = \int \rho(\boldsymbol{r}) V_{nuc}(\boldsymbol{r}) d\boldsymbol{r} + T_s[\rho] + J[\rho] + E_{XC}[\rho]. \tag{4.43}$$

This minimsation then gives the Euler equation

$$\mu = V_{\text{eff}}(\boldsymbol{r}) + \frac{\delta T_s[\rho]}{\delta \rho(\boldsymbol{r})}, \tag{4.44}$$

where the effective potential $V_{\text{eff}}(\boldsymbol{r})$ is,

$$V_{\text{eff}}(\boldsymbol{r}) = V_{nuc}(\boldsymbol{r}) + \frac{\delta J[\rho]}{\delta \rho(\boldsymbol{r})} + \frac{\delta E_{XC}[\rho]}{\delta \rho(\boldsymbol{r})} \tag{4.45}$$

This minimisation would still yield the exact electron density of the system if we could use the exact functional $E_{xc}[\rho]$. Therefore, the density of the non-interacting system with external potential $V_{\text{eff}}(\boldsymbol{r})$ is exactly the same as the density of the real (interacting) system.

Now consider the electronic Hamiltonian for a system of non-interacting electrons in an external potential $V_{\text{eff}}(\boldsymbol{r})$,

$$\hat{H} = -\sum_{i}^{N} \frac{1}{2} \nabla_i^2 + \sum_{i}^{N} V_{\text{eff}}(\boldsymbol{r}_i). \tag{4.46}$$

This is separable and, therefore, the exact wave function is a single Slater determinant constructed from orbitals ϕ_i that are solutions to,

$$\Big(-\frac{1}{2} \nabla_i^2 + V_{\text{eff}}(\boldsymbol{r}) \Big) \phi_i(\boldsymbol{r}) = \epsilon_i \phi_i(\boldsymbol{r}), \tag{4.47}$$

where the density of the non-interacting system is simply,

$$\rho(\boldsymbol{r}) = \sum_{i}^{N} |\phi_i(\boldsymbol{r})|^2, \tag{4.48}$$

and the kinetic energy of the non-interacting system is given by,

$$T_s[\rho] = \sum_{i}^{N} \langle \phi_i | -\frac{1}{2} \nabla^2 | \phi_i \rangle. \tag{4.49}$$

In practice, the introduction of orbitals by Kohn-Sham theory introduces a need for a basis set to describe the orbitals, as in HF theory. Therefore, the orbitals must be optimised with respect to the coefficients of the basis set functions. Hence, we must solve a Fock matrix like problem for the Kohn-Sham orbitals in analogy to (4.29). A final note on the practical use of DFT is that integration can no longer be done analytically due to the introduction of fractional powers of the electron density ρ in an approximation to $E_{xc}[\rho]$. Therefore, numerical integration must be carried out using a set of grid points.

We should emphasise that Kohn-Sham theory is formally exact if we have the exact exchange–correlation functional. However, in practical calculations we must approximate the exchange–correlation energy. The success of Kohn-Sham theory in DFT is that the differences being included

in the exchange–correlation energy of the exact kinetic energy and the non-interacting kinetic energy and the electron–electron repulsion with the Coulomb component are usually small and can be modelled successfully using simple approximations.

Here, we have once more described a situation where each electron is contained within a different one-electron function, within Kohn-Sham theory. This would be classified as unrestricted Kohn-Sham (UKS), except we have neglected the description of spin. However, spin in DFT is not well defined and we will not discuss it here. For a review looking at spin in DFT, see reference [112].

Approximations to the Exchange–Correlation energy

These are usually termed as exchange–correlation functionals as they provide the exchange–correlation energy as a functional of the density. Now we can classify several "levels" of the approximations to the exchange–correlation functional. This can also be classified on "Jacob's ladder", where each class of functional has its own rung [145]. There are five main categories, the first is called Local Density Approximations (LDA). Here, the energy is expressed as an integral of a function of just the local density,

$$E_{xc}[\rho] = \int F\Big(\rho(\boldsymbol{r})\Big) d\boldsymbol{r}. \tag{4.50}$$

The LDA exchange-correlation functionals assume that the local density can be treated as if it is a uniform gas and therefore, a slowly varying function. The most common LDA functional used is the S-VWN, which uses the slater Xα functional [146] for the exchange and the Vosko-Wilks-Nusair (VWN) functional [147] for the correlation. For more specific information on the form of this LDA functional see reference [139, 141]. Nevertheless, there are other LDA functionals available, such as the correlation functional from Perdew [148]. These kinds of exchange–correlation functionals have found a lot of use in physics calculations where extended systems, such as metals, are being calculated as the approximation of the uniform gas is quite valid. However in molecules large errors can be introduced by this approximation.

On the second rung are the Generalised Gradient Approximations (GGAs), where the integrand also depends on the gradient of the density,

$$E_{xc}[\rho] = \int F\Big(\rho(\boldsymbol{r}), \nabla\rho(\boldsymbol{r})\Big) d\boldsymbol{r}. \tag{4.51}$$

Thus, GGA exchange–correlation functionals also include the first derivative of the electron density. This then provides an improved description for cases where the approximation as a uniform electron gas fails, such as a molecular system. However, the inclusion of the first derivative does remove some of the important properties contained within the LDA functionals. The proposed GGA's then include constraints where those properties are kept and so the correct physics remains [139]. There are many GGA exchange-correlation functionals available for use in quantum-chemical programs, many of which are optimised with the calculation of specific properties in mind, such as the KT3 [149, 150] functional for NMR shieldings. The most commonly used GGA functionals are the BP86 [130, 151] and PBE [152] functionals, although in the literature there are a myriad of functionals available along with the options of changing and combining different exchange and correlation functionals (for an overview see reference [153]).

The next step are so-called Meta-GGA's which also consider higher order derivates,

$$E_{xc}[\rho] = \int F\Big(\rho(\boldsymbol{r}), \nabla\rho(\boldsymbol{r}), \nabla^2\rho(\boldsymbol{r})\Big) d\boldsymbol{r}. \tag{4.52}$$

Meta-GGA exchange–correlation functionals build on the principles of the GGA functionals by including higher-order derivatives within the exchange–correlation functional. We will not go into detail here, but refer to references [139, 141]. Commonly found meta-GGA functionals are the TPSS [154, 155] functional and the Minnesota functionals (such as M06-L [156, 157]).

Following this is to include a dependence on the occupied orbitals in the exchange–correlation functional. The most important examples are the hybrid exchange–correlation functionals, which add a fraction of exact exchange from the HF method,

$$E_{xc}[\rho] = \int F\Big(\rho, \nabla\rho(\boldsymbol{r})\Big) d\boldsymbol{r} + \xi E_X^0, \tag{4.53}$$

where ξ is a coefficient between 0 and 1 and dictates the amount of exact exchange included.

Hybrid functionals can be made with any of the previously mentioned exchange–correlation functional classes. The basic idea of hybrid functionals is that with the Kohn-Sham Slater determinant we can include a portion of "exact" exchange calculated as in HF and include it in the exchange–correlation functional. This percentage then replaces that percentage of exchange calculated by the original exchange functional. Many hybrid functionals are available within quantum-chemical program packages, with the most ubiquitous in the literature being B3LYP [158, 159]. However, we also see hybrid functionals of other exchange–correlation functionals, such as PBE0 [160, 161], TPSS-H [154, 155] or M06-2X [156, 157].

The final class belongs to exchange–correlation functionals with a dependence on the virtual orbitals as well. These are usually referred to as double hybrid exchange–correlation functionals, which not only include a contribution of exact exchange from HF methods but also include contributions from more sophisticated wave function methods (e.g. MP2) [162, 163],

$$E_{xc}[\rho] = \int F\Big(\rho(\boldsymbol{r}), \nabla\rho(\boldsymbol{r})\Big) d\boldsymbol{r} + \xi_1 E_X^0 + \xi_2 E_c^{MP2}. \tag{4.54}$$

4.2. Time-Independent Methods for the Calculation of X-ray Spectra

We introduced the concept of excited states and that knowledge of the excited states is required for electronic spectroscopy in chapter 2 and considered the treatment of properties from a time-dependent perspective. This lead to Fermi's golden rule and expressions for the oscillator strengths. We found that the solution of the time-dependent problem reduces to the solution of the time-independent electronic Schrödinger equation for excited states. Therefore, we have two available approaches to the calculation of electronic spectroscopy: time-independent and time-dependent. We must note, both time-independent and time-dependent approaches are equivalent when considering the exact theory and only the introduction of the approximate wave functions gives rise to differences. In a time-independent approach, the excited states are calculated explicitly. The energy differences between ground and excited states then determine the transition frequencies and the wave functions can be used to determine the oscillator strengths as described in detail in chapter 3. With that, we can calculate the electronic spectrum of the molecule. Within the following sections we will introduce several time-independent approaches to the calculation of X-ray spectroscopy.

4.2.1. Configuration Interaction

The configuration interaction (CI) ansatz introduced in section 4.1.1 also provides access to excited states. In the CIS method, only singly excited Slater determinants are included and the expansion coefficients C_i^a are determined using the variational principle. This leads to the eigenvalue equation

$$\boldsymbol{AX} = \omega \boldsymbol{X} \tag{4.55}$$

where ω is the diagonal matrix of excitation energies, $\boldsymbol{X}$ the matrix of expansion coefficients and the elements in $\boldsymbol{A}$ are given by

$$A_{ia,jb} = (\epsilon_a - \epsilon_i)\delta_{ij}\delta_{ab} + \langle ij||ab\rangle, \tag{4.56}$$

where ϵ_a and ϵ_i are the orbital energies and $\langle ij||ab\rangle$ are the two-electron Coulomb and exchange integrals. The $\boldsymbol{A}$ matrix is then diagonalised to get the excitation energies. However, if core-excited states are required in the calculation the way presented here is inefficient. In this case it is possible to restrict the CIS calculation to only the core orbitals [123, 164] (for more information see section 4.4).

However, it has been noted that CIS excitations provide a poor agreement with experiment. Consequently, the inclusion of a perturbative doubles correction to the ansatz was proposed by Head-Gordon et al. [165, 166]. This yields a significant improvement of the calculated excitation energies compared to experiment. The correction to the excitation energies ω_{0n}^{CIS} calculated with CIS is

$$\omega_{0n}^{CIS(D)} = -\frac{1}{4}\sum_{ijab}\frac{(u_{ij}^{ab})^2}{(\epsilon_a + \epsilon_b - \epsilon_i - \epsilon_j) - \omega_{0n}^{CIS}} + \sum_{ia} C_i^a v_i^a \tag{4.57}$$

where

$$u_{ij}^{ab} = \sum_c [\langle ac||bj\rangle C_j^c - \langle ac||bi\rangle C_j^c] + \sum_k [\langle ki||aj\rangle C_k^b - \langle ki||bj\rangle C_k^a], \tag{4.58}$$

$$v_i^a = \frac{1}{2}\sum_{jkbc}\langle jb||kc\rangle (C_i^a a_{jk}^{ca} + C_j^b a_{ik}^{cb} + 2C_j^b a_{ik}^{ac}), \tag{4.59}$$

and a_{ij}^{ab} are amplitudes taken from the MP2 method (for information on MP2 see reference [139]),

$$a_{ij}^{ab} = -\frac{\langle ia||jb\rangle}{(\epsilon_a + \epsilon_b - \epsilon_i - \epsilon_j)}. \tag{4.60}$$

In equation (4.57) the first term is termed the direct contribution and accounts for electron correlation effects of the electron involved in the excitation, while the second indirect term accounts for electron correlation effects between pairs of electrons not involved in the excitation [167].

4.2.2. ΔSCF

The ΔSCF method is considered as a method which takes into account many effects required in the calculation of X-ray spectra. The principle of ΔSCF is that the HF wave function is optimised for the ground state and the specific excited state. The transition energy is then,

$$E_{0n} = E_n - E_0, \tag{4.61}$$

and the intensity is calculated using the ground and excited state wave functions in the integrals shown in chapter 3. However, a few problems arise within ΔSCF methods. The first is that the wave functions are not orthogonal as they were individually optimised without constraints to be orthogonal to one another. The second is that for each excitation the explicit excited state must be calculated. In systems where many excitations are required this is cumbersome and can be prohibitively time intensive. Although as mentioned ΔSCF methods have a few benefits. By optimisation of the excited state wave function any orbital relaxation that occurs due to the core hole is taken into account as well as the core-hole screening.

4.2.3. Static Exchange Method (STEX)

STEX is a derivative of the ΔSCF method. However, unlike the ΔSCF method, it calculates multiple excitation energies in one calculation. STEX however, was originally formulated to allow an improvement on time-dependent HF, as it allows for calculation of core electron excitations as well as including the orbital relaxation which occurs upon excitation, which is neglected in TD-HF [168,169]. The STEX method was developed and described by Ågren et al. in references [168,169]

The way this is accomplished is to use the optimised ionised wave function as the reference and carry out the calculations using the relaxed orbitals, but include all the electrons present in the ground-state wave function. We then describe the motion of the electron, which occurs upon promotion, in the electrostatic field provided by the ionised wave function. The electrostatic field is fixed with respect to the motion of the electron, but the method accounts for the exchange in this interaction within the STEX Hamiltonian,

$$\hat{H}^{STEX} = h + \sum_{i \neq j}^{n/2} (2J_i - K_i) + J_j + K_j, \tag{4.62}$$

where the index j refers to the orbital with the electron removed and i runs over all other occupied orbitals. This Hamiltonian refers to a restricted closed shell molecule, although it can also be formulated for open-shell systems. An important note here is that this Hamiltonian must be applied to the ionised wave function with the electron hole in the j^{th} orbital.

We must also consider that these calculations are usually performed within an atomic orbital (AO) basis set, where within the Hamiltonian we now include the one-electron density matrix D (this enters within the Fock operator). These one-electron density matrices must be altered in STEX due to the electron hole in the core orbital, as these are initially calculated for the closed shell, fully occupied system. For a density matrix corresponding to the restricted doubly occupied system, the modifications are made according to,

$$D^J_{\alpha\beta} = D_{\alpha\beta} - \frac{1}{2} c_{\alpha j} c_{\beta j}, \tag{4.63}$$

$$D^K_{\alpha\beta} = D_{\alpha\beta} - 2 c_{\alpha j} c_{\beta j}, \tag{4.64}$$

where α and β correspond to the AOs within the basis set and $c_{\alpha j}$ is the coefficient of the AO α in the vector of the molecular orbital j. The density matrix $D^J_{\alpha\beta}$ and $D^K_{\alpha\beta}$ correspond to the one-electron density matrices for the Coulomb and exchange terms, respectively.

To summarise, we can break the STEX procedure down into four steps:

(1) The optimisation of the ground-state and core-hole excited state wave function along with the computation of the ionisation potential by ΔSCF procedures.

(2) Computation of the STEX Hamiltonian matrix and, in the AO basis set, the modified core-hole densities.

(3) Transformation of the STEX matrix by projecting out the occupied orbitals from the basis set.

(4) Diagonalisation of the projected STEX matrix to yield eigenvectors and eigenvalues.

The excitation energies from this procedure are then simply calculated as,

$$E^n_{\text{exci}} = (E_{\text{Ion}} - E_{\text{GS}}) + X_n, \tag{4.65}$$

where E^n_{exci} is the excitation energy for excitation n, E_{Ion} and E_{GS} are the total energies for the ionised and ground-state wave function, respectively, and X_n is the STEX eigenvalue for excitation n. It is also possible to calculate the transition moments with this method. The matrix elements, for the electric-dipole oscillator strength are,

$$f_n = \frac{2}{3} E^n_{\text{exci}} \langle \Psi_0 | \hat{\boldsymbol{\mu}} | \Psi^a_j \rangle, \tag{4.66}$$

where Ψ_0 is the ground state wave function, $\hat{\boldsymbol{\mu}}$ is the dipole operator and Ψ^a_j is the excited wave function with an electron from orbital j in orbital a.

4.2.4. ΔDFT

ΔDFT is the terminology we will use to denote an orbital difference method with DFT used for calculating X-ray emission spectra. When calculating emission spectroscopy the process is between occupied orbitals and normal response methods are not available for this purpose as these probe transitions from occupied to virtual orbitals. Therefore, a simple method outlined by Lee et al. [137] can be used for calculating emission spectra (see also refs. [170–172] and references therein for earlier work).

In ΔDFT the transition energies are calculated simply as orbital energy differences from the electronic ground state density,

$$E_{0n} = \epsilon_i - \epsilon_j \tag{4.67}$$

where $\epsilon_{i/j}$ are the orbital energies. The intensity calculations using ΔDFT then only require calculating the integrals shown in chapter 3 between the occupied orbitals.

This method has been shown to be effective for the calculation of K$\beta_{2,5}$ XES spectra of iron complexes [21, 67–69, 137, 173] even though the simplicity of the model neglects many effects. We also use this methodology within our calculations of X-ray emission spectra in chapter 6.

4.2.5. Transition State Potential

The transition state potential method was originally proposed by Slater [146]. It follows the very simple premise as that described in the ΔDFT method in that the transition energies are calculated as simple orbital energy differences. However, the difference of the transition state potential method is that the wave function is optimised for a partially excited state where half an electron resides in the initial orbital and half in the final state. Therefore, the orbitals take into account the partial relaxation due to the core hole [170]. This method has been applied mostly with DFT [170, 174–177] methods.

4.3. Time-Dependent Methods for the Calculation of X-ray Spectra

Time-dependent methods provide a way to calculate excitation energies using linear response theory instead of explicitly calculating each excited state wave function as is done with the time-independent methods. When using linear response theory, in an exact formalism, we are solving for the linear response function,

$$\langle\langle\hat{\mu}_\alpha;\hat{\mu}_\beta\rangle\rangle_\omega = \sum_{n\neq 0}\Big[\frac{\langle\Psi_0|\hat{\mu}_\alpha|\Psi_n\rangle\langle\Psi_n|\hat{\mu}_\beta|\Psi_0\rangle}{\omega-\omega_{0n}} + \frac{\langle\Psi_0|\hat{\mu}_\beta|\Psi_n\rangle\langle\Psi_n|\hat{\mu}_\alpha|\Psi_0\rangle}{\omega_{0n}-\omega}\Big], \tag{4.68}$$

where $\langle\langle\hat{\mu}_\alpha;\hat{\mu}_\beta\rangle\rangle_\omega$ is the polarisability of the molecule at wavelength ω and ω_{0n} ($\hbar\omega_{0n} = (E_n - E_0)$) is the excitation frequency from the ground state to the n^{th} excited state. This expression as stated here is a sum over all the excited states and would therefore require the explicit calculation of all the excited state wave functions. However, when using approximate wave functions we can solve for the linear response equation directly. Thus, to find the excitation energies we find the poles of the linear response function, when $\langle\langle\hat{\mu}_\alpha;\hat{\mu}_\beta\rangle\rangle_\omega \to \infty$.

The next sections will discuss the time-dependent methodology for DFT and HF as well as introduce coupled cluster linear response methods and the complex polarisation propagator.

4.3.1. Time-Dependent DFT (TD-DFT)

The theoretical framework for the time-dependent generalisation of DFT was introduced by Runge and Gross [178] and subsequently the TD-DFT response theory [179] was introduced. Since this introduction time-dependent DFT has become a widely used method in the field of spectroscopy [107, 126, 180–182]. It has a low cost to accuracy ratio compared to many other methods, such as coupled cluster or HF, which means it can be applied to many systems not accessible with high-level wave function methods and still provide reasonable results, in particular for transition metal complexes [116, 124, 126, 183–186].

Here we will introduce the most essential concepts and equations of time-dependent density functional theory. There are multiple ways to derive the time-dependent density functional linear response equations [179, 187, 188]. However, independent of the way chosen for the derivation we end up with an electronic hessian $\boldsymbol{E}$,

$$\boldsymbol{E} = \begin{pmatrix} \boldsymbol{A} & \boldsymbol{B} \\ \boldsymbol{A}^* & \boldsymbol{B}^* \end{pmatrix}, \tag{4.69}$$

where the elements of the matrices $\boldsymbol{A}$ and $\boldsymbol{B}$ are given by,

$$A_{ia,jb} = \delta_{ij}\delta_{ab}(\epsilon_a - \epsilon_i) + 2\langle\phi_i(\boldsymbol{r})\phi_b(\boldsymbol{r'})|\phi_a(\boldsymbol{r})\phi_j(\boldsymbol{r'})\rangle + \langle\phi_i(\boldsymbol{r})\phi_b(\boldsymbol{r'})|f_{XC}|\phi_a(\boldsymbol{r})\phi_j(\boldsymbol{r'})\rangle, \tag{4.70}$$

$$B_{ia,jb} = 2\langle\phi_i(\boldsymbol{r})\phi_b(\boldsymbol{r'})|\phi_j(\boldsymbol{r'})\phi_a(\boldsymbol{r})\rangle + \langle\phi_i(\boldsymbol{r})\phi_b(\boldsymbol{r'})|f_{XC}|\phi_j(\boldsymbol{r'})\phi_a(\boldsymbol{r})\rangle, \tag{4.71}$$

where ϵ_a are the Kohn-Sham orbital energies, $\langle\phi_i(\boldsymbol{r})\phi_b(\boldsymbol{r'})|\phi_a(\boldsymbol{r})\phi_j(\boldsymbol{r'})\rangle$ is the two-electron Coulomb integral and

$$\langle\phi_i(\boldsymbol{r})\phi_b(\boldsymbol{r'})|f_{XC}|\phi_j(\boldsymbol{r'})\phi_a(\boldsymbol{r})\rangle = \iint \phi_i(\boldsymbol{r})\phi_b(\boldsymbol{r'})\Big[\frac{\delta^2 E_{XC}[\rho]}{\delta\rho(\boldsymbol{r})\delta\rho(\boldsymbol{r'})}\Big]\phi_j(\boldsymbol{r'})\phi_a(\boldsymbol{r})d^3\boldsymbol{r}d^3\boldsymbol{r'}, \tag{4.72}$$

are the integrals over the exchange–correlation kernel. With some derivation we can finally arrive at a matrix eigenvalue equation which we can solve to find the poles of the linear response equation (4.68) and hence, the excitation energies,

$$\begin{pmatrix} \boldsymbol{A} & \boldsymbol{B} \\ \boldsymbol{A}^* & \boldsymbol{B}^* \end{pmatrix} \begin{pmatrix} \boldsymbol{X} \\ \boldsymbol{Y} \end{pmatrix} = \omega \begin{pmatrix} 1 & 0 \\ 0 & -1 \end{pmatrix} \begin{pmatrix} \boldsymbol{X} \\ \boldsymbol{Y} \end{pmatrix}, \tag{4.73}$$

where $\boldsymbol{X}$ and $\boldsymbol{Y}$ are eigenvectors and ω is the diagonal matrix of excitation frequencies ($\hbar\omega_{0n} = (E_n - E_0)$).

We can introduce an approximation here, if the excitations are only very weakly coupled, called the Tamm-Dancoff approximation [189] where the $\boldsymbol{B}$ matrix is set to 0 and we solve,

$$\boldsymbol{A}\boldsymbol{X} = \omega\boldsymbol{X}. \tag{4.74}$$

This reduces the size of the problem by half and the loss in accuracy is most often outweighed by the speed up of the calculation.

4.3.2. Time-Dependent HF (TD-HF)

Time-dependent HF will not be discussed in detail as the formalism presented for time-dependent DFT is equivalent. The exchange–correlation functional term in the matrix elements of the response equation (equations (4.70) and (4.71)) are not included [190] and the exchange integral from HF replaces it. We also note that the Tamm-Dancoff approximation may be applied to TD-HF. However, we are then solving the CIS equations mentioned in section 4.2.1.

4.3.3. Coupled Cluster Response Theory

Coupled cluster linear response was recently extended for the calculation of X-ray absorption spectroscopy [191, 192]. However, the applicability of the method is limited due to the computational costs of the coupled cluster methods. A further problem is encountered in the calculation of the higher energy edges. With current implementations all excitations must be calculated and hence, for the K-edge of simple molecules several hundred excitations must be calculated. This is time consuming and unfeasible for many systems. A core-valence separation scheme can be introduced to allow the isolation of excitations, such as only from the $1s$ orbital, however, this can introduce convergence issues.

4.3.4. Complex Polarisation Propagator (CPP)

The complex polarisation propagator method was introduced by Patrick Norman et al. [193, 194]. It is based on linear response theory and introduces a damping factor into the response function.

$$\alpha_{\alpha\beta}(-\omega;\omega) = \frac{1}{\hbar}\sum_{n\neq 0}\Big[\frac{\langle\Psi_0|\hat{\mu}_\alpha|\Psi_n\rangle\langle\Psi_n|\hat{\mu}_\beta|\Psi_0\rangle}{\omega_{0n} - \omega - i\gamma} + \frac{\langle\Psi_0|\hat{\mu}_\beta|\Psi_n\rangle\langle\Psi_n|\hat{\mu}_\alpha|\Psi_0\rangle}{\omega_{0n} + \omega + i\gamma}\Big], \tag{4.75}$$

Therefore, the calculations automatically include the lifetime broadening. The inclusion of the life time broadening allows for the calculation of intensities at energies which are off-resonance.The method also has inherently in its definition a way to isolate and calculate over a specific wavelength

range, meaning excitations at a specific edge of X-ray absorption can be calculated easily. Thus, it has been applied to the calculation of X-ray absorption spectroscopy [195–198]. The formalism may be applied to any method where we are solving the linear response equation (Equation (4.68)). The CPP formalism is also easily adapted to the calculation of circular dichroism spectroscopy of which its been applied extensively [197–200].

4.4. Restriction of the Excitation Matrix

When considering the calculation of X-ray absorption spectroscopy at a specific edge of a molecule (e.g. K-edge or L-edge) a problem arises in that diagonalising the excitation matrix provides all excitation energies. Usually, one solves for the lowest eigenvalues only. Thus, to calculate the relevant excitations for the edge, several thousand excitations must be calculated. This is unfeasible in most systems. Therefore, Stener et al. proposed a method to restrict the excitation matrix to excitations from a subset of occupied orbitals which must be specified before the calculation begins [123]. In practice, this is achieved by shifting all the non-specified orbitals, post–SCF, to much lower energies (in ADF all non-specified orbitals are shifted to -1×10^{-6} E_h). Hence, the lowest energy excitations now occur from the specified orbital and will now be the lowest excitations.

There are also slight modifications to this scheme proposed. In ORCA [201] first the Pipek-Mezey localisation procedure [202] is used to localise the core orbitals and then the localised orbitals are used within the excitation calculation [107] and the excitation matrix is restricted in the same manner as that described by Stener et al..

5. Comparison of Approximations for the Calculation of X-ray Spectra

When performing quantum-chemical calculations there are a variety of approximations to be chosen from. The quantum-chemical methods available for the calculation of X-ray spectra have been discussed in the previous chapter. Here, we will consider only the calculations of X-ray absorption spectra with TD-DFT. However, there are still many choices to be made, such as the basis set or the exchange–correlation functional, along with some technical parameters, such as the integration grid or convergence thresholds in the SCF cycles. Within this chapter, we will explore the effect of these choices on the final results and assess the effect, if any, of a change of the technical parameters in the calculation.

To this end, we chose a set of test systems where differences between the molecules can also be used to assess the overall effect of approximation choice. The complexes were ferrocene, acetylferrocene, vinylferrocene, 1,1'-bis-diphenylphosphinoferrocene and 1,1'-bis-diisopropylphosphinoferrocene. The goal of this comparison is to determine the best choices for the calculation of X-ray spectra of such transition metal complexes, which will be used to calculate the results presented in chapters 6 and 7.

5.1. Choice of Basis Set

An important approximation in all quantum-chemical calculations is the use of a finite basis set. The basis set is used to expand the molecular orbitals (MOs),

$$\phi_i(\boldsymbol{r}) = \sum_\mu C_\mu^{(i)} \chi_\mu(\boldsymbol{r}), \tag{5.1}$$

where $C_\mu^{(i)}$ are the expansion coefficients and $\chi_\mu(\boldsymbol{r})$ is a basis function. The choice of basis set determines the form of the functions χ_μ and also the number/type of functions available in the expansion. In molecular quantum chemistry, the basis functions are usually atom-centred and designed as to mimic atomic orbitals.

Basis sets are usually designated by their size relative to the minimum number of basis functions required to describe a molecule. In a minimal (also known as single-ζ) basis set, there is one basis function per occupied atomic orbital shell. For example, the hydrogen atom will only have a single s function, while for a carbon atom, one uses a $1s$ and a $2s$ function as well as a set of $2p$ functions (i.e., 5 basis functions in total). A double-ζ basis set extends this and uses two sets of functions per atomic orbital shell, i.e. [2s] for H and [4s2p] for C. Similarly, a triple-ζ and a quadruple-ζ basis set use [3s] and [4s] for H and [6s3p] and [8s4p] for C, respectively. The extra functions provide more flexibility to the basis set and may enable a combination of functions that provide a better description of the MO's than the minimal basis set.

In addition, one may introduce polarisation functions. A polarisation function is an atomic function that has an angular momentum one higher than the highest angular momentum within the standard basis set. For example the double-ζ basis set with one polarisation function on a hydrogen atom has two s functions and one set of p functions ([2s1p]). The inclusion of polarisation functions is a requirement for the description of bonds in molecules.

5.1.1. Slater-Type Orbital (STO) Basis Sets

Within the ADF program package, which is used for some of the calculations performed, the basis sets are described using Slater-type basis functions [139],

$$\chi_{\zeta,n,l,m}(r,\theta,\phi) = NY_{l,m}(\theta,\psi)r^{n-1}e^{-\zeta r} \tag{5.2}$$

where ζ is the exponential factor, n, l, m are the principal, angular momentum, and magnetic quantum number, respectively, $Y_{l,m}(\theta,\psi)$ are spherical harmonics and N is a normalisation factor. r, θ and ϕ are spherical coordinates used to describe the position of an electron around the nucleus the basis function is centred on. Slater-type functions have an exponential dependence on the distance between the nucleus and the electron, which mimics the exact orbitals for the hydrogen atom, but do not contain radial nodes. To include the radial nodes, linear combinations of the Slater-type functions must be made. At the nucleus, when $r = 0$, Slater-type functions have a cusp (derivative discontinuity) and at large r the tail decays exponentially.

In ADF, single-ζ to quadruple-ζ basis sets are available [203]. The exponents in the basis sets have been determined through fitting to numerically calculated orbitals. However, for transition metal complexes only those of triple-ζ or higher are available with the inclusion of polarisation functions. Therefore, the basis sets which can be utilised in the calculations are TZP, TZ2P or QZ4P. In the next two sections we will first consider the effect of the basis set on the calculated transition energies, and subsequently the effect on the calculated intensities.

Energies of Transitions

First to consider is the effect of the choice of basis set on the calculated XAS transition energies calculated with ADF [122, 204]. For the following tests, we used the BP86 exchange–correlation functional [130, 131] and an integration grid size 4. To this end, we compare how the energies change on an increase in basis set size from TZ2P to QZ4P. The calculated spectra for ferrocene, acetylferrocene, vinylferrocene and 1,1'-bis-diphenylphosphinoferrocene are shown in figure 5.1. It can be seen that the increase in the size of the basis set only has a minor effect on the excitation energies, with a shift smaller than 0.1 eV to higher energies. If we consider the calculated ionisation threshold (see table 5.1), i.e., the negative 1s orbital energy, the effect is slightly larger, with a shift between 0.1 and 0.2 eV to higher energies.

For two of the complexes, acetylferrocene and vinylferrocene, a splitting of the peak observed in the other complexes is seen (see chapter 6 for a detailed discussion). This allows for a closer look at the effect of the basis set on the relative energies of the transitions. These are listed in table 5.2. Here the basis set size has no effect on the relative energies. Therefore we can conclude that the relative energies are already converged with the TZ2P basis set. Increasing the size of the basis set further only leads to a small shift of the absolute excitation energies, which is due to a change in the Fe 1s orbital energy.

Figure 5.1.: Calculated (TD-DFT/BP86) pre-edge regions of the Fe K-edge XAS spectra of four ferrocene derivatives using either the TZ2P or QZ4P STO basis set.

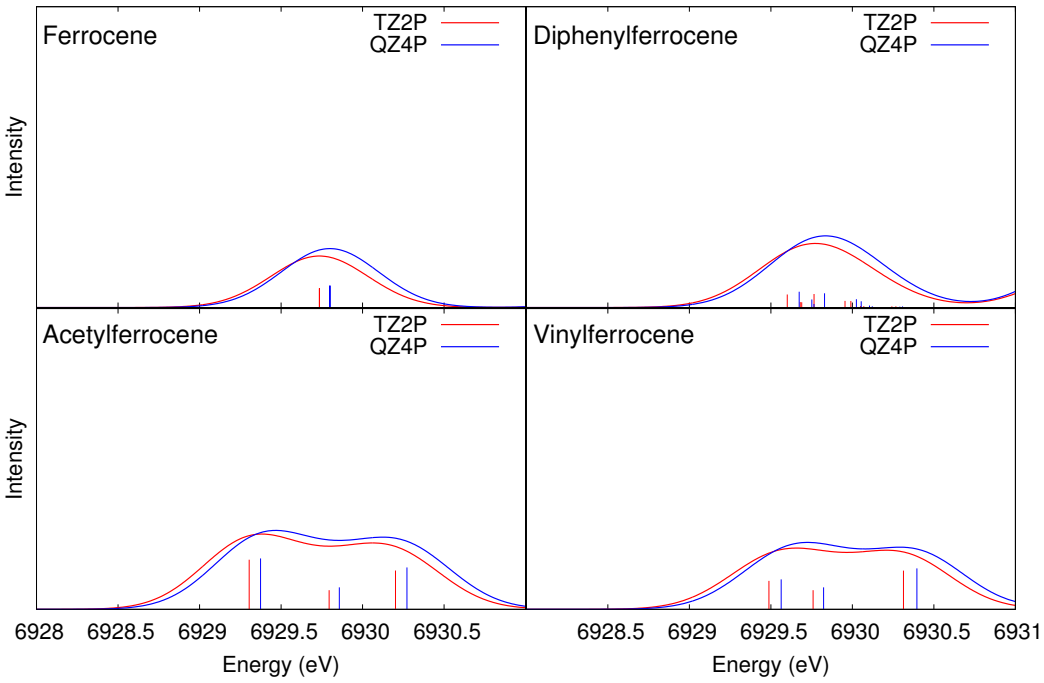

Table 5.1.: Negative orbital energies (DFT/BP86) of the Fe 1*s* orbital, calculated using the TZ2P and QZ4P basis sets for five ferrocene derivatives. The negative Fe 1*s* orbital energy equals the onset of the continuum states and can be identified with the absorption edge.

Complex	Basis set	Ionisation Threshold (eV)
$Fe(Cp)_2$	TZ2P	6931.144
	QZ4P	6931.300
Fe(Cp)(CpAc)	TZ2P	6931.589
	QZ4P	6931.722
Fe(Cp)(CpVinyl)	TZ2P	6931.244
	QZ4P	6931.387
$Fe(CpPPh_2)_2$	TZ2P	6931.364
	QZ4P	6931.503
$Fe(CpP^iPr_2)_2$	TZ2P	6931.184
	QZ4P	6931.393

Intensities of Transitions

The next consideration is the effect of the basis set on the calculated intensities, as the energies of the transitions alone are not enough for an experimental assignment. Here, we calculate the intensities using the origin-independent scheme presented in chapter 3. The intensities can be separated into their constituent parts, electric-dipole and higher-order contributions, and each

Table 5.2.: Relative energies for the splitting between the two lowest peaks - corresponding to transitions into the d_{xz} anti-bonding orbital - with the TZ2P or QZ4P basis sets for acetyl- and vinylferrocene. The splitting is calculated as the difference between the first and third calculated transitions.

Complex	Basis set	Relative Peak Energy (eV)
Fe(Cp)(CpAc)	TZ2P	0.90
	QZ4P	0.90
Fe(Cp)(CpVinyl)	TZ2P	0.83
	QZ4P	0.83

contribution's basis set dependence has to be determined seperately.

Table 5.3 shows the effect of the basis set on the individual contributions to the intensities. The intensities are also shown in the spectra in figure 5.1. The electric-dipole intensities have a very small dependence on the basis set, with an increase two orders of magnitude smaller than the summed intensity when going from TZ to QZ. The only exception is ferrocene, where the dipole intensity vanishes. This means that the electric-dipole intensity can be considered converged when using the TZ2P basis set.

The quadrupole contributions have a larger basis-set dependence, with a change only one order of magnitude smaller than the intensity itself. Therefore, for the quadrupole contributions the QZ4P basis set must be utilised to achieve a result closer to the basis set limit. This observation also indicates that the higher-order intensity contributions converge slower with respect to the basis set size than the electric-dipole contributions. Of course, this will only be relevant for situations in which the quadrupole intensities provide a significant contribution to the total intensity.

5.1.2. Gaussian Type Orbital (GTO) Basis Sets

Within most quantum-chemical program packages, such as ORCA [201] or Turbomole [205, 206], the basis sets are composed of Gaussian-type basis functions [139] of the form

$$\chi_{\zeta,n,l,m}(r,\theta,\phi) = NY_{l,m}(\theta,\psi)r^l e^{-\zeta r^2}. \tag{5.3}$$

Gaussian-type functions provide several benefits compared to Slater-type basis functions. The major point is that two-electron integrals can be calculated analytically using GTOs, whereas with STOs one has to resort to numerical integration. The main drawback of GTOs compared to STOs is that they do not provide the correct shape of the function with respect to the exact atomic orbitals. GTOs do not have the cusp at $r = 0$, but have a continuous derivative, which is zero at $r = 0$. In addition, the tail of the function drops off too rapidly. Therefore, to describe a Slater-type function it has been determined that at least three Gaussian functions are required [139].

For Gaussian basis sets there are several "families" available. Each family is constructed in its own way, using a specific method for the optimisation of the exponents of the primitives. In addition, different strategies for contracting several primitives into one basis function are commonly employed. However, the formulation of a general basis set that is capable of describing all properties accurately has not, so far, been found, even though when increasing the basis set size the results should always converge to the same basis set limit. Therefore, many of the general basis

Table 5.3.: Total intensities (i.e., sum of all the intensities of all excitations before the ionisation threshold) of the calculated Fe K-edge XAS spectra for five ferrocene derivatives calculated with the TZ2P or QZ4P basis set. Also included are the separated summed dipole contribution and summed quadrupole contribution for analysis of the basis set dependence of the different contributions. All intensities are given as dimensionless oscillator strengths.

Complex	Basis set	Total Intensity	Summed Dipole	Summed Quadrupole
$Fe(Cp)_2$	TZ2P	$8.908 \cdot 10^{-06}$	$1.150 \cdot 10^{-16}$	$8.908 \cdot 10^{-06}$
	QZ4P	$1.020 \cdot 10^{-05}$	$7.047 \cdot 10^{-16}$	$1.020 \cdot 10^{-05}$
Fe(Cp)(CpAc)	TZ2P	$2.497 \cdot 10^{-05}$	$1.567 \cdot 10^{-05}$	$9.299 \cdot 10^{-06}$
	QZ4P	$2.663 \cdot 10^{-05}$	$1.597 \cdot 10^{-05}$	$1.066 \cdot 10^{-05}$
Fe(Cp)(CpVinyl)	TZ2P	$2.005 \cdot 10^{-05}$	$1.083 \cdot 10^{-05}$	$9.216 \cdot 10^{-06}$
	QZ4P	$2.155 \cdot 10^{-05}$	$1.100 \cdot 10^{-05}$	$1.055 \cdot 10^{-05}$
$Fe(CpPPh_2)_2$	TZ2P	$1.292 \cdot 10^{-05}$	$4.020 \cdot 10^{-06}$	$8.901 \cdot 10^{-06}$
	QZ4P	$1.429 \cdot 10^{-05}$	$4.089 \cdot 10^{-06}$	$1.020 \cdot 10^{-05}$
$Fe(CpP^iPr_2)_2$	TZ2P	$9.471 \cdot 10^{-06}$	$7.803 \cdot 10^{-07}$	$8.691 \cdot 10^{-06}$
	QZ4P	$1.084 \cdot 10^{-05}$	$8.797 \cdot 10^{-07}$	$9.963 \cdot 10^{-06}$

sets, though able to provide good results for many situations, are optimised as to provide the best result for a given property. For this reason a variety of Gaussian basis sets have been developed of which the most commonly used ones belong to the Dunning, Ahlrichs, Jensens, Pople or ANO basis set families. For more details on Gaussian basis sets we refer to reference [207]. Here, we will use basis sets from the Ahlrichs family.

Once more we will first consider the effect of the basis set on the calculated transition energies, and then the effect on the calculated intensities. The main basis sets used were the def2-TZVPP [208, 209] and the def2-QZVPP [210] basis set on all atoms. These are triple-ζ and quadruple-ζ basis sets, respectively, both including two sets of polarisation functions. In addition, we considered the CP(PPP) basis set on the iron atom with the TZVP basis set (a triple-ζ basis set including one set of polarisation functions) on all other atoms [211] because such a combination has previously been recommended for the calculation of Fe K-edge XAS spectra. The CP(PPP) basis set was designed by Neese for the calculation of core properties and is focused on an improved description of the core orbitals. It is based on the Ahlrichs double-ζ basis set in which the s functions are uncontracted and extra tight s functions are added, along with the incorporation of d functions from the triple-ζ basis set and an inclusion of additional diffuse functions, giving us on the iron atom [17s7p3d1f] functions.

Energies of Transitions

We now need to determine the effect of the basis set size on the absolute transition energies for GTO basis sets. Figure 5.2 shows that the choice of basis set has a significant effect on the energy of the transition. The CP(PPP)+TZVP basis set combination provides the lowest absolute energies, with an average shift to lower energies of 0.59 eV compared to the def2-TZVPP and 0.85 eV to the def2-QZVPP basis set. If we consider the calculated ionisation threshold (see table 5.4) on going

from the CP(PPP)+TZVP basis set to the def2-TZVPP basis set it shifts approximately 0.6 eV to higher energies and by approximately 0.9 eV when going to the def2-QZVPP basis set. This means that relative to the ionisation threshold, there are negligible differences in the transition energies with the different basis sets.

Figure 5.2.: Calculated (TD-DFT/BP86) pre-edge regions of the Fe K-edge XAS spectra of four ferrocene derivatives obtained using either the GTO basis sets CP(PPP)+TZVP, def2-TZVPP or def2-QZVPP.

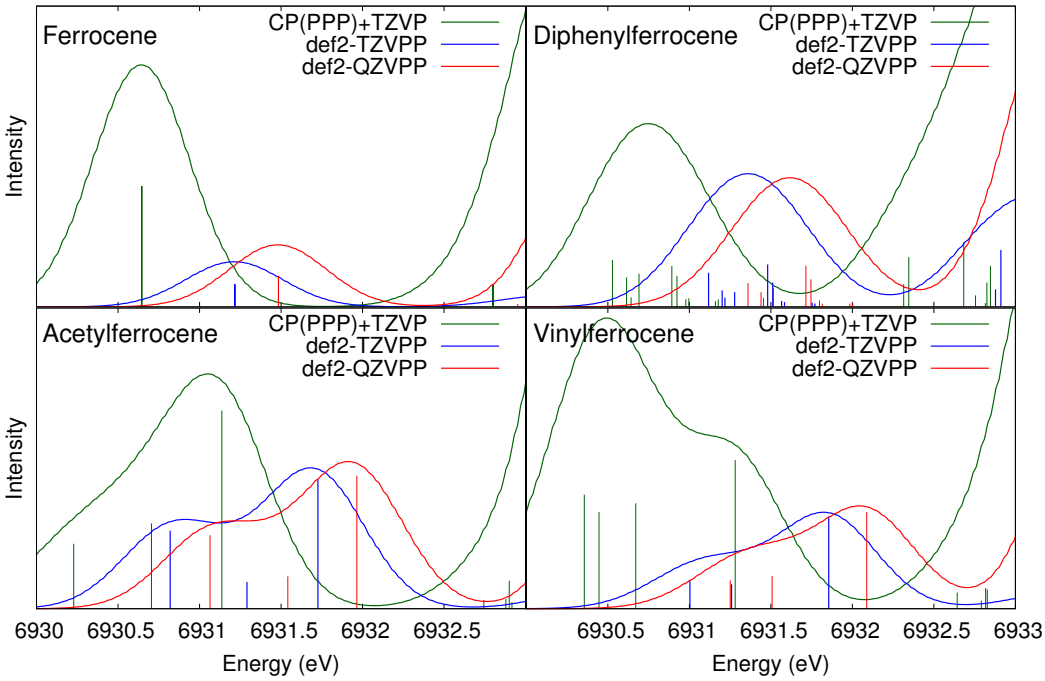

Once more the splitting of one of the transitions in acetylferrocene and vinylferrocene can be used to determine the convergence of the basis set with respect to the relative energies of the transitions. In table 5.5, the splitting energies are listed for the three basis set options, CP(PPP)+TZVP, def2-TZVPP and def2-QZVPP. For acetylferrocene, there are only changes of 0.01 eV on going from the smallest to the largest basis set, but for vinylferrocene there is a difference of 0.09 eV. Thus, even though these energy differences are small compared to the experimental accuracy, the use of the def2-TZVPP basis set or larger is still recommended to provide converged relative energies.

Intensities of Transitions

As before, the calculated dipole-moment and higher-order contributions to the intensities have to be analysed for convergence with respect to the basis set. Here, we consider both a change of size and the number of polarisation functions in the basis set. As ORCA is employed here, the calculated oscillator strengths are origin-dependent and only include the electric-dipole, electric-quadrupole and magnetic-dipole contributions. The origin is placed at the centre of mass of the molecule.

In table 5.6, the effect of the basis set on the individual contributions is given, while the spectra in figure 5.2 show the total oscillator strengths. The electric-dipole intensities have a very small dependence on the basis set, with a difference that is two orders of magnitude smaller

Table 5.4.: Negative orbital energies (DFT/BP86) of the Fe 1*s* orbital, calculated using the CP(PPP)+TZVP, def2-TZVPP and def2-QZVPP basis sets for five ferrocene derivatives. The negative Fe 1*s* orbital energy equals the onset of the continuum states and can be identified with the absorption edge.

Complex	Basis set	Ionisation Threshold (eV)
$Fe(Cp)_2$	CP(PPP)+TZVP	6932.130
	def2-TZVPP	6932.711
	def2-QZVPP	6933.007
Fe(Cp)(CpAc)	CP(PPP)+TZVP	6932.566
	def2-TZVPP	6933.161
	def2-QZVPP	6933.431
Fe(Cp)(CpVinyl)	CP(PPP)+TZVP	6932.226
	def2-TZVPP	6932.834
	def2-QZVPP	6933.102
$Fe(CpPPh_2)_2$	CP(PPP)+TZVP	6932.335
	def2-TZVPP	6932.957
	def2-QZVPP	6933.217
$Fe(CpP^iPr_2)_2$	CP(PPP)+TZVP	6932.222
	def2-TZVPP	6932.845
	def2-QZVPP	6933.099

Table 5.5.: Relative energies for the splitting between the tow lowest peaks - corresponding to transitions into the d_{xz} anti-bonding orbital - with the CP(PPP)+TZVP, def2-TZVPP or def2-QZVPP basis sets for acetyl- and vinylferrocene. The splitting is calculated as the difference between the first and third calculated transitions.

Complex	Basis set	Relative Peak Energy (eV)
Fe(Cp)(CpAc)	CP(PPP)+TZVP	0.91
	def2-TZVPP	0.91
	def2-QZVPP	0.90
Fe(Cp)(CpVinyl)	CP(PPP)+TZVP	0.93
	def2-TZVPP	0.85
	def2-QZVPP	0.84

than the intensity itself on going from def2-TZVPP to def2-QZVPP, but on changing from the CP(PPP)+TZVP basis set the change is only one order of magnitude smaller than the total dipole intensity. Nonetheless, this means that the electric-dipole intensity can be considered converged with respect to the basis set already with the CP(PPP)+TZVP basis set.

The quadrupole contributions have a significantly larger dependence on the basis set. When we go from CP(PPP)+TZVP to def2-TZVPP, the intensity decreases in the same order of magnitude as the summed quadrupole intensity. In ferrocene, this is approximately a 5-fold decrease. On changing from the def2-TZVPP to the def2-QZVPP basis set the changes in the intensity are

smaller and are one order smaller than the total quadrupole intensity. However, this is still a significant change when compared to that of the electric-dipole intensities with the same change in basis set. This observation indicates that the higher-order intensity contributions converge slower with respect to the basis set size than the electric-dipole contributions. Therefore, we conclude that to achieve a result close to the basis set limit, the def2-QZVPP basis set must be used for all calculations where the higher-order quadrupole contributions provide a non-negligible contribution.

Table 5.6.: Total intensities (i.e., sum of all the intensities of all excitations before the ionisation threshold) of the calculated Fe K-edge XAS spectra for five ferrocene derivatives calculated with the CP(PPP)+TZVP, def2-TZVPP or def2-QZVPP basis set. Also included are the separated summed dipole contribution and summed quadrupole contribution for analysis of the basis set dependence of the different contributions. All intensities are dimensionless.

Complex	Basis set	Total Intensity	Summed Dipole	Summed Quadrupole
$Fe(Cp)_2$	CP(PPP)+TZVP	$4.186{\cdot}10^{-05}$	0.000	$4.186{\cdot}10^{-05}$
	def2-TZVPP	$7.809{\cdot}10^{-06}$	0.000	$7.809{\cdot}10^{-06}$
	def2-QZVPP	$1.074{\cdot}10^{-05}$	0.000	$1.074{\cdot}10^{-05}$
Fe(Cp)(CpAc)	CP(PPP)+TZVP	$6.030{\cdot}10^{-05}$	$1.632{\cdot}10^{-05}$	$4.398{\cdot}10^{-05}$
	def2-TZVPP	$4.060{\cdot}10^{-05}$	$1.749{\cdot}10^{-05}$	$2.311{\cdot}10^{-05}$
	def2-QZVPP	$4.134{\cdot}10^{-05}$	$1.710{\cdot}10^{-05}$	$2.424{\cdot}10^{-05}$
Fe(Cp)(CpVinyl)	CP(PPP)+TZVP	$8.046{\cdot}10^{-05}$	$1.205{\cdot}10^{-05}$	$6.841{\cdot}10^{-05}$
	def2-TZVPP	$2.508{\cdot}10^{-05}$	$1.271{\cdot}10^{-05}$	$1.238{\cdot}10^{-05}$
	def2-QZVPP	$2.726{\cdot}10^{-05}$	$1.178{\cdot}10^{-05}$	$1.548{\cdot}10^{-05}$
$Fe(CpPPh_2)_2$	CP(PPP)+TZVP	$3.825{\cdot}10^{-05}$	$3.580{\cdot}10^{-06}$	$3.467{\cdot}10^{-05}$
	def2-TZVPP	$2.765{\cdot}10^{-05}$	$4.676{\cdot}10^{-06}$	$2.298{\cdot}10^{-05}$
	def2-QZVPP	$2.625{\cdot}10^{-05}$	$4.469{\cdot}10^{-06}$	$2.178{\cdot}10^{-05}$
$Fe(CpP^iPr_2)_2$	CP(PPP)+TZVP	$1.527{\cdot}10^{-05}$	$7.550{\cdot}10^{-07}$	$1.452{\cdot}10^{-05}$
	def2-TZVPP	$1.179{\cdot}10^{-05}$	$8.986{\cdot}10^{-06}$	$1.077{\cdot}10^{-05}$
	def2-QZVPP	$1.011{\cdot}10^{-05}$	$9.200{\cdot}10^{-07}$	$9.193{\cdot}10^{-06}$

At this point we have observed that the electric-dipole contributions to the intensity are, for the most part, insensitive to our choice of basis set. As the quadrupole intensities have significant differences, specifically when using the CP(PPP)+TZVP, we decided to look at the importance of the polarisation functions in more detail. Ferrocene was chosen as a test case here because its pre-edge peak contains only quadrupole intensity. Here three pairs of basis sets were compared with differing amounts of polarisation functions. The calculated spectra are shown in figure 5.3. If we first consider the basis set CP(PPP)+TZVP, the number of polarisation functions is severely unbalanced, with many more present on the iron atom compared to the other atoms. In the spectra an intensity much larger than that calculated with either the def2-TZVPP or def2-QZVPP basis set is observed. When compared to a situation where the number of polarisation functions is balanced for all atoms (CP(PPP)+TZVPPP) there is a decrease of the intensity by approximately four fold, to an intensity that is much closer to that calculated using the def2-TZVPP and def2-QZVPP basis sets. In addition, we consider other pairs of basis sets where the number of polarisation functions is balanced, first looking at the Ahlrichs TZVP and TZVPPP basis sets. Here we see

that with the TZVP basis set there is no observable intensity in the spectra, but on increasing the number of polarisation functions to the TZVPPP basis set there is now an observable peak. Therefore, it can be seen that the number of polarisation functions in the molecular basis set has a significant impact on the calculated intensity in this case. However, when we consider the def2-TZVP and def2-TZVPP basis sets, where the number of polarisation functions has been doubled there is no significant change in the calculated intensity of the peak. On the other hand, if the def2-TZVP and TZVP basis sets are compared there is a significant difference in the intensity. The difference between these two basis sets is an added diffuse d function and the inclusion of an f polarisation functions. These additional functions appear to be essential here.

When all comparisons are considered, the most important point to be seen is that the number of polarisation functions present within the molecule should be balanced, otherwise the calculated intensities may be significantly larger than those calculated with a larger basis set. However, if the polarisation functions are balanced, there is no significant change in the calculated intensity on a change in the number of polarisation functions. The Ahlrichs' TZV basis set goes against this observation, which can be attributed to a fewer number of d functions when compared to the def2- basis sets. Finally, another important point so far not discussed is that the change in the number of polarisation functions has no observable effect on the peak position, with changes that are smaller than 0.1 eV.

Figure 5.3.: Ferrocene pre-edge spectra calculated using a variety of basis sets utilising different numbers of polarisation functions.

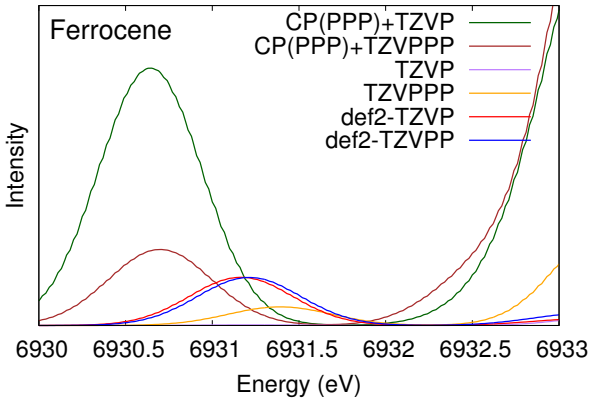

5.1.3. STO vs. GTO

The last consideration with respect to the choice of basis sets is how the use of a GTO or an STO basis set affects the calculated spectra. In figure 5.4 the spectra calculated with comparable size basis sets, but using either GTO or STO functions is shown. We can see that there are many significant differences. However, a problem arises in indicating whether these differences are due to other inherent differences within the programs or a consequence of the different basis sets themselves. As the disentanglement between the effects of the basis set and the differences between the program is not possible, conclusions as to the cause of the differences can not be made. However, the knowledge of the differences between the results obtained with both GTO and STO basis set functions is still necessary for the comparison of results.

The first observation is that there is a significant change in the calculated transition energy, with the GTO basis sets always providing a higher energy. The relative energies are almost identical between the two basis sets. However, in the case of $Fe(CpPPh_2)_2$ the STO basis sets give a smaller relative energy. Secondly, there are also large differences in the intensities. This is not readily apparent in the case of ferrocene where the intensities are very similar between the STO and GTO basis sets. But for acetylferrocene, vinylferrocene and 1,1'-bis(diphenylphosphino)ferrocene the intensities are in general larger with the GTO basis set. In the case of acetylferrocene there is also a reversal of the relative intensities, with the first peak being the most intense for the STO basis sets and the second peak being the most intense for the GTO basis sets. This reversal is also observed for vinylferrocene, though the intensity differences between the two peaks in the spectra are smaller.

Figure 5.4.: Comparison of the STO and GTO basis sets of the same ζ for four ferrocene derivatives.

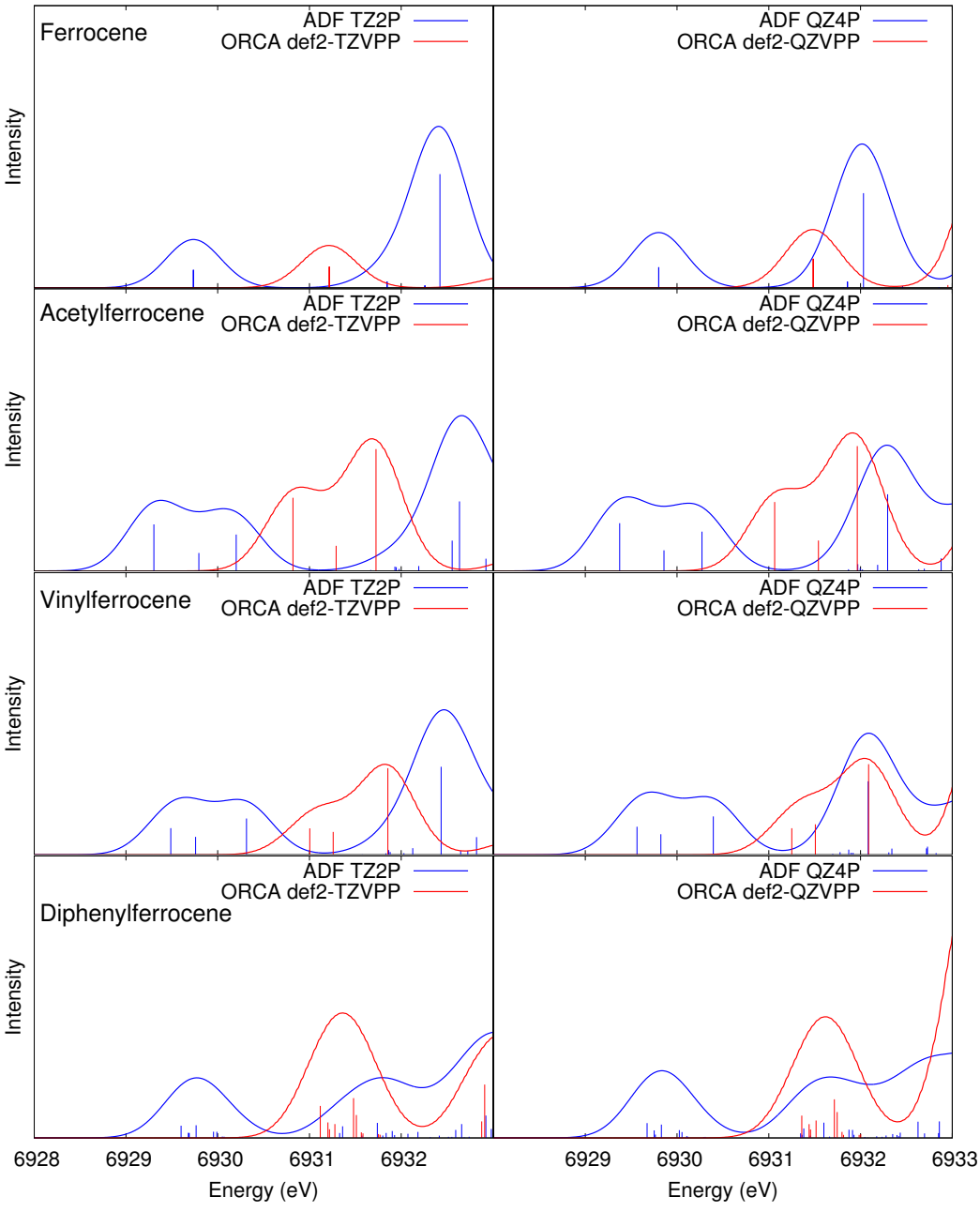

In conclusion, though we observe a shift in the absolute energies, both basis set types provide relative energies in good agreement. The intensities have larger differences due to the basis set function type used in the calculation. However, taking these differences into account both basis sets provide qualitatively the same interpretation of the spectra. Note that the difference in the absolute energies is a moot point as the spectra must be shifted to align with experimental results due to the severe underestimation of the $1s$ core orbital energy when using DFT exchange–correlation functionals (section 5.3 discusses more about the exchange–correlation functionals).

5.2. Program Comparison

In the calculations, three different quantum-chemical program packages have been used: ORCA, ADF and Turbomole (TM). This was necessary because not every program package has every functionality required in the scope of this work. If we are to make a valid comparison between the results calculated with different programs a thorough evaluation of the differences that occur is required. Therefore, we made a study of the differences in the results calculated with each program for vinylferrocene. Within this study the effects of the convergence criteria were explored along with the effect of method choice on the differences between the programs. The convergence levels used are shown in table 5.7. The results presented are the average of the differences from the first ten valence excitations calculated using time-dependent methods. Valence excitations are calculated for this comparison instead of core excitations because Turbomole does not currently have a method available for restricting the excitations to those only from the core orbitals.

Table 5.7.: The different convergence levels used for the program comparison. Convergence check mode in ORCA, 0 means all convergence criteria are checked and 2 means the the change in the total energy and the one-electron energy is checked (calculation is converged if ΔE_{tot}<TolE and ΔE_1<$1{\cdot}10^3$×TolE or the ratio of the total energy and the one-electron energy becomes fixed).

Convergence level	SCF energy threshold (E_h)	Threshold of density (RMS)	Davidson residual threshold	Grid size	Other information
Standard	$1 \cdot 10^{-6}$	$1 \cdot 10^{-6}$	$1 \cdot 10^{-6}$	ORCA: 4 TM: m4	ORCA: Convergence Check mode = 2
		ADF: N/A		ADF: Te Velde 4	
Medium	$1 \cdot 10^{-8}$	$1 \cdot 10^{-8}$	$1 \cdot 10^{-6}$	ORCA: 4 TM: m4	ORCA: Convergence Check mode = 0
		ADF: N/A		ADF: Te Velde 4	
High	$1 \cdot 10^{-10}$	$1 \cdot 10^{-10}$	$1 \cdot 10^{-6}$	ORCA: 4 TM: m4	ORCA: Convergence Check mode = 0
		ADF: N/A		ADF: Te Velde 4	
Default	$1 \cdot 10^{-6}$	ORCA: $1 \cdot 10^{-6}$ TM: $1 \cdot 10^{-7}$	TM: $1 \cdot 10^{-5}$	ORCA: 4 TM: m3	ORCA: Convergence Check mode = 2
		ADF: N/A	ADF: $1 \cdot 10^{-6}$	ADF: Te Velde 4	

Unless otherwise stated, for ORCA and Turbomole all calculations used the def2-SVP basis set with the RI-J approximation, using the def2-SVP/J auxiliary basis set. The HF calculations do not utilise the RI-JK approximation. For the ADF calculations, a DZP basis set was used for all excitation calculations, except that the TZP basis set had to be used for the iron atom, because a

DZP basis set is not available. In all ORCA and Turbomole calculations, the maximum dimension of the expansion space used in the Davidson diagonalisation in the TD-DFT/TD-HF calculations was set to 100, except for in the default calculations with ORCA where this was set to 150. Finally the Tamm-Dancoff approximation (TDA) was used in ORCA and Turbomole for the calculation of the excitations, or in the case of HF the equivalent approximation, configuration interaction singles (CIS).

Table 5.8 shows the average differences from excitation energy calculations using HF, S-VWN or BP86 calculated in both ORCA and Turbomole. As both programs utilise the same definition for the total energy of the system we can also use this as a comparison between the programs. On moving from HF to DFT the differences in the total energy of the system increases to a maximum with BP86. However with a given exchange–correlation functional the differences are almost constant with respect to the convergence criteria and the grid size used. The total energy difference is more sensitive to the convergence criteria in HF, however, the differences are extremely small (μE_h) with the standard convergence criteria. For the average excitation energy differences we see the opposite trend, with a decrease in the differences on using a DFT method. Using DFT the differences are almost independent of the choice of functional, grid size and convergence criteria. Even with HF the differences are two orders of magnitude smaller than the transition energies and do not depend on the convergence criteria.

Importantly we must also consider the comparability of the calculated intensities between programs. The average dipole intensity differences are at least two orders of magnitude smaller than the calculated average dipole intensity for all method options. The differences are also almost independent of the choice of functional, grid size and convergence criteria. However, with HF tightening the convergence criteria reduces the differences by an order of magnitude. Finally, we consider the average differences in the calculated quadrupole intensity. In most calculations the differences are an order of magnitude smaller than the average calculated quadrupole intensity. Also, as for the average dipole intensity differences, the average quadrupole intensity differences are almost constant with respect to the convergence criteria, grid size and exchange–correlation functional choice. Once more, with HF a difference is seen on a change in the convergence criteria, albeit small compared to the change in the average dipole intensity differences.

From these results we can conclude that the results obtained with ORCA and Turbomole are directly comparable. At the default settings for both programs using the def2-QZVPP basis set the differences are almost identical as to the other average DFT result differences, the exception being that the difference in the quadrupole is slightly larger. However, the default convergence settings are sufficient to provide results which can be directly compared.

Table 5.9 shows the average differences from excitation energy calculations using HF, S-VWN or BP86 calculated in both ORCA and ADF. We must note that the largest difference between the programs is the basis set. We shall first consider the average difference in the excitation energies. The differences remain constant within a given methodology and, therefore, can be considered independent of the convergence criteria and the grid size. Although, the differences in the average excitation energies decrease on going from HF to DFT methods and a further decrease on changing from the S-VWN to the BP86 exchange–correlation functional is observed within the DFT methods. We must note that ADF calculates the HF integrals using density fitting [212], which gives rise to the larger differences observed. The average differences in the dipole intensities are constant with respect to the choice of exchange–correlation functional, grid size and convergence criteria and are two orders of magnitude smaller than the average dipole intensity. However, the HF average dipole differences are larger, but they are still one order of magnitude smaller than the average dipole intensity for HF and are also mostly independent of

Table 5.8.: Comparison of results from ORCA and Turbomole for different convergence criteria and grid size using HF, S-VWN or BP86. Differences are averaged over the first 10 calculated valence excitations. The average excitation values for the different methods range from $1.23 \cdot 10^{-1}$ to $1.61 \cdot 10^{-1}$ E_h, average dipole intensities range from $1.99 \cdot 10^{-3}$ to $2.44 \cdot 10^{-3}$ for DFT methods and $7.01 \cdot 10^{-2}$ to $7.02 \cdot 10^{-2}$ for HF and the average quadrupole intensities range from $3.81 \cdot 10^{-9}$ to $6.057 \cdot 10^{-9}$ for DFT and $8.23 \cdot 10^{-7}$ to $9.43 \cdot 10^{-7}$ for HF.

Method	Convergence level	Grid size	Δ_{TotE} (E_h)	Average ΔE_{exc} (E_h)	Average Δ_{Dipole}	Average $\Delta_{Quadrupole}$
HF	Standard	-	$-1.826 \cdot 10^{-06}$	$1.061 \cdot 10^{-03}$	$-1.519 \cdot 10^{-04}$	$9.763 \cdot 10^{-08}$
	Medium	-	$-5.882 \cdot 10^{-08}$	$1.050 \cdot 10^{-03}$	$-3.541 \cdot 10^{-05}$	$1.191 \cdot 10^{-07}$
S-VWN	Standard	Final grid 4 (434 Lebedev)	$3.949 \cdot 10^{-05}$	$4.068 \cdot 10^{-04}$	$3.443 \cdot 10^{-05}$	$8.431 \cdot 10^{-10}$
	Medium	Final grid 4 (434 Lebedev)	$4.304 \cdot 10^{-05}$	$4.041 \cdot 10^{-04}$	$3.440 \cdot 10^{-05}$	$8.442 \cdot 10^{-10}$
		Final grid 3 (302 Lebedev)	$-6.080 \cdot 10^{-06}$	$3.852 \cdot 10^{-04}$	$3.223 \cdot 10^{-05}$	$8.392 \cdot 10^{-10}$
		Final grid 5 (590 Lebedev)	$2.064 \cdot 10^{-05}$	$4.116 \cdot 10^{-04}$	$3.412 \cdot 10^{-05}$	$8.431 \cdot 10^{-10}$
	High	Final grid 4 (434 Lebedev)	$4.279 \cdot 10^{-05}$	$4.044 \cdot 10^{-04}$	$3.435 \cdot 10^{-05}$	$8.442 \cdot 10^{-10}$
BP86	Standard	Final grid 4 (434 Lebedev)	$3.172 \cdot 10^{-02}$	$3.664 \cdot 10^{-04}$	$3.609 \cdot 10^{-05}$	$8.238 \cdot 10^{-10}$
	Medium	Final grid 4 (434 Lebedev)	$3.173 \cdot 10^{-02}$	$3.542 \cdot 10^{-04}$	$3.665 \cdot 10^{-05}$	$8.234 \cdot 10^{-10}$
		Final grid 3 (302 Lebedev)	$3.171 \cdot 10^{-02}$	$3.618 \cdot 10^{-04}$	$3.193 \cdot 10^{-05}$	$8.162 \cdot 10^{-10}$
		Final grid 5 (590 Lebedev)	$3.180 \cdot 10^{-02}$	$3.648 \cdot 10^{-04}$	$3.645 \cdot 10^{-05}$	$8.244 \cdot 10^{-10}$
	High	Final grid 4 (434 Lebedev)	$3.173 \cdot 10^{-02}$	$3.542 \cdot 10^{-04}$	$3.667 \cdot 10^{-05}$	$8.234 \cdot 10^{-10}$
	Default	Final grid 4 (434 Lebedev)	$3.169 \cdot 10^{-02}$	$3.726 \cdot 10^{-04}$	$3.323 \cdot 10^{-05}$	$8.204 \cdot 10^{-10}$
BP86 /def2-QZVPP	Default	Final grid 4 (434 Lebedev)	$3.177 \cdot 10^{-02}$	$3.683 \cdot 10^{-04}$	$3.039 \cdot 10^{-05}$	$1.179 \cdot 10^{-09}$

the choice of convergence criteria.

The final major comparable value is the calculated quadrupole intensities, and we can see that, like the average dipole intensities differences they can be considered mostly independent of the convergence criteria and grid size. However, there is a noted difference between the S-VWN and BP86 results, nevertheless the differences are on the same order with both functionals. These differences are one order of magnitude smaller than the average calculated quadrupole intensity for the DFT methods. Once more the HF average differences are large, although still one order of magnitude smaller than the average calculated quadrupole intensity and can be considered constant with the choice of convergence criteria. The final column in table 5.9 shows the average difference between sum of the intensity components calculated with ORCA and ADF, but these will not be discussed further as their major contributor is the dipole intensity and, therefore, they

have the same behaviour as the dipole intensities.

Table 5.9.: Comparison of results from ORCA and ADF for different convergence criteria and grid size using HF, s-VWN or BP86. Differences are averaged over the first 10 calculated valence excitations. COM = Centre of Mass, Qζ = def2-QZVPP or QZ4P. The average excitation values for the different methods range from $1.20 \cdot 10^{-1}$ to $1.61 \cdot 10^{-1}$ E_h, average dipole intensities range from $2.02 \cdot 10^{-3}$ to $2.44 \cdot 10^{-3}$ for DFT methods and $6.08 \cdot 10^{-2}$ to $7.01 \cdot 10^{-2}$ for HF and the average quadrupole intensities range from $3.98 \cdot 10^{-9}$ to $6.77 \cdot 10^{-9}$ for DFT and $9.42 \cdot 10^{-7}$ to $9.95 \cdot 10^{-7}$ for HF. The average $f^{\mu+Q+m}$ ranges from $2.02 \cdot 10^{-3}$ to $2.45 \cdot 10^{-3}$ for DFT methods and $6.08 \cdot 10^{-2}$ to $7.01 \cdot 10^{-2}$ for HF.

Method	Convergence level	Grid size	Average ΔE_{exc} (E_h)	Average Δ_{Dipole}	Average $\Delta_{Quadrupole}$	Average $\Delta_{f^{\mu+Q+m}}$
HF	Standard	-/Te Velde 4	$2.186 \cdot 10^{-02}$	$9.118 \cdot 10^{-03}$	$-5.228 \cdot 10^{-08}$	$9.117 \cdot 10^{-03}$
	Medium	-/ Te Velde 4	$2.186 \cdot 10^{-02}$	$9.237 \cdot 10^{-03}$	$-5.211 \cdot 10^{-08}$	$9.237 \cdot 10^{-03}$
(S-)VWN	Standard	Final grid 4/Te Velde 4 (434 Lebedev)	$2.259 \cdot 10^{-03}$	$-4.966 \cdot 10^{-05}$	$-5.594 \cdot 10^{-10}$	$-4.968 \cdot 10^{-05}$
	Medium	Final grid 4/Te Velde 4 (434 Lebedev)	$2.256 \cdot 10^{-03}$	$-4.955 \cdot 10^{-05}$	$-5.584 \cdot 10^{-10}$	$-4.957 \cdot 10^{-05}$
	Medium	Final grid 3/Te Velde 3 (302 Lebedev)	$2.289 \cdot 10^{-03}$	$-4.216 \cdot 10^{-05}$	$-5.200 \cdot 10^{-10}$	$-4.218 \cdot 10^{-05}$
	Medium	Final grid 5/Te Velde 5 (590 Lebedev)	$2.232 \cdot 10^{-03}$	$-4.480 \cdot 10^{-05}$	$-5.496 \cdot 10^{-10}$	$-4.482 \cdot 10^{-05}$
	High	Final grid 4/Te Velde 4 (434 Lebedev)	$2.257 \cdot 10^{-03}$	$-4.961 \cdot 10^{-05}$	$5.584 \cdot 10^{-10}$	$-4.963 \cdot 10^{-05}$
BP86	Standard	Final grid 4/Te Velde 4 (434 Lebedev)	$1.370 \cdot 10^{-05}$	$-5.908 \cdot 10^{-05}$	$-8.766 \cdot 10^{-10}$	$-5.911 \cdot 10^{-05}$
	Medium	Final grid 4/Te Velde 4 (434 Lebedev)	$4.300 \cdot 10^{-06}$	$-5.916 \cdot 10^{-05}$	$-8.776 \cdot 10^{-10}$	$-5.919 \cdot 10^{-05}$
	Medium	Final grid 3/Te Velde 3 (302 Lebedev)	$2.770 \cdot 10^{-05}$	$-3.792 \cdot 10^{-05}$	$-7.801 \cdot 10^{-10}$	$-3.795 \cdot 10^{-05}$
	Medium	Final grid 5/Te Velde 5 (590 Lebedev)	$-2.520 \cdot 10^{-05}$	$-5.095 \cdot 10^{-05}$	$-8.531 \cdot 10^{-10}$	$-5.098 \cdot 10^{-05}$
	High	Final grid 4/Te Velde 4 (434 Lebedev)	$4.300 \cdot 10^{-06}$	$-5.915 \cdot 10^{-05}$	$-8.776 \cdot 10^{-10}$	$-5.918 \cdot 10^{-05}$
	Default	Final grid 4/Te Velde 4 (434 Lebedev)	$1.370 \cdot 10^{-05}$	$-5.908 \cdot 10^{-05}$	$-8.766 \cdot 10^{-10}$	$-5.911 \cdot 10^{-05}$
BP86 (COM (origin))	Default	Final grid 4/Te Velde 4 (434 Lebedev)	$1.370 \cdot 10^{-05}$	$-5.908 \cdot 10^{-05}$	$7.362 \cdot 10^{-10}$	$-5.911 \cdot 10^{-05}$
BP86 /(Qζ)	Default	Final grid 4/Te Velde 4 (434 Lebedev)	$-4.742 \cdot 10^{-04}$	$2.262 \cdot 10^{-04}$	$-7.130 \cdot 10^{-10}$	$2.261 \cdot 10^{-04}$

From these results we can conclude that results obtained with ADF are comparable to those obtained using ORCA and, therefore, also Turbomole. At the default settings using the quadruple-ζ basis set we see a slight increase in the average differences of the excitation energies and the dipole intensities. Nevertheless, the differences are still smaller than the average calculated intensity. Therefore, we conclude that the default settings for the convergence criteria are sufficient for

results which can be compared.

5.3. Comparison of Exchange–Correlation Functionals

With the knowledge of the comparability of results obtained using different programs, we can compare the features of spectra calculated with different exchange–correlation functionals and can consider functionals from different programs. We will use both the ORCA and ADF program packages and calculate the spectra for ferrocene and acetylferrocene using the BP86 [130, 131] and B3LYP [158, 159, 213] exchange–correlation functionals in both programs as examples of a pure and a hybrid functional, respectively. In addition, we considered the LB94 [214] exchange–correlation potential, which is designed to have the correct asymptotic form of the potential in the outer region. With ADF, we also employed the SAOP [215, 216] potential, which also has the correct asymptotic form, but which should provide a better description of the inner region compared to LB94. The reason for the better description of the inner region of the potential in SAOP is that the SAOP potential uses different potentials for the outer and inner regions so as to correctly reproduce the shell structure of the exact potential. For all of these calculations the def2-QZVPP [210] or QZ4P [203] basis sets were used in ORCA and ADF, respectively.

The XAS spectra calculated for ferrocene are shown in figure 5.5. It can be seen that with the BP86 functional there is only one peak present before the ionisation threshold, and this qualitative description holds in both programs. Quantitatively, there is a shift in absolute values (see section 5.1.3). The intensities are very similar and the BP86 spectra obtained with ORCA and ADF can be considered equivalent. For the B3LYP spectra, one expects larger differences due to the differences in the calculation of the HF exact exchange. Qualitatively, both programs again provide the same picture. Quantitatively, a shift in absolute values is observed and closer to the ionisation threshold larger differences can be seen. In relation to BP86, the relative energy to the ionisation threshold of the first peak is increased to about 5 eV with both programs. This shift occurs because the hybrid functional B3LYP gives an exchange–correlation potential that resembles the exact asymptotic form in the outer region to some degree.

Now if we consider the asymptotically correct functionals LB94 and SAOP, an immediate difference is observed in the spectra. More peaks are now present below the ionisation threshold, and upon inspection one finds that these are excitations to Rydberg states. For LB94 the absolute energies of the transitions are also much higher. Again in relation to the ionisation threshold the relative energy of the first peak is increased compared to the BP86 spectra. For SAOP the absolute transition energies are in the same range as those of the BP86 functional, but the energy of the first peak is lower. In relation to the ionisation threshold, the relative energy has increased to approximately 5 eV compared to the BP86 spectra, similar to the result obtained with B3LYP. In this case instead of a region containing very few transitions after the first peak with B3LYP, SAOP has transitions which, as in the case with LB94, correspond to Rydberg states. There are distinct similarities between the spectra calculated with the SAOP and LB94 functionals for ferrocene, with a very similar intensity distribution for the first two new peaks. In conclusion, the BP86 and B3LYP exchange–correlation functionals are adequate to calculate the spectra when Rydberg states need not be considered. Although, if Rydberg states are important for the description of the spectra then the LB94 or SAOP potentials must be employed. However, in the case of XAS, the experimental measurements are usually performed in the solid state where the Rydberg states are quenched. Therefore, the BP86 or B3LYP spectra provide an adequate description for the calculation of XAS spectra.

Figure 5.5.: Spectra of ferrocene calculated with TD-DFT using the BP86, B3LYP, SAOP and LB94 exchange–correlation functionals within the ADF and ORCA program packages using the QZ4P or def2-QZVPP basis set, respectively. Each functional is plotted on the energy scale of the calculated absolute transition energies. The blue line indicates the ionisation threshold (i.e., the negative Fe 1*s* orbital energy) of the given functional for the calculation.

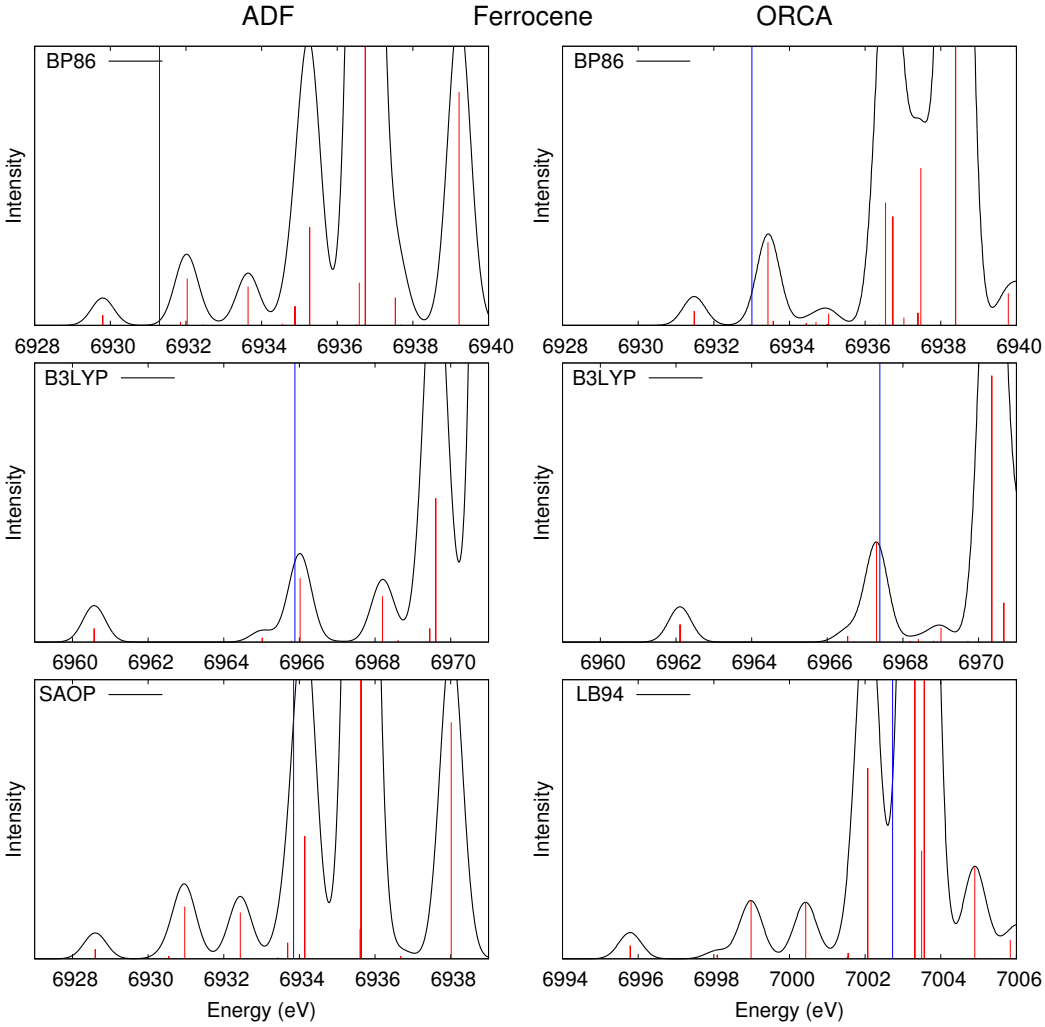

This comparison is also considered for the substituted ferrocenes, where more features are present in the spectra. In figure 5.6 the spectra for acetylferrocene are shown. The vinylferrocene spectra will not be discussed here as they provide the same conclusions. Again for BP86 we see a qualitative equivalency between the two programs. Quantitatively, the absolute energies provide the same conclusions as for ferrocene, but the intensities, as discussed in the basis set comparison (see section 5.1.3), reverse in which is the most intense peak between ADF and ORCA. On going to the B3LYP spectra, once more the absolute energies and the relation to the ionisation threshold are the same as for ferrocene. The biggest difference for B3LYP is that the relative energy of the split transition is significantly increased and there are two distinct peaks approximately 4 eV apart. This will be discussed in more detail in section 5.4. On moving to the LB94 and SAOP functionals the first three transitions are identical to those calculated with the BP86 functional and again, new peaks now appear before the ionisation threshold which correspond to Rydberg

Figure 5.6.: Spectra of acetylferrocene calculated with TD-DFT using the BP86, B3LYP, SAOP and LB94 exchange–correlation functionals within the ADF and ORCA program packages using the QZ4P or def2-QZVPP basis set, respectively. Each functional is plotted on the energy scale of the calculated absolute transition energies. The blue line indicates the ionisation threshold (i.e., the negative Fe 1*s* orbital energy) of the given functional for the calculation.

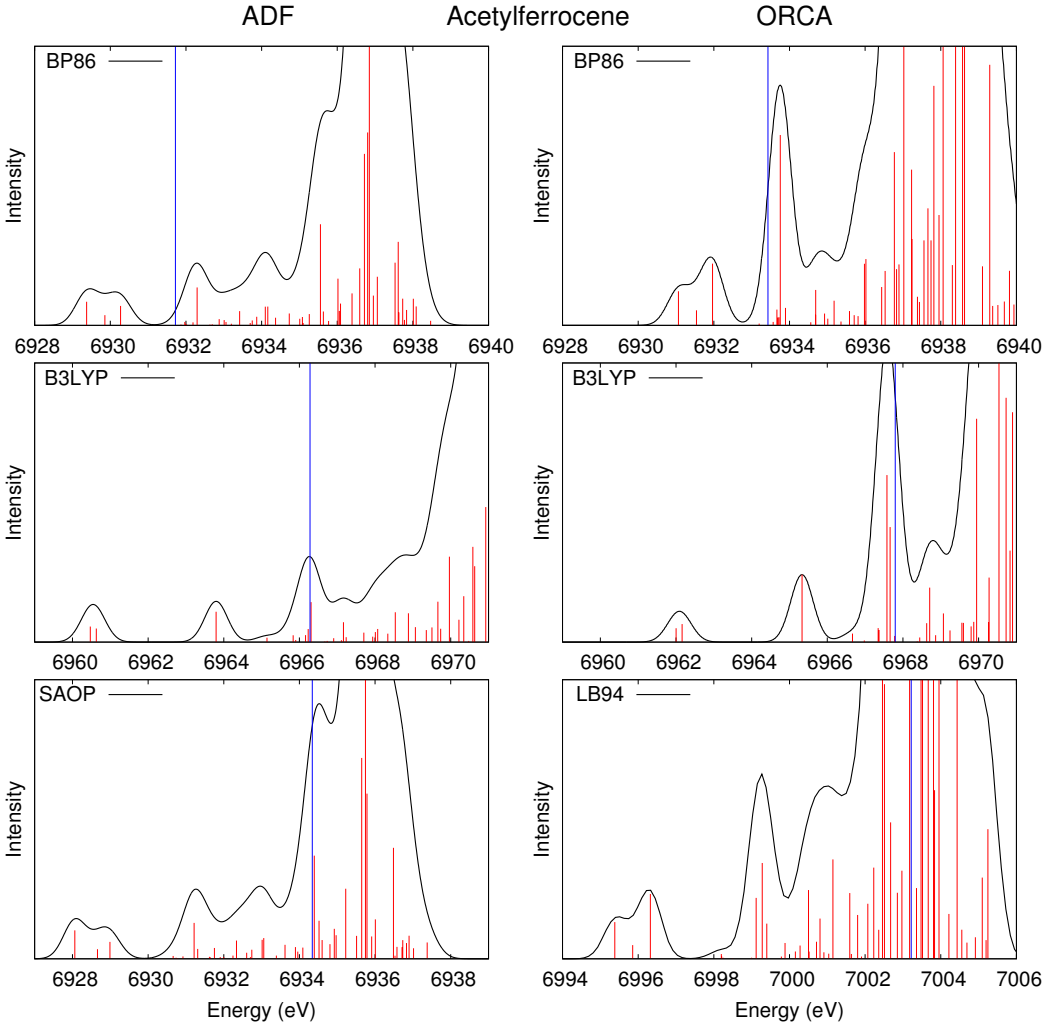

states. In relation to the ionisation threshold the first peak once more is at lower energies compare to the BP86 spectra. For SAOP the relative energy to the ionisation threshold is approximately 6 eV, and for LB94 approximately 8 eV. Again, we can conclude here that for the calculation of XAS spectra the BP86 and B3LYP exchange–correlation functionals provide an adequate description due to the quenching of the Rydberg states in the solid state experimental measurements, which precludes the need for the SAOP and LB94 potentials.

It is commonly known that TD-DFT severely underestimates the absolute transition energies [117] and that to compare to experiment requires a shift of the spectra [184]. This shift is found to be constant for a given functional and basis set and is therefore systematic. Therefore, rather than compare absolute energies it is more important to compare the relative energies of transitions between complexes and internally, if a complex has more than one transition. In conclusion, the four exchange–correlation functionals provide the same qualitative picture for the non-Rydberg

transitions, with LB94, SAOP and BP86 providing almost identical relative energies between complexes and internally. However, an improved description of Rydberg states is not necessary for the calculation of the XAS spectra of interest here and therefore, the BP86 and B3LYP exchange–correlation functional provide an adequate description of the molecular system for these calculations.

5.4. Hartree-Fock Exchange

In section 5.3 a large increase of the relative energies was seen for acetylferrocene on the inclusion of Hartree-Fock (HF) exchange into the functional. In experiment the splitting is 1.82 eV (see chapter 6 for a detailed discussion), and with 0% HF exchange (BP86 exchange–correlation functional/def2-TZVPP) the splitting was calculated as 0.85 eV and the inclusion of 20% HF exchange (B3LYP exchange–correlation functional/def2-TZVPP) this was calculated as 3.64 eV. Therefore, we will investigate the effect of the amount of HF exact exchange included in the functional has on the relative energy between the peaks for the test system vinylferrocene.

In table 5.10 and figure 5.7 is shown the relative energy of the two peaks in the calculated spectra with respect to the amount of HF exchange included in the B3LYP exchange–correlation functional. All these calculations were carried out using the def2-TZVPP basis set in the ORCA program package. For comparison, a time-dependent HF calculation is also included. Figure 5.7 shows a linear relationship between the calculated relative energy of the two peaks in the spectra and the percentage of HF exchange included in the B3LYP functional until 50%. However, between 50% and 75% the relative energy becomes 0 eV. This can be attributed to the orbitals which comprise the two transitions becoming more localised. The transitions are comprised of the d_{xz} anti-bonding orbital and the cyclopentadienyl (Cp) π-orbitals, which conjugate to the π^*-orbitals on the vinyl substituent leading to the observed splitting in the spectra. However, after 50% HF exchange inclusion in the B3LYP exchange–correlation functional, the conjugation of the Cp orbital with the vinyl π^*-orbital disappears, providing the same transitions as those seen for pure ferrocene. Although, in the time-dependent HF calculations there is a slight inclusion of a vinyl π-orbital in the d_{xz} anti-bonding orbital but it is not conjugated with the π-system of the Cp rings.

Table 5.10.: Relative energies of the peaks in the TD-DFT calculated vinylferrocene spectra with different percentage inclusion of HF exact exchange within the B3LYP functional.

%HF Exact Exchange	Splitting Energy (eV)
0	0.84
5	1.37
10	2.07
15	2.84
20	3.64
50	8.91
75	0.00
100	0.00
100 (HF)	0.00

Figure 5.7.: The effect of the amount of HF exact exchange included in the B3LYP functional on the calculated relative energy of the peaks in the vinylferrocene spectra.

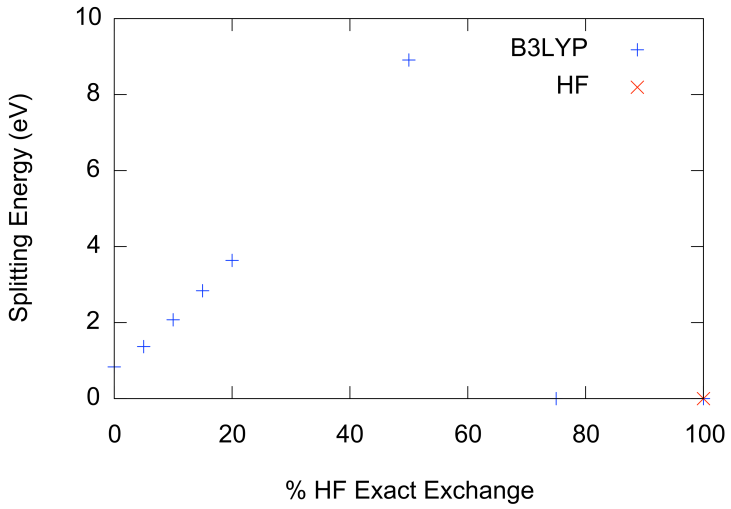

From these calculations we can conclude that HF exchange has a significant impact on the calculated relative energies and that to reproduce the experimental relative energy a HF exchange of approximately 7% would need to be included in the B3LYP exchange–correlation functional. However, tuning the exchange–correlation functional to the desired result is not preferable and we need to find an exchange–correlation functional that provides the correct relative energy. Therefore, we also need a benchmark calculation using a high-level wave function theory method to find how close we can get using quantum-chemical methods to the experimental result.

5.5. Relativistic Effects

As the excitations we are interested in are coming from the core orbitals, there is the question of the importance of relativistic effects to the results. Here we will analyse the effect of relativistics on the final results for four of the complexes discussed so far, calculated with both ADF and ORCA. In ADF we will consider only the zeroth order regular approximation (ZORA) [217–221] along with the use of scaled orbital energies within the TD-DFT calculations. In ORCA we will also consider ZORA [222], but will also consider the Douglas-Kroll-Hess second order relativistic Hamiltonian (DKH(2)) [223, 224]. Within these calculations we will then compare the calculated absolute transition energies and absolute intensities along with the relative energies and relative intensities (using the ferrocene results as a reference) which will enable us to come to a conclusion on the importance of the inclusion of relativistic effects on the results.

The results calculated with ORCA are shown in table 5.11. We can see that the inclusion of scalar relativistic effects significantly increases the absolute transition energy. If we consider first the case when using the ZORA [222], the shift required to align to experiment is reduced from 181.72 to 30.96 eV. This can be attributed to a change in the energy of the 1s orbital [184]. Considering the calculated intensities, these in general increase slightly on the inclusion of the relativistics. For DKH(2) [223, 224] the absolute energies are also increased, but the shift required for alignment is only decreased to 128.59 eV. With DKH(2) the intensities are also significantly affected, with the quadrupole intensities increasing. This effect is most prominent for ferrocene,

where only quadrupole intensity is present, but is also seen in the increase of the intensity for the other complexes.

Table 5.11.: Energies and intensities calculated with TD-DFT (using ORCA) for four ferrocene derivatives using the BP86 functional and the def2-QZVPP basis set in a non-relativistic calculation, and inclusion of relativistic effects using the scalar relativistic ZORA approximation or the scalar relativistic DKH(2) hamiltonian.

	Non-Relativistic		Scalar ZORA		DKH(2)	
Complex	Absolute Energy (eV)	Absolute Intensity	Absolute Energy (eV)	Absolute Intensity	Absolute Energy (eV)	Absolute Intensity
$Fe(Cp)_2$	6931.48	$1.074 \cdot 10^{-05}$	7082.24	$1.581 \cdot 10^{-05}$	6984.61	$2.277 \cdot 10^{-05}$
Fe(Cp)(CpAc)	6931.06	$1.271 \cdot 10^{-05}$	7082.44	$1.234 \cdot 10^{-05}$	6984.18	$1.271 \cdot 10^{-05}$
	6931.97	$2.303 \cdot 10^{-05}$	7083.33	$2.494 \cdot 10^{-05}$	6985.07	$2.882 \cdot 10^{-05}$
Fe(Cp)(CpVinyl)	6931.25	$1.053 \cdot 10^{-05}$	7082.40	$1.422 \cdot 10^{-05}$	6984.37	$1.979 \cdot 10^{-05}$
	6932.09	$1.672 \cdot 10^{-05}$	7083.22	$1.767 \cdot 10^{-05}$	6985.19	$2.003 \cdot 10^{-05}$
$Fe(CpPPh_2)_2$	6931.62	$2.625 \cdot 10^{-05}$	7086.42	$2.915 \cdot 10^{-05}$	6984.70	$3.553 \cdot 10^{-05}$

Table 5.12 shows the relative energies and intensities calculated with ORCA, always taking the ferrocene complex from that methodology as the reference value. For ZORA there is a large change in the relative energies, which does not follow experimental trends. In the extent of some of the differences in the relative energies between complexes, such as 1,1'-bis(diphenylphosphino)ferrocene and ferrocene, these values are erroneously large. In terms of the relative intensities we see in general the same pattern as for the non-relativistic case, but the relative values are reduced. This is primarily observed in the case of the first transition for acetylferrocene where the relative intensity has the most discrepancy. This difference is due to the fact that this transition is primarily dipole allowed, and the relativistic effects primarily affect the size of the quadrupole transitions. That is, this transition's intensity is not significantly altered by the inclusion of ZORA but the intensity for ferrocene is, therefore giving this a much lower relative intensity.

For DKH(2) a similar trend is observed as to that for ZORA, except the increase in the quadrupole intensities is even larger. Therefore, the transitions that are dominated by dipole contributions will be, relative to the ferrocene, drastically reduced. The relative energies though are not affected by the inclusion of DKH(2) and any changes compared to the non-relativistic case are negligible.

Table 5.13 shows the absolute values for the transitions calculated with ADF. On the inclusion of ZORA [217–221] the absolute energies are increased, which means the shift required to align with experiment is reduced from 183.39 to 58.84 eV. The absolute intensities only change in the numbers one order of magnitude smaller than the total intensity. Within ADF there is also the option to calculate the TD-DFT routine using scaled ZORA orbital energies, which is meant to improve excitation energies calculated with ZORA. These results again differ only slightly for the intensities, and the absolute energies are reduced by 61.75 eV (for ferrocene) compared to ZORA and the shift required for alignment with experiment is increased to 120.59 eV.

More important are the relative values, which are shown in table 5.14 for the BP86 exchange–correlation functional and which can be seen in figure 5.8 for both the BP86 and B3LYP exchange–correlation functionals. The relative energies are in general reduced from the non-relativistic calculations, although it is more significant for acetyl- and vinylferrocene than for diphenylferrocene.

Table 5.12.: Relative Energies and intensities (using ferrocene as a reference) from experiment and calculated with TD-DFT (using ORCA) for four ferrocene derivatives using the BP86 functional and the def2-QZVPP basis set in a non-relativistic calculation, and inclusion of relativistic effects using the scalar relativistic ZORA approximation or the scalar relativistic DKH(2) Hamiltonian.

	Experimental		Non-Relativistic		Scalar ZORA		DKH(2)	
Complex	Relative Energy (eV)	Relative Intensity	Relative Energy (eV)	Relative Intensity	Relative Energy (eV)	Relative Intensity	Relative Energy (eV)	Relative Intensity
$Fe(Cp)_2$	0.00	1.00	0.00	1.00	0.00	1.00	0.00	1.00
Fe(Cp)(CpAc)	0.04	0.80	-0.42	1.18	0.20	0.78	-0.43	0.56
	1.52	1.02	0.49	2.14	1.09	1.58	0.46	1.27
Fe(Cp)(CpVinyl)	0.06	0.85	-0.23	0.98	0.16	0.90	-0.24	0.87
	1.88	1.04	0.61	1.56	0.98	1.12	0.58	0.88
$Fe(CpPPh_2)_2$	0.08	0.54	0.14	2.44	4.18	1.84	0.09	1.56

Table 5.13.: Energies and intensities calculated with TD-DFT (using ADF) for four ferrocene derivatives using the BP86 functional and the QZ4P basis set in a non-relativistic calculation, and inclusion of relativistic effects using the scalar relativistic ZORA approximation. Also included are results using scaled ZORA orbital energies for the TD-DFT module.

	Non-Relativistic		Scalar ZORA		Scalar ZORA+Scaled Orbitals	
Complex	Absolute Energy (eV)	Absolute Intensity	Absolute Energy (eV)	Absolute Intensity	Absolute Energy (eV)	Absolute Intensity
$Fe(Cp)_2$	6929.80	$1.020 \cdot 10^{-05}$	7054.35	$9.699 \cdot 10^{-06}$	6992.60	$9.530 \cdot 10^{-06}$
Fe(Cp)(CpAc)	6929.37	$1.181 \cdot 10^{-05}$	7054.00	$1.167 \cdot 10^{-05}$	6992.25	$1.162 \cdot 10^{-05}$
	6930.27	$9.721 \cdot 10^{-06}$	7054.66	$9.244 \cdot 10^{-06}$	6992.91	$9.199 \cdot 10^{-06}$
Fe(Cp)(CpVinyl)	6929.56	$1.206 \cdot 10^{-05}$	7054.28	$1.166 \cdot 10^{-05}$	6992.54	$1.152 \cdot 10^{-05}$
	6930.40	$9.495 \cdot 10^{-06}$	7054.80	$9.119 \cdot 10^{-06}$	6993.06	$9.089 \cdot 10^{-06}$
$Fe(CpPPh_2)_2$	6929.84	$1.429 \cdot 10^{-05}$	7054.40	$1.366 \cdot 10^{-05}$	6992.66	$1.349 \cdot 10^{-05}$

The relative intensities are also insignificantly altered and the changes observed on going from non-relativistic to ZORA calculations can be neglected. The use of the scaled ZORA orbital energies also introduces only negligible differences.

In conclusion, in ADF we see that the inclusion of scalar relativistic effects in the TD-DFT calculation of the X-ray spectra only affects the absolute energies and reduces the shift required to align the calculated spectra with experiment. Although there is a slight decrease of the intensity when using ZORA, this is systematic throughout all transitions as it is caused by the contraction of the $1s$ orbital. Therefore, the differences in the relative intensities are negligible. However, when we include relativistic effects in the TD-DFT calculations in ORCA we arrive at a different conclusion. Once more a large effect is observed on the absolute transition energies, but there

Table 5.14.: Relative Energies and intensities (using ferrocene as a reference) calculated with TD-DFT (using ADF) for four ferrocene derivatives using the BP86 functional and the QZ4P basis set in a non-relativistic calculation, and inclusion of relativistic effects using the scalar relativistic ZORA approximation. Also included are results using scaled ZORA orbital energies for the TD-DFT module.

	Non-Relativistic		Scalar ZORA		Scalar ZORA+scaled orbitals	
Complex	Relative Energy (eV)	Relative Intensity	Relative Energy (eV)	Relative Intensity	Relative Energy (eV)	Relative Intensity
$Fe(Cp)_2$	0.00	1.00	0.00	1.00	0.00	1.00
Fe(Cp)(CpAc)	-0.43	1.16	-0.35	1.20	-0.35	1.22
	0.47	0.95	0.31	0.95	0.31	0.97
Fe(Cp)(CpVinyl)	-0.24	1.18	-0.07	1.20	-0.06	1.21
	0.60	0.93	0.45	0.94	0.46	0.95
$Fe(CpPPh_2)_2$	0.04	1.40	0.05	1.41	0.06	1.42

Figure 5.8.: Calculated pre-edge XAS spectra of five ferrocene derivatives obtained non-relativistically (left) and by considering scalar relativistic effects using the ZORA approximation (right). Results are shown for the BP86 and the B3LYP exchange–correlation functionals.

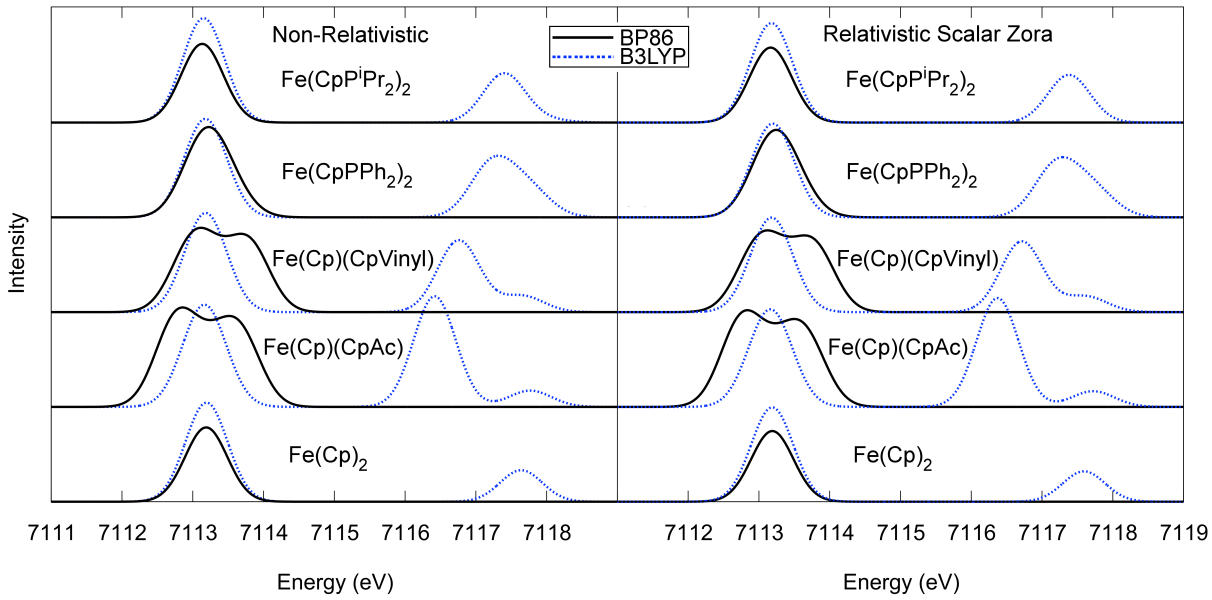

are also significant differences in the calculated intensities. The relative transition energies and intensities also have large changes on the inclusion of relativistic effects. However, these changes are not systematic, as with ADF, and the reason behind these differences is unclear. The largest effect of the inclusion of relativistic effects is the stabilisation of the $1s$ core orbital and a contraction of the size of the core orbitals, the transition intensities should decrease by a constant value as the intensity matrix elements will be smaller due to a smaller overlap between the initial and final

states. However, the intensities calculated in ORCA with the inclusion of relativistic effects do not follow what is expected and currently we do not know the reason.

To the final conclusion of whether or not relativistic effects should be included in the TD-DFT calculations of X-ray absorption spectra, we can see from the ADF calculations that the inclusion is not necessary. A reason for the minimal effect of relativistic effects on the calculation of X-ray absorption spectra is that X-ray absorption spectroscopy probes the valence orbitals, where relativistic effects are negligible. Consequently, it is the valence orbitals which determine the spectra, not the core orbital.

5.6. Summary

In section 5.1 we looked at the effect of the size of the basis set on the calculated X-ray spectra, considering both STO and GTO basis sets. We found that in both cases the energies could be considered converged with the use of a triple-ζ basis set. However, for the calculation of the quadrupole intensities the quadruple-ζ basis set was required. Also, with the GTO basis sets we saw the need to have a balanced number of polarisation functions present throughout the entire complex because when unbalanced, the intensities were unfeasibly large when compared with larger basis sets. Therefore, we conclude that the use of quadruple-ζ basis sets is essential for the calculation of X-ray spectra as the intensities are important for the final comparison to experiment.

As we use multiple quantum-chemical program packages in the next chapters, we had to determine the comparability of the results obtained with each program. We discussed this in section 5.2 and can conclude that ORCA and Turbomole have differences much smaller than the calculated values and that these values are constant with convergence level and grid size between either HF or DFT methods. However, the differences change on going from HF to DFT methods. The same conclusion can be reached for the results between ADF and ORCA. Although, the differences are larger for the average excitation energies. However, from this comparison it can be seen that the results between ADF, ORCA and Turbomole using DFT methods can be compared. The results obtained using HF in ADF can be compared although consideration of the larger differences between ADF and ORCA must be taken into account.

Section 5.3 considered the effect of the choice of exchange–correlation functional on the TD-DFT calculated spectra. We conclude that for the calculation of X-ray spectra, which experimentally are most often measured in the solid state, the non-asymptotically corrected BP86 non-hybrid and B3LYP hybrid functionals provide an adequate description of the molecular system as the Rydberg states are quenched in the experiment. However, if the inclusion of Rydberg states is necessary then the use of the SAOP or LB94 functionals is recommended. From the observations made here on the differences in the spectra on the inclusion of HF exchange into the exchange–correlation functional, we also looked at the effect the amount of HF exchange included in the functional has on the relative energies of vinylferrocene in section 5.4. We see a linear relationship between the relative energies and the amount of HF exchange from 0% to 50%, after which the splitting becomes 0 eV.

As we are concerned with performing calculations on transition metal complexes, the question of the importance of relativistic effects also arises. Therefore, we assessed the effect of the inclusion of relativistic effects within the TD-DFT calculations of the X-ray absorption spectra in both ADF and ORCA for four ferrocene derived complexes in section 5.5. We found that the inclusion of relativistic effects within the ADF calculations only had a minimal effect on the final results. The

largest difference was in the calculated absolute energies, which reduced the shift of the energy scale required to align the results with experiment. However, with the inclusion of relativistic effects in the ORCA calculations significant differences in the calculated intensities are observed, which do not comply with the expectations of the results on the inclusion of scalar relativistic effects. From these tests we conclude that the inclusion of relativistic effects in the calculation of the X-ray absorption spectra is not necessary.

We finally conclude that the best combination of approximations to use for the TD-DFT calculation of X-ray absorption spectra are the BP86 or B3LYP exchange–correlation functionals with a quadruple-ζ basis set (def2-QZVPP/QZ4P) and without the inclusion of relativistic effects, as these will provide at least a qualitative means of interpretation of the experimental spectra. These calculations can be performed in either ORCA, ADF or Turbomole as the differences in the results with each program have been analysed and are smaller than the calculated values for both the intensities and the energies. However, currently only ORCA and ADF are capable of calculating X-ray spectra by isolating the 1s core orbital excitations (see chapter 4 for more detail).

6. X-ray Spectroscopy of Ferrocene Derivatives

X-ray spectroscopy at synchrotrons has become a widely used and powerful tool in studying many chemical processes [9–16]. X-ray absorption spectroscopy in particular has found a firm footing in analysing catalytic processes [24, 225–228] of transition metal complexes and has contributed important insights into catalytic reactions and the underlying molecular mechanisms [12, 72, 229–231]. To be specific to a catalytic centre of interest, such studies are typically performed at the metal edge, i.e., core electrons of a central metal atom are excited. The extended X-ray absorption fine structure (EXAFS) region can provide information on the geometric structure around the metal centre (i.e., on the type, number and distance of coordinating atoms) [232–234] and the X-ray absorption near edge structure (XANES) region of the XAS spectra currently provides information on the qualitative oxidation state of the central metal atom [62, 63, 102, 235], but also contains information on the electronic structure of the complex. However, the sensitivity to light atoms is generally limited to the nearest neighbour shell, while XAS is "blind" to changes beyond the directly coordinating atoms [108, 236], changes in the electronic structure caused by structural modifications in this second coordination shell can hardly be detected. Since XAS investigations enable *in situ* studies under nearly any experimental condition without adopting the system parameters to the experiment [237, 238], it would be highly desirable to overcome these limitations. This would greatly increase the applicability of X-ray spectroscopy for studying chemical processes in catalysis.

In K-edge XAS experiments, the first unoccupied states reached by the 1s electron after excitation are metal d-states. However, as such a $1s \rightarrow nd$ transition is dipole forbidden, the resulting so-called pre-edge signals (pre-edge peaks) are of weak intensity [12]. If molecular complexes and catalysts are considered, these pre-edge peaks contain detailed information about the lowest unoccupied molecular orbitals (LUMOs). So far, the lifetime broadening of conventional K-edge XAS experiments limits their applicability for probing these unoccupied states. On the other hand, in L-edge XAS [239] a more intense $2p \rightarrow nd$ transition can be employed [240], but because of the use of low energy radiation, *in situ* studies of catalytic reactions are not possible with this technique. Therefore, a hard X-ray technique with better resolution of the final d-states than in conventional XAS is required to probe the electronic structure of catalysts.

X-ray emission-based methods open new opportunities for chemical research at synchrotron sources. They are based on the high energy resolution detection of the fluorescence radiation emitted by a sample after irradiation with X-rays [70]. To achieve an appropriate resolution, a dedicated experimental setup consisting of a high flux, high brilliance synchrotron X-ray source and a Rowland-type spectrometer equipped with analyser crystals as shown in figure 6.1 is usually employed [70]. The usage of analyser crystals in combination with a double crystal monochromator (DCM) allows for the recording of X-ray absorption near edge structure (XANES) spectra by monitoring the intensity of a selected fluorescence decay channel while sweeping the incident energy of the DCM or the measurement of X-ray emission spectra (XES) by keeping the incident energy constant, at a value above the edge, and sweeping the analyser crystals over a selected range of emission

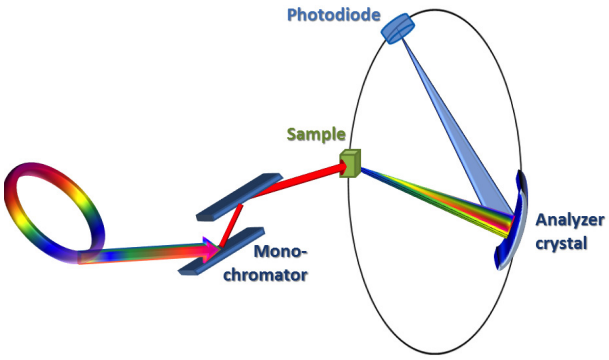

Figure 6.1.: Schematic representation of the experimental setup required for X-ray emission-based spectroscopic methods. This setup can be employed both for recording HERFD-XANES and V2C-XES spectra.

energies.

As long as non-local effects are absent, the described mode of recording XANES spectra is formally equivalent to conventional XANES experiments [70], in which all fluorescence channels are summed up to yield the total absorption cross section $\sigma_{abs} = \sum_i \sigma_i$. However, by selecting a single fluorescence channel, an energy resolution smaller than the life time of the final state of the absorption process can be reached [78, 79]. This final state in the case of K-edge XANES spectra is characterised by a $1s$ core hole and an additional electron in an empty electronic state. Experiments using a setup as shown in figure 6.1 are called high energy resolution fluorescence detection XANES (HERFD-XANES) [50, 241, 242]. They can be used to probe unoccupied electronic states with a resolution not available in conventional XAS. In particular, this sharpens the very weak signals of dipole-forbidden transitions.

It is therefore surprising that HERFD-XAS measurements have not been applied to overcome the limitations of conventional XAS with respect to processes involving molecular complexes, like in homogeneous catalysis. So far, HERFD-XAS has been applied mainly to heterogeneous catalytic processes [11, 16, 241, 243, 244] and enzymatic systems [68, 107, 137, 173, 184, 245, 246]. In addition, HERFD-XAS has been used to elucidate the structure of of protein models with iron centres [228]. However, these complexes show structural differences already in the first coordination shell. Nothing is known about the power of HERFD-XAS to resolve structural differences beyond the nearest neighbour coordinating atoms and their influence on the electronic structure at the central metal atom.

Herein, we want to bridge this gap by pioneering HERFD-XAS studies on transition metal complexes, which show that this technique is even sensitive for substitution effects at ligands coordinated to a metal centre, i.e., effects which are not accessible to conventional EXAFS analysis. As a first target, we investigate changes in the electronic structure of ferrocene derivatives induced by substituents at the cyclopentadienyl (Cp) rings. As indicated in figure 6.2, the ferrocene structural motif remains unchanged throughout the study. Only the substituents are changed, which affects the electronic structure at the iron centre.

Such ferrocene-derived compounds play an important role in catalysis [247–250], in particular in bimetallic catalytic systems [24], as well as the preparation of switchable self assembling monolayers (SAMs) [251] and electronic compounds [252]. Consequently, ferrocene and its derivatives [69, 240, 253, 254] as well as other metallocenes [253, 255, 256] have been studied extensively with X-ray spectroscopic methods.

Herein, we demonstrate that these subtle changes can be probed by HERFD-XANES and explained with TD-DFT calculations. The influence of substituting groups at the Cp ring on the electronic structure has been studied both experimentally and theoretically [257–259]. However these experimental studies are limited to soft X-ray absorption spectroscopy [240,254], which cannot be used for *in situ* studies due to the low radiation energy and photoelectron spectroscopy [259] or X-ray emission experiments [107] that only provide information about the occupied orbitals. Here we demonstrate how the complementary information on unoccupied orbitals can be probed with hard X-rays.

Figure 6.2.: Illustration of the model systems used to demonstrate the resolving power of HERFD-XANES and V2C-XES with respect to changes beyond the first coordination sphere.

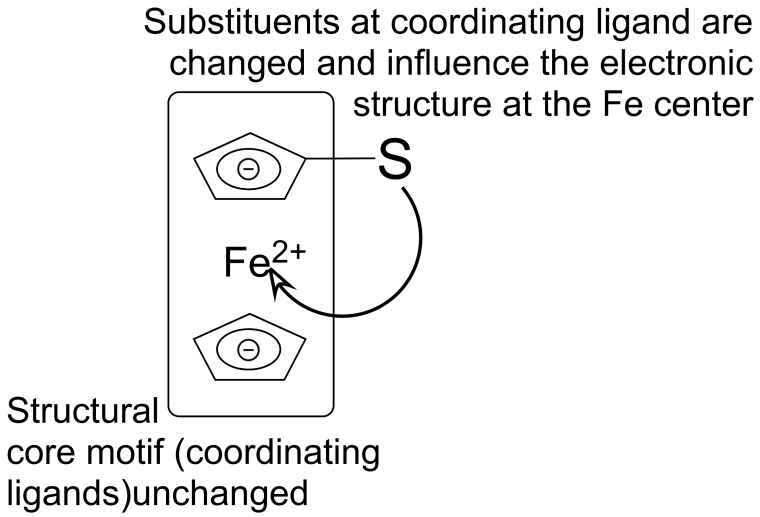

The described experimental setup also allows for a second type of experiment. In a so-called valence-to-core (V2C) XES experiment, the $1s$ electron is non-resonantly excited into the continuum far above the ionisation threshold, and the following radiative relaxation of a valence electron into the core hole is detected. This valence electron originates from an occupied electronic state. While sweeping the emission energy, the different occupied states are thus probed in a K$\beta_{2,5}$ (V2C) emission experiment. The K$\beta_{2,5}$ emission process is reduced by a factor of 500 and around 60 in intensity compared to the Kα and K$\beta_{1,3}$ emission where the core hole is filled by low-lying $2p$ and $3p$ electrons, respectively, but it is the only transition with sufficient sensitivity to ligand effects [260]. As the occupied valence states are strongly determined by the chemical environment of the central metal atom, this method is also sensitive to the identity of the ligands as well as the geometry of the immediate ligand environment in catalytically active metal complexes [67, 68]. Figure 6.3 summarises the transitions of the two described methods.

Note that these two techniques provide complementary information [227]. By means of V2C-XES and HERFD-XANES, details about both occupied and unoccupied electronic states, respectively, are available under almost any experimental condition. For the interpretation of such X-ray spectra, and for relating the observed transitions to the electronic structure, quantum-chemical calculations are essential (for reviews, see, e.g., refs. [105, 115]). In many cases, already rather simple approaches based on (time-dependent) density functional theory (DFT) [107,116,137,173, 184,261] can guide the assignment and interpretation of X-ray spectra [21,69,262].

In addition to HERFD-XANES for probing unoccupied states, we also explore the sensitivity of

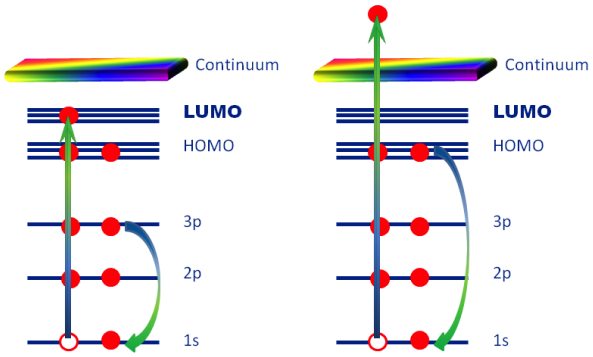

Figure 6.3.: Qualitative representation of the processes observed in HERFD-XANES (left) and V2C-XES (right) within a molecular orbital picture. In HERFD-XANES, a core electron is excited to unoccupied molecular orbitals and the intensity of the K$\beta_{1,3}$ emission is measured, whereas in V2C-XES, the relaxation of an electron from an occupied molecular orbital following the creation of a core hole is probed.

V2C-XES to changes in the occupied electronic structure caused by substitution within the second coordination sphere. V2C-XES is becoming a popular tool in catalysis characterisation because of its sensitivity to the composition within the first coordination sphere as well as the information it provides on the occupied electronic states [21, 67–69, 137, 173].

6.1. Results

6.1.1. Molecular Test Set of Ferrocene Derived Complexes

To compare the chemical sensitivity of HERFD-XANES and V2C-XES, in particular their ability to detect changes in the electronic structure induced by substitutions in the second coordination shell, we consider ferrocene and complexes derived from it. The test set for this comparison, shown in figure 6.4, consists of ferrocene ((a)$FeCp_2$) and ferrocene derivatives containing substituents on the cyclopentadienyl (Cp^-) rings. In acetylferrocene ((f)Fe(Cp)(CpAc)) and in vinylferrocene ((e)Fe(Cp)(CpVinyl)) this substituent contains a π-bond that is conjugated with the cyclopentadienyl ring, whereas in 1,1'-bis-diphenylphosphinoferrocene (d)($Fe(CpPPh_2)_2$) and in 1,1'-bis-diisopropylphosphinoferrocene ((c)$Fe(CpP^iPr_2)_2$) there are phosphine substituents at both cyclopentadienyl rings. Decamethylferrocene ((b)$Fe(Cp^*)_2$ replaces all hydrogens of the Cp rings with methyl groups. In addition, ferrocenium ((g)$[FeCp_2]^+$) is included within the test set. Note that in all seven complexes, the first coordination shell around the iron atom is identical, whereas the different substituents are part of the second coordination sphere. The optimised molecular structures as obtained from DFT calculations are shown in figure 6.5.

The starting point for the discussion of the electronic structure of the ferrocene derived complexes is to consider the molecular orbital (MO) diagram of the relevant orbitals of the unsubstituted ferrocene. The MO diagram obtained from density functional theory (DFT) calculations is shown in figure 6.6.

For HERFD-XANES we must consider the unoccupied orbitals and the lowest energy transition would be to the LUMO, which is the doubly degenerate e_{1g} orbital [1] and is the anti-bonding

[1] Even though the calculations are performed for the more stable eclipsed conformation (D_{5h} symmetry) of ferro-

Figure 6.4.: Test set of ferrocene-derived compounds (a)-(g) subjected to HERFD-XANES and V2C-XES measurements and (TD-)DFT calculations.

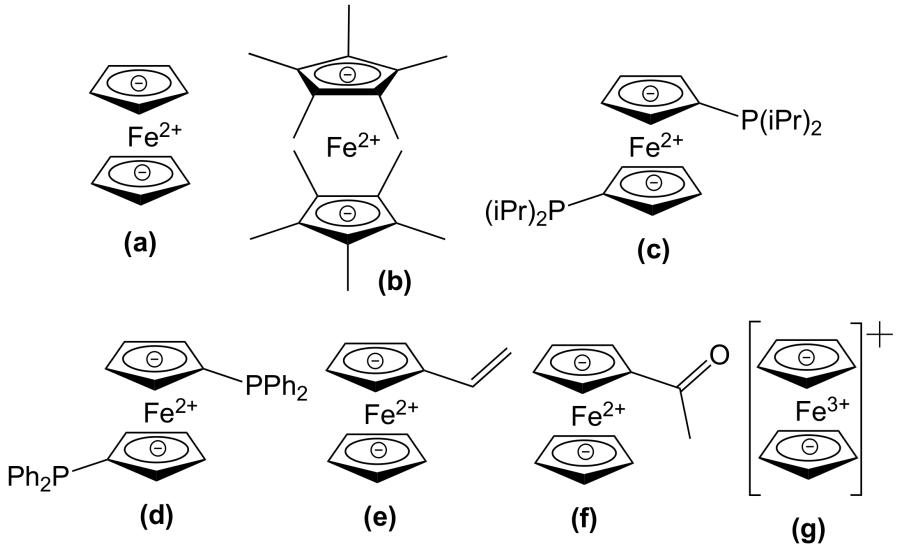

Figure 6.5.: Optimised molecular structures of the lowest-energy conformers of complexes (a)-(g).

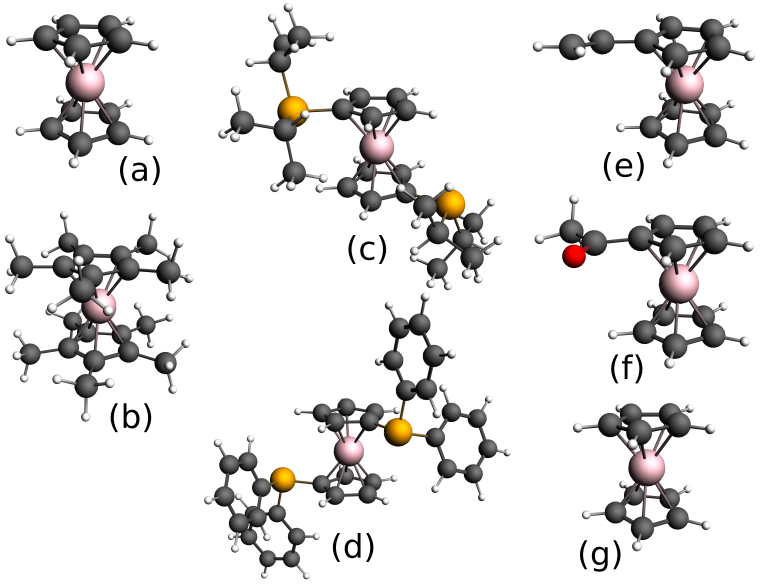

combination of the Fe d_{xz}- and d_{yz}-orbitals with the p-orbitals of the Cp ligands.

For V2C-XES we must consider the occupied molecular orbitals of ferrocene in figure 6.6 (see also the discussion in ref. [69]). The highest occupied molecular orbital (HOMO), e_{2g}, and the HOMO-1, a_{1g}, are combinations of the remaining iron d-orbitals, namely of the $d_{x^2-y^2}$ and d_{xy} orbitals, and of the d_{z^2} orbital, respectively, with the cyclopentadienyl π-orbitals. The MOs at lower energies are composed primarily of the cyclopentadienyl π-orbitals followed by cyclopentadienyl σ-orbitals at even lower orbital energies. For the occupied orbitals with e_{1u} or a_{2u} symmetry

cene, we follow the common convention of using orbital labels referring to the staggered conformation [6]

Figure 6.6.: Molecular orbital (MO) diagram of ferrocene focusing on the occupied valence orbitals. The ordering of the orbitals as well as the isosurface plots of the MOs have been obtained from a DFT calculation using the BP86 exchange–correlation functional.

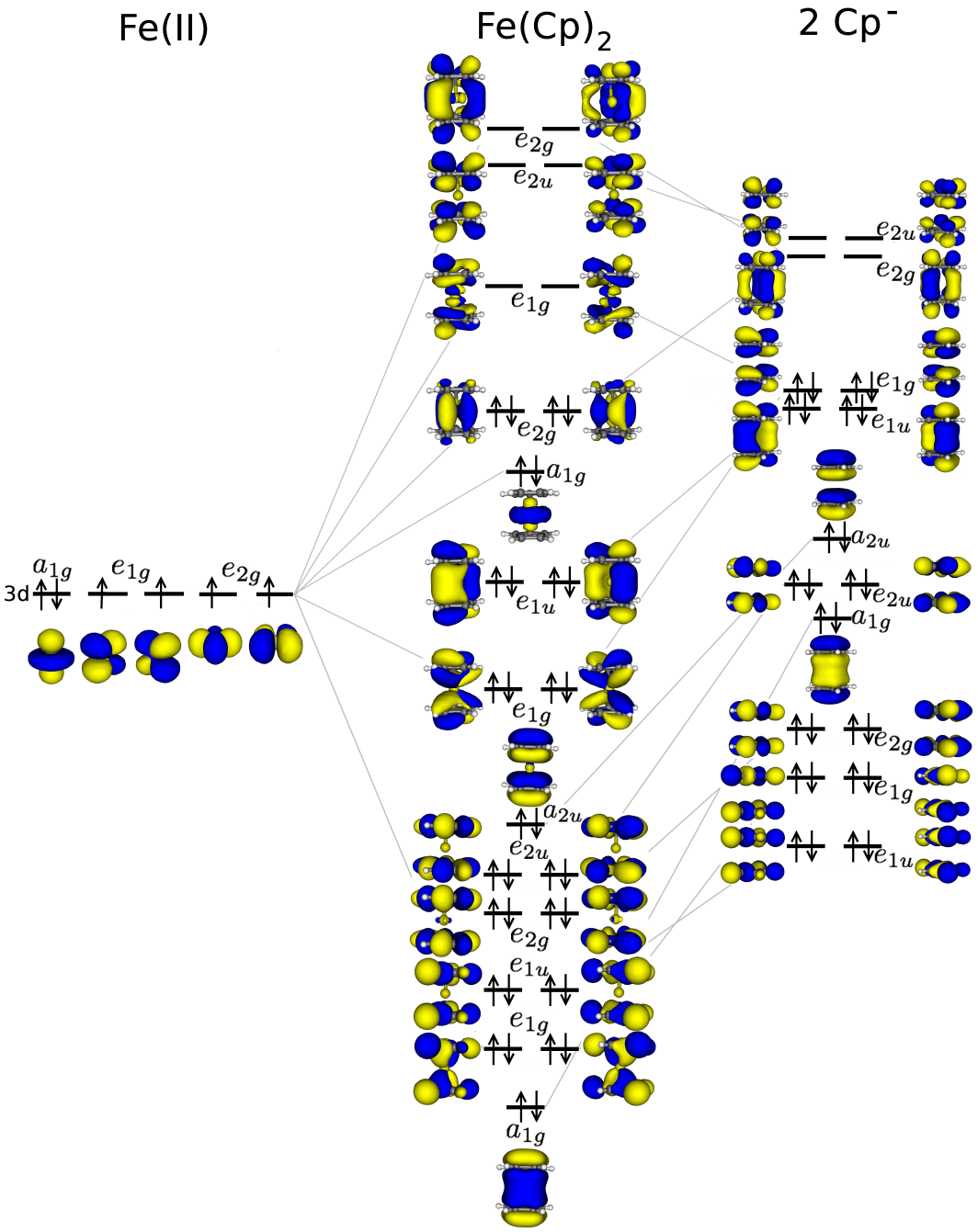

(i.e., those with the same symmetry as the Fe p-orbitals and the electric-dipole operator) there are also small contributions from the iron p-orbitals [69]. The occupied e_{1g} orbital is the only one of the occupied orbitals within the relevant energy range shown here that has large d-orbital contributions. In fact, this e_{1g} orbital is the bonding combination of the iron d_{xz} and d_{yz} orbitals with cyclopentadienyl π-orbitals, whereas the unoccupied e_{1g} orbitals discussed above is the corresponding anti-bonding combination.

6.1.2. Interpretation of the HERFD-XANES Spectra

To begin with, we will discuss the results obtained using HERFD-XANES. First a comparison of conventional transmission mode XANES with the corresponding HERFD-XANES spectra recorded at the K$\beta_{1,3}$ main line of ferrocene (a), Fe(CpPPh$_2$)$_2$ (d), and Fe(Cp)(CpAc) (f) are shown in figure 6.7, which indicate the resolving power of the HERFD-XANES measurements and provides grounds for considering the chemical sensitivity of HERFD-XANES.

Figure 6.7.: Comparison of conventional (dashed line) and HERFD-XANES (solid line) spectra for complexes (a), (d) and (f). The enlarged pre-edge peak region is shown on the right; the spectra have been shifted for clarity.

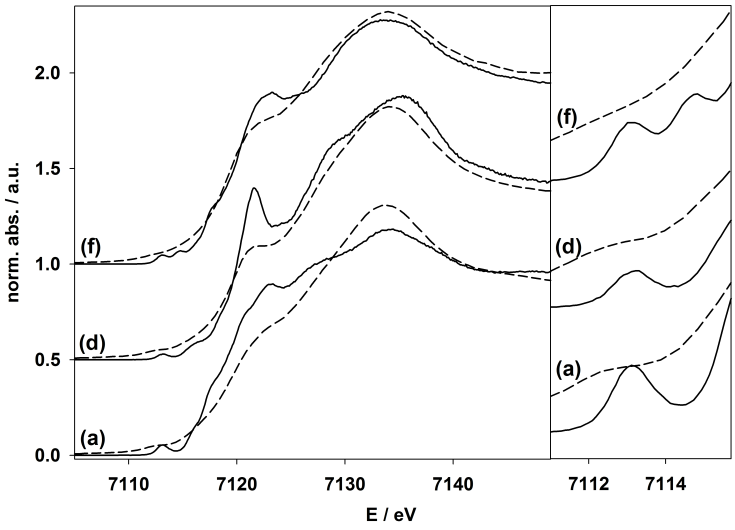

Although significant differences in the electronic structure are expected due to the acetyl or the two diphenylphosphino substituents, hardly any effects are observed in the conventional transmission XANES spectra. In the HERFD-XANES spectra, the net signal broadening is reduced from approximately 5 eV to 1.5 eV. This reveals significant differences in the $1s \rightarrow 3d$ pre-edge peak region around 7113 eV as well as for the region around 7121 eV, which can now be used for detailed comparison with calculations.

The pre-edge peak at 7113.2 eV in the XANES spectrum of ferrocene can be assigned to the dipole-forbidden transition from the Fe $1s$ orbital to the e_{1g} orbitals in the MO diagram (see figure 6.6). Changes in these lowest unoccupied orbitals are induced by different substituents on the Cp ligands, which can be identified by comparing the HERFD-XANES pre-edge peaks. Only the high resolution of these spectra allows for a deconvolution, and the isolated pre-edge peaks of (a)-(g) are depicted in figure 6.8. The positions and relative intensities of the isolated pre-edge peaks are summarised in Table 6.1.

To complement the experimental results and to allow for an assignment of the observed pre-edge peaks to unoccupied molecular orbitals, we have performed TD-DFT calculations [107, 123, 184], using both the non-hybrid BP86 exchange–correlation functional [130, 151] and the B3LYP hybrid functional [158, 159]. The calculated spectra are included in figure 6.8, and the unoccupied orbitals corresponding to these pre-edge peak transitions are depicted in figure 6.9.

For ferrocene (a), the LUMO is degenerate and there is only a single pre-edge peak with a weak quadrupole intensity caused by the $1s \rightarrow e_{1g}$ transition (see figure 6.9) [27, 108, 253]. We note that

Table 6.1.: Positions and relative intensities of the isolated HERFD-XANES pre-edge peaks compared to the TD-DFT calculations (BP86/def2-QZVPP and B3LYP/def2-QZVPP). The peak positions are given as energy differences relative to the pre-edge peak in ferrocene and the relative intensities are normalised to the ferrocene pre-edge peak. For the calculated intensities, the percentage of electric-dipole contribution to the intensities is also included

Complex	Experimental		TD-DFT/BP86		TD-DFT/B3LYP	
	E_{rel}	Rel. Int.	E_{rel}	Rel. Int.	E_{rel}	Rel. Int.
(a) $Fe(Cp)_2$	0.00	1.00	0.00	1.00(0%D)	0.00	1.00(0%D)
(b) $Fe(Cp^*)_2$	0.07	0.84	0.02	0.96(0%D)	0.04	0.99(0%D)
(c) $Fe(CpP^iPr_2)_2$	0.04	0.66	−0.05	0.94(10%D)	−0.03	0.93(7%D)
(d) $Fe(CpPPh_2)_2$	0.08	0.54	0.14	2.44(39%D)	−0.01	1.01(1%D)
(e) Fe(Cp)(CpAc)	0.04	0.88	−0.42	1.18(73%D)	−0.01	0.90(10%D)
	1.52	1.02	0.49	2.14(34%D)	3.23	1.91(53%D)
(f) Fe(Cp)(CpVinyl)	0.06	0.85	−0.23	0.98(34%D)	0.00	0.95(2%D)
	1.88	1.04	0.61	1.56(51%D)	3.56	0.88(70%D)
(g) $[Fe(Cp)_2]PF_6$	−1.63	0.33	−1.59	0.26(1%D)	−2.24	0.30(1%D)
	0.42	0.52	0.42	1.31(29%D)	0.60	1.17(29%D)

the TD-DFT calculations provide identical results for the eclipsed and the staggered conformation. For $Fe(Cp^*)_2$ (b) the LUMO is unchanged since the methyl substituents have very little effect on the intensity and energy of the calculated pre-edge peak, which agrees with the experimental spectra. For the phosphine-substituted ferrocenes, $Fe(CpP^iPr_2)_2$ (c) and $Fe(CpPPh_2)_2$ (d), the position of the experimentally observed pre-edge peak agrees with the one in ferrocene, but its intensity decreases. Although great care was taken in the experiment to avoid particles size and self-absorption effects, they cannot be fully excluded since no angle dependent measurements were carried out. The effect of different isomers can be excluded as they do not affect the energy levels. For $Fe(CpP^iPr_2)_2$, the calculations show that the degeneracy of the LUMO is only slightly lifted. The substituents cause a small distortion of the two LUMO orbitals (see figure 6.9), which leads to a splitting of ca. 0.1 eV. However, this does not affect the calculated pre-edge peak intensity. For $Fe(CpP^iPr_2)_2$, both BP86 and B3LYP provide almost identical results. On the other hand, for $Fe(CpPPh_2)_2$ the p-orbitals of the phenyl rings mix with those of the Cp rings in the BP86 calculations, resulting in very delocalised orbitals. Altogether, there are ten unoccupied orbitals that contribute to the calculated pre-edge peak (two examples are included in figure 6.9). This mixing lifts the symmetry of the LUMO orbitals and introduces large electric-dipole contributions. Thus, a significant increase of the calculated pre-edge peak intensity is found in the BP86 calculation. However, this increase does not agree with the experimental observation. On the other hand, with the hybrid B3LYP functional the corresponding orbitals are localised either on the Cp rings or on the phenyl rings. In this case, only two orbitals that resemble the LUMO in ferrocene contribute to the pre-edge peak, and the calculated intensity is similar to the one in $Fe(CpP^iPr_2)_2$. By combining the experimental and computational results, we can conclude that in $Fe(CpPPh_2)_2$ the phenyl rings do not contribute to the LUMO.

For Fe(Cp)(CpVinyl) (e) and Fe(Cp)(CpAc) (f) two pre-edge peaks, which are split by 1.82 eV and 1.48 eV, respectively, are observed in the experimental spectra with an intensity ratio of 1:1.22 and 1:1.16 respectively. From these values as well as figure 6.7, it is evident that the resolution of these two transitions is only possible by HERFD-XANES. A similar splitting has been observed

Figure 6.8.: Left: Normalised, isolated pre-edge peaks from the experimental HERFD-XANES spectra of complexes (a)-(g). Right: Pre-edge peaks from TD-DFT calculations with BP86/def2-QZVPP (black dash-dotted line) and B3LYP/def2-QZVPP (grey solid line) (0.7 eV FWHM).

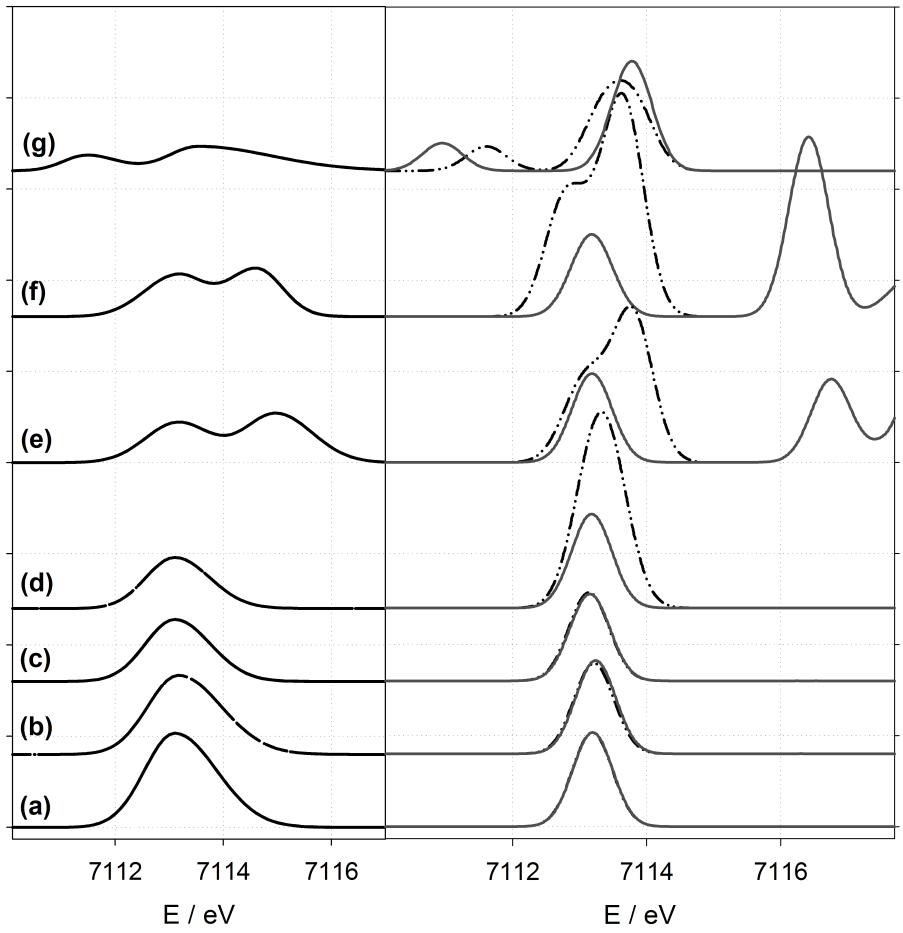

previously in L-edge spectra of $Fe(CpAc)_2$, where a value of 1.12 eV is found [240]. This splitting can be understood with the help of our TD-DFT calculations. The p-orbitals of the acetyl and vinyl substituents interact with one of the LUMO orbitals, resulting in the two orbitals shown in figure 6.9. As these are not symmetric anymore, the intensity of the transitions to these orbitals increases and is now dominated by the electric-dipole contribution. On the other hand, the other orbital (see figure 6.9) is perpendicular to the substituent p-orbitals and remains unchanged. The transition to this orbital only has a small quadrupole intensity. Even though BP86 and B3LYP provide a very similar orbital picture, the splitting between the two pre-edge peaks is too small with BP86, whereas it is overestimated with the B3LYP hybrid functional.

Finally, in ferrocenium (g) there is a vacancy in the e_{2g} orbital, which is occupied in ferrocene. Therefore, in the HERFD-XANES spectrum the first pre-edge peak appears 1.6 eV lower in energy than in ferrocene. The second pre-edge peak, which is due to the transition to the unoccupied e_{1g} orbital, is shifted by ca. 0.4 eV to higher energies. This is qualitatively reproduced by the TD-DFT calculations, but these underestimate the intensity of the first pre-edge peak and predict a too large intensity for the second pre-edge peak. However, the treatment of excitations in open-shell molecules within (TDDFT) is problematic and cannot account for multiplet effects [263–265], which might be important for ferrocenium [254].

Figure 6.9.: Isosurface plots of the unoccupied molecular orbitals probed by the pre-edge peak transitions as obtained from TD-DFT calculations with BP86/def2-QZVPP (left) and with B3LYP/def2-QZVPP (right). In cases where more than one orbital transition contributes to one excitation, the corresponding linear combination of unoccupied orbitals is shown. In the BP86 calculations for $Fe(CpPPh_2)_2$ (d) ten individual excitations to different unoccupied orbitals contribute to the pre-edge peak, of which only two are shown here

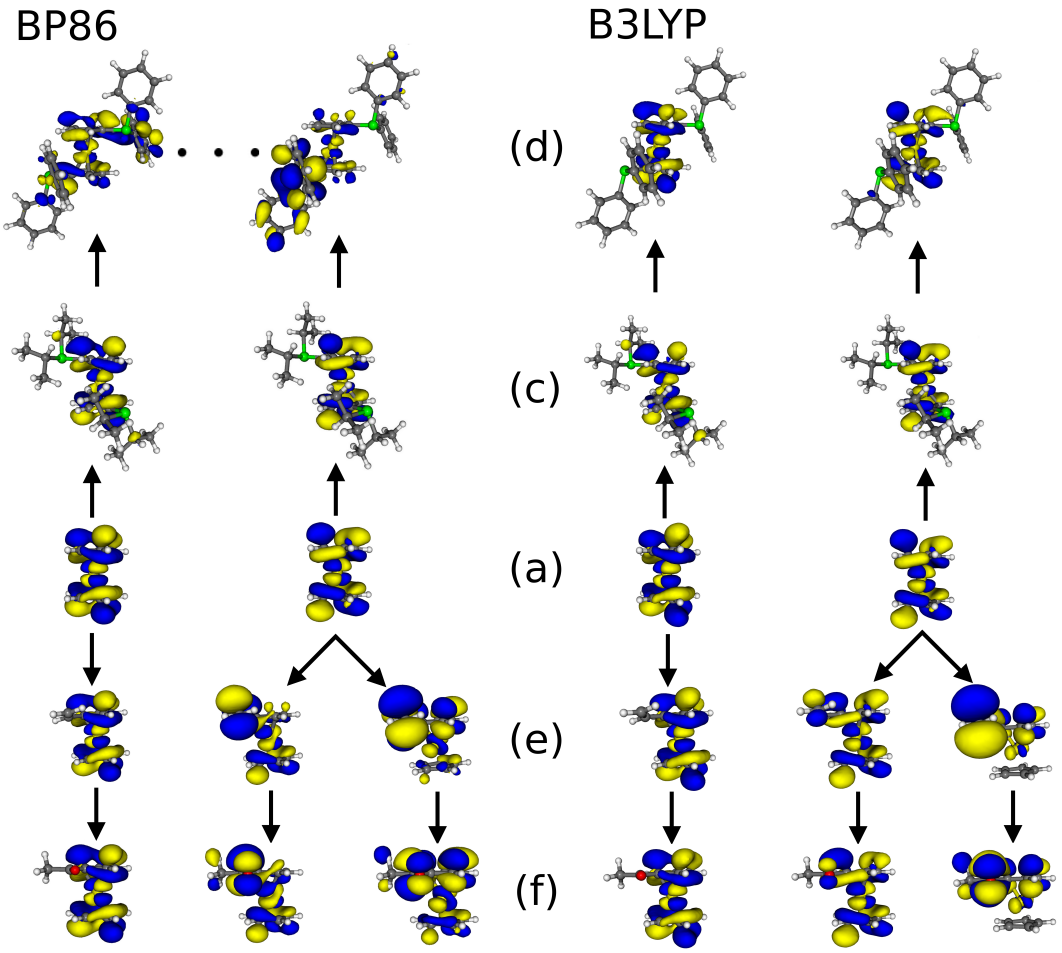

6.1.3. Interpretation of the V2C-XES Spectra

Figure 6.10 shows the experimental HERFD-XANES spectra (left) and V2C-XES spectra (right) for this set of molecules. The HERFD-XANES spectra have been discussed in detail earlier in section 6.1.2. Of particular interest are the pre-edge peaks which are very sensitive to subtle changes in the electronic structure at the iron centre. These pre-edge peaks have been highlighted in figure 6.10. However, all the V2C-XES spectra of the ferrocene derivatives appear identical to those of ferrocene. Even in ferrocenium (g), where the increased oxidation state of the iron centre leads to significant changes in the pre-edge region and shifts the ionisation edge to higher energies in the HERFD-XANES spectra, the V2C-XES spectrum remains qualitatively unchanged, although shifted to higher energies. For a detailed comparison of the V2C-XES spectra of ferrocene and ferrocenium, which differ in the oxidation state of the iron atom, we refer to reference [69]. In the following, we will focus on the Fe(II) complexes (a)–(f). Here, we leave out $Fe(Cp^*)_2$, (b), because its spectra are identical to those of ferrocene.

Figure 6.10.: Experimental HERFD-XANES spectra (left) and V2C-XES spectra recorded at an excitation energy of 7300 eV (right). The labels (a) and (c)-(g) refer to the ferrocene derivatives as listed in figure 6.4.

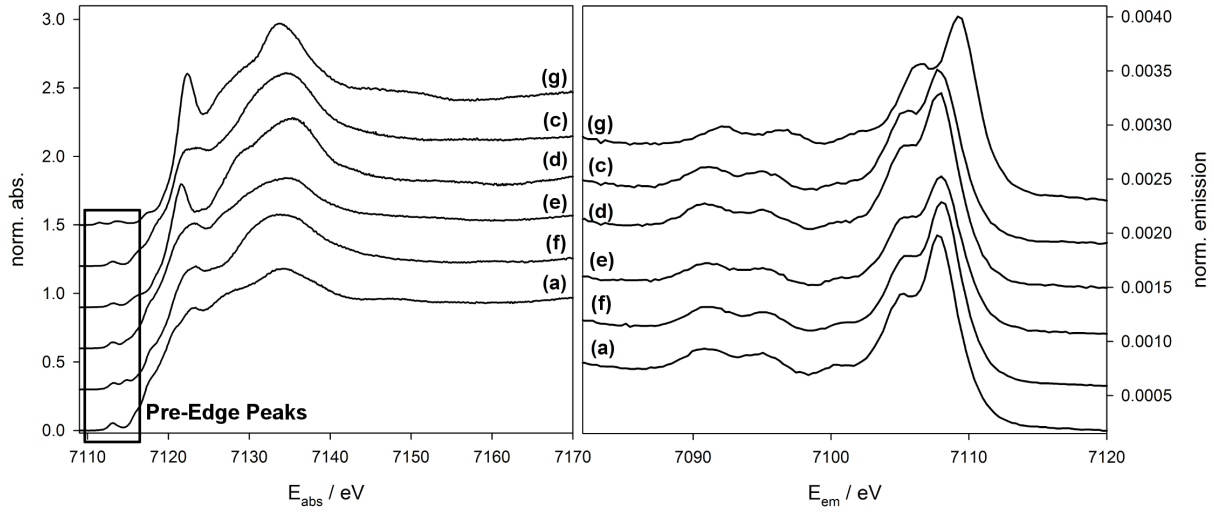

The differences observed in the HERFD-XANES spectra of the other complexes arise from perturbations of the e_{1g} orbital due to the presence of the substituent group as discussed in the previous section. In acetyl- and vinylferrocene, the anti-bonding π^*-orbital of the substituent interacts with one of the degenerate e_{1g} orbitals and splits it into two orbitals appearing at different energies. Consequently, two distinct peaks are observed in the pre-edge region. This assignment of the HERFD-XANES pre-edge peaks is shown in the upper part of figure 6.11 for ferrocene and vinylferrocene. With these results in mind, it can be expected that such substituents on the cyclopentadienyl rings will lead to significant perturbations of the occupied MOs as well.

The background-corrected experimental (left) and calculated V2C-XES spectra (right) of ferrocene (a) and the substituted ferrocenes (c)–(f) are compared in figure 6.12. For the experimental spectra, the deconvolution of the spectra is included in the figure. There are five peaks in the deconvolution of the experimental spectra, with those at higher energies (i.e., between ca. 7105 and 7108 eV) having the largest intensities. The positions, intensities, and widths of the peaks as

Figure 6.11.: Calculated pre-edge HERFD-XANES (top) (0.7 eV FWHM) and V2C-XES (bottom) (1.5 eV FWHM) spectra for ferrocene (left) and vinylferrocene (right). The calculated spectra are shown for both BP86 (black solid line) and B3LYP (blue dashed line). For the BP86 calculation, the individual transitions are included as red sticks. Alongside the calculated spectra, the corresponding MO diagrams, as obtained from a DFT calculation with the BP86 exchange–correlation functional, are shown. In the MO diagram of ferrocene, the orbitals belonging to the same irreducible representations as the dipole operator (e_{1u} and a_{2u}) are highlighted in blue, whereas the e_{1g} orbitals are highlighted in red. All other orbitals do not contribute significantly to the spectra and are shown in grey. The same colours are used for the corresponding orbitals in vinylferrocene.

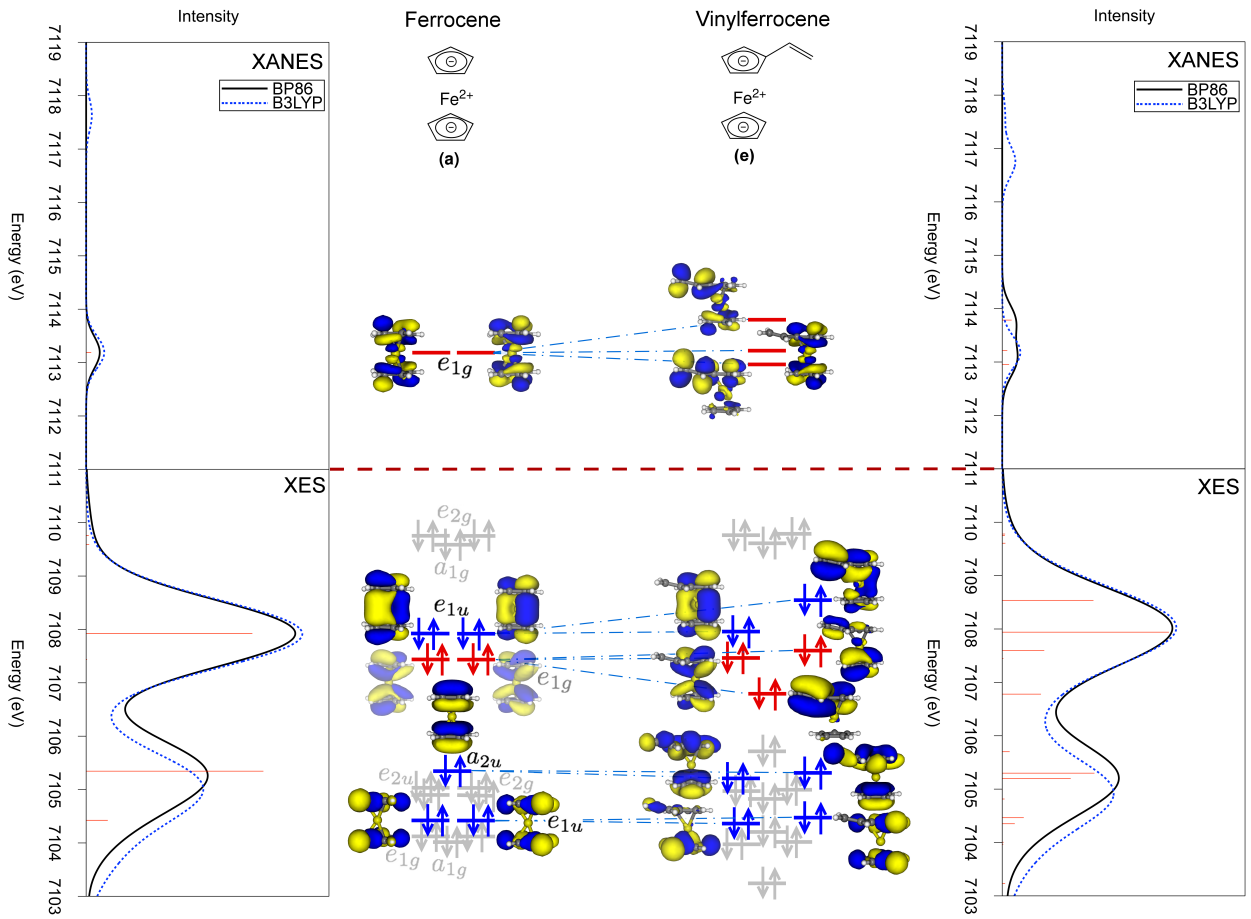

extracted from this deconvolution are listed in table 6.2. We note that for ferrocene our results are consistent with those of ref. [69], with some deviations for the peaks at lower energies, which can be attributed to the different procedures used for subtracting the tail of the Kβ main line. The two intense peaks at higher energy can be fitted with a FWHM of about 3 eV, while the peaks at lower energies are significantly broader and show a FWHM of up to 6 eV.

Comparing the experimental spectra in figure 6.12 (top left), there is no observable difference between the experimental spectra of ferrocene and the different substituted ferrocenes. This is confirmed when inspecting the positions and intensities extracted from the deconvolution given in table 6.2. For the two peaks at ca. 7105 and 7108 eV the differences in the peak position are in all cases below 0.2 eV, which is within the experimental uncertainty. Slightly larger shifts occur for the lower energy peaks in some cases, especially for the third peak. However, this peak is rather weak and the shifts might be artefacts of the deconvolution. The intensities are very similar for all (substituted) ferrocenes as well. For the substituted ferrocenes the intensity of the highest-energy peak is decreased by up to ca. 15 %, while the intensity differences are even smaller for all other peaks. Finally, difference spectra comparing the substituted ferrocenes (c)–(f) to ferrocene are included in figure 6.12 (bottom). In all cases, these difference spectra only show a negative feature at ca. 7108 eV, corresponding to the decrease of the intensity of this peak. However, the difference spectra show no indication for shifts of peaks or for a significant broadening of individual peaks.

The calculated V2C-XES spectra are included in figure 6.12 (top right) and show a good agreement with experiment. In particular, the intensity patterns are reproduced satisfactorily. This holds both for the calculations with the BP86 and with the B3LYP exchange–correlation functional. The only difference between the two functionals is a shift of the lower energy peaks. Comparing the calculated energies and intensities to those extracted by deconvoluting the experimental spectra (see table 6.2), this good agreement of theory and experiment is confirmed. For the positions of the peaks at lower energies, B3LYP provides a better agreement with errors below 0.3 eV, whereas BP86 overestimates the energies of these peaks by up to 1.5 eV. Nevertheless, both functionals agree for the relative intensities of all peaks, and for both functionals the calculated intensities match those extracted from the experimental spectra with errors below 10–15 %. The only exceptions are the intensities of the third peak at ca. 7101 eV, which are calculated significantly smaller than those extracted from the deconvolution of the spectra. This good agreement of the experimental and calculated spectra shows that the rather simple computational methodology applied here is adequate for an assignment of the V2C-XES spectra (see section 6.3.2).

To answer the question why the changes in the electronic structure due to substitution at the cyclopentadienyl ring are observable in HERFD-XANES but not in V2C-XES, we have to assign the V2C-XES spectra and relate the observed transitions to the underlying electronic structure. As a starting point, we consider the calculated spectrum of ferrocene, shown in figure 6.11 alongside the corresponding MO diagram. The two peaks at ca. 7108 eV and at ca. 7105 eV can be assigned to transitions from the occupied e_{1u} and a_{2u} orbitals, respectively, to the Fe 1s core orbital. These occupied e_{1u} and a_{2u} orbitals have the same symmetry as the dipole operator (i.e., they belong to the same irreducible representation) and the corresponding transitions are, therefore, dipole-allowed. They gain intensity through the admixture of Fe p-orbitals to the occupied e_{1u} and a_{2u} orbitals. For the second occupied e_{1u}-orbital, corresponding to a transition at 7104.4 eV, the Fe p-orbital contribution is negligible and the corresponding intensity almost vanishes. The occupied e_{1u} and a_{2u} orbitals, which correspond to these dipole-allowed transitions, are highlighted in blue in figure 6.11.

As discussed above, the occupied e_{1g} orbital is the only orbital in the considered energy range that has significant d-orbital contributions. However, the transition from the occupied e_{1g} orbital

Figure 6.12.: Experimental (left) and calculated (right) V2C-XES spectra (1.5 eV FWHM) for the (substituted) ferrocenes (a) and (c)-(f). For the experimental spectra, the tail of the Kβ main line has been subtracted, and the deconvolution of the experimental spectrum is also included. The V2C-XES spectra calculated with DFT are shown both for the BP86 (black solid lines) and the B3LYP (blue dashed line) exchange–correlation functionals. The bottom left spectra shows the experimental difference spectra using ferrocene as a reference.

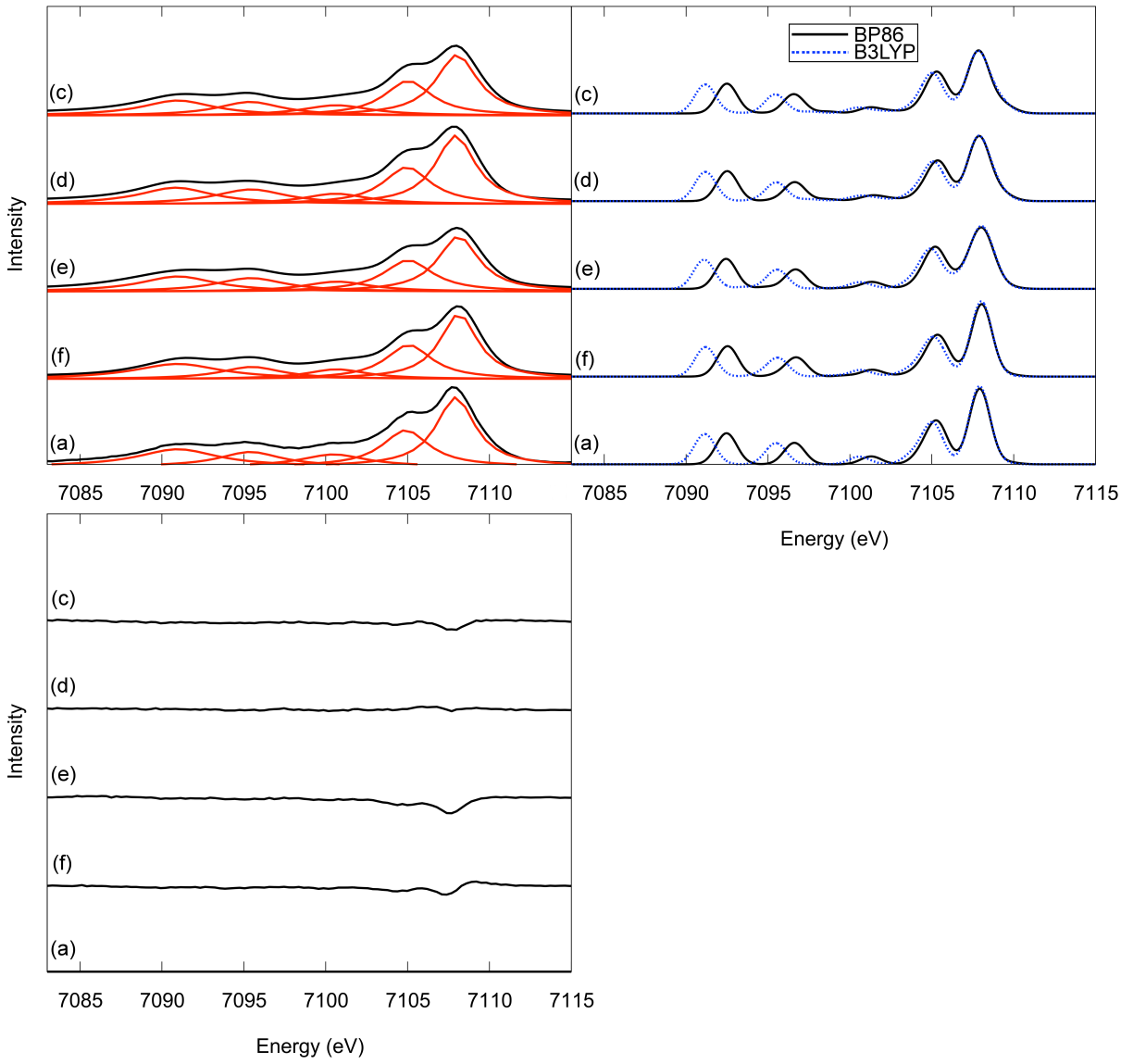

Table 6.2.: Energies (E_{rel}, in eV), intensities (Rel. Int.), and full width at half maximum (FWHM, in eV) extracted from the deconvolution of the experimental spectra compared to the energies and intensities predicted with DFT calculations using the BP86 and B3LYP exchange–correlation functionals. All energies are given as shifts relative to the highest energy peak in ferrocene at 7107.94 eV, and intensities are normalised to the one of this peak.

Complex	Experimental			DFT/BP86		DFT/B3LYP	
	E_{rel}	Rel. Int.	FWHM	E_{rel}	Rel. Int.	E_{rel}	Rel. Int.
(a) $Fe(Cp)_2$	0.00	1.00	2.87	0.00	1.00	0.00	1.00
	−3.05	0.63	3.45	−2.66	0.65	−2.91	0.63
	−7.44	0.29	4.83	−6.63	0.10	−7.34	0.10
	−12.54	0.34	4.60	−11.31	0.28	−12.44	0.27
	−16.96	0.51	5.90	−15.46	0.40	−16.78	0.38
(f) Fe(Cp)(CpAc)	0.20	0.91	2.78	0.12	0.96	0.11	0.97
	−2.86	0.58	3.42	−2.57	0.66	−2.84	0.64
	−7.25	0.22	4.56	−6.55	0.10	−7.29	0.09
	−12.42	0.28	4.52	−11.21	0.27	−12.35	0.26
	−16.91	0.44	5.91	−15.39	0.39	−16.73	0.37
(e) Fe(Cp)(CpVinyl)	0.17	0.84	3.02	0.10	1.02	0.11	1.02
	−2.99	0.57	3.62	−2.71	0.62	−3.00	0.59
	−7.22	0.25	5.01	−6.59	0.10	−7.31	0.09
	−12.51	0.35	5.19	−11.24	0.26	−12.37	0.25
	−16.95	0.42	5.55	−15.48	0.39	−16.82	0.37
(d) $Fe(CpPPh_2)_2$	−0.01	1.03	2.96	−0.03	0.98	−0.03	0.98
	−2.88	0.55	3.11	−2.56	0.63	−2.83	0.61
	−6.48	0.30	5.76	−6.46	0.10	−7.19	0.10
	−12.76	0.41	5.70	−11.29	0.26	−12.43	0.25
	−17.35	0.46	6.01	−15.41	0.39	−16.74	0.37
(c) $Fe(CpP^iPr_2)_2$	0.09	0.94	3.08	−0.07	0.99	−0.08	0.99
	−2.90	0.61	3.48	−2.62	0.61	−2.90	0.59
	−7.27	0.27	5.14	−6.63	0.11	−7.37	0.11
	−12.55	0.33	4.74	−11.35	0.25	−12.48	0.24
	−16.96	0.40	5.31	−15.43	0.38	−16.75	0.36

to the 1s core orbital is dipole-forbidden and thus only has quadrupole intensity. Consequently, it is orders of magnitude weaker than the dipole-allowed transitions from the occupied e_{1u} and a_{2u} orbitals. Nevertheless, by analogy with the corresponding unoccupied e_{1g} orbital probed in the HERFD-XANES spectra, the occupied e_{1g} orbital might also be sensitive to substitutions at the cyclopentadienyl ligands. Therefore, it is highlighted in red in figure 6.11. For all other occupied orbitals in this energy range the transitions to the Fe 1s core orbital are dipole forbidden and their intensities are negligible. These orbitals are shown in grey in figure 6.11. Note that the two peaks at lower energies (i.e., at ca. 7092.5 eV and at ca. 7096.5 eV) are due to transitions from cyclopentadienyl σ-orbitals and are not included in figure 6.11.

For the ferrocene derivatives featuring π-substituents at the cyclopentadienyl ring (i.e., acetyl- and vinylferrocene), we expect significant changes to the occupied MOs. First, we consider vinylferrocene (e), for which the HERFD-XANES (top) and V2C-XES (bottom) spectra are included in figure 6.11, alongside the corresponding MO diagram. In this MO diagram, we indicate the connection to the corresponding orbitals in ferrocene and use the same colours introduced above (i.e., orbitals corresponding to dipole-allowed transitions in ferrocene are shown in blue, whereas orbitals corresponding to quadrupole transitions in ferrocene are shown in red). The substitution at the cyclopentadienyl ring makes a large impact on all of the occupied orbitals and compared to ferrocene, all relevant orbitals are perturbed. First, the degeneracy of the e_{1u} orbitals is lost due to mixing with the substituent π-orbitals, and it is split into two orbitals separated by ca. 0.6 eV. Therefore, there are now two distinct transitions contributing to the highest energy peak in the V2C-XES spectrum, resulting in a slight broadening of the calculated peak. Second, the occupied a_{2u} orbital interacts with orbitals of the substituent and is split into two orbitals. However, the splitting is significantly smaller in this case, but none of these changes are observable in the spectrum because the occurring splitting of less than 1 eV is smaller than the resolution of the spectrum.

In the HERFD-XANES spectra, the sensitivity to the π-substituents is due to their effect on the unoccupied e_{1g} orbital. For the V2C-XES spectra, a similar splitting of the corresponding occupied e_{1g} orbital is found in the calculations. Indeed, the occupied e_{1g} orbital splits into two occupied orbitals in vinylferrocene and the resulting e_{1g}-like orbitals both have significant dipole intensity. These become observable as a contribution to the calculated spectra, but their intensity is still four times smaller than the one of the unperturbed e_{1u}-like orbital. Therefore, the e_{1u} peak dominates in this region and hides this splitting of the occupied e_{1g} orbital. The only change to the calculated spectrum is a slight broadening of the peak, which cannot be resolved in experiment.

Finally, we note that while for the calculation of the HERFD-XANES spectra we found that the splitting between the two unoccupied e_{1g}-like orbitals is extremely dependent on the choice of the functional, this is not the case of the corresponding occupied orbitals. Here, the splitting between the occupied e_{1g}-like orbitals calculated with BP86 and B3LYP only differ by approximately 0.1 eV.

For acetylferrocene (b), the second example of a ferrocene bearing a π-substituent at the cyclopentadienyl ring, a similar picture is obtained. The assignment of the calculated spectra to MOs is shown in figure 6.13. Here, the occupied orbitals introduced by the π-substituent appear at a lower energy and interact with the occupied a_{2u} orbital. This leads to a splitting of ca. 0.7 eV for the transition corresponding to the second peak (i.e., the one at ca. 7105 eV) in the V2C-XES spectrum, resulting in a slight broadening of this peak. However, as for vinylferrocene, this broadening is not resolved in the experimental spectrum. The occupied e_{1u} orbitals are only slightly affected (with a splitting smaller than 0.1 eV) and the quadrupole transition from the occupied e_{1g} orbital to the 1s core orbital does not gain significant dipole intensity by mixing with substituent

Figure 6.13.: Calculated pre-edge HERFD-XANES (top) (0.7 eV FWHM) and V2C-XES (bottom) (1.5 eV FWHM) spectra for acetylferrocene. The calculated spectra are shown for both BP86 (black solid line) and B3LYP (blue dashed line). For the BP86 calculation, the individual transitions are included as red sticks. Alongside the calculated spectra, the corresponding MO diagrams, as obtained from a DFT calculation with the BP86 exchange–correlation functional, are shown for both ferrocene and acetylferrocene.

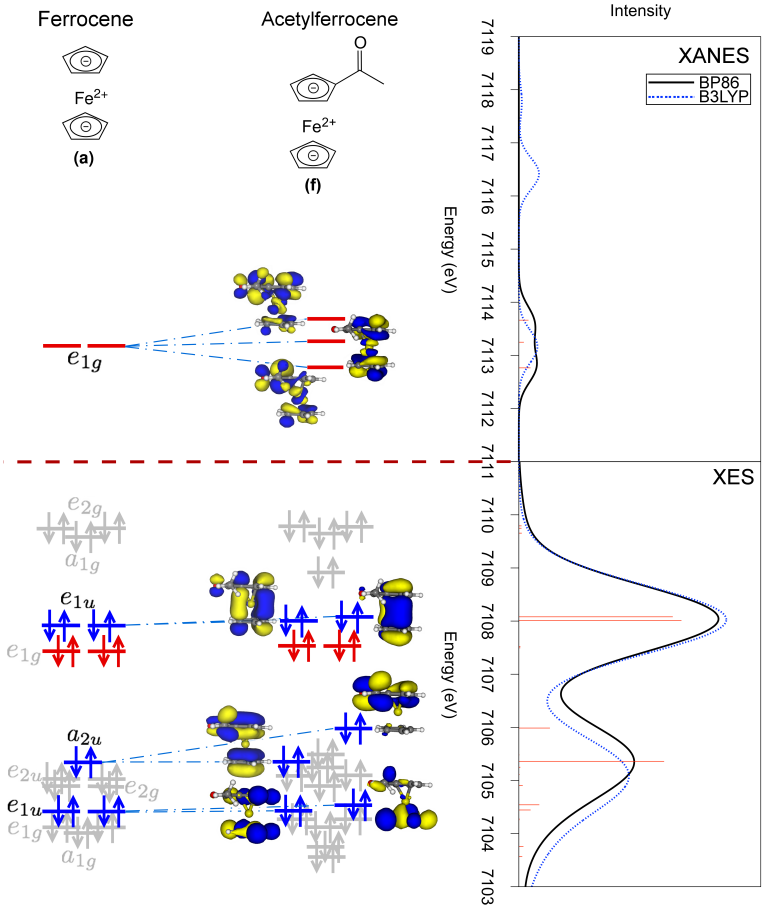

π-orbitals.

For $Fe(CpPPh_2)_2$ and $Fe(CpP^iPr_2)_2$, in which phosphine substituents have been introduced at the cyclopentadienyl rings, the pre-edge peaks in HERFD-XANES spectra are unchanged [108] (i.e., the substituent orbitals do not alter the unoccupied e_{1g} orbital significantly). The same observation can be made for the occupied orbitals probed in the V2C-XES spectra. For $Fe(CpP^iPr_2)_2$, the assignment of the calculated spectra is shown in figure 6.14. Here, the occupied orbitals corresponding to intense transitions in the V2C-XES spectrum appear at almost the same energies as in ferrocene. However, there are many additional occupied orbitals originating from the substituents. Some of these gain a small intensity by mixing with occupied orbitals with contributions at the iron atom, but these are small compared to the intense transitions from the occupied e_{1u}- and a_{2u}-like orbitals. For $Fe(CpPPh_2)_2$, there is an even larger number of occupied orbitals within the relevant energy range, but the overall picture is very similar and none of the additional occupied orbitals affects the V2C-XES spectrum.

Figure 6.14.: Calculated pre-edge HERFD-XANES (top) (0.7 eV FWHM) and V2C-XES (bottom) (1.5 eV FWHM) spectra for diisopropylferrocene. The calculated spectra are shown for both BP86 (black solid line) and for B3LYP (blue dashed line). For the BP86 calculation, the individual transitions are included as red sticks. Alongside the calculated spectra, the corresponding MO diagrams, as obtained from a DFT calculation with the BP86 exchange–correlation functional, are shown for both ferrocene and diisopropylferrocene.

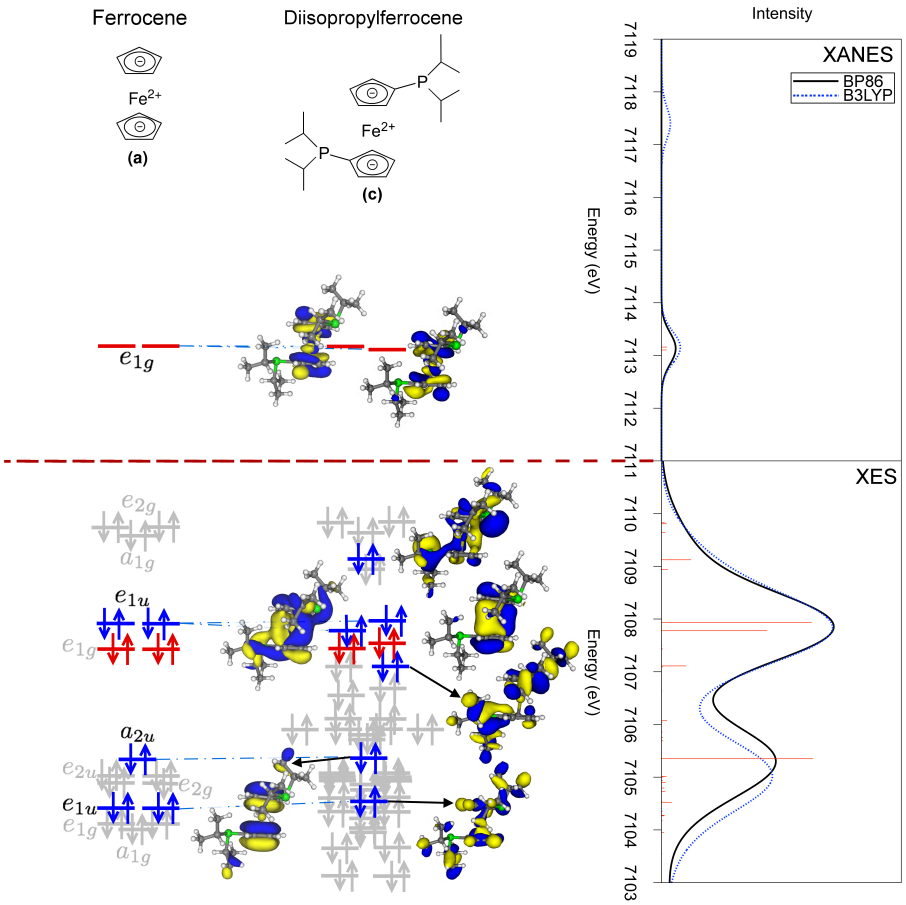

In summary, while for the examples considered here the substituents at the cyclopentadienyl ring(s) do affect the occupied orbitals, these differences cannot be resolved in the experimental V2C-XES spectra. In some cases, occupied orbitals that are degenerate in ferrocene are split, but the splitting is smaller than 0.6 eV. In other cases, in particular for the occupied e_{1g} orbital in vinylferrocene (corresponding to a quadrupole transition in ferrocene), the splitting is larger, but is hidden by more intense dipole-allowed transitions at similar energy.

To estimate the experimental resolution required to detect these differences, the calculated spectra plotted using different broadenings for the individual transitions are shown in figures 6.15 together with the corresponding difference spectra. With a FWHM of 3.0 eV, corresponding to the experimental spectra reported here, only a very small broadening of the most intense peak can be observed in the difference spectra. This becomes more pronounced when decreasing the FWHM, but only with a FWHM of 1.0 eV do indications for the splitting of some transitions appear in the difference spectra. Finally, for a FWHM of 0.5 eV these additional transitions can be identified as separate peaks in the calculated spectra.

Figure 6.15.: Calculated V2C-XES spectra plotted using Gaussian broadening with varying Full-Width Half-Maximum and the corresponding calculated difference spectra compared to ferrocene.

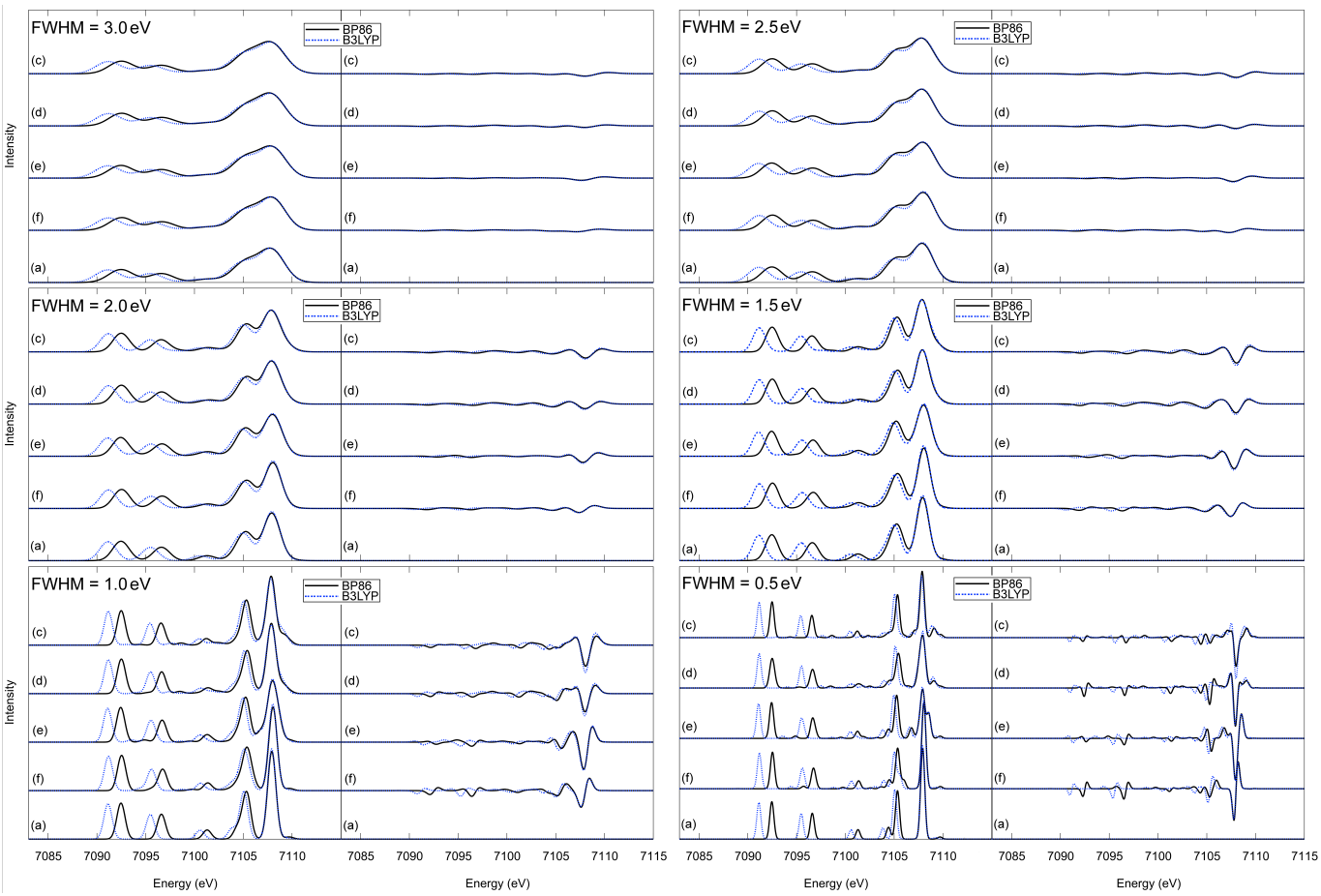

6.2. Conclusions

In conclusion, we could show how HERFD-XANES spectroscopy is able to reveal electronic transitions in the pre-edge peak region of K-edge XAS spectra, which are sensitive to substituents at the cyclopentadienyl ligand of ferrocene compounds. Application of the HERFD technique thus makes metal K-edge spectroscopy as sensitive to electronic changes as L-edge XAS, but using hard X-rays. We also considered the chemical sensitivity of the valence-to-core region of the XES spectra, with the aim of observing differences in the occupied orbitals comparable to those observed in the unoccupied orbitals in the HERFD-XANES spectra. While for HERFD-XANES, we have shown that the pre-edge peaks are sensitive to such changes, this is not the case for V2C-XES.

To understand this different chemical sensitivity, the experiments have been complemented with DFT calculations, which allow for an assignment of the transitions to molecular orbitals. For the calculation of V2C-XES spectra, the simple ΔDFT approach of ref. [137] already provides a good agreement with experiment. In contrast to the TD-DFT calculations of the HERFD-XANES spectra, these calculations are less sensitive to the choice of the exchange–correlation functional and the calculations are in quantitative agreement with experiment. On the other hand, the calculations of the HERFD-XANES spectra do not provide a quantitative agreement with experiment. Nevertheless, they still allow for a reliable assignment of the observed pre-edge peaks and make it possible to identify the unoccupied molecular orbitals probed by these transitions.

The pre-edge peaks in HERFD-XANES can be assigned as dipole-forbidden transitions to unoccupied d-orbitals. In particular, for the LUMO in ferrocene, one of the degenerate e_{1g} orbital splits into two e_{1g}-like orbitals in acetyl- and vinylferrocene because of mixing with the substituent's π-orbitals. On the other hand, the V2C-XES spectra are dominated by dipole-allowed transitions originating from occupied ligand orbitals, with small Fe p-orbital contributions. These orbitals are less affected by substituents beyond the first coordination shell. Even though a splitting of the occupied e_{1g} orbital occurs due to substitution with an acetyl or vinyl group, it is not observable in the V2C-XES spectra. The increased intensity of the split e_{1g}-like orbitals are still significantly smaller than the dipole-allowed transition corresponding to the unperturbed e_{1u}-like orbital.

For resolving the differences in the occupied orbitals caused by substitutions beyond the first coordination shell, it would be necessary to increase the resolution of experimental V2C-XES spectra. In principle, this would be possible by using analyser crystals with a higher intrinsic resolution due to applied Bragg reflection, but at the price of reduced flux. However, even in this case, the lifetime broadening of the $1s$ core hole would still limit the experimental resolution. Since in HERFD-XANES the lifetime broadening of the $1s$ core hole is removed to a large extent, the resolution of V2C-XES would always be less than in HERFD-XANES.

While the specific results discussed here apply only to the considered example of substituted ferrocenes, we expect some observations to be more general. First, the pre-edge region in K-edge XAS spectra of transition metal complexes contains in most cases only the dipole-forbidden transitions to metal d-orbitals. These will in general be very sensitive to substitution, both for directly coordinated ligands and possibly also beyond the first coordination shell. Therefore, with the possibility to resolve such subtle changes in these orbitals, with HERFD-XANES, these measurements provide a very sensitive analytical tool. On the other hand, the V2C-XES spectra are dominated by dipole-allowed transitions originating from orbitals with contributions from metal p-orbitals. Thus, changes in occupied metal d-orbitals will hardly be detectable because the corresponding transitions are much weaker. We note that a smaller sensitivity of XES compared to XAS to structural changes has also been observed for the nitrogen K-edge of alanine peptides

in solution [266].

To conclude, we have shown that HERFD-XANES provides a probe sensitive enough to determine changes within the electronic structure due to substitutions in the second coordination sphere and that combining the experiment with TD-DFT calculations an understanding of these changes within the electronic structure can be reached. However, the V2C region of XES cannot distinguish these changes in the electronic structure due to substitution in the second coordination shell, at least for the substituted ferrocenes considered here.

Thus the sensitivity of the pre-edge in HERFD-XANES provides unique opportunities for studying the electronic structure of transition metal complexes and for overcoming the current limitations of XAS. Therefore it can be considered as a tool of very high potential for the element specific in situ investigation of substituent effects at coordinating ligands on the electronic structure of transition-metal complexes. Even though V2C-XES is less sensitive to changes in the second coordination shell, it provides information on the occupied electronic states. In this respect it is, therefore, complementary to HERFD-XANES. Moreover, V2C-XES can still be a useful tool for distinguishing different oxidation states of transition metal centres, as shown here for ferrocene and ferrocenium, and for determining the identity and geometrical arrangement of the ligands in the first coordination shell. Therefore, both HERFD-XANES and V2C-XES can help provide explanations of catalytic activity, with HERFD-XANES providing these at the electronic level.

6.3. Methodology

6.3.1. Experimental

The HERFD-XANES and V2C-XES experiments were performed by Matthias Bauer (TU Kaiserslautern) at beamline ID26 at the European Synchrotron Radiation Facility [267]. For a detailed description of the methodology used (experimental set up, measurement procedures, etc.), please see the supporting information of reference [108] for the HERFD-XANES measurements and the methods section of reference [268] for the V2C-XES measurements.

6.3.2. Computational

Geometry optimisations of the molecular complexes were performed with the quantum chemical program package ADF2010.01 [122,269,270] using the density functional BP86 [130,151] with the TZP basis set. For complexes where different stable conformers exist, all were optimised and the lowest energy structures were used for the following calculations. For all considered compounds, the ground-state is the low-spin state ($S = 0$). For the lowest energy conformations see figure 6.5.

Calculated XAS spectra always refer to these lowest energy structures, but almost identical results are obtained for the other possible conformers. The XANES spectra are then calculated for these structures with the ORCA program package [201] and the ADF2012 program package [122, 204, 270] using time-dependent density functional theory (TD-DFT). Within ORCA, Ahlrichs' def2-QZVPP basis set [209] was used, while within ADF the QZ4P Slater-type orbital basis set was utilised. The results presented in section 6.1.2 are obtained with ORCA, whereas the results in section 6.1.3 are obtained with ADF. To judge the sensitivity of our results to the exchange correlation functional, we employed both the BP86 non-hybrid functional [130, 151] and the B3LYP hybrid functional [158, 159]. To selectively target core excitations, the TD-DFT

calculations were restricted to excitations originating from the Fe 1s orbital (restricted-channel approximation) [123, 124, 184]. Such restricted-channel TD-DFT calculations have been applied extensively for K-edge XAS spectra of transition metal complexes [107, 116, 186, 245, 271, 272].

However, TD-DFT systematically underestimates the excitation energies of core excitations [184]. Therefore, for comparison with experiment the energy scale must be shifted. In ORCA the shifts are 181.97 eV and 151.08 eV and in ADF the shifts are 183.39 eV and 152.62 eV for the BP86 and B3LYP functionals, respectively. These shifts are chosen such that the energy of the pre-edge peak in ferrocene agrees with experiment. While these shifts are rather large, they do not affect the relative position of the peaks. For Fe K-edge XAS, it has been demonstrated previously that despite the large absolute errors, the selective TD-DFT approach used here can provide relative excitation energies and intensities with an accuracy that allows for a direct comparison with experiment [184]. The relative excitation energies are determined by the valence orbitals and, therefore, not affected significantly by errors in the description of the core orbital. The largest part of the shift in the absolute excitation energies is due to the neglect of relativistic effects for the 1s core orbital. Including scalar relativistic effects, in the ADF calculations, with the zeroth-order regular approximation (ZORA) [132, 133] reduces the shifts to 58.84 eV for BP86 and to 27.51 eV for B3LYP, but does not change the overall spectra.

With the BP86 non-hybrid functional, all relevant excitations are transitions from the Fe 1s orbital to a single unoccupied orbital. In this case, these orbitals are shown in figure 6.9. With the B3LYP hybrid functionals, some excitations are combinations of several such transitions. In these cases, figure 6.9 shows the corresponding linear combination of unoccupied orbitals. This is possible here because all excitations originate from the Fe 1s orbitals. All orbital isosurface plots in figures 6.6, 6.9, 6.11, 6.13 and 6.14 were prepared with Molekel [273] and use an isosurface value of +/- 0.025 atomic units.

For the calculation of XES spectra we use the ADF2012 program package [122, 204, 270] and we follow the work of Lee et al. [137] (see also refs. [170–172] and references therein for earlier work). This is a frozen orbital, one-electron ΔDFT approach which uses orbital energy differences between occupied orbitals, $\epsilon_{1s} - \epsilon_i$, to model the X-ray emission energies. Even though it is the simplest possible approximation for the calculation of XES spectra, it has been shown to work reliably for V2C-XES spectra of transition metal complexes [67–69, 116, 137, 172]. We employed the QZ4P basis set and used both the non-hybrid exchange–correlation functional BP86 and the hybrid functional B3LYP.

The calculated V2C-XES spectra were shifted by 182.86 eV and 148.82 eV for BP86 and B3LYP, respectively, where these shifts are chosen such that the energy of the highest energy V2C-XES peak in ferrocene agrees with experiment. As discussed above for the XAS spectra, the largest contributions to these shifts originate from the neglect of relativistic effects, the neglect of core-hole relaxation, and the errors in the exchange–correlation functional. If scalar-relativistic corrections are included via the ZORA approximation, the shifts are reduced to 58.36 eV for BP86 and 23.79 eV for B3LYP, but the overall V2C-XES spectra do not change.

For calculating the intensities in ADF of both the XANES and V2C-XES spectra, we adopted the origin-independent approach described in chapter 3. However, for the V2C-XES spectra the initial and final state in the transition moments are now the Fe 1s core orbital and the other occupied orbitals. However, in ORCA this method for the oscillator strengths is not implemented and only the electric-quadrupole and magnetic-dipole contributions are calculated. These contributions are origin-dependent. Therefore, to address this problem, Neese and co-workers proposed to choose the origin such that the sum of quadrupole and magnetic dipole contribution is minimised [107]. However, we found that in cases where the dipole contribution is non-zero, but very small compared

to the quadrupole contribution, this procedure places the origin far away from the molecule, which is not physically reasonable as it leads to a very slow convergence of the multipole expansion. Therefore, we placed the origin at the iron atom in all our calculations and used the non-origin adjusted results given by ORCA.

7. X-ray Absorption Spectroscopy of Iron Carbonyl Complexes

Transition metal carbonyls play an important role in many scientific areas. The binding of CO to enzymatic centres is often crucial in their biological activity [274] and they also play an important role in catalytic processes such as the Fischer-Tropsch process [275–279]. These processes are often not based on iron, even though the Fischer-Tropsch process has been documented to occur with iron [280, 281]. Nevertheless, iron carbonyl complexes are of interest and several studies look into their catalytic properties [282–286]. Such work is mostly motivated by the desire to replace expensive catalysts based on rare elements such as ruthenium or platinum by cheap iron catalysts. Most of these catalytic reactions are due to the ease of the (photo-)dissociation of a carbonyl ligand in the iron carbonyl complexes [285–287]. Due to their importance they have also been studied spectroscopically [286, 288].

The transition metal carbonyl complexes are also important from a different perspective. They are a text-book example in inorganic chemistry for transition metal complexes obeying the 18 electron rule. The metal centre(s) coordinates to a set of ligands which will provide enough electrons to fill the valence shell [7]. Therefore, they also provide a basis for introducing the concept of metal-metal bonding, which may occur upon an incomplete valence shell [6, 8]. We can understand and interpret many properties of complexes through their electronic structure. In the simplest case this is expressed through the use of and molecular orbital diagrams. Experimentally, electronic spectroscopy offers a method of probing the electronic structure. Specifically, X-ray spectroscopy offers a local probe of the electronic structure, with X-ray absorption probing the unoccupied electronic states and X-ray emission probing the occupied electronic states.

However, high-energy electronic spectroscopy has been mostly neglected with regards to iron carbonyl complexes. X-ray absorption measurements, widely used in catalyst characterisation, are also sparse in the literature, with only a few examples in the last years [239, 289–292]. Though these papers report X-ray spectra, their primary purpose is not the investigation of the spectra themselves but the spectra are used to answer a different question, such as the cause of dark channels in the measured spectra in solution [239] or to follow reaction dynamics [289].

Here, we will investigate the HERFD-XANES spectra with regards to their interpretation and the presence of any correspondence in the spectra between the different iron carbonyl complexes. HERFD-XANES is used due to its high-resolution which provides a more detailed pre-edge structure and therefore, as shown in chapter 6, more information on the electronic structure of the complexes. For this we will use a test set of five iron carbonyl complexes consisting of iron pentacarbonyl, diiron nonacarbonyl, triiron dodecacarbonyl, iron tricarbonyl cyclooctadiene and diiron tetracarbonyl dicyclopentadiene for which the Lewis structures are shown in figure 7.1. These experimental spectra were measured by Matthias Bauer (TU Kaiserslautern).

Before we go any further, we review results from calculations already published for the iron carbonyls. Fronzoni et al. published calculations of the X-ray absorption spectra for a series of transition metal complexes, which included $Fe(CO)_5$. They used CIS to calculate the transition

Figure 7.1.: Lewis structures of the five iron carbonyl complexes considered in this work. a) $Fe(CO)_5$, b) $Fe_2(CO)_9$, c) $Fe_3(CO)_{12}$, d) $Fe_2(CO)_4Cp_2$ and e) $Fe(CO)_3C_8H_{12}$

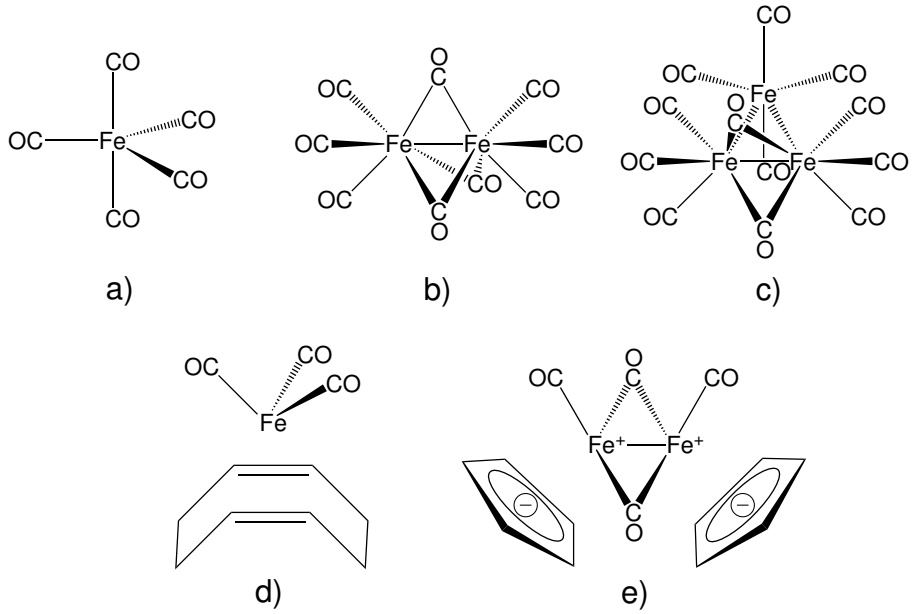

energies and employed the dipole approximation for the intensities [293]. However, as previously mentioned in chapter 3, the dipole approximation is usually not sufficient for the calculation of K-edge transition metal spectra where $1s \rightarrow 3d$ transitions are observed. Therefore, these results may not include all relevant excitations for the interpretation of the X-ray absorption spectra at the K-edge. Also multiple scattering calculations have been performed for comparison to experimental spectra [291, 292].

Though the literature available on the calculation of X-ray absorption spectroscopy is limited, many computational studies consider iron carbonyl complexes. For $Fe(CO)_5$, there are has been interest in its molecular structure and the accuracy of available methods in reproducing the structure from X-ray diffraction experiments [294, 295]. However, there are not many papers considering the electronic structure, but reference [296] used computations to help understand several properties of $Fe(CO)_5$. Compared to $Fe(CO)_5$, the literature available on the bi- and triiron carbonyl complexes is extensive. Once again a lot of studies focus on the molecular structure of $Fe_2(CO)_9$ [180, 294, 297, 298] as well as its photodissociation [180]. The interest in the molecular structure largely stems from the question of whether or not a metal-metal bond exists between the two iron centers [299–302]. Within many of these studies the calculated electronic structure of $Fe_2(CO)_9$ is used to aid in the determination. Finally, $Fe_3(CO)_{12}$ has been studied extensively in terms of its molecular structure, both experimentally [303–306] and theoretically [294, 295, 297, 307, 308]. As in the case of $Fe_2(CO)_9$, many of the theoretical studies also consider the underlying electronic structure of the metal cluster to aid in understanding the bonding characteristics.

As mentioned earlier, we will also consider two substituted iron carbonyl complexes. Substituted iron carbonyl complexes are considered important for studying interactions between two reactive metal sites [309] as well as altering reactivity [310, 311]. Therefore, the literature available on the character of substituted iron carbonyl complexes is extensive [310–314]. Nevertheless, the substituted iron complexes presented here are not commonly considered in literature [309,315–318].

In the first section of this chapter we will discuss the electronic structure and HERFD-XANES spectrum of $Fe(CO)_5$ and use TD-DFT calculations to interpret the spectrum. The second section considers the HERFD-XANES spectra of the bi- and trimetallic iron carbonyl systems along with their interpretation using TD-DFT calculations. The third section discusses the substituted iron complexes and the interpretation of their HERFD-XANES spectra. Finally, we present the conclusions. The computational methods used within this work is given at the end of this chapter.

7.1. Revisiting the Electronic Structure of $Fe(CO)_5$

First, we consider the simplest iron carbonyl complex $Fe(CO)_5$, which has a trigonal bipyramidal structure with D_{3h} symmetry. As a starting point for the discussion of $Fe(CO)_5$, we will consider a schematic representation of its molecular orbital (MO) diagram, see figure 7.2. In the D_{3h} point group the d-orbitals of the iron atom belong to three irreducible representations (irreps). The iron d_{z^2} orbital belongs to the totally symmetric A_1' irrep, whereas the d_{xy}, $d_{x^2-y^2}$ and d_{xz}, d_{yz} pairs belong to the two degenerate irreps E' and E'', respectively. These combine with the carbonyl ligand orbitals of the same symmetry. The carbonyl σ-orbitals belong to the irreps $2A_1'$, A_2'' and E'', whilst the carbonyl π-orbitals belong to the irreps A_2', A_2'', $2E'$ and $2E''$. From these we can expect the A_1' d-orbital to interact with the A_1' σ carbonyl orbitals. The A_1' carbonyl orbitals are composed of the σ-bonding orbitals that are formed by the p-orbitals pointing along the carbonyl bond axes. These interact with the iron d_{z^2} orbital to form a bonding and an anti-bonding

combination of ligand and metal orbitals with A_1' symmetry. The E'' d-orbitals will interact with only the E'' π-orbitals of the carbonyls, whereas the E' d-orbitals can interact with both σ and π carbonyl orbitals as they both have orbital combinations with the correct symmetry. This can be seen in the unoccupied orbitals of the E' symmetry in figure 7.2 where there is some minor inclusion of a σ carbonyl orbital on the carbonyl ligand with no π contributions, whereas all other carbonyl ligand orbitals are the π-orbitals. Using the character table we can determine whether an X-ray transition from the iron $1s$ to these orbitals will have dipole or quadrupole intensity. Transitions to the A_1' and E'' MOs are only quadrupole allowed, whereas those to E' MO's are both quadrupole and dipole allowed.

Figure 7.2.: A schematic molecular orbital diagram of $Fe(CO)_5$ constructed from density functional calculations. (Isosurface plots of the orbitals have been obtained with BP86, but the unoccupied orbitals are arranged in the energetical order in which they appear within the B3LYP calculations.

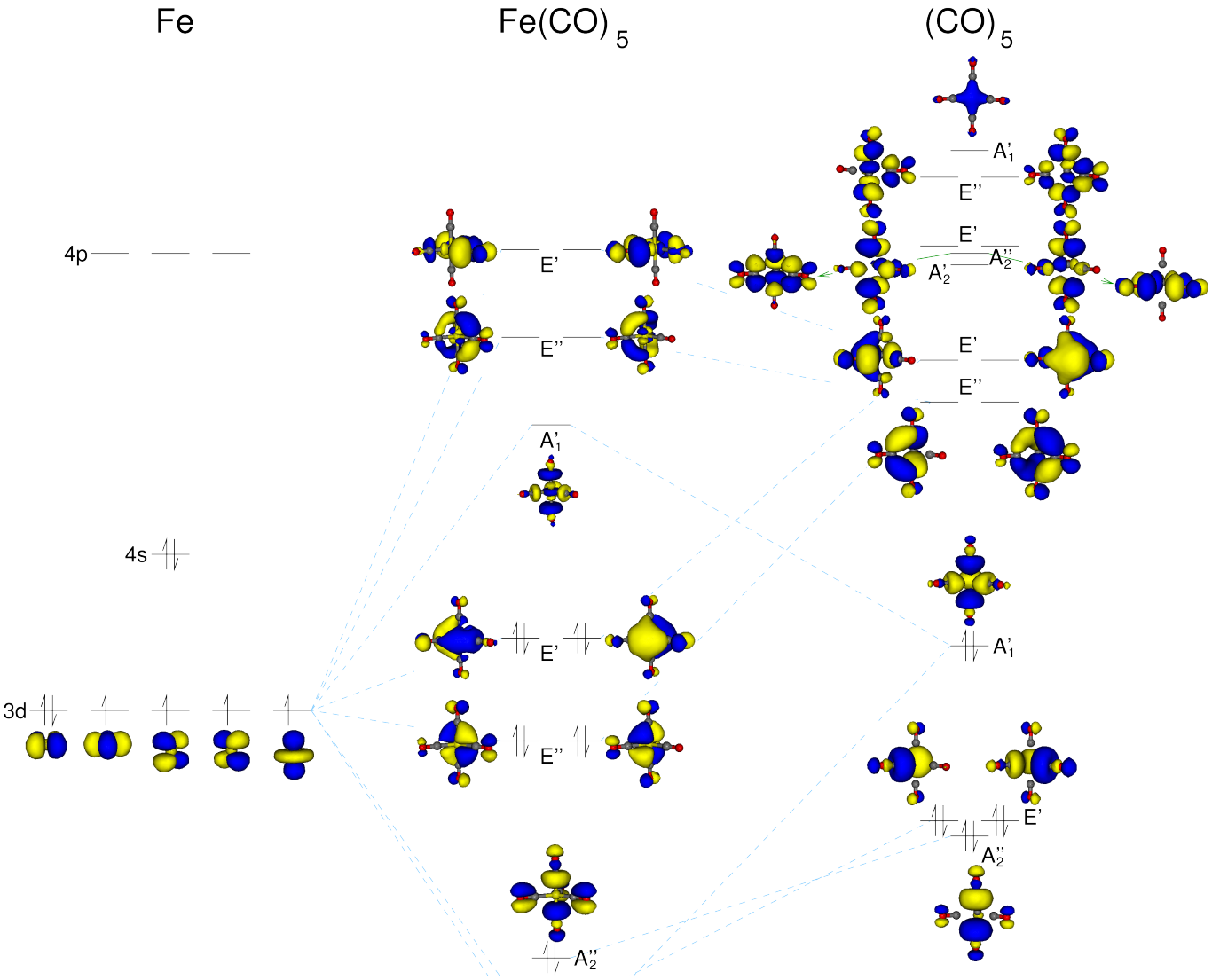

The first five unoccupied orbitals contain all five d-orbitals of the iron atom and will be the main contributors to the pre-edge spectra at the iron K-edge. Figure 7.3a contains both the calculated and experimental spectra of $Fe(CO)_5$. Therein, the experimental spectrum has three distinct

peaks, labeled A, B and C. Previous experimental X-ray absorption spectra of $Fe(CO)_5$ at the K-edge of iron show only one peak in the pre-edge spectra [239, 289]. This clearly shows that the use of HERFD-XANES reveals more detail in the experimental spectra. Within the experimental spectra we can assign both peaks A and B to the pre-edge. However, peak C, with a significant increase in intensity compared to peaks A and B, is most likely due to dipole-allowed transitions to Rydberg states.

Now we turn our attention to the calculated spectra. Qualitatively, BP86 provides a spectrum with one intense peak and B3LYP provides a spectrum with three distinct features with lower intensities. Therefore, (qualitatively) we can conclude that the B3LYP exchange–correlation functional provides results that are more accurate to the experimental spectrum for this complex. To further understand the differences between BP86 and B3LYP we must consider the transitions that make up the spectra. The peak in the BP86 spectrum contains twelve contributing transitions lying very close together. If we were to consider an MO diagram constructed solely from the BP86 calculation the ordering of the MO's would be different to that shown in figure 7.2, with the lowest energy MO being the E'' followed by the A_1' and then several orbitals later the E'. However, the energy difference between the two lowest energy orbitals is smaller than 0.1 eV and the difference between the first and last orbital is only 2.3 eV. Thus, once broadening of the peak due to the core hole lifetime is taken into account we only see the one peak in the calculated spectrum.

The peaks in the B3LYP spectrum are well separated with the contributions to each peak well defined. The lowest energy transition is to the A_1' orbitals followed by transitions to the two degenerate representations E'' and E'. The distinct peaks can be attributed to the energy separation of the transitions with the difference between A_1' and E'' being 1.7 eV and the difference between the first and last transition being 5.4 eV.

Peak A in the B3LYP spectrum consists of transitions to the anti-bonding A_1' orbital composed of the iron d_{z^2} orbital and the carbonyl σ-orbitals. Peak B contains the transitions to both degenerate symmetry representations E'' and E' (in that order), respectively, containing the other four d-orbitals of the iron atom. The isosurface plots of the (combinations of unoccupied) orbitals observed in these peaks are shown in figure 7.4. These agree with the unoccupied orbitals obtained with BP86 (shown in the MO diagram in figure 7.2). However, as the spectrum obtained with B3LYP shows a better agreement with experiment, the orbital ordering extracted from the B3LYP spectrum has been used in the MO diagram of figure 7.2. Table 7.1 shows the dipole and quadrupole contributions to the intensities of the transitions, separated into the transitions that contribute to the peaks. We can see that the contributions for $Fe(CO)_5$ follow what is expected from symmetry considerations: Peak A (A_1') is composed entirely of quadrupole intensity and peak B (E'' and E') has a small dipole contribution due to the transition into the E' orbitals.

7.2. Bi- and Trinuclear Iron Carbonyls $Fe_2(CO)_9$ and $Fe_3(CO)_{12}$

For $Fe_2(CO)_9$, the experimental and calculated spectra are shown in figure 7.3b. There are three observable features in the experimental spectrum labelled A, B and C. Previously published K-edge spectra for $Fe_2(CO)_9$ show only one distinct peak in the pre-edge spectrum, again showing the capability of HERFD-XANES. Within the experimental spectra we can assign both peaks A and B to the pre-edge. However, peak C is once again most likely due to transitions to Rydberg states. Therefore, we will focus on peaks A and B in the following. If we compare the spectrum to the one of $Fe(CO)_5$, we immediately see that the pre-edge features have a much higher intensity

Figure 7.3.: X-ray absorption spectra of $Fe(CO)_5$, $Fe_2(CO)_9$ and $Fe_3(CO)_{12}$ calculated with the BP86 and B3LYP exchange–correlation functionals and the experimental results. For the calculated spectra the blue vertical line indicates the ionisation threshold (i.e. the negative of the energy of the 1s core orbital).

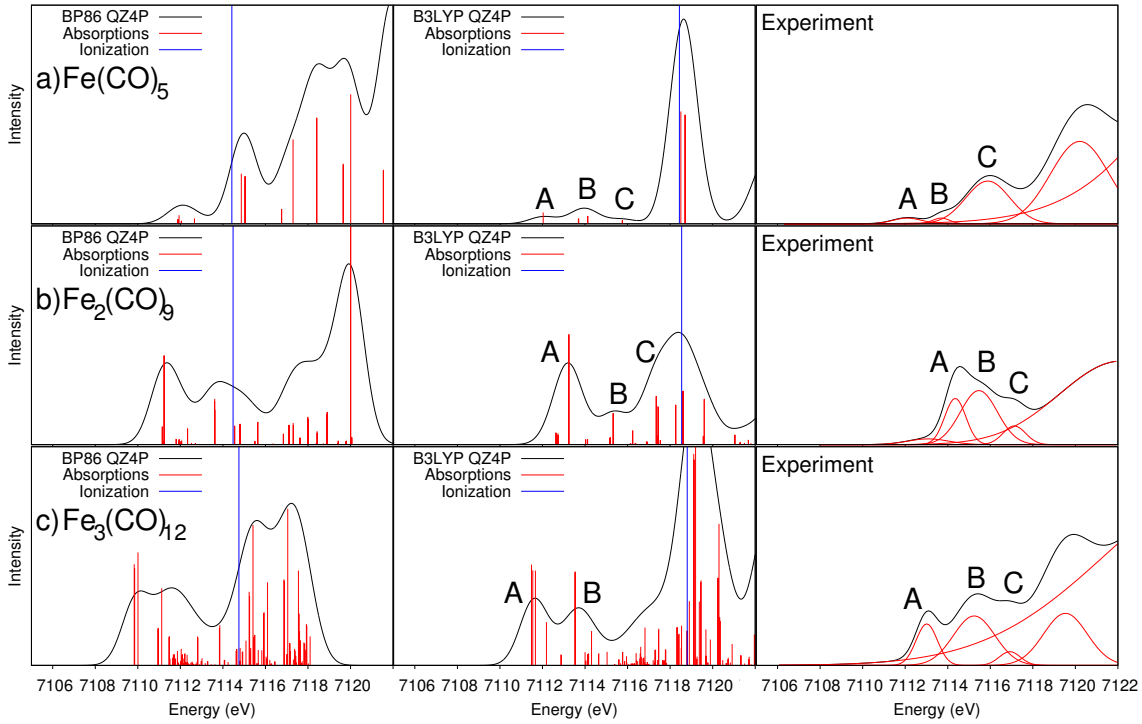

Table 7.1.: The percentage of dipole and quadrupole contributions to the transition intensity for the most intense transitrions in the calculated B3LYP spectra.

Complex	Peak	%Dipole	%Quadrupole
a) $Fe(CO)_5$	A	0.0	100.0
	B-1	0.0	100.0
	B-2	25.2	74.8
b) $Fe_2(CO)_9$	A	96.3	3.7
	B	100.0	0.0
c) $Fe_3(CO)_{12}$	A-1	92.7	7.3
	A-2	78.0	22.0
	B-1	95.4	4.6
	B-2	88.8	11.2
d) $Fe(CO)_3C_8H_{12}$	A	87.1	12.9
e) $Fe_2(CO)_4Cp_2$	A-1	82.6	17.4
	A-2	96.0	4.0
	B-1	97.6	2.4
	B-2	91.5	8.5

Figure 7.4.: Isosurface plots of the unoccupied orbitals probed by the pre-edge transitions as obtained from TD-DFT calculations with B3LYP/QZ4P, separated and sorted into the peaks they contribute to for $Fe(CO)_5$, $Fe_2(CO)_9$ and $Fe_3(CO)_{12}$. All plots shown are linear combinations of orbital contributions (see Computational Methodology). Only the unoccupied orbitals corresponding to the major contributions to the peak intensity are shown here. Shown below the unoccupied orbitals are the isolated iron orbital contributions to them, in which only the part of the orbitals that is within a radius of 1 Å around the iron atoms is included. The coloured dots indicate the iron atom (1*s* orbital) from which the transition originates.

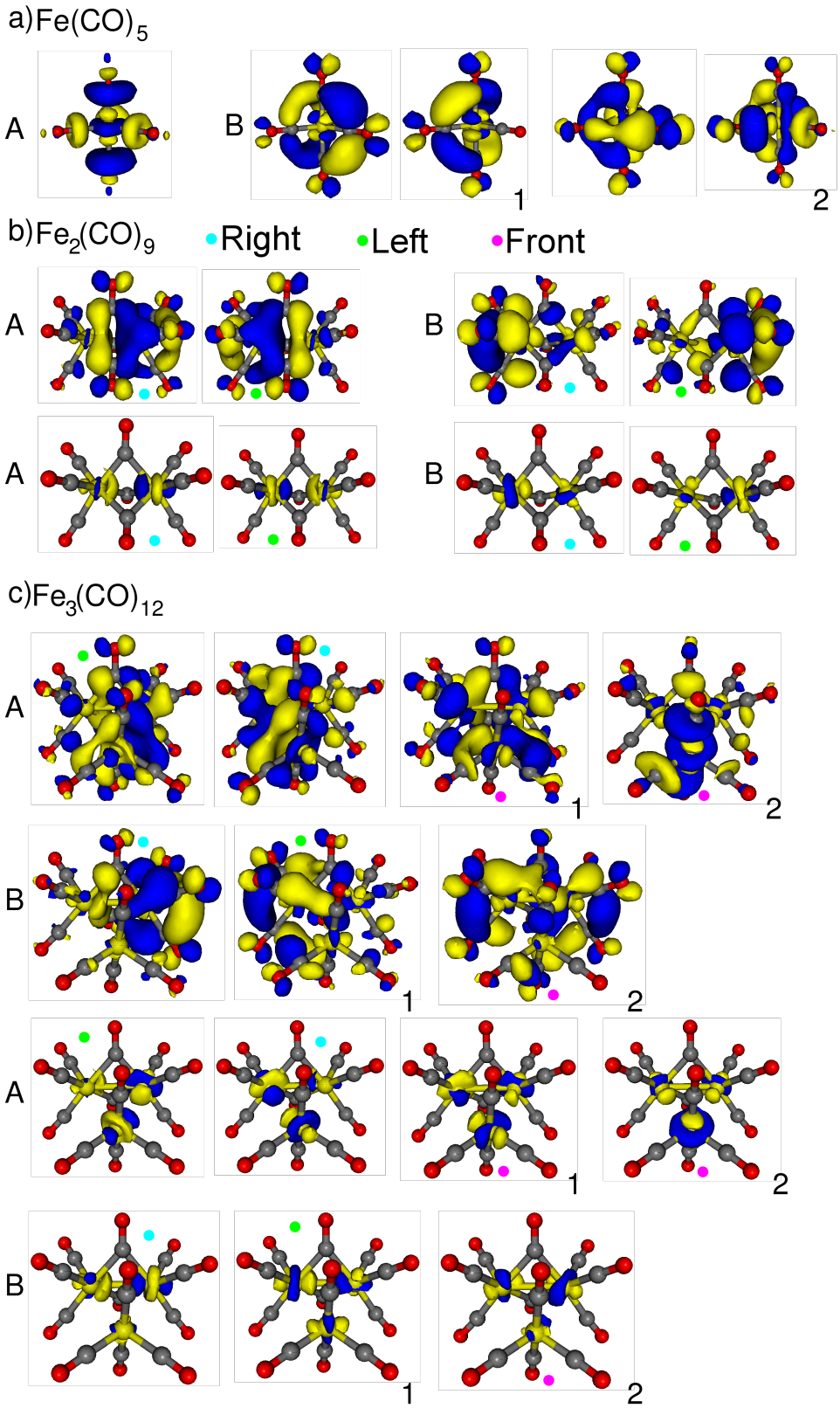

and that all three peaks are shifted to higher energies.

First, we compare the spectra calculated with both the BP86 and B3LYP exchange–correlation functionals. BP86 calculates a spectrum with only two distinct features before the ionisation threshold, whereas B3LYP calculates three distinct features, which correlates more accurately with what is observed in experiment. Therefore, we will only discuss the B3LYP results in the following. The isosurface plots of the (combination of) unoccupied orbitals that are probed with a significant intensity contribution are plotted in figure 7.4. To highlight the contributions of the iron orbitals, figure 7.4 also includes isosurface plots that only cover a radius of 1 Å around the iron atoms. These plots show that peak A is comprised of transitions to the anti-bonding σ^*-orbital of the metal-metal bond, which is composed of the d_{z^2} iron orbitals. The two excitations are an excitation from each core orbital to a combination of unoccupied orbitals. Both $Fe(CO)_5$ and $Fe_2(CO)_9$ have the same point group and the major transitions is to an orbital with the major iron contribution being the iron d_{z^2} orbitals. Thus, why is peak A in $Fe_2(CO)_9$ shifted to higher energies and why does it have a much larger intensity than its counterpart in $Fe(CO)_5$? The main reason for the large increase in intensity is that even though the molecular point group is the same, the symmetry of the iron centres has been reduced. In $Fe_2(CO)_9$ neither lie in the horizontal mirror plane and the lowest energy d_{z^2} combination belongs to the A_2'' irrep. Therefore, the corresponding transition becomes dipole-allowed. This is seen in table 7.1, where for the transitions in peak A mostly dipole contributions to the intensity are seen. The change in energy of the peak can be rationalised by a combination of factors: In $Fe_2(CO)_9$ the d_{z^2} orbitals now interact with the π^* ligand orbitals, which pushes it to higher energies. At the same time the change in the ligand field of the iron centre from a pentagonal bipyramidal to an octahedral ligand field (where the d_{z^2} is not involved in the bonding of the ligands) lowers the energy. In addition, the interaction of the two d_{z^2} orbitals from the iron centres increased the energy of the transition to the anti-bonding d_{z^2}-d_{z^2} orbital.

Peak B has a more complicated assignment. From the isosurface plots in figure 7.4 we can see that one of the iron atom orbitals is a d_{z^2} and the other belongs to the degenerate pair of d_{xz} and d_{yz} iron orbitals. The second transition is a mirror image of the first with the phase of the d_{z^2} reversed. The transitions originate from the iron atom upon which the $d_{xz/yz}$-like orbital resides. Therefore, this can be considered a linear combination of transitions which occur from both the A and B peaks of $Fe(CO)_5$.

Finally we consider $Fe_3(CO)_{12}$ where the experimental and calculated spectra are shown in figure 7.3c. The experimental spectrum once more has three observable features which we have labelled A, B and C, and we focus on the pre-edge peaks A and B. If we compare the spectrum to the one of $Fe_2(CO)_9$ we can see that the features shift to lower energy and that the intensity of peak A is slightly reduced while peak B has a larger intensity. Now we consider the calculated spectra. Again, we will only discuss the B3LYP spectrum, which show a better agreement with experiment and in the following consider only peaks A and B. The isosurface plots of the (combination of) unoccupied orbitals that are probed with a significant intensity contribution are plotted in figure 7.4, along with the corresponding iron orbital contribution. Peak A has four main contributing transitions. The first two transitions are from the two $Fe_2(CO)_8$ core orbitals to σ^* anti-bonding orbitals between the $Fe_2(CO)_8$ backbone and the $Fe(CO)_4$ moiety. The next transition originates from the $1s$ orbital of the $Fe(CO)_4$ group to a completely anti-bonding orbital where all three possible metal-metal bonds are out of phase. The final transition also originates from the $1s$ of the $Fe(CO)_4$ group, but goes to an orbital which resembles a σ^*-orbital between the $Fe(CO)_4$ group and the $Fe_2(CO)_8$ and has a possibility of σ-like interactions between the iron centres of the $Fe_2(CO)_8$ backbone. Peak B contains three main transitions, in which orbitals from the

$Fe_2(CO)_8$ backbone are the main contributor. The first two transitions are to σ^* anti-bonding metal-metal bond orbitals of the backbone, with only ever a small orbital inclusion from the third iron centre. The third and final major contributing transition is to an orbital with a possible bonding interaction between the iron centres of the $Fe_2(CO)_8$ backbone.

To understand the changes in spectral intensity observed we must first consider the symmetry of the molecule. Compared to $Fe(CO)_5$ and $Fe_2(CO)_9$ the molecular point group has been reduced from D_{3h} to C_{2v}. This reduction in symmetry provides more possibilities for a dipole-allowed transition. Hence, the increase in intensity of peak B can be expected. However, the slight decrease in intensity of peak A compared to peak A of $Fe_2(CO)_9$, is not so easy to rationalise. If we look at the percentage contributions of the transition intensities to the peak shown in table 7.1 we can see that the main intensity contribution for all transitions is dipole. On the other hand, the amount of quadrupole intensity contribution to the peak has also increased relative to $Fe_2(CO)_9$. The peaks also shift to lower energies than in $Fe_2(CO)_9$ and the reason is clear when we consider the molecular orbitals. On the introduction of the $Fe(CO)_4$ group to the $Fe_2(CO)_8$ a third set of *d*-orbitals are introduced which can interact with the σ/σ^*-orbitals of the $Fe_2(CO)_8$ backbone. When one of the *d*-orbitals interact it then splits these two orbitals into three orbitals and thus, shifting the first available unoccupied orbitals to lower energies. Therefore, the features in the pre-edge are shifted to lower energies.

From all the observations discussed it becomes clear how the introduction of a second iron centre affects the electronic structure. A large part of the differences can be explained through a reduction of the symmetry of the individual iron centres and hence, their individual electronic structures. Moreover, we can see a correspondence between peak A of $Fe(CO)_5$ and $Fe_2(CO)_9$ in that they both consist of iron d_{z^2} orbitals. A subsequent correspondence can be made to peak A of $Fe_3(CO)_{12}$ in that this peak consists only of σ^*-orbitals, the same as for peak A of $Fe_2(CO)_9$.

7.3. Substituted Iron Carbonyl Complexes

However, the pure iron carbonyl complexes are not the only complexes of interest. Therefore, we will also consider the effect of substitution of one or more carbonyl groups on the pre-edge X-ray absorption spectra and thus, also the electronic structure.

$Fe(CO)_3C_8H_{12}$ is a single iron atom complex where two of the CO groups in $Fe(CO)_5$ have been changed for a cyclooctadiene. In figure 7.5 we show the spectra of $Fe(CO)_3C_8H_{12}$ as well as $Fe(CO)_5$ for comparison. In the experimental spectrum of $Fe(CO)_3C_8H_{12}$, we observe one pre-edge feature which has a large intensity increase as well as a shift to higher energies compared to $Fe(CO)_5$. The calculated BP86 spectrum shows one peak with a large intensity, while B3LYP leads to two distinct features. In terms of the experiment both provide the correct picture with one high-intensity peak. However, due to the previous observations for the pure carbonyls, we will only discuss the B3LYP results. We must note that neither exchange–correlation functional reproduces the energy shift, only the intensity increase.

To understand what changes occur on substitution of the two carbonyl groups for the C_8H_{12}, we consider the isosurface plots of the unoccupied orbitals that are probed with a significant intensity contribution. These are plotted in figure 7.6 along with the corresponding isolated iron contribution. Peak A of $Fe(CO)_3C_8H_{12}$ contains a $d_{xz/yz}$ like orbital, which is the anti-bonding orbital between the iron and the C_8H_{12} group. Therefore, we can infer that the substitution of the C_8H_{12} reduces the energy of one of the $d_{xz/yz}$ orbitals, because in $Fe(CO)_5$, the transitions to these orbitals were in the second pre-edge peak. The apparent loss of degeneracy of the $d_{xz/yz}$ orbitals

Figure 7.5.: X-ray absorption spectra for $Fe(CO)_5$ and $Fe(CO)_3C_8H_{12}$. Top: experimental spectra; middle: BP86 calculated spectra; bottom: B3LYP calculated spectra.

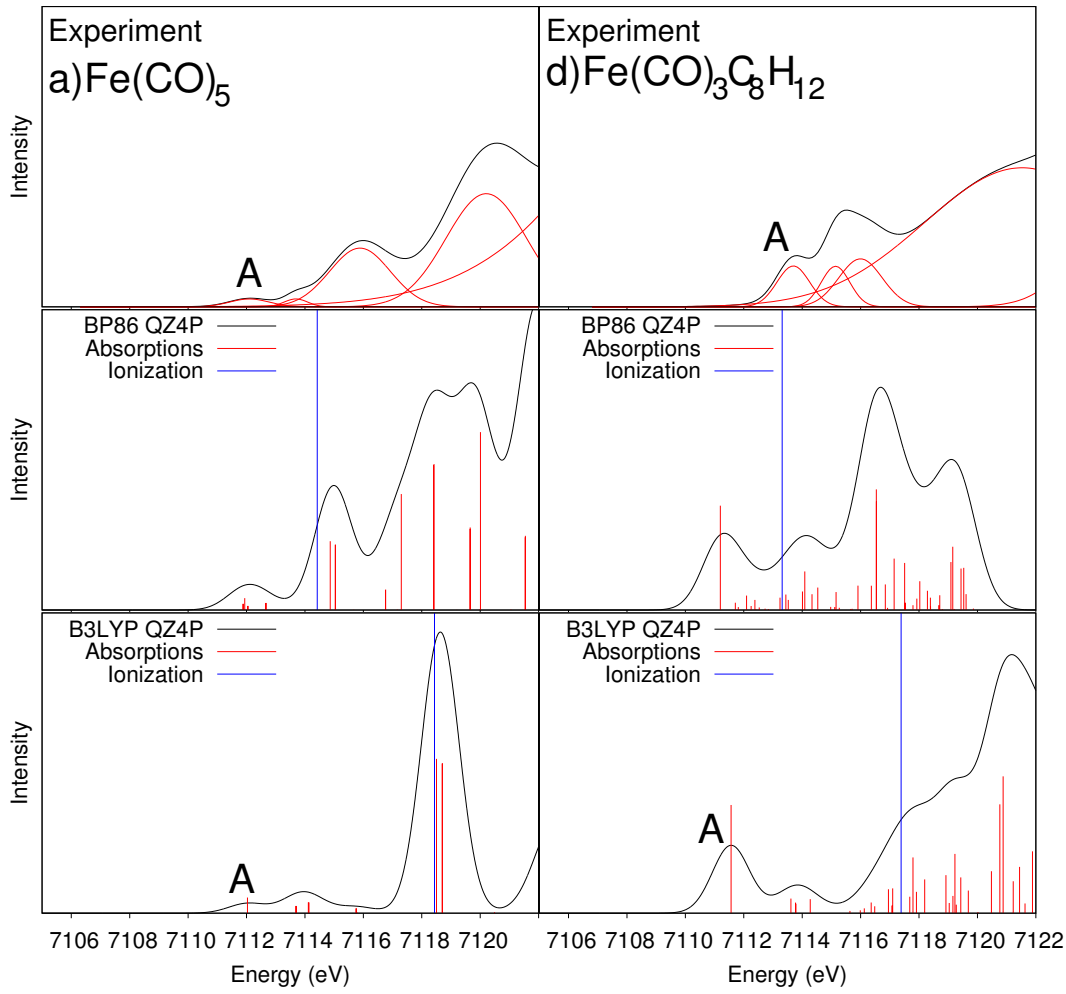

Figure 7.6.: Isosurface plots of the unoccupied orbitals probed by the pre-edge transitions as obtained from TD-DFT calculations with B3LYP/QZ4P, separated and sorted into the peaks they contribute to for $Fe(CO)_3C_8H_{12}$ and $Fe_2(CO)_4Cp_2$. All plots shown are linear combinations of orbital contributions (see Computational Methodology). Only the unoccupied orbitals corresponding to the major contributions to the peak intensity are shown here. Shown below the unoccupied orbitals are the isolated iron orbital contributions to them, in which only the part of the orbital that is within a radius of 1 Å around the iron atoms is included. The coloured dots indicate the iron atom (1*s* orbital) from which the transition originates.

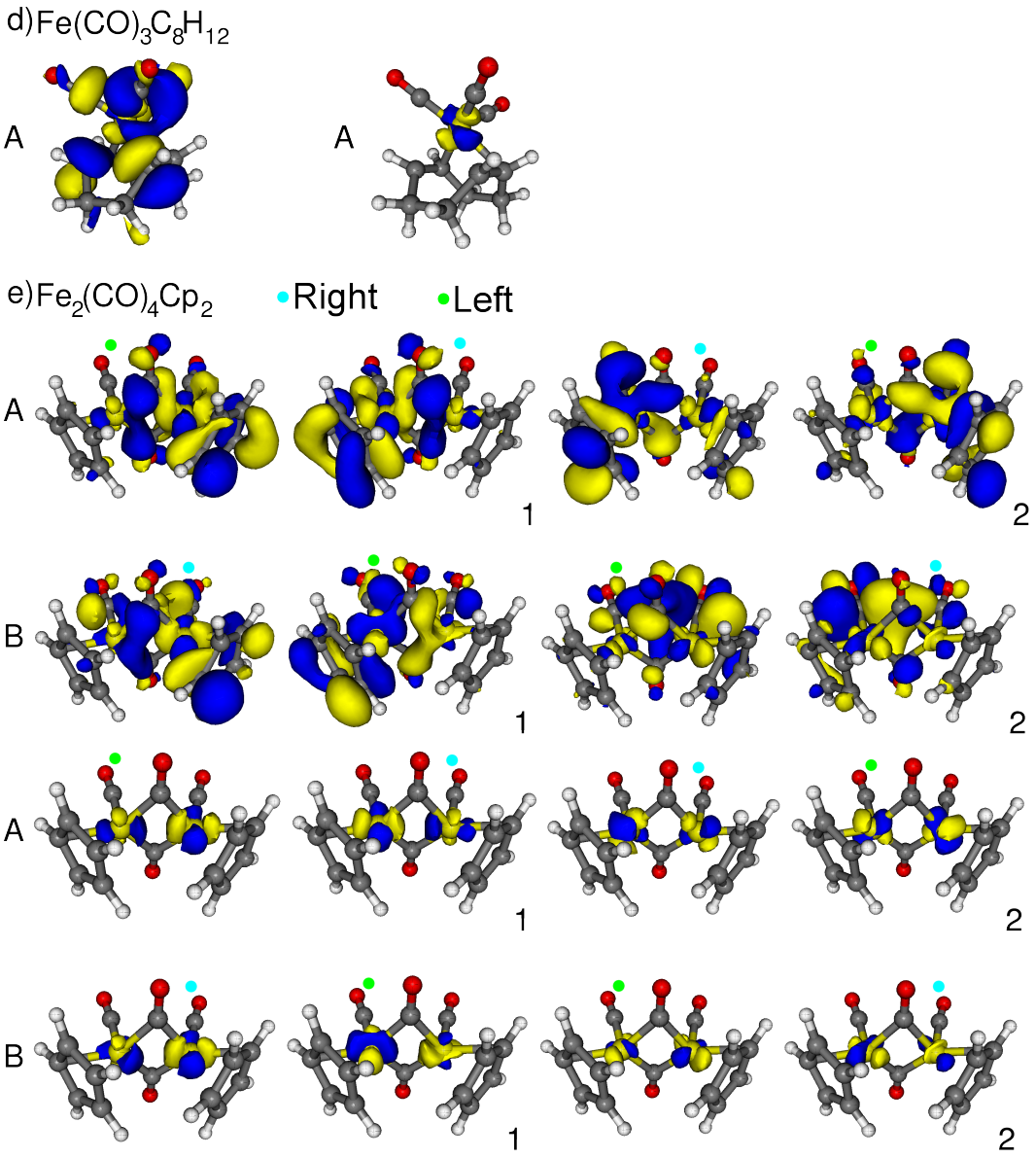

can be explained through the bonding/anti-bonding interaction. Only one of the two orbitals will be in the right orientation to interact with the π-orbitals of the C_8H_{12} group and thus, will have its energy altered. However, the energy shift observed in experiment is not reproduced, so we cannot analyse this shift further. Nevertheless, the large increase in intensity can be explained. We can see that in table 7.1 the primary intensity contribution is now the electric-dipole. This can be attributed to the almost complete loss of symmetry upon coordination of the C_8H_{12}, which means that any restriction to whether or not the dipole transition will occur is relaxed and thus, we observe dipole intensity.

We also considered a bimetallic substituted iron carbonyl system, $Fe_2(CO)_4Cp_2$, where five of the CO groups in $Fe_2(CO)_9$ have been replaced with two cyclopentadiene groups (one on each iron atom). Figure 7.7 shows the experimental and calculated spectra of $Fe_2(CO)_9$ and $Fe_2(CO)_4Cp_2$. In the experimental spectrum of $Fe_2(CO)_4Cp_2$ we observe two distinguishable pre-edge features, labelled A and B. Compared to the spectrum of $Fe_2(CO)_9$ no significant shift in the peak positions is observed, however there is a significant increase in the intensity of both features. Now we consider the calculated spectra. BP86 only provides one peak with a very large intensity, whereas B3LYP provides three discernible peaks, which correlates more accurately with the experimental observations. Therefore, we will only discuss the B3LYP spectra in the following. In the B3LYP spectra we will only consider the first two calculated peaks, labelled A and B in figure 7.7. To this end, the isosurface plots of the unoccupied orbitals that are probed with a significant intensity contribution are plotted in figure 7.6 along with the corresponding isolated iron orbital contribution.

Peak A is comprised of four transitions, two from each core orbital. The first two transitions are to orbitals which have a $d_{xz/yz}$-like appearance and an anti-bonding σ^* of the metal-metal bond, along with anti-bonding characteristics for one of the iron atoms with the accompanying Cp ring π-orbitals. The final two transitions are once again to $d_{xz/yz}$-like orbitals with an anti-bonding character with the Cp ring π-orbitals, except rotated by approximately 90 degrees around the Cp ring. Peak B of $Fe_2(CO)_4Cp_2$ also contains four main transitions, two from each core orbital. The first two transitions are to orbitals with significant anti-bonding characteristics between a $d_{xz/yz}$-like orbital and the Cp ring π-orbitals on one of the irons. However unlike in peak A, the other iron atom has a d_{z^2}-like appearance. The final two transitions have a $d_{x^2-y^2/xy}$-like appearance for the iron orbitals and from figure 7.6 appear to be anti-bonding orbitals for the metal-CO bonds.

The large increase in the intensity of both pre-edge peaks in relation to the pre-edge peaks of $Fe_2(CO)_9$ can be explained through the decrease in the symmetry of the complex. The same as was observed for $Fe(CO)_3C_8H_{12}$. We can see in table 7.1 that the intensity is mainly due to dipole contributions. However, as the $Fe_2(CO)_9$ peaks were also primarily composed of dipole transitions, only the loss of symmetry and thus, relaxation of the selection rules for the dipole mechanism can account for the increase in the intensity.

In conclusion, we can see that substitution of carbonyl groups for a group containing π-orbitals reduces the symmetry and thus, the intensity of the spectra increases. Also the inclusion of π-orbital containing substituents lowers the energy of the $d_{xz/yz}$-like orbitals so that now these comprise the peaks present in the pre-edge spectra, not the d_{z^2}-like orbital combinations which dominated the pure iron carbonyl complex spectra.

Figure 7.7.: X-ray absorption spectra for $Fe_2(CO)_9$ and $Fe_2(CO)_4Cp_2$. Top: experimental spectra; middle: BP86 calculated spectra; bottom: B3LYP calculated spectra.

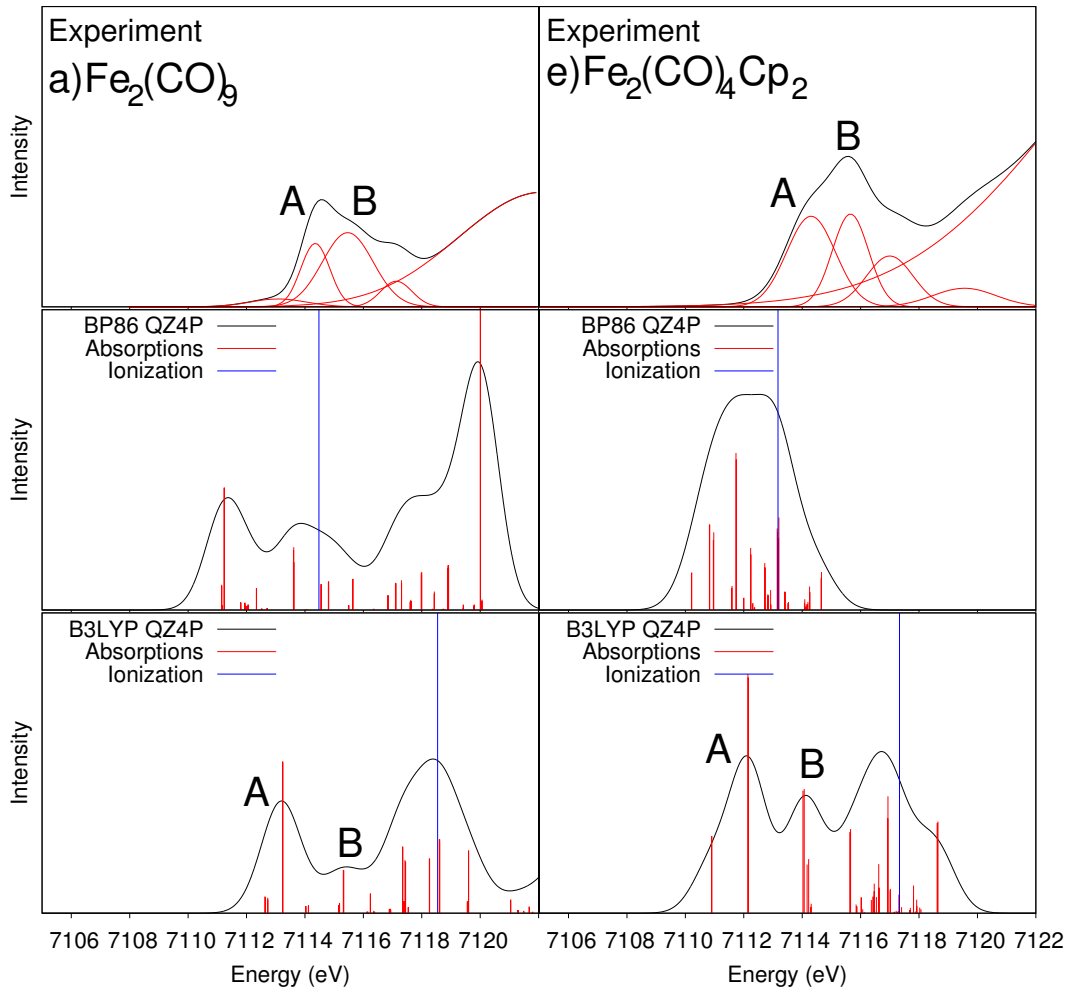

7.4. Conclusions

To investigate the capability of HERFD-XANES spectroscopy to determine new information about the electronic structure of iron carbonyl complexes, we performed calculations on three pure and two substituted iron carbonyl complexes using both the BP86 and B3LYP density functionals. These were then compared to experiment, in order to assign the experimental spectra and to extract information on the electronic structure.

First, we found that the iron carbonyl spectra are better reproduced by B3LYP than by BP86 where BP86 provides transitions too close in energy. This underestimation of energy differences between transitions was also observed in the ferrocene systems discussed in chapter 6. However, while B3LYP does provide a better result in comparison, the results are still not quantitative, with relative energies between complexes very different from experiment and relative intensities not being reproduced. Therefore, the calculated spectra can only be used to obtain a qualitative understanding. This calls for the development of more accurate wave function-based methods that are applicable to multi-nuclear transition metal carbonyls.

For the pure iron carbonyl complexes, we have seen that the first pre-edge peak in the mono-, bi- and trimetallic iron carbonyl complexes is comprised of d_{z^2}-like orbitals. In $Fe_2(CO)_9$ and in $Fe_3(CO)_{12}$, these are the anti-bonding σ^*-orbitals of the metal-metal bonds. Also we observe a general trend of the energy changes for the lowest energy peak (peak A) on going from a mono- to a bi- and then a trimetallic system, even if the relative energies between the complexes are not correctly predicted by B3LYP. Nevertheless, the trend in the intensities of peak A between complexes in the experimental spectra is reproduced.

Peak B has a slightly more complicated explanation. However, though no correspondence was seen between $Fe(CO)_5$ and $Fe_2(CO)_9$, a clear correspondence in the orbitals of the transitions was seen between $Fe_2(CO)_9$ and $Fe_3(CO)_{12}$ for this peak and it can be assigned to mixed iron d-orbital contributions with σ/σ^* interactions.

Finally, we looked at the effect of substitution of carbonyl ligands for ligands containing a π-system on the X-ray absorption spectra and thus, the electronic structure of the iron carbonyl complexes. For this two structures were used, $Fe(CO)_3C_8\,H_{12}$ and $Fe_2(CO)_4Cp_2$. Comparable with experimental results, in the calculations we saw an increase in the intensity of the spectra and we were able to attribute this to the lowering of the symmetry of the complex. This loss of symmetry then leads to an increase in dipole intensity, which provides the increased overall spectral intensity. Moreover, the inclusion of the π-system lowered the energy of specific d-orbitals, namely $d_{xz/yz}$-like orbitals, which then became the main components of the pre-edge transitions. Therefore, no direct correspondence could be made between peak A of either complex with their reference pure iron carbonyl complex. However, the transition in $Fe(CO)_3C_8H_{12}$ can be related to a transition in peak B of $Fe(CO)_5$ and a correspondence between the lower intensity transitions of peak B in the spectra of $Fe_2(CO)_4Cp_2$ could be made with the main transitions in peak B of $Fe_2(CO)_9$.

To conclude, we have shown that HERFD-XANES can provide information on the electronic structure of iron carbonyl complexes, and that a clear correspondence can be seen on going from mono- to bi- and trimetallic systems for the major transitions in the peak. Moreover, we have shown that substitution of carbonyl groups with a π-orbital containing substituent will lower the energy of $d_{xz/yz}$ orbitals. This capability of tuning the electronic structure of the iron atom has implications for optimising the effect of catalysts through altering their electronic structure.

7.5. Computational Methodology

Geometry optimisations of the molecular complexes were performed with the ADF2012 program package [122, 204, 270] using the density functional BP86 [130, 151] with the TZP basis set. The initial structures for a)-c) were obtained from reference [6]. For all considered compounds, the ground state is the low-spin state (S = 0).

The XANES spectra for the iron carbonyl complexes were then calculated using time-dependent density functional theory (TD-DFT). To selectively target core excitations, the TD-DFT calculations were restricted to excitations originating from the Fe 1*s* orbitals [123, 124]. Such restricted-channel TD-DFT calculations have been applied extensively for K-edge XAS spectra of transition metal complexes [107,116,186,245,271,272]. The effect of the exchange–correlation functional was judged by performing the calculations with both the non-hybrid functional BP86 and the hybrid functional B3LYP [158, 159]. The QZ4P Slater-type orbital basis set was applied in all TD-DFT calculations. We must note that all calculations are run without the inclusion of symmetry and that this results in localised core orbitals for the bi- and trimetallic systems.

The BP86 spectra were shifted by 180.62 eV and the B3LYP spectra by 150.08 eV for comparison to experiment. These shifts are chosen such that the energy of the first peak in the calculated spectrum of ironpentacarbonyl agrees with the first peak in the experimental spectrum. While these shifts are rather large, they do not affect the relative position of the peaks. For Fe K-edge XAS, it has been demonstrated previously that despite the large absolute errors, the selective TD-DFT approach used here can provide relative excitation energies and intensities with an accuracy that allows for a direct comparison with experiment [184]. The intensity of the spectra with complexes containing more than one core excitation centre in the calculation of the spectra were divided by the number of iron atoms included in the calculation to normalise the spectra.

It has previously been argued [107], that for molecules with equivalent core orbitals it is necessary to localise the core hole before performing the TD-DFT calculation. However in the calculations presented here no delocalisation of the core orbitals was observed and therefore, localisation of the core orbitals was not required.

All orbital isosurface plots in figures 7.2, 7.4 and 7.6 were prepared with Molekel [273] and use an isosurface value of +/-0.025 atomic units. With the B3LYP hybrid functionals, some excitations are combinations of several orbital transitions. Figure 7.4 and 7.6 shows the corresponding linear combination of unoccupied orbitals. This is possible due to the excitations originating from the same localised Fe 1*s* core orbitals.

8. Summary

In this thesis we have discussed both theoretical developments for the calculation of X-ray spectra and application of quantum-chemical methods to the calculation and interpretation of experimental X-ray spectra. In the applications we focused on the use of high-resolution measurements which provided more detail in the experimental spectra.

The first project considered the calculation of the HERFD-XANES spectra of a test set of ferrocene derivatives (Chapter 6), where the structure within the first coordination shell is unchanged and only in the second coordination shell are modifications introduced. The HERFD-XANES spectra showed marked differences in the pre-edge region for some of the ferrocene derivatives. This demonstrated that HERFD-XANES can probe changes in the electronic structure induced by structural changes beyond the first coordination shell. We used TD-DFT to simulate and interpret the pre-edge features within the HERFD-XANES spectra. Using the combination of TD-DFT and HERFD-XANES we were able to identify that introduction of a π-orbital containing substituent to the cyclopentadienyl ring introduced a second peak within the spectra. However, TD-DFT did not provide a quantitative interpretation of the spectra, only a qualitative interpretation of the HERFD-XANES spectra. Nevertheless, this was sufficient to demonstrate that HERFD-XANES provides a sensitive probe of electronic structure changes in transition metal complexes.

The second project was the derivation and implementation of an origin-independent formulation for the calculation of oscillator strengths (Chapter 3). This arose due to the observation of the origin-dependence of the oscillator strengths in our first project (where only the electric-dipole, magnetic-dipole and electric-quadrupole terms are included). We found that one must consistently include all terms of the same order in the wave vector to achieve an origin-independent formulation and in this case, two additional terms are required (electric-dipole–electric-octupole and electric-dipole–magnetic-quadrupole).

Within the third project we considered the calculation of the V2C-XES spectra of the ferrocene derivatives test set (Chapter 6). We explored the sensitivity of the V2C-XES region in comparison to the HERFD-XANES experiments to changes in the electronic structure. We calculated the V2C-XES using a simple ΔDFT methodology and thus, interpreted the experimental spectra. We observed that the V2C-XES spectra are not sensitive to electronic structure changes because any changes that occur are hidden by the intense dipole-allowed transitions in the spectra. We also note that the simple ΔDFT methodology employed provides calculated spectra in excellent agreement with experiment.

Finally, we considered the HERFD-XANES spectra of five iron carbonyl complexes and whether they could provide new insights into the electronic structure of the iron carbonyl complexes (Chapter 7). Once more we find that HERFD-XANES provides more detailed information on the electronic structure of transition metal complexes and the changes that occur upon changes in the ligand field than conventional XANES measurements. With the use of TD-DFT in conjunction with the experimental spectra we were able to determine correlations between transitions observed in the mono-, bi- and trimetallic species and interpret the changes in the electronic structure that occur upon substitution of carbonyl ligands. However, as before we can only obtain a qualitative

interpretation with TD-DFT.

To conclude, within this thesis we have shown that HERFD-XANES provides a sensitive probe to electronic structure changes in transition metal complexes and that with the use of TD-DFT we can obtain a qualitative interpretation. We also considered V2C-XES spectra and their calculation using ΔDFT, and though V2C-XES provides useful information it is not as sensitive as HERFD-XANES to the underlying electronic structure. However, the methods utilised in the calculation of the X-ray spectra only provide a qualitative interpretation. More work must be done on developing theoretical methods to attain a quantitative interpretation of the experimental spectra.

Therefore, future research on this subject has several areas which must be explored. The first is to test more exchange–correlation functionals. However, to know if the results from a functional provide an improved calculated spectrum we need a benchmark calculation, e.g. one using a higher-level wave function method, such as approximate coupled cluster methods. The second area is to include environment effects into the calculation. All calculations presented within this work only consider the isolated molecule, whereas all experimental measurements for X-ray are either in the solid state or solution. The final area is to consider more sophisticated approaches to the calculation of X-ray spectra, in particular for X-ray emission (not only considering a higher-level wave function method). Here, we have simulated both absorption and emission separately and as one-photon problems. However, X-ray emission is actually a process which should be described as a two-photon process (using quadratic response), whilst absorption must occur first before the emission process can occur. This would open up possibilities for a quantum-chemical simulation of other X-ray spectroscopic methods as well, specifically RIXS.

9. Zusammenfassung

Gegenstand der vorliegenden Arbeit ist die Entwicklung theoretischer Methoden für die Berechnung von Röntgenspektren, sowie die Anwendung quantenmechanischer Methoden zur Interpretation experimenteller Röntgenspektren. In den Anwendungen standen hochauflösende Messungen im Vordergrund, die mehr Details in den experimentellen Spektren aufweisen.

Gegenstand des ersten Projekts war die Untersuchung des Einflusses von Liganden bei höchenergieaufgeliste fluoreszenz-detektiate Röntgen-Nahkanten-Absorptions-Spektroskopie (HERFD-XANES-Spektroskopie) anhand eines Testsatzes aus Ferrocenderivaten (Kapitel 6), bei welchen die Struktur innerhalb der ersten Koordinationssphäre unverändert bleibt und nur die zweite Koordinationssphäre geändert wird. Die HERFD-XANES-Spektren zeigen Unterschiede kurz vor der Kante für manche der Ferrocenderivate. Dies zeigt, dass HERFD-XANES Strukturänderungen außerhalb der ersten Koordinationssphäre detektieren kann. Für die Berechnung der HERFD-XANES-Spektren wurde Zeitabhängige Dichtefunctionaltheorie (TD-DFT) verwendet. Durch die Verbindung von TD-DFT und HERFD-XANES konnte gezeigt werden, dass die Einführung von Liganden mit π-Orbital am Cyclopentadienyl-Ring einen zweiten Peak im Spektrum erzeugen. Die Verwendung von TD-DFT erlaubt keine quantitative, sondern nur eine qualitative Interpretation. Dies reicht jedoch aus um zu zeigen, dass mit HERFD-XANES eine genaue Untersuchung von Änderungen in der elektronischen Struktur von Übergangsmetallkomplexen möglich ist.

Das zweite Projekt beschäftigte sich mit der Herleitung und Implementierung einer vom Ursprung unabhängigen Formulierung für die Berechnung von Oszillatorenstärken (Kapitel 3). Dieses Projekt ergab sich aus dem ersten Projekt, bei dem vom Ursprung abhängigen Oszillatorenstärken beobachtet wurden. Ursache hierfür ist die Tatsache, dass nicht alle Terme für die Berechnung der Oszillatorenstärke berücksichtigt werden. Wir konnten zeigen, dass jeweils alle Terme gleicher Ordnung berechnet werden müssen, damit die Formulierung vom Ursprung unabhängig wird. Konkret müssen daher die beiden zusätzlichen Terme aus elektrischem Dipol-elektrischem Oktupol sowie elektrischem Dipol-magnetischem Quadrupol berücksichtigt werden.

Das dritte Projekt beschäftigte sich mit der Berechnung von Valenz-zu-Rempf Röntgenemissions-Spektroskopie (V2C-XES-Spektren) des Ferrocen-Testsatzes (Kapitel 6). Hierbei wurde die Empfindlichkeit der V2C-Region mit den HERFD-XANES-Untersuchungen bezüglich Änderungen in der elektronischen Struktur verglichen. Die V2C-XES-Berechnungen erfolgten mithilfe eines einfachen ΔDFT-Ansatzes. Wir fanden, dass die V2C-XES-Spektren nicht empfindlich bezüglich Änderungen der elektronischen Struktur sind, da die Änderungen hinter den intensiven, dipolerlaubten Übergängen versteckt bleiben. Es muss betont werden, dass es sich bei der Fehlerquelle nicht um den ΔDFT-Ansatz handelt, da mit diesem gute Übereinstimmungen mit experimentellen Daten erhalten wird.

Das vierte Projekt beschäftigte sich mit HERFD-XANES-Spektren von fünf Eisen-Carbonyl-Komplexen und mit der Frage, ob diese tiefere Einblicke in die elektronische Struktur von Eisen-Carbonyl-Komplexen generell liefern können (Kapitel 7). Auch in diesem Projekt konnten wir zeigen, dass HERFD-XANES sehr detaillierte Informationen für die elektronische Struktur von Übergangsmetallkomplexen bereitstellt, während konventionelle XANES-Spektren nicht ausreichend

Informationen liefern. Durch die Verwendung von TD-DFT in Verbindung mit den experimentellen Spektren konnten wir eine Korrelation zwischen Übergängen in mono-, bi- sowie trimetallischen Verbindungen nachweisen und die Änderungen bei Substituierung der Carbonyl-Liganden interpretieren. Durch die Verwendung von TD-DFT kann auch hier keine quantitative, sondern nur eine qualitative Auswertung erfolgen.

Im Rahmen der vorliegenden Arbeit konnte gezeigt werden, dass HERFD-XANES eine sehr empfindliche Methode zur Untersuchung von Übergangsmetallkomplexen darstellt und mit TD-DFT ein qualitatives Verständnis erreicht werden kann. Im Gegensatz dazu stehen V2C-XES-Spektren, die hilfreiche Informationen bereitstellen können, jedoch nicht so empfindlich wie HERFD-XANES in Bezug auf Änderungen in der elektronischen Struktur sind. Da die verwendeten Ansätze nur eine qualitative Interpretation erlauben, stellt die Entwicklung von Methoden, die eine quantitative Interpretation ermöglichen, einen wichtigen Beitrag dar.

Zukünftige Arbeiten müssen sich daher mit unterschiedlichen Bereichen beschäftigen. Zunächst sollten mehrere DFT-Funktionale getestet werden. Um abschätzen zu können, ob ein neues Funktional tatsächlich ein verbessertes Spektrum liefert, muss mit genauen, wellenfunktionsbasierten Methoden, zum Beispiel genäherten Coupled-Cluster-Methoden, verglichen werden. Darüber hinaus wurden alle vorgestellten Berechnungen für isolierte Moleküle durchgeführt. Daher sollten Umgebungseffekte in den Rechnungen berücksichtigt werden, da die experimentellen Arbeiten in Lösungen oder am Festkörper durchgeführt wurden. Letztendlich müssen verbesserte Ansätze für die Berechnung von Röntgenspektren entwickelt werden, insbesondere nicht die Verwendung von linearer, sondern quadratischer Antworttheorie, da es sich bei Röntgenemission um einen Zwei-Photonen-Prozess handelt. Eine solche Weiterentwicklung eröffnet darüber hinaus Möglichkeiten für quantenchemische Berechnungen weiterer Röntgenspektren, insbesondere RIXS.

A. List of Abbreviations

Ac	Acetyl
ADF	Amsterdam Density Functional
ANO	Atomic Natural Orbital
AO	Atomic Orbital
BO	Born-Oppenheimer
CAS-SCF	Complete Active Space Self Consistent Field
CC	Coupled Cluster
CD	Circular Dichroism
CI	Configuration Interaction
CIS	Configuration Interaction Singles
CIS(D)	Configuration Interaction Singles with Perturbative Doubles
Cp	Cyclopentadienyl
CPP	Complex Polarisation Propagator
DCM	Double Crystal Monochromator
DFT	Density Functional Theory
DKH	Douglas-Kroll-Hess
EXAFS	Extended X-ray Absorption Fine Structure
FWHM	Full Width Half Maximum
GGA	Generalised Gradient Approximation
GTO	Gaussian Type Orbital
HERFD	High Energy Resolution Fluorescence Detection
HF	Hartree-Fock
HOMO	Highest Occupied Molecular Orbitals
irrep	Irreducible Representation
LDA	Local Density Approximation
LUMO	Lowest Unoccupied Molecular Orbital
MCD	Magnetic Circular Dichroism

MO	Molecular Orbital
NCD	Natural Circular Dichroism
Ph	Phenyl
RHF	Restricted Hartree-Fock
RI	Resolution of Identity
RIXS	Resonant Inelastic X-ray Scattering
SOMO	Singly Occupied Molecular Orbital
STEX	Static Exchange
STO	Slater Type Orbital
TD-CC	Time-Dependent Coupled Cluster
TD-DFT	Time-Dependent Density Functional Theory
TD-HF	Time-Dependent Hartree-Fock
TM	Turbomole
UHF	Unrestricted Hartree-Fock
UKS	Unrestricted Kohn-Sham
UV-Vis	Ultra-Violet–Visible Spectroscopy
V2C	Valence-to-Core
XANES	Xray Absorption Near Edge Structure
XAS	X-ray Absorption Spectroscopy
XES	X-ray Emission Spectroscopy
XMCD	X-ray Magnetic Circular Dichroism
XNCD	X-ray Natural Circular Dichroism
ZORA	Zeroth Order Regular Approximation

B. Copyright Permissions

Chapters 3, 5 and 6 contain in part material that has already been published as articles in scientific peer-reviewed journals. The copyright permissions for published and submitted material are granted from the right owners. In detail they are:

Results, tables and figures in chapter 3 are reproduced in part with permission from: S. Bernadotte, A. J. Atkins, Ch. R. Jacob, *Origin-independent calculation of quadrupole intensities in X-ray spectroscopy*, J. Chem. Phys. **137**, 204106 (2012). Copyright **2012** American Institute of Physics.

Figure 5.8 in chapter 5 is reproduced in part with permission from: A. J. Atkins, M. Bauer, Ch. R. Jacob, *The chemical sensitivity of X-ray spectroscopy: high energy resolution XANES versus X-ray emission spectroscopy of substituted ferrocenes*, Phys. Chem. Chem. Phys. **15**, 8095 (2013). Copyright **2013** Royal Society of Chemistry.

Results, tables and figures in chapter 6 are reproduced in part with permission from: A. J. Atkins, M. Bauer, Ch. R. Jacob, *Probing the Electronic Structure of Substituted Ferrocenes with High-Resolution XANES Spectroscopy*, Chem.-Eur. J. **18**, 7021 (2012). Copyright **2012** John Wiley & Sons, Inc..

Results, tables and figures in chapter 6 are reproduced in part with permission from: A. J. Atkins, M. Bauer, Ch. R. Jacob, *The chemical sensitivity of X-ray spectroscopy: high energy resolution XANES versus X-ray emission spectroscopy of substituted ferrocenes*, Phys. Chem. Chem. Phys. **15**, 8095 (2013). Copyright **2013** Royal Society of Chemistry.

C. List of Publications

Andrew J. Atkins, Christoph R. Jacob, Matthias Bauer,
Probing the Electronic Structure of Substituted Ferrocenes with High-Resolution XANES Spectroscopy,
Chemistry: A European Journal **18**, 7021 (2012).

Stephan Bernadotte, Andrew J. Atkins, Christoph R Jacob,
Origin-independent calculation of quadrupole intensities in X-ray spectroscopy,
Journal of Chemical Physics **137**, 204106 (2012).

Andrew J. Atkins, Matthias Bauer, Christoph R. Jacob,
The chemical sensitivity of X-ray spectroscopy: high energy resolution XANES versus X-ray emission spectroscopy of substituted ferrocenes
Physical Chemistry Chemical Physics **15**, 8095 (2013).

D. Acknowledgments

First, I would like to say that my time in Karlsruhe and Germany has been spectacular and I have loved every moment. The new experiences and the people I have met have helped me get to this point in my life.

More specifically, I would like to thank my supervisor Dr. Christoph R. Jacob, without whom the work presented in this thesis would not have been possible. Also I would like to thank him for all the effort he put in in my first year teaching me about aspects of quantum mechanics and his patience, guidance and support in the subsequent years which has only helped me become a better scientific researcher. I also wish to thank Prof. Dr. Willem Klopper for the advice he has given me as my co-supervisor and the hospitality he has shown me during my time here in Karlsruhe.

I would also like to thank Dr. Gregory Chasse, without whom I may never have developed an interest in quantum mechanics and computational chemistry research. He also pushed me to go abroad for my Ph.D. as a learning experience and to enable me to grow as a person and for this advice I can only be grateful as I followed it and it brought me to Germany where I have been able to learn so much more than just science.

Coworkers past and present must also be mentioned, for they have provided many interesting and insightful conversations over the years and have made the office I work in a more interesting place to be. I would also like to mention all my colleagues working in Wim Klopper's group who have been extremely friendly and have made my working environment a truly enjoyable experience.

Specifically, I would like to thank Konstantinos Vogiatzis for instilling in me an interest in long bike rides and consequently both he and Andrey Yachmenev for many wonderful days spent cycling through the Schwarzwald and the mountains of Austria. I will always have fond memories of those times and the amazing places we visited.

Special thanks goes to Adam Kubas, Jens Keller, Aleksander Milenkoski, Konstantinos Vogiatzis, Matthew Kundrat, Dorota Jakubczyk, Andrey Yachmenev, Martin Hartmann, Pawel Panek and Carmen Cardenal Pac for some amazing times in Karlsruhe and to my best friends from Bangor University; James McDonagh, Tori Woollam and Hettie Miles who have been with me through a lot and for all the support they have given me. I would also like to thank everybody at the KIT fencing club who have been so friendly and welcoming and helped me with learning German.

Penultimately, I would like to give thanks to my scientific collaborators Matthias Bauer and Stephan Bernadotte whom brought my attention to the interesting problems presented within this thesis.

Finally, I thank my parents for everything they have done for me when I was growing up and for all the love and care they have provided over the years. My only hope is that my Dad would be proud of me if he was here to see this achievement in my life. I would also like to thank my brother Nick Atkins, who has given me much advice over the years, many interesting conversations on a variety of topics and finally for always being willing to play board games with me when we are both around.

Bibliography

[1] *IUPAC. Compendium of Chemical Terminology, 2nd ed. (the "Gold Book"). Compiled by A. D. McNaught and A. Wilkinson. Blackwell Scientific Publications, Oxford (1997). XML on-line corrected version: http://goldbook.iupac.org (2006-) created by M. Nic, J. Jirat, B. Kosata; updates compiled by A. Jenkins. ISBN 0-9678550-9-8. doi:10.1351/goldbook.*

[2] E.-C. Yang, D. N. Hendrickson, W. Wernsdorfer, M. Nakano, L. N. Zakharov, R. D. Sommer, A. L. Rheingold, M. Ledezma-Gairaud, and G. Christou, J. Appl. Phys. **91**, 7382 (2002).

[3] J. J. Sokol, A. G. Hee, and J. R. Long, J. Am. Chem. Soc. **124**, 7656 (2002).

[4] R. Sessoli and A. K. Powell, Coordin. Chem. Rev. **253**, 2328 (2009).

[5] M. Bradbury and N. R. Baker, BBA-Bioenergetics **635**, 542 (1981).

[6] F. A. Cotton and G. Wilkinson, *Advanced Inorganic Chemistry: A comprehensive Text 4th edition*, John Wiley & sons Inc, 1980.

[7] M. Beckett and A. Platt, *The Periodic Table at a Glance*, Blackwell Publishing, 2006.

[8] P. Atkins, T. Overton, J. Rourke, M. Weller, and F. Armstrong, *Inorganic Chemistry 4th edition*, Oxford University Press, 2006.

[9] D. Koningsberger and R. Prins, editors, *X-ray Absorption: Principles, Applications, Techniques of EXAFS, SEXAFS, and XANES*, John Wiley & sons Inc, 1988.

[10] J.-D. Grunwaldt, D. Lützenkirchen-Hecht, M. Richwin, S. Grundmann, B. S. Clausen, and R. Frahm, J. Phys. Chem. B **105**, 5161 (2001).

[11] J. Singh, C. Lamberti, and J. A. v. Bokhoven, Chem. Soc. Rev. **39**, 4754 (2010).

[12] M. Bauer and C. Gastl, Phys. Chem. Chem. Phys. **12**, 5575 (2010).

[13] M. W. Tew, M. Janousch, T. Huthwelker, and J. A. van Bokhoven, J. Catal. **283**, 45 (2011).

[14] B. P. C. Hereijgers, T. M. Eggenhuisen, K. P. de Jong, H. Talsma, A. M. J. van der Eerden, A. M. Beale, and B. M. Weckhuysen, J. Phys. Chem. C **115**, 15545 (2011).

[15] M. Bauer, R. Schoch, L. Shao, B. Zhang, A. Knop-Gericke, M. Willinger, R. Schlögl, and D. Teschner, J. Phys. Chem. C **116**, 22375 (2012).

[16] E. Kleymenov, J. Sa, J. Abu-Dahrieh, D. Rooney, J. A. v. Bokhoven, E. Troussard, J. Szlachetko, O. V. Safonova, and M. Nachtegaal, Catal. Sci. Technol. **2**, 373 (2012).

[17] J. E. Penner-Hahn, Coordin. Chem. Rev. **190–192**, 1101 (1999).

[18] P. A. Lee, P. H. Citrin, P. Eisenberger, and B. M. Kincaid, Rev. Mod. Phys. **53**, 769 (1981).

[19] T. E. Westre, P. Kennepohl, J. G. DeWitt, B. Hedman, K. O. Hodgson, and E. I. Solomon, J. Am. Chem. Soc. **119**, 6297 (1997).

[20] N. Sun, L. V. Liu, A. Dey, G. Villar-Acevedo, J. A. Kovacs, M. Y. Darensbourg, K. O. Hodgson, B. Hedman, and E. I. Solomon, Inorg. Chem. **50**, 427 (2011).

[21] K. M. Lancaster, M. Roemelt, P. Ettenhuber, Y. Hu, M. W. Ribbe, F. Neese, U. Bergmann, and S. DeBeer, Science **334**, 974 (2011).

[22] Y. Nicolet, C. Cavazza, and J. Fontecilla-Camps, J. Inorg. Biochem. **91**, 1 (2002).

[23] M. Dong, G. Wang, Z. Qin, J. Wang, T. Liu, S. Yuan, and H. Jiao, J. Phys. Chem. A **111**, 1515 (2007).

[24] S. H. Eitel, M. Bauer, D. Schweinfurth, N. Deibel, B. Sarkar, H. Kelm, H.-J. Krüger, W. Frey, and R. Peters, J. Am. Chem. Soc. **134**, 4683 (2012).

[25] P. Atkins and R. Friedman, *Molecular Quantum Mechanics*, Oxford University Press, 2011.

[26] F. Schwabl, *Quantenmechanik (Qm I) Eine einführung*, Springer-Verlag, 1998.

[27] S. Bernadotte, A. J. Atkins, and C. R. Jacob, J. Chem. Phys. **137**, 204106 (2012).

[28] C. Baiocchi, M. C. Brussino, E. Pramauro, A. B. Prevot, L. Palmisano, and G. Marc, Int. J. Mass. Spectrom. **214**, 247 (2002).

[29] B. Tan and D. N. Soderstrom, J. Chem. Educ. **66**, 258 (1989).

[30] T. Inoue, Y. Kubozono, S. Kashino, Y. Takabayashi, K. Fujitaka, M. Hida, M. Inoue, T. Kanbara, S. Emura, and T. Uruga, Chem. Phys. Lett. **316**, 381 (2000).

[31] H. Guo, J. Jiang, Y. Shi, Y. Wang, J. Liu, and S. Dong, J. Phys. Chem. B **108**, 10185 (2004).

[32] G. Grubert, M. Wark, N. I. Jaeger, G. Schulz-Ekloff, and O. P. Tkachenko, J. Phys. Chem. B **102**, 1665 (1998).

[33] G. Kalyuzhny, A. Vaskevich, G. Ashkenasy, A. Shanzer, and I. Rubinstein, J. Phys. Chem. B **104**, 8238 (2000).

[34] W. W. Yu and X. Peng, Angew. Chem. Int. Ed. **41**, 2368 (2002).

[35] W. Liu, B. Etschmann, J. Brugger, L. Spiccia, G. Foran, and B. McInnes, Chem. Geol. **231**, 326 (2006).

[36] R. A. Goldbeck, O. Einarsdottir, T. D. Dawes, D. B. O'Connor, K. K. Surerus, J. A. Fee, and D. S. Kliger, Biochemistry-US **31**, 9376 (1992).

[37] S. M. Kelly, T. J. Jess, and N. C. Price, BBA-Proteins Proteomics **1751**, 119 (2005).

[38] Q. Xu, J. Nelson, and T. M. Bricker, BBA-Bioenergetics **1188**, 427 (1994).

[39] F. Eker, K. Griebenow, and R. Schweitzer-Stenner, J. Am. Chem. Soc. **125**, 8178 (2003).

[40] R. Banerjee, G. Basu, S. Roy, and P. Chène, J. Pept. Res. **60**, 88 (2002).

[41] D. K. Smith and F. Diederich, Chem.-Eur. J. **4**, 1353 (1998).

[42] S. Bernhard, K. Takada, D. J. Díaz, H. D. Abruña, and H. Mürner, J. Am. Chem. Soc. **123**, 10265 (2001).

[43] S. Filippone, E. E. Maroto, A. Martín-Domenech, M. Suarez, and N. Martín, Nature Chemistry **1**, 578 (2009).

[44] E. Samu, P. Huszthy, L. Somogyi, and M. Hollósi, Tetrahedron-Asymmetr. **10**, 2775 (1999).

[45] E. Keinan, E. Benory, S. C. Sinha, A. Sinha-Bagchi, D. Eren, Z. Eshhar, and B. S. Green, Inorg. Chem. **31**, 5433 (1992).

[46] S. Doniach, K. Hodgson, I. Lindau, P. Pianetta, and H. Winick, J. Synchotron Radiat. **4**, 380 (1997).

[47] G. v. d. Laan and I. W. Kirkman, J. Phys.-Condens. Mat. **4**, 4189 (1992).

[48] R. K. Hocking, E. C. Wasinger, F. M. F. de Groot, K. O. Hodgson, B. Hedman, and E. I. Solomon, J. Am. Chem. Soc. **128**, 10442 (2006).

[49] G. Cressey, C. M. B. Henderson, and G. v. d. Laan, Phys. Chem. Miner. **20**, 111 (1993).

[50] J. Singh, M. Tromp, O. V. Safonova, P. Glatzel, and J. A. van Bokhoven, Catal. Today **145**, 300 (2009).

[51] J. Müller, O. Jepsen, and J. Wilkins, Solid State Commun. **42**, 365 (1982).

[52] J. Petiau, G. Calas, D. Petitmaire, A. Bianconi, M. Benfatto, and A. Marcelli, Phys. Rev. B **34**, 7350 (1986).

[53] G. Kalkowski, G. Kaindl, W. D. Brewer, and W. Krone, Phys. Rev. B **35**, 2667 (1987).

[54] B. Dobson and G. Greaves, Nucl. Instrum. Meth. B. **68**, 111 (1992).

[55] T. Glaser, B. Hedman, K. O. Hodgson, and E. I. Solomon, Acc. Chem. Res. **33**, 859 (2000).

[56] S. E. Shadle, B. Hedman, K. O. Hodgson, and E. I. Solomon, J. Am. Chem. Soc. **117**, 2259 (1995).

[57] E. I. Solomon, B. Hedman, K. O. Hodgson, A. Dey, and R. K. Szilagyi, Coordin. Chem. Rev. **249**, 97 (2005).

[58] F. Neese, B. Hedman, K. O. Hodgson, and E. I. Solomon, Inorg. Chem. **38**, 4854 (1999).

[59] S. H. Choi, B. R. Wood, J. A. Ryder, and A. T. Bell, Phys. Scripta , 688 (2005).

[60] J. Frommer, M. Nachtegaal, I. Czekaj, T.-C. Weng, and R. Kretzschmar, J. Phys. Chem. A **113**, 12171 (2009).

[61] T. Yamamoto, X-ray Spectrom. **37**, 572 (2008).

[62] M. Wilke, F. Farges, P.-E. Petit, G. E. Brown, and F. Martin, Am. Mineral. **86**, 714 (2001).

[63] G. Giuli, E. Paris, K.-U. Hess, D. B. Dingwell, M. R. Cicconi, S. G. Eeckhout, K. T. Fehr, and P. Valenti, Am. Mineral. **96**, 631 (2011).

[64] G. Dräger, R. Frahm, G. Materlik, and O. Brümmer, Phys. Status Solidi B **146**, 287 (1988).

[65] F. D. Vila, T. Jach, W. T. Elam, J. J. Rehr, and J. D. Denlinger, J. Phys. Chem. A **115**, 3243 (2011).

[66] G. Peng, F. M. F. deGroot, K. Haemaelaeinen, J. A. Moore, X. Wang, M. M. Grush, J. B. Hastings, D. P. Siddons, and W. H. Armstrong, J. Am. Chem. Soc. **116**, 2914 (1994).

[67] C. J. Pollock and S. DeBeer, J. Am. Chem. Soc. **133**, 5594 (2011).

[68] M. A. Beckwith, M. Roemelt, M.-N. Collomb, C. DuBoc, T.-C. Weng, U. Bergmann, P. Glatzel, F. Neese, and S. DeBeer, Inorg. Chem. **50**, 8397 (2011).

[69] K. M. Lancaster, K. D. Finkelstein, and S. DeBeer, Inorg. Chem. **50**, 6767 (2011).

[70] P. Glatzel and U. Bergmann, Coordin. Chem. Rev. **249**, 65 (2005).

[71] L. J. P. Ament, M. van Veenendaal, T. P. Devereaux, J. P. Hill, and J. van den Brink, Rev. Mod. Phys. **83**, 705 (2011).

[72] J. Singh, R. C. Nelson, B. C. Vicente, S. L. Scott, and J. A. v. Bokhoven, Phys. Chem. Chem. Phys. **12**, 5668 (2010).

[73] M. van Veenendaal, Phys. Rev. Lett. **96**, 117404 (2006).

[74] L.-C. Duda, J. Nordgren, G. Dräger, S. Bocharov, and T. Kirchner, J. Electron. Spectrosc. **110–111**, 275 (2000).

[75] G. Chabot-Couture, J. N. Hancock, P. K. Mang, D. M. Casa, T. Gog, and M. Greven, Phys. Rev. B **82**, 035113 (2010).

[76] A. Kotani and S. Shin, Rev. Mod. Phys. **73**, 203 (2001).

[77] F. Gel'mukhanov and H. Ågren, Phys. Rep. **312**, 87 (1999).

[78] H. Hayashi, Y. Udagawa, W. A. Caliebe, and C.-C. Kao, Chem. Phys. Lett. **371**, 125 (2003).

[79] K. Hämäläinen, D. P. Siddons, J. B. Hastings, and L. E. Berman, Phys. Rev. Lett. **67**, 2850 (1991).

[80] P. Glatzel, M. Sikora, S. G. Eeckhout, O. V. Safonova, G. Smolentsev, G. Pirngruber, J. A. van Bokhoven, J.-D. Grunewaldt, and M. Tromp, AIP Conf. Proc. **879**, 1731 (2007).

[81] R. D. Peacock and B. Stewart, J. Phys. Chem. B **105**, 351 (2001).

[82] P. Carra and R. Benoist, Phys. Rev. B **62**, R7703 (2000).

[83] G. Schütz, W. Wagner, W. Wilhelm, P. Kienle, R. Zeller, R. Frahm, and G. Materlik, Phys. Rev. Lett. **58**, 737 (1987).

[84] B. T. Thole, P. Carra, F. Sette, and G. van der Laan, Phys. Rev. Lett. **68**, 1943 (1992).

[85] P. Carra, Jpn. J. Appl. Phys. **32S2**, 279 (1993).

[86] G. Schütz, M. Knülle, and H. Ebert, Phys. Scripta **1993**, 302 (1993).

[87] M. Altarelli, Phys. Rev. B **47**, 597 (1993).

[88] P. Carra, B. T. Thole, M. Altarelli, and X. Wang, Phys. Rev. Lett. **70**, 694 (1993).

[89] C. Piamonteze, P. Miedema, and F. M. F. de Groot, Phys. Rev. B **80**, 184410 (2009).

[90] O. Šipr and H. Ebert, Phys. Rev. B **72**, 134406 (2005).

[91] V. N. Antonov, A. P. Shpak, and A. N. Yaresko, Low Temp. Phys+ **34**, 1 (2008).

[92] D. P. Siddons, M. Hart, Y. Amemiya, and J. B. Hastings, Phys. Rev. Lett. **64**, 1967 (1990).

[93] L. Alagna, T. Prosperi, S. Turchini, J. Goulon, A. Rogalev, C. Goulon-Ginet, C. Natoli, R. Peacock, and B. Stewart, Phys. Rev. Lett. **80**, 4799 (1998).

[94] J. Goulon, F. Sette, C. Moise, A. Fontaine, D. Perey, P. Rudolf, and F. Baudelet, Jpn. J. Appl. Phys. **32S2**, 284 (1993).

[95] J. Goulon, C. Goulon-Ginet, A. Rogalev, V. Gotte, C. Malgrange, C. Brouder, and C. R.

Natoli, J. Chem. Phys. **108**, 6394 (1998).

[96] B. Stewart, R. D. Peacock, L. Alagna, T. Prosperi, S. Turchini, J. Goulon, A. Rogalev, and C. Goulon-Ginet, J. Am. Chem. Soc. **121**, 10233 (1999).

[97] A. Rogalev, J. Goulon, F. Wilhelm, K. A. Kozlovskaya, E. N. Ovchinnikova, L. V. Soboleva, A. F. Konstantinova, and V. E. Dmitrienko, Crystallogr. Rep.+ **53**, 384 (2008).

[98] J. Goulon, A. Rogalev, F. Wilhelm, N. Jaouen, C. Goulon-Ginet, and C. Brouder, J. Phys.-Condens. Mat. **15**, S633 (2003).

[99] A. Rogalev, J. Goulon, and F. Wilhelm, C. R. Phys. **9**, 642 (2008).

[100] G. R. Shulman, Y. Yafet, P. Eisenberger, and W. E. Blumberg, P. Natl. Acad. Sci. USA **73**, 1384 (1976).

[101] K. Ray, T. Petrenko, K. Wieghardt, and F. Neese, Dalton T. , 1552 (2007).

[102] R. Sarangi, L. Yang, S. G. Winikoff, L. Gagliardi, C. J. Cramer, W. B. Tolman, and E. I. Solomon, J. Am. Chem. Soc. **133**, 17180 (2011).

[103] D. Cabaret, A. Bordage, A. Juhin, M. Arfaoui, and E. Gaudry, Phys. Chem. Chem. Phys. **12**, 5619 (2010).

[104] H. Ikeno, T. Mizoguchi, Y. Koyama, Z. Ogumi, Y. Uchimoto, and I. Tanaka, J. Phys. Chem. C **115**, 11871 (2011).

[105] V. Carravetta, H. Ågren, and V. Barone, Computational X-Ray Spectroscopy, in *Computational Strategies for Spectroscopy: from Small Molecules to Nano Systems*, pages 137–205, Wiley, Hoboken, New Jersey, 2011.

[106] J. Lehtola, M. Hakala, A. Sakko, and K. Hämäläinen, J. Comput. Chem. **33**, 1572–1585 (2012).

[107] S. DeBeer George, T. Petrenko, and F. Neese, Inorg. Chim. Acta **361**, 965 (2008).

[108] A. J. Atkins, C. R. Jacob, and M. Bauer, Chem.-Eur. J. **18**, 7021 (2012).

[109] L. D. Barron, *Molecular Light Scattering and Optical Activity*, Cambridge University Press, Cambridge, 2nd edition, 2004.

[110] E. B. Graham and R. E. Raab, Proc. R. Soc. Lond. A **430**, 593 (1990).

[111] R. McWeeny, *Spins in Chemistry*, Dover Publications, Mineola, N.Y., 2004.

[112] C. R. Jacob and M. Reiher, Int. J. Quantum Chem. **112**, 3661 (2012).

[113] E. B. Graham and R. E. Raab, Proc. Roy. Soc. Ser. A **456**, 1193 (2000).

[114] N. A. Besley, M. J. G. Peach, and D. J. Tozer, Phys. Chem. Chem. Phys. **11**, 10350 (2009).

[115] N. A. Besley and F. A. Asmuruf, Phys. Chem. Chem. Phys. **12**, 12024 (2010).

[116] M. Roemelt, M. A. Beckwith, C. Duboc, M.-N. Collomb, F. Neese, and S. DeBeer, Inorg. Chem. **51**, 680 (2012).

[117] F. Neese, Coordin. Chem. Rev. **253**, 526 (2009).

[118] S. J. A. van Gisbergen, J. G. Snijders, and E. J. Baerends, Comput. Phys. Commun. **118**, 119 (1999).

[119] J. Autschbach and T. Ziegler, J. Chem. Phys. **116**, 891 (2002).

[120] J. Autschbach, T. Ziegler, S. J. A. van Gisbergen, and E. J. Baerends, J. Chem. Phys. **116**, 6930 (2002).

[121] Theoretical Chemistry, Vrije Universiteit Amsterdam, ADF, Amsterdam Density Functional program, URL: http://www.scm.com.

[122] G. te Velde, F. M. Bickelhaupt, E. J. Baerends, C. Fonseca Guerra, S. J. A. van Gisbergen, J. G. Snijders, and T. Ziegler, J. Comput. Chem. **22**, 931 (2001).

[123] M. Stener, G. Fronzoni, and M. de Simone, Chem. Phys. Lett. **373**, 115 (2003).

[124] K. Ray, S. DeBeerGeorge, E. Solomon, K. Wieghardt, and F. Neese, Chem.-Eur. J. **13**, 2783 (2007).

[125] T. Tsuchimochi, M. Kobayashi, A. Nakata, Y. Imamura, and H. Nakai, J. Comput. Chem. **29**, 2311 (2008).

[126] N. Schmidt, R. Fink, and W. Hieringer, J. Chem. Phys. **133**, 054703 (2010).

[127] A. Kovyrshin and J. Neugebauer, J. Chem. Phys. **133**, 174114 (2010).

[128] W. Liang, S. A. Fischer, M. J. Frisch, and X. Li, J. Chem. Theory Comput. **7**, 3540 (2011).

[129] K. Lopata, B. E. Van Kuiken, M. Khalil, and N. Govind, J. Chem. Theory Comput. **8**, 3284 (2012).

[130] A. D. Becke, Phys. Rev. A **38**, 3098 (1988).

[131] J. P. Perdew, Phys. Rev. B **33**, 8822 (1986).

[132] E. van Lenthe, E. J. Baerends, and J. G. Snijders, J. Chem. Phys. **99**, 4597 (1993).

[133] E. van Lenthe, E. J. Baerends, and J. G. Snijders, J. Chem. Phys. **101**, 9783 (1994).

[134] E. van Lenthe, J. G. Snijders, and E. J. Baerends, J. Chem. Phys. **105**, 6505 (1996).

[135] E. van Lenthe, A. Ehlers, and E.-J. Baerends, J. Chem. Phys. **110**, 8943 (1999).

[136] S. DeBeer George, P. Brant, and E. I. Solomon, J. Am. Chem. Soc. **127**, 667 (2005).

[137] N. Lee, T. Petrenko, U. Bergmann, F. Neese, and S. DeBeer, J. Am. Chem. Soc. **132**, 9715 (2010).

[138] R. Merlin, P. Natl. Acad. Sci. USA **106**, 1693 (2009), PMID: 19188589.

[139] F. Jensen, *Introduction to Computational Chemistry: Second Edition*, Wiley-Blackwell, 2nd edition edition, 2006.

[140] T. Helgaker, P. Jørgensen, and J. Olsen, *Molecular Electronic Structure Theory*, John Wiley & Sons, Chichester, 2000.

[141] P.-O. Widmark, editor, *European Summerschool in Quantum Chemistry 2011*, Lund University, 2011.

[142] P. Hohenberg and W. Kohn, Phys. Rev. **136**, B864 (1964).

[143] M. Levy, P. Natl. Acad. Sci. USA **76**, 6062 (1979), PMID: 16592733.

[144] W. Kohn and L. J. Sham, Phys. Rev. **140**, A1133 (1965).

[145] J. P. Perdew and K. Schmidt, AIP Conf. Proc. **577**, 1 (2001).

[146] J. C. Slater and K. H. Johnson, Phys. Rev. B **5**, 844 (1972).

[147] S. H. Vosko, L. Wilk, and M. Nusair, Can. J. Phys. **58**, 1200 (1980).

[148] J. P. Perdew and Y. Wang, Phys. Rev. B **45**, 13244 (1992).

[149] T. W. Keal and D. J. Tozer, J. Chem. Phys. **119**, 3015 (2003).

[150] T. W. Keal and D. J. Tozer, J. Chem. Phys. **121**, 5654 (2004).

[151] J. P. Perdew, Phys. Rev. B **33**, 8822 (1986).

[152] J. P. Perdew, K. Burke, and M. Ernzerhof, Phys. Rev. Lett. **77**, 3865 (1996).

[153] C. J. Cramer and D. G. Truhlar, Phys. Chem. Chem. Phys. **11**, 10757 (2009).

[154] J. Tao, J. P. Perdew, V. N. Staroverov, and G. E. Scuseria, Phys. Rev. Lett. **91**, 146401 (2003).

[155] V. N. Staroverov, G. E. Scuseria, J. Tao, and J. P. Perdew, J. Chem. Phys. **119**, 12129 (2003).

[156] Y. Zhao and D. G. Truhlar, J. Chem. Phys. **125**, 194101 (2006).

[157] Y. Zhao and D. G. Truhlar, Theor. Chem. Acc. **120**, 215 (2008).

[158] A. D. Becke, J. Chem. Phys. **98**, 5648 (1993).

[159] C. Lee, W. Yang, and R. G. Parr, Phys. Rev. B **37**, 785 (1988).

[160] M. Ernzerhof and G. E. Scuseria, J. Chem. Phys. **110**, 5029 (1999).

[161] C. Adamo and V. Barone, J. Chem. Phys. **110**, 6158 (1999).

[162] Y. Zhao, B. J. Lynch, and D. G. Truhlar, J. Phys. Chem. A **108**, 4786 (2004).

[163] S. Grimme, J. Chem. Phys. **124**, 034108 (2006).

[164] N. A. Besley, Chem. Phys. Lett. **390**, 124 (2004).

[165] M. Head-Gordon, R. J. Rico, M. Oumi, and T. J. Lee, Chem. Phys. Lett. **219**, 21 (1994).

[166] M. Head-Gordon, D. Maurice, and M. Oumi, Chem. Phys. Lett. **246**, 114 (1995).

[167] F. A. Asmuruf and N. A. Besley, Chem. Phys. Lett. **463**, 267 (2008).

[168] H. Ågren, V. Carravetta, O. Vahtras, and L. G. Pettersson, Chem. Phys. Lett. **222**, 75 (1994).

[169] H. Ågren, V. Carravetta, O. Vahtras, and L. G. M. Pettersson, Theor. Chem. Acc. **97**, 14 (1997).

[170] L. Triguero, L. G. M. Pettersson, and H. Ågren, Phys. Rev. B **58**, 8097 (1998).

[171] A. Nilsson and L. G. M. Pettersson, Surf. Sci. Rep. **55**, 49 (2004).

[172] G. Smolentsev, A. V. Soldatov, J. Messinger, K. Merz, T. Weyhermüller, U. Bergmann, Y. Pushkar, J. Yano, V. K. Yachandra, and P. Glatzel, J. Am. Chem. Soc. **131**, 13161 (2009).

[173] M. U. Delgado-Jaime, B. R. Dible, K. P. Chiang, W. W. Brennessel, U. Bergmann, P. L. Holland, and S. DeBeer, Inorg. Chem. **50**, 10709 (2011).

[174] M. Stener, A. Lisini, and P. Decleva, Chem. Phys. **191**, 141 (1995).

[175] C.-H. Hu and D. P. Chong, Chem. Phys. Lett. **262**, 733 (1996).

[176] L. Triguero, L. G. M. Pettersson, and H. Ågren, J. Phys. Chem. A **102**, 10599 (1998).

[177] B. Brena, P. E. M. Siegbahn, and H. Ågren, J. Am. Chem. Soc. **134**, 17157 (2012).

[178] E. Runge and E. K. U. Gross, Phys. Rev. Lett. **52**, 997 (1984).

[179] M. E. Casida, *Time-dependent density functional response theory for molecules*, volume 1, World Scientific: Singapore, 1995.

[180] L. Bertini, C. Greco, L. De Gioia, and P. Fantucci, J. Phys. Chem. A **110**, 12900 (2006).

[181] N. A. Besley and A. Noble, J. Phys. Chem. C **111**, 3333 (2007).

[182] S. I. Bokarev, O. S. Bokareva, and O. Kühn, J. Chem. Phys. **136**, 214305 (2012).

[183] J. Schwitalla and H. Ebert, Phys. Rev. Lett. **80**, 4586 (1998).

[184] S. DeBeer George, T. Petrenko, and F. Neese, J. Phys. Chem. A **112**, 12936 (2008).

[185] A. Nakata, Y. Imamura, and H. Nakai, J. Chem. Theory Comput. **3**, 1295 (2007).

[186] P. Chandrasekaran, S. C. E. Stieber, T. J. Collins, L. Que, Jr., F. Neese, and S. DeBeer, Dalton T. **40**, 11070 (2011).

[187] A. Dreuw and M. Head-Gordon, Chem. Rev. **105**, 4009 (2005).

[188] A. S. P. Gomes and C. R. Jacob, Annu. Rep. Prog. Chem. Sect. C: Phys. Chem. **108**, 222 (2012).

[189] S. Hirata and M. Head-Gordon, Chem. Phys. Lett. **314**, 291 (1999).

[190] T. Helgaker, S. Coriani, P. Jørgensen, K. Kristensen, J. Olsen, and K. Ruud, Chem. Rev. **112**, 543 (2012).

[191] S. Coriani, O. Christiansen, T. Fransson, and P. Norman, Phys. Rev. A **85** (2012).

[192] S. Coriani, T. Fransson, O. Christiansen, and P. Norman, J. Chem. Theory Comput. **8**, 1616 (2012).

[193] P. Norman, D. M. Bishop, H. Jørgen Aa. Jensen, and J. Oddershede, J. Chem. Phys. **115**, 10323 (2001).

[194] P. Norman, D. M. Bishop, H. J. A. Jensen, and J. Oddershede, J. Chem. Phys. **123**, 194103 (2005).

[195] U. Ekström, P. Norman, V. Carravetta, and H. Ågren, Phys. Rev. Lett. **97**, 143001 (2006).

[196] U. Ekström and P. Norman, Phys. Rev. A **74**, 042722 (2006).

[197] A. Jiemchooroj, U. Ekström, and P. Norman, J. Chem. Phys. **127**, 165104 (2007).

[198] A. Jiemchooroj and P. Norman, J. Chem. Phys. **128**, 234304 (2008).

[199] A. Jiemchooroj and P. Norman, J. Chem. Phys. **126**, 134102 (2007).

[200] S. Villaume and P. Norman, Chirality **21**, E13 (2009).

[201] F. Neese et al., ORCA: An ab initio , DFT, and Semiempirical Electronic Structure Package, Version 2.8.0; University of Bonn; Bonn, Germany, Program, 2010.

[202] J. Pipek and P. G. Mezey, J. Chem. Phys. **90**, 4916 (1989).

[203] E. Van Lenthe and E. J. Baerends, J. Comput. Chem. **24**, 1142 (2003).

[204] ADF2012, SCM, Theoretical Chemistry, Vrije Universiteit, Amsterdam, The Netherlands, http://www.scm.com, Program.

[205] R. Ahlrichs et al., TURBOMOLE, URL: http://www.turbomole.com.

[206] R. Ahlrichs, M. Bär, M. Häser, H. Horn, and C. Kölmel, Chem. Phys. Lett. **162**, 165 (1989).

[207] J. G. Hill, Int. J. Quantum Chem. **113**, 21 (2013).

[208] A. Schäfer, H. Horn, and R. Ahlrichs, J. Chem. Phys. **97**, 2571 (1992).

[209] F. Weigend and R. Ahlrichs, Phys. Chem. Chem. Phys. **7**, 3297 (2005).

[210] F. Weigend, F. Furche, and R. Ahlrichs, J. Chem. Phys. **119**, 12753 (2003).

[211] F. Neese, Inorg. Chim. Acta **337**, 181 (2002).

[212] M. A. Watson, N. C. Handy, and A. J. Cohen, J. Chem. Phys. **119**, 6475 (2003).

[213] P. J. Stephens, F. J. Devlin, C. F. Chabalowski, and M. J. Frisch, J. Phys. Chem.-US **98**, 11623 (1994).

[214] R. van Leeuwen and E. J. Baerends, Phys. Rev. A **49**, 2421 (1994).

[215] O. Gritsenko, P. Schipper, and E. Baerends, Chem. Phys. Lett. **302**, 199 (1999).

[216] P. R. T. Schipper, O. V. Gritsenko, S. J. A. van Gisbergen, and E. J. Baerends, J. Chem. Phys. **112**, 1344 (2000).

[217] E. van Lenthe, A. Ehlers, and E. Baerends, J. Chem. Phys. **110**, 8943 (1999).

[218] E. van Lenthe, E. Baerends, and J. Snijders, J. Chem. Phys. **99**, 4597 (1993).

[219] E. van Lenthe, E. Baerends, and J. Snijders, J. Chem. Phys. **101**, 9783 (1994).

[220] E. van Lenthe, J. Snijders, and E. Baerends, J. Chem. Phys. **105**, 6505 (1994).

[221] E. B. E. van Lenthe, R. van Leeuwen and J. Snijders, Int. J. Quantum Chem. **57**, 281 (1996).

[222] C. van Wüllen, J. Chem. Phys. **109**, 392 (1998).

[223] B. A. Hess, Phys. Rev. A **33**, 3742 (1986).

[224] G. Jansen and B. A. Hess, Phys. Rev. A **39**, 6016 (1989).

[225] J. O. Moulin, J. Evans, D. S. McGuinness, G. Reid, A. J. Rucklidge, R. P. Tooze, and M. Tromp, Dalton T. , 1177 (2008).

[226] H. Junge et al., Chem.-Eur. J. **18**, 12749 (2012).

[227] J. Szlachetko, M. Nachtegaal, J. Sá, J.-C. Dousse, J. Hoszowska, E. Kleymenov, M. Janousch, O. V. Safonova, C. König, and J. A. v. Bokhoven, Chem. Commun. **48**, 10898 (2012).

[228] A. Mijovilovich, H. Hayashi, N. Kawamura, H. Osawa, P. C. A. Bruijnincx, R. J. M. Klein Gebbink, F. M. F. de Groot, and B. M. Weckhuysen, Eur. J. Inorg. Chem. **2012**, 1589 (2012).

[229] D. Ferri, M. S. Kumar, R. Wirz, A. Eyssler, O. Korsak, P. Hug, A. Weidenkaff, and M. A. Newton, Phys. Chem. Chem. Phys. **12**, 5634 (2010).

[230] P. Ghigna, S. Pin, G. Spinolo, M. A. Newton, M. Zema, S. C. Tarantino, G. Capitani, and F. Tatti, Phys. Chem. Chem. Phys. **12**, 5547 (2010).

[231] N. Guo, B. R. Fingland, W. D. Williams, V. F. Kispersky, J. Jelic, W. N. Delgass, F. H. Ribeiro, R. J. Meyer, and J. T. Miller, Phys. Chem. Chem. Phys. **12**, 5678 (2010).

[232] C. Bolm, M. Martin, G. Gescheidt, C. Palivan, T. Stanoeva, H. Bertagnolli, M. Feth, A. Schweiger, G. Mitrikas, and J. Harmer, Chem.-Eur. J. **13**, 1842 (2007).

[233] A. S. K. Hashmi, C. Lothschütz, M. Ackermann, R. Doepp, S. Anantharaman, B. Marchetti, H. Bertagnolli, and F. Rominger, Chem.-Eur. J. **16**, 8012 (2010).

[234] M. Tromp, J. A. van Bokhoven, A. M. Arink, J. H. Bitter, G. van Koten, and D. C. Koningsberger, Chem.-Eur. J. **8**, 5667 (2002).

[235] F. Di Benedetto, F. D'Acapito, G. Fornaciai, M. Innocenti, G. Montegrossi, L. A. Pardi, S. Tesi, and M. Romanelli, Phys. Chem. Miner. **37**, 283 (2009).

[236] M. Bauer, S. Müller, G. Kickelbick, and H. Bertagnolli, New J. Chem. **31**, 1950 (2007).

[237] M. Rohr, J.-D. Grunwaldt, and A. Baiker, J. Catal. **229**, 144 (2005).

[238] J.-D. Grunwaldt and A. Baiker, Phys. Chem. Chem. Phys. **7**, 3526 (2005).

[239] M. Bauer, T. Stalinski, and E. F. Aziz, ChemPhysChem **12**, 2088 (2011).

[240] E. Otero, R. G. Wilks, T. Regier, R. I. R. Blyth, A. Moewes, and S. G. Urquhart, J. Phys. Chem. A **112**, 624 (2008).

[241] J. Singh, E. M. C. Alayon, M. Tromp, O. V. Safonova, P. Glatzel, M. Nachtegaal, R. Frahm, and J. A. van Bokhoven, Angew. Chem. Int. Ed. **47**, 9260 (2008).

[242] F. M. F. de Groot, M. H. Krisch, and J. Vogel, Phys. Rev. B **66**, 195112 (2002).

[243] S. G. Eeckhout, O. V. Safonova, G. Smolentsev, M. Biasioli, V. A. Safonov, L. N. Vykhodtseva, M. Sikora, and P. Glatzel, J. Anal. Atom. Spectrom. **24**, 215 (2009).

[244] J. Sá et al., Catal. Sci. Technol. **2**, 794 (2012).

[245] C. C. Scarborough, S. Sproules, T. Weyhermüller, S. DeBeer, and K. Wieghardt, Inorg. Chem. **50**, 12446 (2011).

[246] J. B. H. Strautmann, C.-G. Freiherr von Richthofen, G. Heinze-Brückner, S. DeBeer, E. Bothe, E. Bill, T. Weyhermüller, A. Stammler, H. Bögge, and T. Glaser, Inorg. Chem. **50**, 155 (2011).

[247] M. Bochmann, J. Chem. Soc. Dalton , 255 (1996).

[248] H. H. Brintzinger, D. Fischer, R. Mülhaupt, B. Rieger, and R. M. Waymouth, Angew. Chem. Int. Ed. **34**, 1143 (1995).

[249] D. Veghini, L. M. Henling, T. J. Burkhardt, and J. E. Bercaw, J. Am. Chem. Soc. **121**, 564

(1999).

[250] R. C. J. Atkinson, V. C. Gibson, and N. J. Long, Chem. Soc. Rev. **33**, 313 (2004).

[251] U. Siemeling, D. Rother, and C. Bruhn, Organometallics **27**, 6419 (2008).

[252] H. Schottenberger, K. Wurst, and M. R. Buchmeiser, J. Organomet. Chem. **584**, 301 (1999).

[253] M. Ruiz-Lopez, M. Loos, J. Goulon, M. Benfatto, and C. Natoli, Chem. Phys. **121**, 419 (1988).

[254] E. Otero, N. Kosugi, and S. G. Urquhart, J. Chem. Phys. **131**, 114313 (2009).

[255] J. Estephane et al., J. Phys. Chem. C **113**, 7305 (2009).

[256] J. Estephane et al., J. Phys. Chem. C **114**, 4451 (2010).

[257] J. Martin, J. Baker, and P. Pulay, J. Comput. Chem. **30**, 881 (2009).

[258] G. Zhang, H. Zhang, M. Sun, Y. Liu, X. Pang, X. Yu, B. Liu, and Z. Li, J. Comput. Chem. **28**, 2260 (2007).

[259] A. Boccia, A. G. Marrani, S. Stranges, R. Zanoni, M. Alagia, M. Cossi, and M. F. Iozzi, J. Chem. Phys. **128**, 154315 (2008).

[260] R. Jenkins, R. Manne, R. Robin, and C. Senemaud, X-ray Spectrom. **20**, 149 (1991).

[261] S. DeBeer George and F. Neese, Inorg. Chem. **49**, 1849 (2010).

[262] R. K. Hocking, S. D. George, Z. Gross, F. A. Walker, K. O. Hodgson, B. Hedman, and E. I. Solomon, Inorg. Chem. **48**, 1678 (2009).

[263] J. F. Berry, S. D. George, and F. Neese, Phys. Chem. Chem. Phys. **10**, 4361 (2008).

[264] C. Daul, Int. J. Quantum Chem. **52**, 867 (1994).

[265] T. Ziegler and A. Rauk, Theor. Chim. Acta **46**, 1 (1977).

[266] W. Hua, Y.-J. Ai, B. Gao, H. Li, H. Ågren, and Y. Luo, Phys. Chem. Chem. Phys. **14**, 9666 (2012).

[267] C. Gauthier, V. A. Solé, R. Signorato, J. Goulon, and E. Moguiline, J. Synchotron Radiat. **6**, 164 (1999).

[268] A. J. Atkins, M. Bauer, and C. R. Jacob, Phys. Chem. Chem. Phys. **15**, 8095 (2013).

[269] ADF2010, SCM, Theoretical Chemistry, Vrije Universiteit, Amsterdam, The Netherlands, Program.

[270] C. F. Guerra, J. G. Snijders, G. t. Velde, and E. J. Baerends, Theor. Chem. Acc. **99**, 391 (1998).

[271] P. Banerjee, S. Sproules, T. Weyhermüller, S. DeBeer George, and K. Wieghardt, Inorg. Chem. **48**, 5829 (2009).

[272] C. C. Scarborough, S. Sproules, C. J. Doonan, K. S. Hagen, T. Weyhermüller, and K. Wieghardt, Inorg. Chem. **51**, 6969 (2012).

[273] U. Varetto, Molekel, swiss national supercomputing cnetre, manno, switzerland, Program, 2009.

[274] P. S. Singh, H. C. Rudbeck, P. Huang, S. Ezzaher, L. Eriksson, M. Stein, S. Ott, and R. Lomoth, Inorg. Chem. **48**, 10883 (2009).

[275] A. Chen, M. Kaminsky, G. L. Geoffroy, and M. A. Vannice, J. Phys. Chem.-US **90**, 4810 (1986).

[276] M. Kollár, A. De Stefanis, H. E. Solt, M. R. Mihályi, J. Valyon, and A. A. Tomlinson, J. Mol. Catal. A-Chem. **333**, 37 (2010).

[277] C. Li, P. Wang, W. Ying, and D. Fang, Petrol. Sci. Technol. **29**, 1546 (2011).

[278] H. P. Withers, K. F. Eliezer, and J. W. Mitchell, Ind. Eng. Chem, Res. **29**, 1807 (1990).

[279] S. Lögdberg, M. Lualdi, S. Järås, J. C. Walmsley, E. A. Blekkan, E. Rytter, and A. Holmen, J. Catal. **274**, 84 (2010).

[280] C. Zhang, G. Zhao, K. Liu, Y. Yang, H. Xiang, and Y. Li, J. Mol. Catal. A-Chem. **328**, 35 (2010).

[281] B. H. Davis, Catal. Today **141**, 25 (2009).

[282] H. Kuroda, Pure Appl. Chem. **64**, 1449 (1992).

[283] P. Johnston, G. Hutchings, N. Coville, K. Finch, and J. Moss, Appl. Catal. A-Gen **186**, 245 (1999).

[284] L. Bañares, T. Baumert, M. Bergt, B. Kiefer, and G. Gerber, Chem. Phys. Lett. **267**, 141 (1997).

[285] F. Gãrtner, B. Sundararaju, A.-E. Surkus, A. Boddien, B. Loges, H. Junge, P. Dixneuf, and M. Beller, Angew. Chem. Int. Ed. **48**, 9962 (2009).

[286] P. T. Snee, C. K. Payne, S. D. Mebane, K. T. Kotz, and C. B. Harris, J. Am. Chem. Soc. **123**, 6909 (2001).

[287] M. Wrighton, Chem. Rev. **74**, 401 (1974).

[288] W. Edgell, W. Wilson, and R. Summitt, Spectrochim. Acta **19**, 863 (1963).

[289] B. Ahr, M. Chollet, B. Adams, E. M. Lunny, C. M. Laperle, and C. Rose-Petruck, Phys. Chem. Chem. Phys. **13**, 5590 (2011).

[290] J. M. Ramallo-López, E. J. Lede, F. G. Requejo, J. A. Rodriguez, J.-Y. Kim, R. Rosas-Salas, and J. M. Domínguez, J. Phys. Chem. B **108**, 20005 (2004).

[291] T. Lee, E. Welch, and C. G. Rose-Petruck, J. Phys. Chem. A **108**, 11768 (2004).

[292] T. Lee, F. Benesch, Y. Jiang, and C. G. Rose-Petruck, Chem. Phys. **299**, 233 (2004).

[293] G. Fronzoni, P. Decleva, and A. Lisini, Chem. Phys. **174**, 57 (1993).

[294] J. H. Jang, J. G. Lee, H. Lee, Y. Xie, and H. F. Schaefer, J. Phys. Chem. A **102**, 5298 (1998).

[295] P. Hirva, M. Haukka, M. Jakonen, and M. A. Moreno, J. Mol. Model. **14**, 171 (2008).

[296] D. Guenzburger, E. Baggio-Saitovitch, M. A. De Paoli, and H. Manela, J. Chem. Phys. **80**, 735 (1984).

[297] E. Hunstock, C. Mealli, M. J. Calhorda, and J. Reinhold, Inorg. Chem. **38**, 5053 (1999).

[298] Q. Li, Y.-N. Li, T. Wang, S.-G. Wang, C.-F. Huo, Y.-W. Li, J. Wang, and H. Jiao, ChemPhysChem **14**, 1573 (2013).

[299] W. Heijser, E. J. Baerends, and P. Ros, Faraday Symp. Chem. S **14**, 211 (1980).

[300] C. W. Bauschlicher, J. Chem. Phys. **84**, 872 (1986).

[301] J. Reinhold, O. Kluge, and C. Mealli, Inorg. Chem. **46**, 7142 (2007).

[302] J. Reinhold, A. Barthel, and C. Mealli, Coordin. Chem. Rev. **238–239**, 333 (2003).

[303] F. A. Cotton and D. L. Hunter, Inorg. Chim. Acta **11**, L9 (1974).

[304] F. A. Cotton and J. M. Troup, J. Am. Chem. Soc. **96**, 4155 (1974).

[305] D. Braga, L. Farrugia, F. Grepioni, and B. F. Johnson, J. Organomet. Chem. **464**, C39 (1994).

[306] N. Binsted, S. L. Cook, J. Evans, G. N. Greaves, and R. J. Price, J. Am. Chem. Soc. **109**, 3669 (1987).

[307] J. Li and K. Jug, Inorg. Chim. Acta **196**, 89 (1992).

[308] D. Braga, F. Grepioni, E. Tedesco, M. J. Calhorda, and P. E. M. Lopes, J. Chem. Soc. Dalton , 3297 (1995).

[309] S. Xu, J. Zhang, B. Zhu, B. Wang, X. Zhou, and L. Weng, J. Organomet. Chem. **626**, 186 (2001).

[310] B. E. Bursten and R. F. Fenske, Inorg. Chem. **18**, 1760 (1979).

[311] J. Cawse, R. Fiato, and R. Pruett, J. Organomet. Chem. **172**, 405 (1979).

[312] B. Dickens and W. L. Lipscomb, Molecular and Valence Structures of Complexes of Cyclooctatetraene With Iron Tricarbonyl, Technical report, DTIC Document, 1962.

[313] I. Butler and H. Spendjian, J. Organomet. Chem. **18**, 145 (1969).

[314] H. Li, H. Feng, W. Sun, Y. Xie, R. B. King, and H. F. Schaefer, Eur. J. Inorg. Chem. **2011**, 2746 (2011).

[315] O. S. Mills, Acta Crystallogr. **11**, 620 (1958).

[316] R. J. Haines and A. L. Du Preez, Inorg. Chem. **8**, 1459 (1969).

[317] R. F. Bryan, P. T. Greene, M. J. Newlands, and D. S. Field, J. Chem. Soc. A , 3068 (1970).

[318] R. F. Bryan and P. T. Greene, J. Chem. Soc. A , 3064 (1970).